

Interim Progress Report
for the period January 1 - August 31, 1991

on

**ANALYSIS OF ELECTROMAGNETIC INTERFERENCE FROM
POWER SYSTEM PROCESSING AND TRANSMISSION
COMPONENTS FOR SPACE STATION FREEDOM**

Grant No. NAG3-1126

*GRANT
N-32-CR*

by

37976

Peter W. Barber
Principal Investigator

P-224

and

Nabeel A.O. Demerdash
Co-Principal Investigator

Research Assistants: R. Wang, B. Hurysz, Z. Luo

Department of Electrical and Computer Engineering
Clarkson University
Potsdam, NY 13699-5720

Consultants: Hugh W. Denny and David P. Millard
Georgia Tech Research Institute

Submitted to

Power Management and Distribution Systems Branch
Mail Stop 500-102
NASA - Lewis Research Center
21000 Brookpark Road
Cleveland, OH 44135

(NASA-CR-186564) ANALYSIS OF
ELECTROMAGNETIC INTERFERENCE FROM POWER
SYSTEM PROCESSING AND TRANSMISSION
COMPONENTS FOR SPACE STATION FREEDOM Interim
Progress Report, 1 Jan. - 31 Aug. 1991

N91-30393

Unclas
G3/32 0037976

Interim Progress Report
for the period January 1 - August 31, 1991

on

**ANALYSIS OF ELECTROMAGNETIC INTERFERENCE FROM
POWER SYSTEM PROCESSING AND TRANSMISSION
COMPONENTS FOR SPACE STATION FREEDOM**

Grant No. NAG3-1126

by



Peter W. Barber
Principal Investigator

and



Nabeel A.O. Demerdash
Co-Principal Investigator

Research Assistants: R. Wang, B. Hurysz, Z. Luo

Department of Electrical and Computer Engineering
Clarkson University
Potsdam, NY 13699-5720

Consultants: Hugh W. Denny and David P. Millard
Georgia Tech Research Institute

ANALYSIS OF ELECTROMAGNETIC INTERFERENCE FROM POWER SYSTEM PROCESSING AND TRANSMISSION COMPONENTS FOR SPACE STATION FREEDOM

1 Introduction

The goal of this research project is to analyze the potential effects of electromagnetic interference (EMI) originating from power system processing and transmission components for Space Station Freedom. The approach consists of four steps:

1. Develop analytical tools (models and computer programs).
2. Conduct parameterization (what if?) studies.
3. Predict the global space station EMI environment.
4. Provide a basis for modification of EMI standards.

This report summarizes work performed during the period January 1 - August 31, 1991.

2 Device Models

This portion of the investigation centers on the development of computer models which can be used to predict the local electromagnetic fields for various power system components or devices, including various transmission line configurations. Recent work is summarized in the Master's thesis of Mr. Zemin Luo, which is attached as Appendix A.

3 Radiation Sources

This portion of the investigation centers on the development of computer models to simulate the propagation of electromagnetic waves in the ionospheric plasma and the radiation from antennas simulating EMI sources on the space station. Recent work is summarized in the Master's thesis of Mr. Brian J. Hurysz, which is attached as Appendix B.

4 Future Work

Continuing work involves an investigation of $\mathbf{v} \times \mathbf{B}$ effects and the development of a more sophisticated method-of-moments model of the space station.

Appendix A

Electromagnetic Fields Surrounding Transmission
Lines in Space Station Applications using Finite
Elements and Ballooning Methods for Simulation of
Infinite Boundaries

CLARKSON UNIVERSITY

ELECTROMAGNETIC FIELDS SURROUNDING
TRANSMISSION LINES IN SPACE STATION
APPLICATIONS USING FINITE ELEMENTS AND
BALLOONING METHODS FOR SIMULATION OF
INFINITE BOUNDARIES

A THESIS

BY

ZEMIN LUO

DEPARTMENT OF ELECTRICAL AND COMPUTER ENGINEERING

SUBMITTED IN PARTIAL FULFILLMENT OF THE REQUIREMENTS
FOR THE DEGREE OF
MASTER OF SCIENCE
(ELECTRICAL ENGINEERING)

September 1991

Accepted by the Graduate School

Date

DEAN

The undersigned have examined the thesis entitled
ELECTROMAGNETIC FIELDS SURROUNDING TRANSMISSION LINES IN
SPACE STATION APPLICATIONS USING FINITE ELEMENTS AND
BALLOONING METHODS FOR SIMULATION OF INFINITE BOUNDARIES

presented by Zemin Luo, a candidate for the degree of
Master of Science, and hereby certify that it is worthy of acceptance.

Date

ADVISOR Nabeel A.O. Demerdash

EXAMINING COMMITTEE

Peter W. Barber

Nabeel A.O. Demerdash

Hossein Salehfar

Abstract

Ballooning techniques in conjunction with the two dimensional finite element (2DFE) method are described for modeling and computing a two dimensional (2D) magnetostatic field in a two-wire parallel-pair transmission line problem in an unbounded region. Solutions using the combined ballooning 2DFE method are shown in this thesis to agree closely with analytical solutions for the two-wire parallel-pair transmission line in the same unbounded region. These 2DFE techniques are used here to study the effects of magnetic shielding and the effects of defects in such shielding. The distribution and profiles of magnetic fields surrounding such transmission lines are studied, for future use of investigating electromagnetic compatibility aspects associated with power processors and systems in the future Space Station Freedom. The combined ballooning 2DFE method is developed further for a 2D diffusion type (eddy-current) field and then applied to solve the problem in the two-wire parallel-pair transmission line with a conductive shield. Various cases such as the effects of conductive shielding thickness, and the effects of defective shielding are considered.

Furthermore, in this thesis, a closed-form solution for the magnetostatic case in a two-wire twisted-pair transmission line is derived using *Biot – Savart Law*. The flux density comparisons between twisted-pair and parallel-pair cases are carried out and the effects of the length of the pitch of the twisted-pair line on the magnetic field profiles are obtained. The results shown in this thesis imply that a three-dimensional (3D) ballooning method using finite elements is needed for the magnetic shielding case as well as in the quasi-static diffusion type case. This quasi-static class can involve transmission lines in plasma, with or without conductive metallic shielding.

Acknowledgements

The author wishes to express his deep appreciation to Professor N.A.O.Demerdash who provided the guidance, encouragement and inspiration necessary for the completion of this thesis. The many ideas and suggestions offered by professor Demerdash form the backbone of this thesis.

The author would also like to extend gratitude to the following individuals: Professor Peter W. Barber, and Professor Hossein Salehfar who served on the author's examining committee for their concerns and support in this research work.

Also, the author wishes to acknowledge the funding support received from NASA Lewis Research Center for this work under Grant No. NAG3-1126 which made this work possible.

Contents

Abstract	iii
Acknowledgements	iv
1 INTRODUCTION	1
1.1 Background and Literature Search	1
1.2 Definition of the Problem	3
2 THEORETICAL BACKGROUND	6
2.1 Formulation - the Governing Differential Equations	6
2.2 The Finite Element Method	8
3 COMPARISONS BETWEEN THE CLOSED-FORM SOLUTION AND 2DFE SOLUTION FOR THE TWO-WIRE PARALLEL-PAIR CASE	13
3.1 The Closed-Form Solution	13
3.2 The 2DFE Solution	15
3.3 Comparisons Between the Closed-Form Solution and 2D-FE Solution	16
4 THE BALLOONING MODEL IN THE 2D MAGNETOSTATIC CASE	29
4.1 Ballooning Technique in the Magnetostatic Case	30
4.2 Exploration of the 2DFE Ballooning Model by Test Examples	35
4.3 The Effects of the Shielding and the Effects of Defects	36

5	THE BALLOONING MODEL IN THE 2D DIFFUSION QUASI-STATIC CASE	70
5.1	The 2DFE Ballooning Model in the Quasi Static Case	70
5.2	The 2DFE Solution Using Ballooning Techniques with Conductive Shielding	74
5.3	The 2DFE Solution Using Ballooning Techniques with Defects of the Conductive Shielding	76
6	CLOSED FORM SOLUTION OF THE TWISTED-PAIR TRANSMISSION LINE	108
6.1	The Derivation of the Formulation	108
6.2	The Computation of Flux Densities	113
7	CONCLUSIONS AND FUTURE WORK	127
7.1	Conclusions	127
7.2	Future Work	129
	Bibliography	131

List of Tables

3.1	Comparison Between MVP's Obtained From Analytical and 2DFE Methods at Locations Away From the Conductors	25
3.2	Comparison Between Flux Densities Obtained From Analytical and 2DFE Methods at Locations Away From the Conductors	26
3.3	Comparison Between MVP's Obtained From Analytical and 2DFE Methods at Locations Close to the Conductors	27
3.4	Comparison Between Flux Densities Obtained from Analytical and 2DFE Methods at Locations Close to the Conductors	28
4.1	MVP Comparison Between Analytical and 2DFE Ballooning Solutions for $m=0, 2$ and 5	50
4.2	MVP Comparison Between Analytical and 2DFE Ballooning Solutions for $m=10, 20$ and 30	51
4.3	Flux Density Comparison Between Analytical and 2DFE Ballooning Solutions for $m=0, 2$	52
4.4	Flux Density Comparison Between Analytical and 2DFE Ballooning Solutions for $m=5, 10$	53
4.5	Flux Density Comparison Between Analytical and 2DFE Ballooning Solutions for $m=20, 30$	54
4.6	Flux Density Values in Cases of Shielding Materials With Various Relative Permeabilities Without Defects	68
4.7	Flux Density With Defective Shielding for Various Defect Angles δ , for a Shielding Material With $\mu_r = 1000$	69

List of Figures

2.1	The First Order Triangular Finite Element	12
3.1	The Two-Wire Parallel-Pair Transmission Line Geometry	17
3.2	Equipotential Contours in the Immidiate Vicinity of the Two-Wire Conductors Obtained From the Analytical Method	18
3.3	Equipotential Contours Beyond the Vicinity of the Two-Wire Conduc- tors Obtained From the Analytical Method	19
3.4	The Geometry of the Region in the Immediate Vicinity of the Two- Wire Conductors	20
3.5	The FE Grid in the Immediate Vicinity of the Two-Wire Conductors	21
3.6	Equipotential Contours in the Immediate Vicinity of the Two-Wire Conductors Obtained From the 2DFE Method	22
3.7	The FE Grid Beyond the Immidiate Vicinity of the Two-Wire Conductors	23
3.8	Equipotential Contours Beyond the Vicinity of the Two-Wire Conduc- tors Obtained From the 2DFE Method	24
4.1	Interior FE Grid With Boundary Γ_0 for the Parallel-Pair Transmission Line	38
4.2	The Nature of FE Grids in Bounded Exterior Regions for Ballooning Puroses	39
4.3	FE Grids for the Parallel-Pair Transmission Line With and Without Ballooning	40
4.4	Geometry of a Two-Wire Parallel-Pair Transmission Line Case	41
4.5	FE Grid for the Two-Wire Parallel-Pair Transmission Line Case . . .	42

4.6	MVP Equipotentials for the Parallel-Pair Case Obtained From the Analytical Solution	43
4.7	MVP Equipotentials Obtained From the FE Solutions With Natural Open Boundary Conditions - No Ballooning	44
4.8	MVP Equipotentials Obtained From the FE Solutions With 2 Ballooning Layers	45
4.9	MVP Equipotentials Obtained From the FE Solutions With 5 Ballooning Layers	46
4.10	MVP Equipotentials Obtained From the FE Solutions With 10 Ballooning Layers	47
4.11	MVP Equipotentials Obtained From the FE Solutions With 15 Ballooning Layers	48
4.12	MVP Equipotentials Obtained From the FE Solutions With 20 Ballooning Layers	49
4.13	Finite Elements Chosen for MVP and Flux Density Data Comparisons in Tables (4.1) Through (4.5)	55
4.14	The Parallel-Pair MVP Equipotentials Obtained From FE Solutions With Ballooning (m=15) Including Shielding ($\mu_r = 10$)	56
4.15	The Parallel-Pair MVP Equipotentials Obtained From FE Solutions With Ballooning (m=15) Including Shielding ($\mu_r = 100$)	57
4.16	The Parallel-Pair MVP Equipotentials Obtained From FE Solutions With Ballooning (m=15) Including Shielding ($\mu_r = 1000$)	58
4.17	The Parallel-Pair MVP Equipotentials Obtained From FE Solutions With Ballooning (m=15) Including Shielding ($\mu_r = 5000$)	59
4.18	Finite Elements at Which the Effects of Shielding on Flux Densities are Given in Table(4.6)	60
4.19	Geometry of a Defective Shield Case ($\delta = 10^\circ$)	61
4.20	The Parallel-Pair MVP Equipotentials Obtained With Ballooning (m=15) Including a Defective Shielding Case ($\mu_r = 1000, \delta = 10^\circ$)	62
4.21	Geometry of a Defective Shield Case ($\delta = 20^\circ$)	63

4.22	The Parallel-Pair MVP Equipotentials Obtained With Ballooning (m=15) Including a Defective Shielding Case ($\mu_r = 1000, \delta = 20^\circ$)	64
4.23	Geometry of a Defective Shield Case ($\delta = 30^\circ$)	65
4.24	The Parallel-Pair MVP Equipotentials Obtained With Ballooning (m=15) Including a Defective Shielding Case ($\mu_r = 1000, \delta = 30^\circ$)	66
4.25	Finite Elements at Which the Effects of Defective Shielding on Flux Densities are Given in Table (4.7)	67
5.1	Geometry of a Two-Wire Parallel-Pair Transmission Line Case	78
5.2	The Parallel-Pair MVP Equipotentials Obtained From FE Solutions for $f = 0Hz$ With Conductive Shielding Without Ballooning - The Natural Open Boundary	79
5.3	The Parallel-Pair MVP Equipotentials Obtained From FE Solutions With Ballooning (m=2) for $f = 0Hz$ With Conductive Shielding . . .	80
5.4	The Parallel-Pair MVP Equipotentials Obtained From FE Solutions With Ballooning (m=5) for $f = 0Hz$ With Conductive Shielding . . .	81
5.5	The Parallel-Pair MVP Equipotentials Obtained From FE Solutions With Ballooning (m=10) for $f = 0Hz$ With Conductive Shielding . .	82
5.6	The Parallel-Pair MVP Equipotentials Obtained From FE Solutions With Ballooning (m=20) for $f = 0Hz$ With Conductive Shielding . .	83
5.7	The Parallel-Pair MVP Equipotentials Obtained From FE Solutions for $f = 400Hz$ With Conductive Shielding Without Ballooning - The Natural Open Boundary	84
5.8	The Parallel-Pair MVP Equipotentials Obtained From FE Solutions With Ballooning (m=2) for $f = 400Hz$ With Conductive Shielding .	85
5.9	The Parallel-Pair MVP Equipotentials Obtained From FE Solutions With Ballooning (m=5) for $f = 400Hz$ With Conductive Shielding .	86
5.10	The Parallel-Pair MVP Equipotentials Obtained From FE Solutions With Ballooning (m=10) for $f = 400Hz$ With Conductive Shielding .	87
5.11	The Parallel-Pair MVP Equipotentials Obtained From FE Solutions With Ballooning (m=20) for $f = 400Hz$ With Conductive Shielding .	88

5.12	The Parallel-Pair MVP Equipotentials Obtained From FE Solutions for $f = 2kHz$ With Conductive Shielding Without Ballooning - The Natural Open Boundary	89
5.13	The Parallel-Pair MVP Equipotentials Obtained From FE Solutions With Ballooning ($m=2$) for $f = 2kHz$ With Conductive Shielding . .	90
5.14	The Parallel-Pair MVP Equipotentials Obtained From FE Solutions With Ballooning ($m=5$) for $f = 2kHz$ With Conductive Shielding . .	91
5.15	The Parallel-Pair MVP Equipotentials Obtained From FE Solutions With Ballooning ($m=10$) for $f = 2kHz$ With Conductive Shielding .	92
5.16	The Parallel-Pair MVP Equipotentials Obtained From FE Solutions With Ballooning ($m=20$) for $f = 2kHz$ With Conductive Shielding .	93
5.17	The Parallel-Pair MVP Equipotentials Obtained From FE Solutions for $f = 20kHz$ With Conductive Shielding Without Ballooning - The Natural Open Boundary	94
5.18	The Parallel-Pair MVP Equipotentials Obtained From FE Solutions With Ballooning ($m=2$) for $f = 20kHz$ With Conductive Shielding .	95
5.19	The Parallel-Pair MVP Equipotentials Obtained From FE Solutions With Ballooning ($m=5$) for $f = 20kHz$ With Conductive Shielding .	96
5.20	The Parallel-Pair MVP Equipotentials Obtained From FE Solutions With Ballooning ($m=10$) for $f = 20kHz$ With Conductive Shielding .	97
5.21	The Parallel-Pair MVP Equipotentials Obtained From FE Solutions With Ballooning ($m=20$) for $f = 20kHz$ With Conductive Shielding .	98
5.22	Finite Elements at Which the Effects of Shielding Thickness on Flux Densities are Given in Figures(5.23) Through (5.25)	99
5.23	Flux Density Magnitudes With Ballooning ($m=10$) and no Defects With a Conductive Shield Thickness, $\Delta_s=0.1$ in, for $f=0$ Hz, 400 Hz, 2 kHz, 20 kHz and 100 kHz, for a Current $I=500$ A	100
5.24	Flux Density Magnitudes With Ballooning ($m=10$) and no Defects With a Conductive Shield Thickness, $\Delta_s=0.05$ in, for $f=0$ Hz, 400 Hz, 2 kHz, 20 kHz and 100 kHz, for a Current $I=500$ A	101

5.25 Flux Density Magnitudes With Ballooning ($m=10$) and no Defects With a Conductive Shield Thickness, $\Delta_s=0.025$ in, for $f=0$ Hz, 400 Hz, 2 kHz, 20 kHz and 100 kHz, for a Current $I=500$ A	102
5.26 The Parallel-Pair MVP Equipotentials Obtained From FE Solutions With Ballooning ($m=10$) for $f = 400Hz$ - the Case of a Conductive Shield With an Angular Defect, $\delta = 10^\circ$ Shield Thickness, $\Delta_s=0.025$ in, for a Current $I=500$ A	103
5.27 The Parallel-Pair MVP Equipotentials Obtained From FE Solutions With Ballooning ($m=10$) for $f = 400Hz$ - the Case of a Conductive Shield With an Angular Defect, $\delta = 20^\circ$ Shield Thickness, $\Delta_s=0.025$ in, for a Current $I=500$ A	104
5.28 The Parallel-Pair MVP Equipotentials Obtained From FE Solutions With Ballooning ($m=10$) for $f = 400Hz$ - the Case of a Conductive Shield With an Angular Defect, $\delta = 30^\circ$, Shield Thickness, $\Delta_s=0.025$ in, for a Current $I=500$ A	105
5.29 Finite Elements at Which the Effects of Defective Shielding on Flux Densities are Given in Figure(5.30)	106
5.30 Flux Density Magnitudes With Ballooning ($m=10$) and a Conductive Shield With an Angular Defect, $\delta = 20^\circ$, Shield Thickness, $\Delta_s=0.025$ in, for $f=0$ Hz, 400 Hz, 2 kHz, 20 kHz and 100 kHz, for a Current $I=500$ A	107
6.1 Isometric View of the Twisted-Pair Geometry and Locations Where the B Fields are Computed	115
6.2 Two-Wire (Twisted-Pair) Transmission Line	116
6.3 Twisted-Pair Cross Section at $\theta = 0^\circ$	117
6.4 Flux Density Components B_x and B_y for the Parallel-Pair in the $x - y$ Plane ($I = 500A$)	118
6.5 Flux Density Components B_x and B_y for the Twisted-Pair for a Pitch, $h = 5"$ ($=12.7$ cm) in the $\theta = 0^\circ$ Plane ($I = 500A$)	119

6.6	Flux Density Component B_x for the Twisted-Pair for a Pitch, $h = 5'' (=12.7 \text{ cm})$ in the $\theta = 0^\circ$ Plane ($I = 500A$)	120
6.7	Flux Density Components B_x and B_y for the Twisted-Pair for a Pitch, $h = 5'' (=12.7 \text{ cm})$ in the $\theta = 90^\circ$ Plane ($I = 500A$)	121
6.8	Flux Density Component B_x for the Twisted-Pair for a Pitch, $h = 5'' (=12.7 \text{ cm})$ in the $\theta = 90^\circ$ Plane ($I = 500A$)	122
6.9	Magnitude of Flux Density Component $ B_x _{max}$ for Different Pitch Lengths ($I = 500A$)	123
6.10	Magnitude of Flux Density Component $ B_y _{max}$ for Different Pitch Lengths ($I = 500A$)	124
6.11	Magnitude of Flux Density Component $ B_z _{max}$ for Different Pitch Lengths ($I = 500A$)	125
6.12	Magnitude of Flux Density $ B _{max}$ for Different Pitch Lengths ($I = 500A$)	126

Chapter 1

INTRODUCTION

This work is one portion of a large research project centering on the "Analysis of Electromagnetic Interference from Power System Processing and Transmission Components for Space Station Freedom ", and is concerned with aspects of developing device models for power system processing components and transmission lines in aerospace, where an infinite boundary and a plasma environment exist.

1.1 Background and Literature Search

One of the purposes of this work is to develop capabilities to compute the electromagnetic fields surrounding two-wire parallel-pair transmission lines and other possible transmission line configurations in aerospace applications, which can be solved as two dimensional (2D) problems with infinite (open) boundaries.

The finite element method was applied to magnetostatic field solutions which involved the calculation of electromagnetic fields in bounded regions governed by quasi-Poissonian partial differential equations (PDE) in 1970 [1]. Boundary conditions involving Neumann, Dirichlet and periodicity types were involved [1]. While such boundary conditions occur when magnetic fields are confined by magnetic-type or conductive-type materials, there are many problems without such confinement. Many field problems are unbounded; i.e., they cannot be encased within a finite boundary along which either the normal or tangential component of the field may be

specified. As a consequence, the actual boundary is at infinity, with the potential zero thereupon. When dealing with integral methods, this boundary condition is automatically taken care of and a greater economy of nodes and elements are given, however, the integral methods have disadvantages in that the resulting matrices are dense and their formulation and inversion are much less straightforward than the equivalent differential approach. However, it is difficult to account for partial differential equation (p.d.e.) inhomogeneities with differential methods for an infinite boundary. On the other hand, differential methods can easily account for PDE inhomogeneities, while requiring that the boundary be nearby so that the global matrix for the bounded region solution is not excessively large. Approximating an infinite (open) boundary by a closer one makes the potential fall (or rise) more rapidly and distorts the solution from the true open boundary results.

In a large number of electric and magnetic field problems, the solution requires the representation of a boundary which is remote from the region of interest. Typical of this class of problems are the single-sided linear machine, bus-bar impedance, and so on. There is, consequently, a need for a technique to combine a differential approach in the region containing all the field sources and materials with a simple representation of the exterior empty space. Thus additional work by Lowther (1978) [3], and Antunes (1982) [2], on a recursive (ballooning) finite element technique was developed for 2D planar magnetostatic field problems with open boundaries extending to infinity. Brauer (1982) [4] developed that ballooning technique for axisymmetric problems and general skin effect problems in which the eddy current is confined in the interior region and the Laplacian equation is satisfied in the exterior region.

Sometimes one is interested in the fields in both an interior region and an exterior region in a given problem. However, the above mentioned ballooning technique only uses the exterior region for the solution of the interior region. The solution of the exterior region cannot be obtained by the ballooning technique. Overcoming this difficulty with exterior field problems has spurred a whole new area of research activity; as a result, several schemes are now available for tackling this aspect. Some types of algorithms of semi-analytic methods (or hybrid harmonic/finite element method) tackling open boundary problems were presented by Lee and Cendes (1987) [5], Chari

(1987) [6], and Chari and Bedrosian (1987,1988) [7, 8] respectively. They used a circle as a boundary. The solution in the exterior region is obtained analytically and matched to the interior finite element solution.

To study the electromagnetic fields surrounding a two-wire parallel-pair transmission line in aerospace applications, a ballooning technique can be used because we are only interested in the fields in the interior region near the wires. However, no such ballooning techniques have been found in any literature for that type of problems because eddy current fields can exist in both the interior region and exterior region in the expected plasma environment of Space Station Freedom. This thesis will derive a new 2DFE ballooning method for the problem with eddy currents in both the interior region and exterior region and with an open boundary. Then this new ballooning 2DFE method is applied in this research which will be defined further in the next section.

The other purpose of this work is to develop models which can help engineers in studying the electromagnetic fields surrounding a two-wire twisted-pair transmission line and possible other configurations. To the best of this author's knowledge, no similar papers on such problem have been found in the literature. It is one of the purposes of this work to explain the nature of the field caused by this type of transmission lines. In this thesis, we only consider the magnetostatic case for the two-wire twisted-pair transmission line without shielding so that the closed-form analytical formulation can be employed to deal with this possible three dimensional (3D) problem. The results of this investigation will show the necessity of the need for the ballooning in conjunction with 3DFE methods to solve the eddy current problem with a twisted-pair transmission line with shielding.

1.2 Definition of the Problem

This research work centers on the development of computer models which can be used to predict the local electromagnetic fields with infinite boundary for various power system components or devices in aerospace applications, and specifically the case of the Space Station Freedom.

The effort is started in the magnetostatic case and is developed in the quasi-static case because of the existence of a plasma environment surrounding the Space Station. The first power system component to be analyzed is the two-wire parallel-pair transmission line with no shielding. This example is chosen because it is the simplest case of a two-wire transmission line for which there exists an analytical solution for comparison with and verification of the detailed FE modeling which will follow.

A two-dimensional finite element (2DFE) method will be used to obtain the local electromagnetic field distributions surrounding power system components and devices. In order to simulate the problem with the open boundary, a ballooning technique is introduced. With the ballooning technique, a matrix recursion algorithm is derived for a 2D problem in the static case and incorporated into the 2DFE method. This combined 2DFE ballooning method is applied to the example. The validity of this 2DFE method with the ballooning technique is demonstrated by comparison of the results with those of the analytical solution in the magnetostatic case with no shielding.

In the magnetostatic case, the 2DFE ballooning method is applied to the two-wire parallel-pair transmission line with continuous permeable cylindrical shields to determine the effects of the shielding. This method is applied further to the study of the field distributions resulting from discontinuities in permeable shielding surfaces due to accidental damage or to deliberate hardware design necessities.

The 2DFE ballooning model is developed in this work for the AC cases with frequencies in the Hz, and kHz ranges. In the AC case, the magnetic vector potential is a function of time. Assuming that the MVP varies sinusoidally, we can use phasor vectors in the problems. The field in the plasma environment can be equivalent to the eddy current field. A complex 2DFE model for eddy current problems is obtained and a complex matrix recursion algorithm is derived using the ballooning technique. In this thesis, it is shown how the AC ballooning is working in each chosen frequency ($f = 0$ Hz, 400 Hz, 2 kHz, and 20 kHz). With the AC 2DFE ballooning method, the effects of conductive shielding are studied in lower frequencies and higher frequencies. The effects of defective conducting shielding are also considered in a certain frequency ($f = 400$ Hz). The relations between the flux density magnitude and shield thickness

are shown in both defective shields and shields without defect cases.

The investigation of a 3D closed-form analytical formulation using the *Biot – Savart Law* is depicted for the magnetostatic field surrounding the two-wire twisted-pair transmission line. That formulation is an integral expression and the Gaussian numerical integral method is needed for the computer program. The results of this investigation indicate whether the near-field or the far-field are of 3D nature. Several different lengths of pitches are chosen for the flux density component comparisons, which also show that this problem cannot be simplified by a 2D solution approach. The 3D nature of this field means that it will be necessary to use 3DFE analysis to evaluate the magnetic material-type or eddy current-type electromagnetic shields and other related studies.

Chapter 2

THEORETICAL BACKGROUND

2.1 Formulation - the Governing Differential Equations

In this chapter the differential equation governing the magnetic fields within a two dimensional (2D) continuum is derived from Maxwell's equations and the definition of the magnetic vector potential. For the purpose of this study, the magnetic fields surrounding the two-wire parallel-pair transmission line are treated as being two dimensional (2D) in nature of the infinitely long transmission line case. Consequently, the conductor current can have a component in the axial-direction only. The materials within this continuum are assumed isotropic.

The fields in such a device are governed by Maxwell's equations, equations (2-1) through (2-4), as follows [11]:

$$\nabla \cdot \bar{B} = 0 \tag{2.1}$$

$$\nabla \cdot \bar{D} = \rho \tag{2.2}$$

$$\nabla \times \bar{H} = \bar{J}_s + \bar{J}_e + \frac{\partial \bar{D}}{\partial t} \tag{2.3}$$

$$\nabla \times \bar{\mathbf{E}} = -\frac{\partial \bar{\mathbf{D}}}{\partial t} \quad (2.4)$$

All the symbols used throughout this thesis are defined in the list of symbols (Appendix A). The constitutive relationships are:

$$\bar{\mathbf{B}} = \mu \bar{\mathbf{H}} = \frac{1}{\nu} \bar{\mathbf{H}} \quad (2.5)$$

$$\bar{\mathbf{D}} = \epsilon \bar{\mathbf{E}} \quad (2.6)$$

$$\bar{\mathbf{J}}_e = \sigma \bar{\mathbf{E}} \quad (2.7)$$

The magnetic vector potential $\bar{\mathbf{A}}$ and the magnetic flux density $\bar{\mathbf{B}}$ are related as:

$$\bar{\mathbf{B}} = \nabla \times \bar{\mathbf{A}} \quad (2.8)$$

The x and y components of $\bar{\mathbf{A}}$ are zero in the 2D case, therefore $\bar{\mathbf{B}}$ can be rewritten as follows:

$$\bar{\mathbf{B}} = \frac{\partial A_z}{\partial y} \bar{\mathbf{a}}_x - \frac{\partial A_z}{\partial x} \bar{\mathbf{a}}_y \quad (2.9)$$

Rewriting the curl of $\bar{\mathbf{A}}$ in terms of the magnetic field intensity gives:

$$\nu \bar{\mathbf{B}} = \bar{\mathbf{H}} = \nu(\nabla \times \bar{\mathbf{A}}) \quad (2.10)$$

Substituting Equation(2.10) into the third Maxwell equation, Equation(2.3), one obtains:

$$\nabla \times \bar{\mathbf{H}} = \nabla \times (\nu \nabla \times \bar{\mathbf{A}}) = \bar{\mathbf{J}}_s + \bar{\mathbf{J}}_e + \frac{\partial \bar{\mathbf{D}}}{\partial t} \quad (2.11)$$

In 2D cartesian coordinates Equation(2.11) becomes:

$$\frac{\partial}{\partial x} \left(\nu \frac{\partial A_z}{\partial x} \right) + \frac{\partial}{\partial y} \left(\nu \frac{\partial A_z}{\partial y} \right) = -(\bar{J}_{s_z} + \bar{J}_{e_z} + \frac{\partial \bar{D}_z}{\partial t}) \quad (2.12)$$

In the static case, the eddy current density component, $\bar{\mathbf{J}}_e$, and the displacement current density component, $\partial \bar{\mathbf{D}}/\partial t$ are both equal to zero, hence the contributions due to these terms will be zero. In the diffusion (eddy current) case, the displacement current is very small compared to the source current. For this reason, the contribution

of the displacement current can be neglected. Assuming that the magnetic vector potentials are functions of time which vary sinusoidally in both the diffusion (eddy current) case and high frequency radiation case, one can use phasor form equations in the frequency domain in these two cases. For convenience the subscripts of A_z and J_z will be dropped in future developments and discussions throughout this thesis. Equation(2.12) can therefore be rewritten as follows in the static case:

$$\frac{\partial}{\partial x}\left(\nu\frac{\partial A}{\partial x}\right) + \frac{\partial}{\partial y}\left(\nu\frac{\partial A}{\partial y}\right) = -J_s \quad (2.13)$$

In the diffusion (eddy current) case, one can write the following:

$$\frac{\partial}{\partial x}\left(\nu\frac{\partial \tilde{A}}{\partial x}\right) + \frac{\partial}{\partial y}\left(\nu\frac{\partial \tilde{A}}{\partial y}\right) = -\tilde{J}_s + j\omega\sigma\tilde{A} \quad (2.14)$$

Also, in the high frequency radiation case, one can write the following:

$$\frac{\partial}{\partial x}\left(\nu\frac{\partial \tilde{A}}{\partial x}\right) + \frac{\partial}{\partial y}\left(\nu\frac{\partial \tilde{A}}{\partial y}\right) = -\tilde{J}_s + j\omega\sigma\tilde{A} - \omega^2\epsilon\tilde{A} \quad (2.15)$$

These are the well known nonlinear Poisson's equations in cartesian coordinates.

Usually, the reluctivity, ν , is a function of both position and magnetic flux density which is dependent upon the curl of the magnetic vector potential. However, in this work, no nonlinear magnetic materials are expected to be encountered. Hence, ν is assumed as a constant in the various anticipated nonmagnetic materials. Accordingly, the above three non-linear Poisson's equations become linear equations. In other words, the reluctivity, ν , can be moved outside of the partial derivative operators.

Obviously a closed form solution is nearly impossible to solve the magnetic fields surrounding a two-wire parallel-pair transmission line with any shielding. One must look towards numerical techniques . One of the best methods is the finite element method which will be briefly summerized in the following section.

2.2 The Finite Element Method

The finite element method is used to solve bounded problems. Consider a 2D magnetic field problem with Dirichlet and Neumann boundary conditions. In the static case,

one can formulate the problem as follows:

$$\begin{cases} \nu(\frac{\partial^2 A}{\partial x^2} + \frac{\partial^2 A}{\partial y^2}) = -J_s & (\text{Governing p.d.e.}) \\ A = 0 & (\text{Dirichlet}) \\ \nu \cdot \frac{\partial A}{\partial n} = 0 & (\text{Neumann}) \end{cases} \quad (2.16)$$

From variational principles it was previously shown that the appropriate energy functional [11] for this problem is:

$$F(A) = \int \int_R [\frac{1}{2} \{ \frac{1}{\mu} (\frac{\partial A}{\partial y})^2 + \frac{1}{\mu} (\frac{\partial A}{\partial x})^2 \} - J_s \cdot A] dx dy \quad (2.17)$$

Minimization of $F(A)$ is equivalent to solving the partial differential equation (p.d.e.) with Dirichlet or Neumann boundary conditions [11]. The solution region R can be divided into many subregions (finite elements) on which interpolation functions of the MVP's are defined. There are many different types of element shapes and interpolation functions which are applicable to the finite element discretization [11]. Here, first order triangular elements R_e are chosen and interpolation functions can be obtained in the form of polynomials of first order. The value of the MVP at any point $P(x, y)$ within this triangle is given by [11]:

$$A_e(x, y) = N_l A_l + N_m A_m + N_n A_n \quad (2.18)$$

where $N_l, N_m,$ and N_n are the form (or shape) functions which are complete first degree polynomials. Meanwhile, $A_l, A_m,$ and A_n are the values of the MVPs at the vertices of the triangle, e , in Figure(2.1). These polynomials are of the form:

$$\begin{bmatrix} N_l \\ N_m \\ N_n \end{bmatrix} = \begin{bmatrix} a_l & b_l & c_l \\ a_m & b_m & c_m \\ a_n & b_n & c_n \end{bmatrix} \cdot \begin{bmatrix} 1 \\ x \\ y \end{bmatrix} \quad (2.19)$$

the constants $a_i, b_i,$ and c_i are determined subject to the following conditions:

$$\begin{aligned} N_l = 1, \quad N_m = N_n = 0 & \quad \text{at } P(x_l, y_l) \\ N_m = 1, \quad N_l = N_n = 0 & \quad \text{at } P(x_m, y_m) \\ N_n = 1, \quad N_m = N_l = 0 & \quad \text{at } P(x_n, y_n) \end{aligned} \quad (2.20)$$

Therefore, the expressions of the form (or shape) functions can be rewritten as follows:

$$\begin{bmatrix} N_l \\ N_m \\ N_n \end{bmatrix} = \frac{1}{2\Delta} \begin{bmatrix} p_l & q_l & r_l \\ p_m & q_m & r_m \\ p_n & q_n & r_n \end{bmatrix} \begin{bmatrix} 1 \\ x \\ y \end{bmatrix} \quad (2.21)$$

where: Δ is the area of the triangular element, e , and

$$r_l = x_n - x_m, q_l = y_m - y_n, p_l = x_m y_n - x_n y_m$$

$$r_m = x_l - x_n, q_m = y_n - y_l, p_m = x_n y_l - x_l y_n$$

$$r_n = x_m - x_l, q_n = y_l - y_m, p_n = x_l y_m - x_m y_l$$

where, $2\Delta = p_l + p_m + p_n$.

Now, one can write the interpolation function of the MVP in one element, e , as follows:

$$A_e(x, y) = \frac{1}{2\Delta} \sum_{i=l,m,n} (p_i + q_i x + r_i y) A_i \quad (2.22)$$

Substituting $A_e(x, y)$ into the previous functional equation and minimizing it, one can get the following equation in matrix form [11]:

$$S^e A^e = I^e \quad (2.23)$$

In expanded form we have:

$$\begin{bmatrix} S_{ll}^e & S_{lm}^e & S_{ln}^e \\ S_{ml}^e & S_{mm}^e & S_{mn}^e \\ S_{nl}^e & S_{nm}^e & S_{nn}^e \end{bmatrix} \begin{bmatrix} A_l \\ A_m \\ A_n \end{bmatrix} = \begin{bmatrix} I_l \\ I_m \\ I_n \end{bmatrix} \quad (2.24)$$

where:

$$S_{ij}^e = \frac{\nu}{4\Delta} (r_i r_j + q_i q_j) \quad i, j = l, m, n \quad (2.25)$$

$$I_i = \frac{\Delta J_z}{3} \quad i = l, m, n \quad (2.26)$$

It should be noted that

$$\Delta = \frac{1}{2} \begin{vmatrix} 1 & 1 & 1 \\ x_l & x_m & x_n \\ y_l & y_m & y_n \end{vmatrix} \quad (2.27)$$

The element matrices \underline{S}^e given in the above summary are only valid for element e . Representation of the entire region R requires that these element matrices be assembled into a global coefficient matrix \underline{S} . Then a global matrix equation can be obtained as follows, after imposition of the proper boundary conditions:

$$\underline{S} \cdot \underline{A} = \underline{I} \quad (2.28)$$

The assembly process can be briefly summarized as follows:

Step(1): Initialize all entries of the \underline{S} and \underline{I} matrices to zero.

Step(2): Add each contribution of an element matrix \underline{S}^e to its corresponding location in the global \underline{S} matrix.

Step(3): Add each entry of the element matrix \underline{I}^e to its corresponding location in the global forcing function, \underline{I} .

Step(4): Repeat step(2) and step(3) until all the elements have been assembled.

now the system of Equation(2.28) would be ready for the numerical solutions.

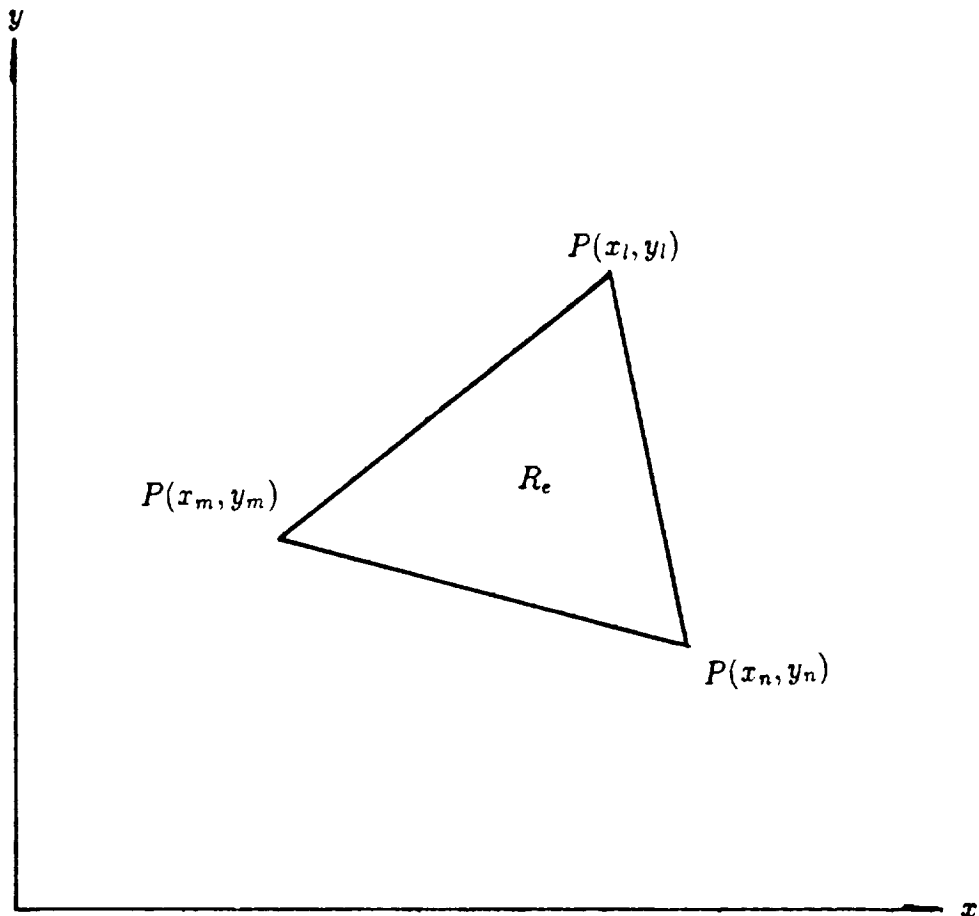


Figure 2.1: The First Order Triangular Finite Element

Chapter 3

COMPARISONS BETWEEN THE CLOSED-FORM SOLUTION AND 2DFE SOLUTION FOR THE TWO-WIRE PARALLEL-PAIR CASE

In this chapter, the magnetostatic fields surrounding a two-wire parallel-pair transmission line which is shown in Figure(3.1) are computed by the analytical and 2DFE methods. The results are compared for verification purposes.

3.1 The Closed-Form Solution

According to *Ampere's circuital law*:

$$\oint \vec{H} \cdot d\vec{l} = I \tag{3.1}$$

one can get the following equations for conductor #1 in Figure(3.1):

$$\oint \vec{H}_1 \cdot d\vec{l}_1 = I \quad (3.2)$$

$$\int_0^{2\pi} H_1 r_1 d\alpha_1 = I \quad (3.3)$$

Hence,

$$H_1 \cdot 2\pi r_1 = I \quad (3.4)$$

Therefore,

$$H_1 = \frac{I}{2\pi r_1} \quad (3.5)$$

That is,

$$H_{1,x} = -H_1 \sin(\alpha_1) = -\frac{I}{2\pi r_1} \frac{y}{r_1} \quad (3.6)$$

$$H_{1,y} = H_1 \cos(\alpha_1) = \frac{I}{2\pi r_1} \frac{x - \frac{W}{2}}{r_1} \quad (3.7)$$

Similarly, one can obtain the equations for conductor #2, Figure(3.1):

$$H_{2,x} = H_2 \sin(\alpha_2) = \frac{I}{2\pi r_2} \frac{y}{r_2} \quad (3.8)$$

$$H_{2,y} = -H_2 \cos(\alpha_2) = -\frac{I}{2\pi r_2} \frac{x + \frac{W}{2}}{r_2} \quad (3.9)$$

With superposition of the fields due to the two conductors, the expressions of the total flux density can be obtained as follows:

$$B_x = \frac{\mu I}{2\pi} y \left(\frac{1}{r_2^2} - \frac{1}{r_1^2} \right) \quad (3.10)$$

$$B_y = \frac{\mu I}{2\pi} \left(\frac{x - \frac{W}{2}}{r_1^2} - \frac{x + \frac{W}{2}}{r_2^2} \right) \quad (3.11)$$

Because of the definition:

$$\nabla \times \bar{A} = \bar{B} \quad (3.12)$$

in the 2D case, equation(3.12) yields the following:

$$B_x = \frac{\partial A}{\partial y} \quad (3.13)$$

$$B_y = -\frac{\partial A}{\partial x} \quad (3.14)$$

Substituting equation(3.10) into (3.13) and integrating yields the following result:

$$A = \frac{\mu I}{2\pi} \ln\left(\frac{r_2}{r_1}\right) \quad (3.15)$$

the quantities r_1 and r_2 are defined in Figure(3.1). With the above formulations, the MVP and flux density were computed for the case of Figure(3.1). The equipotentials near to the conductors are shown in Figure(3.2) and the equipotentials away from the conductors are shown in Figure(3.3). The MVP values and the flux density values at various locations were computed and are listed in Tables(3.1) through (3.4).

3.2 The 2DFE Solution

Let us consider the region shown in Figure(3.4), which has a natural open boundary near to the conductors. In conductor # 1, a current of $I=500$ A flows in the direction out of the plane of the paper, and in conductor # 2, a same value of the current flows in the opposite direction. Its FE grid is shown in Figure(3.5). This bounded problem can be solved using the 2DFE method summarized in the previous chapter. The equipotentials obtained from the FE method with the grid of Figure(3.5) are shown in Figure(3.6). One also needs to investigate the distribution of the magnetic fields away from the conductors. Taking a region which has a remote open natural boundary as shown in Figur(3-7), we can solve this bounded problem using the 2DFE method and obtain the equipotentials shown in Figur(3.8). In the case of Figure(3.7), some MVP values and flux density values at various locations are listed in Tables(3.1) through (3.4).

3.3 Comparisons Between the Closed-Form Solution and 2D-FE Solution

In the two above sections, the analytical method and the 2DFE method were used to solve the same problem. The “true” solution obtained from the analytical method was compared with the solution obtained from the 2DFE method. If the solution obtained from the 2DFE method is not within reasonable bounds in comparison to the true closed form analytical one, means of improvement in the 2DFE method, and solution algorithm need to be arrived at.

Comparison between Figure(3.2) and Figure(3.6) leads one to conclude that the equipotential lines obtained from the 2DFE method are obviously different from the closed form solution. And comparing between Figure(3.3) and Figure(3.8), one finds that in the area near to the conductors, the equipotential lines obtained from the analytical method and 2DFE method are not much different, but in the area close to the boundary, the lines are heavily distorted. The value comparisons for the MVP's and flux densities are given in Tables(3.1) through (3.4). From these tables, it is seen that the near-fields (close to the conductors) obtained from the 2DFE method have higher accuracy and the far-fields (close to the boundary) obtained from the 2DFE method have lower accuracy. In the other words, the more remote the boundary, the less difference the near-fields have from the analytical solutions.

The facts from the above comparisons leads one to conclude that the farther away the boundary in a problem the more improvement are obtained in the near-field solution. In the engineering problems, it is not possible and not necessary to include an infinite boundary. Accordingly, it is better to have a recursion algorithm to extend the boundary to as far away as possible, and to stop the recursion once no further additional improvement can be achieved. That is the essence of the ballooning technique which will be discussed in the next chapter.

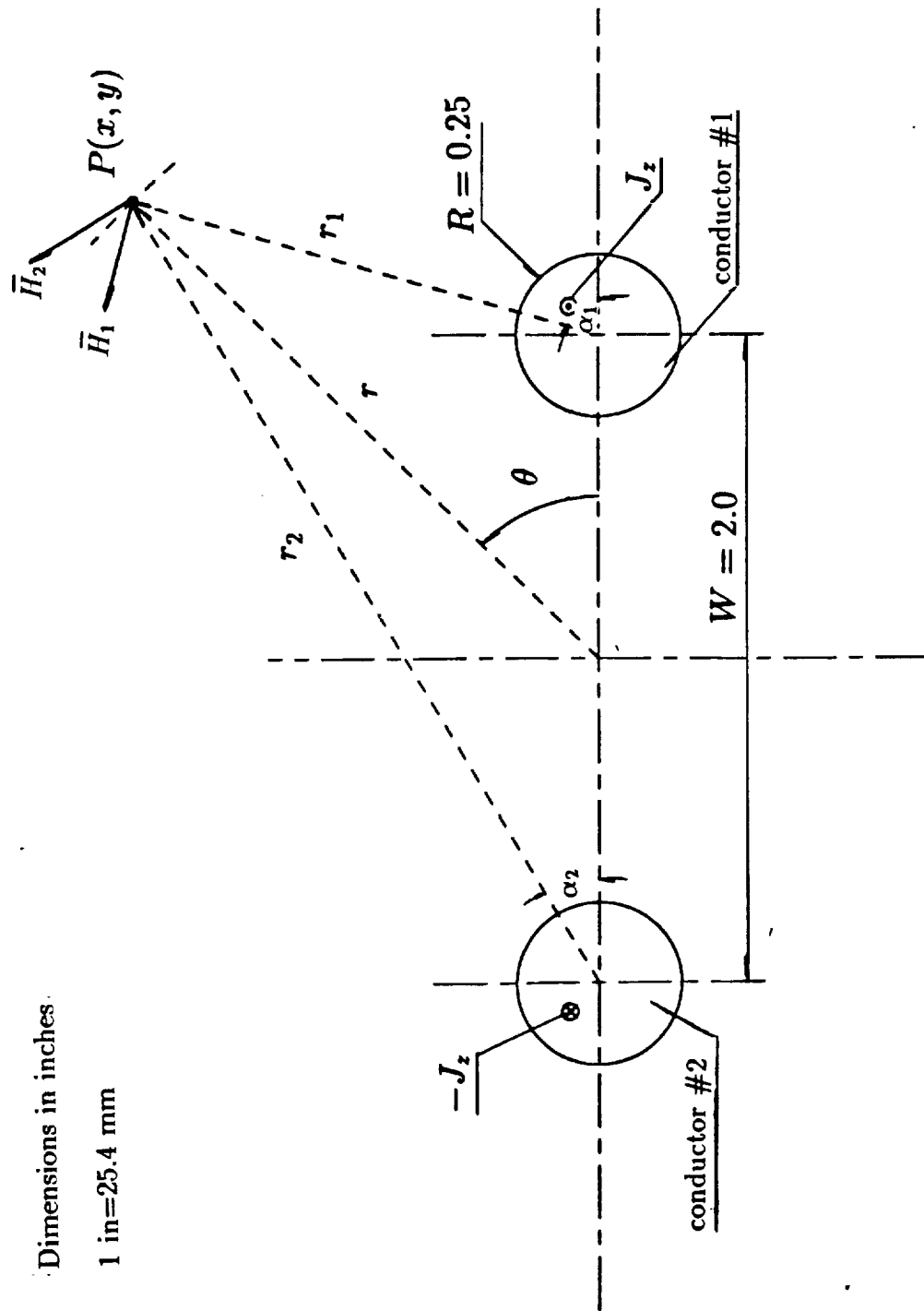


Figure 3.1: The Two-Wire Parallel-Pair Transmission Line Geometry

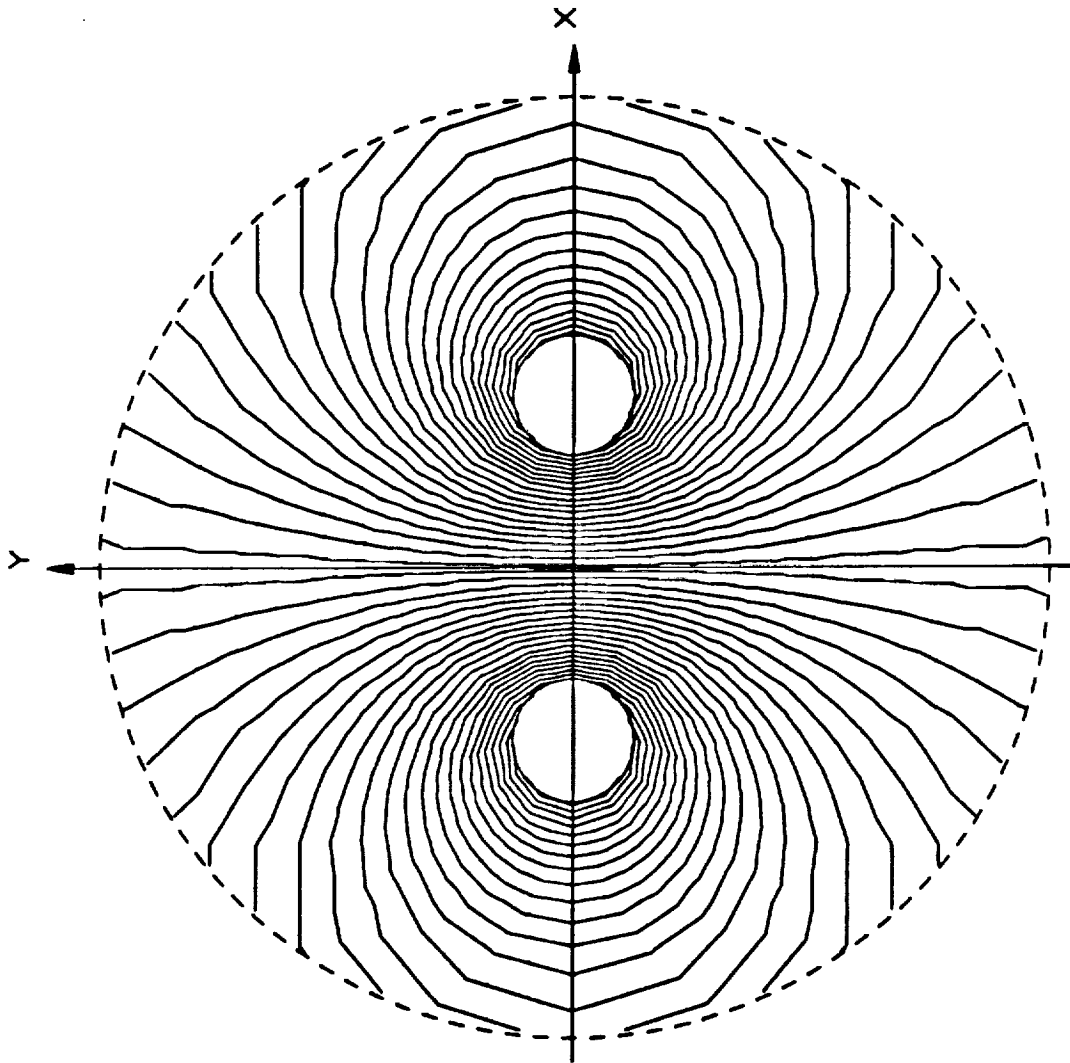


Figure 3.2: Equipotential Contours in the Immediate Vicinity of the Two-Wire Conductors Obtained From the Analytical Method

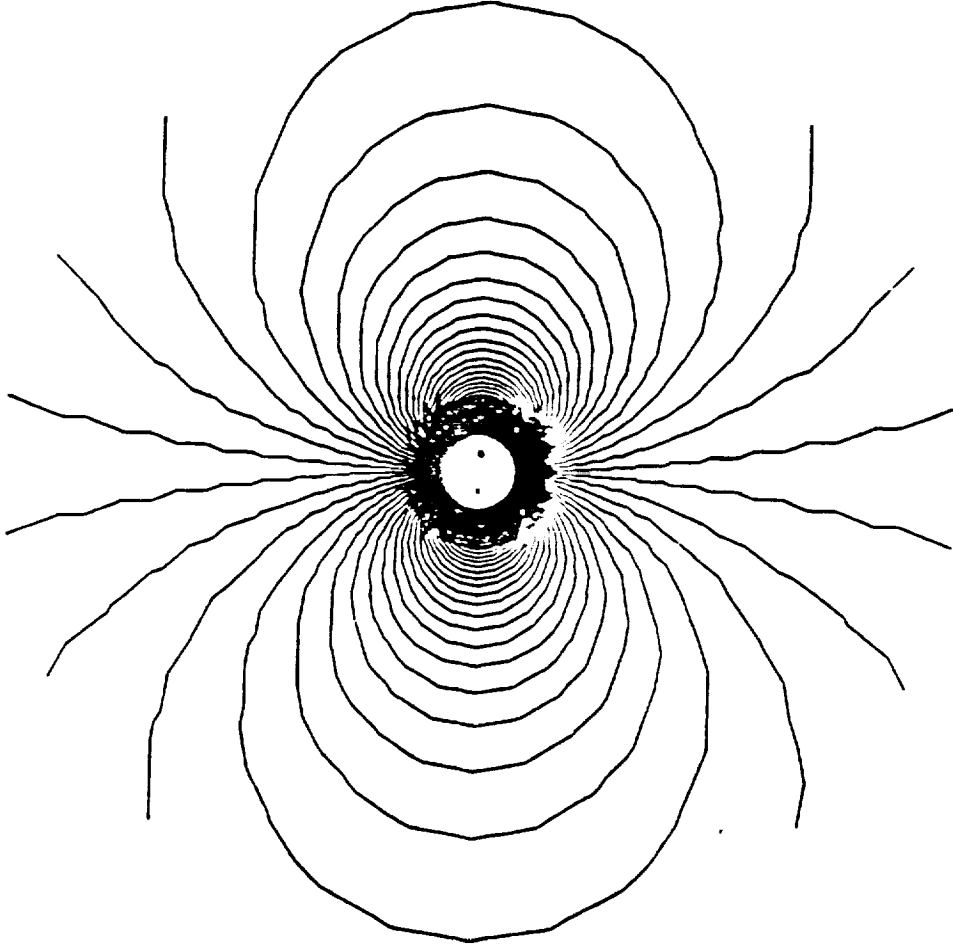


Figure 3.3: Equipotential Contours Beyond the Vicinity of the Two-Wire Conductors
Obtained From the Analytical Method

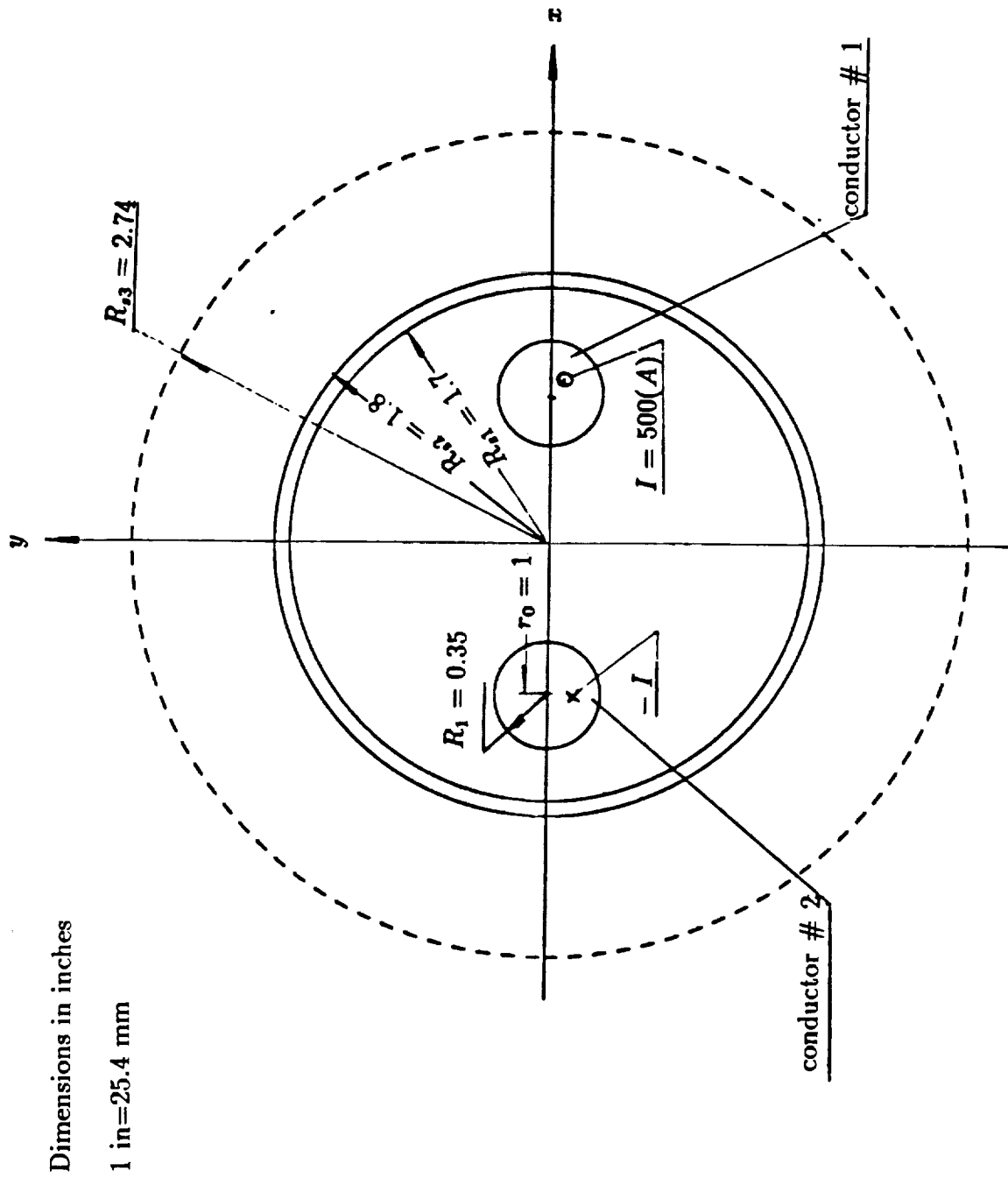


Figure 3.4: The Geometry of the Region on the Immediate Vicinity of the Two-Wire Conductors

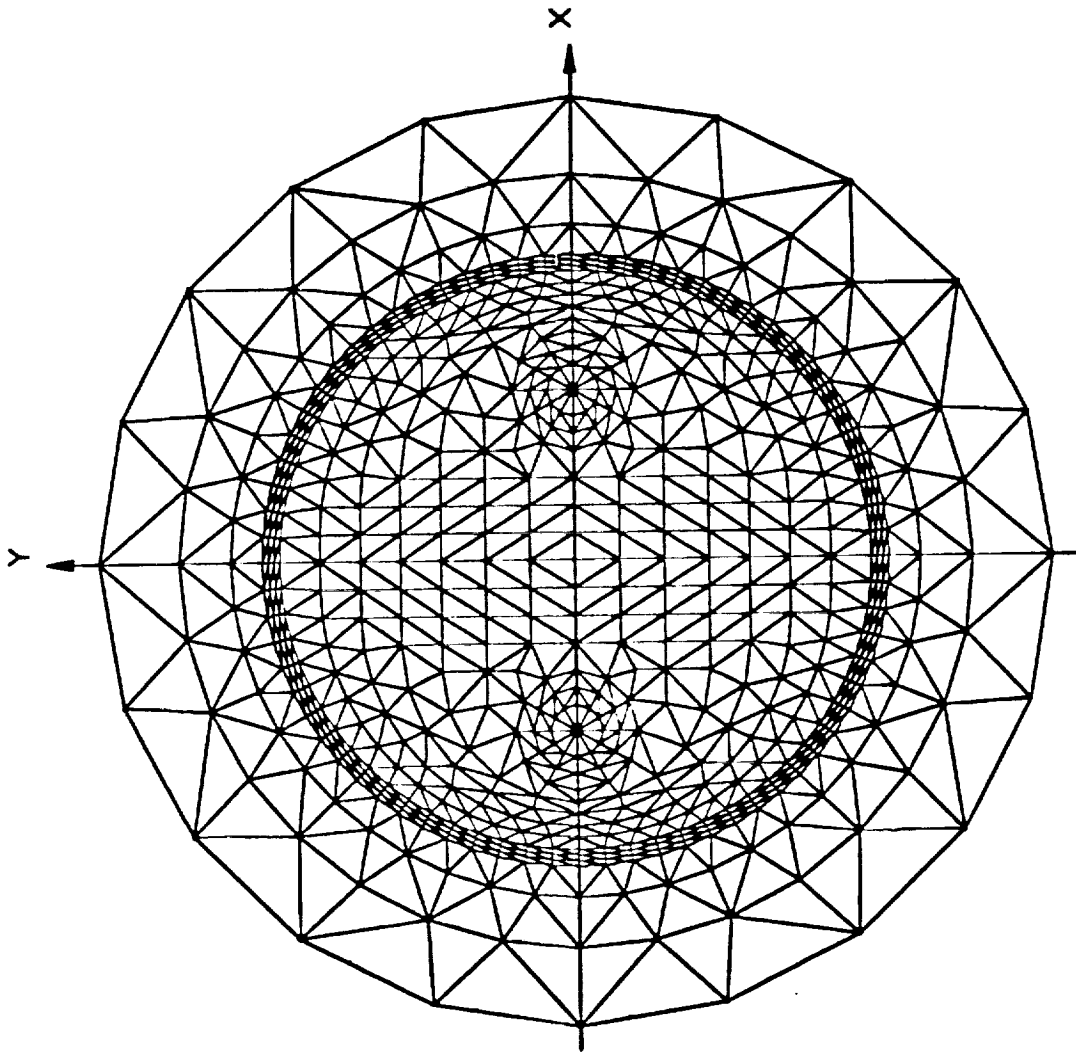


Figure 3.5: The FE Grid in the Immediate Vicinity of the Two-Wire Conductors

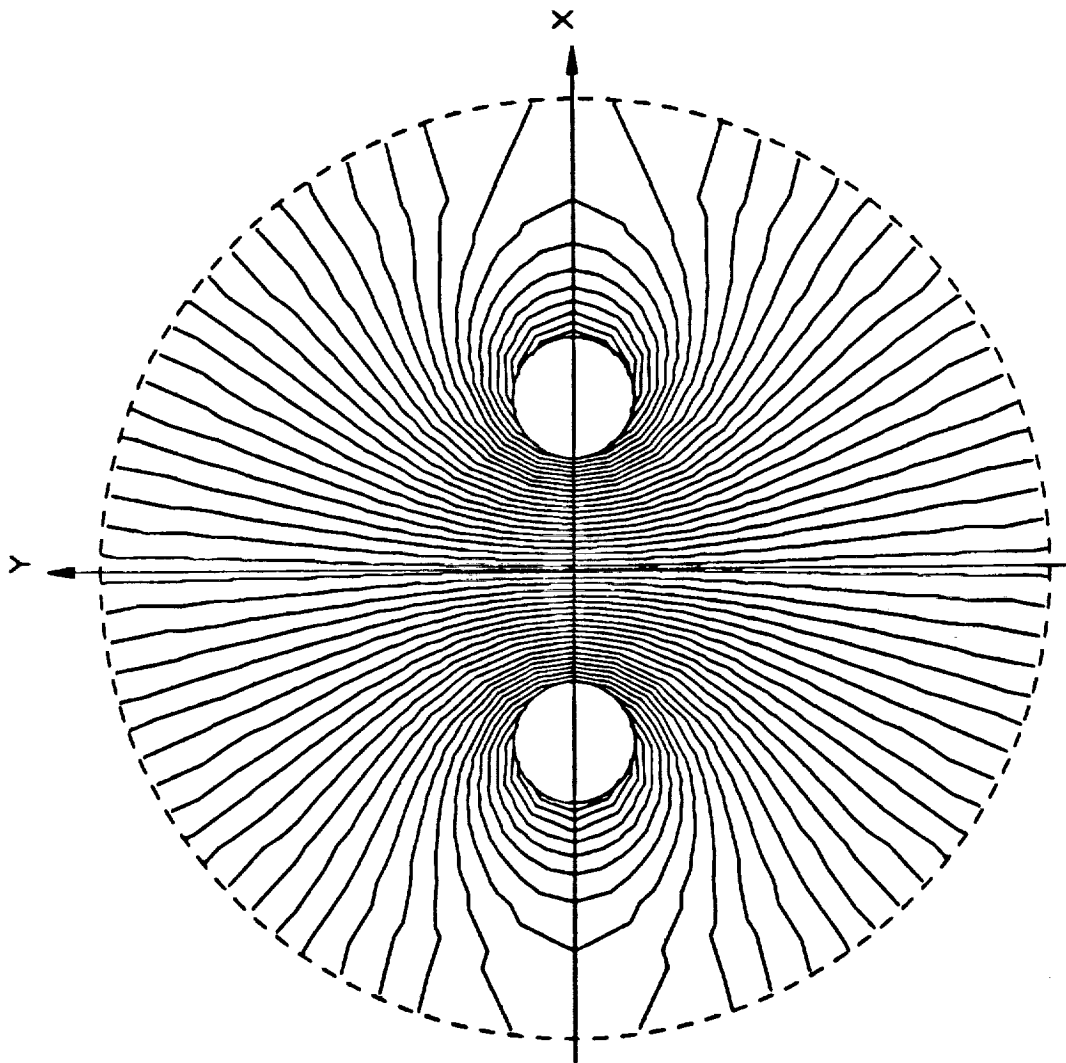


Figure 3.6: Equipotential Contours in the Immediate Vicinity of the Two-Wire Conductors Obtained From the 2DFE Method

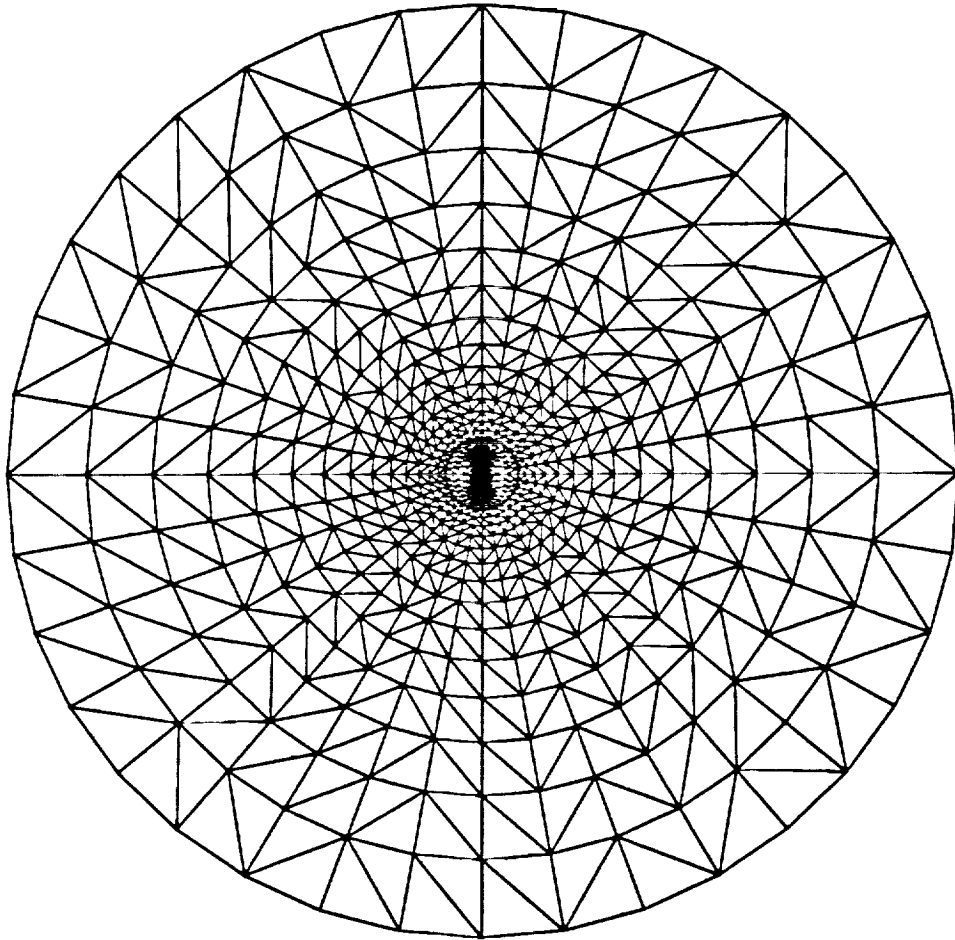


Figure 3.7: The FE Grid Beyond the Immediate Vicinity of the Two-Wire Conductors

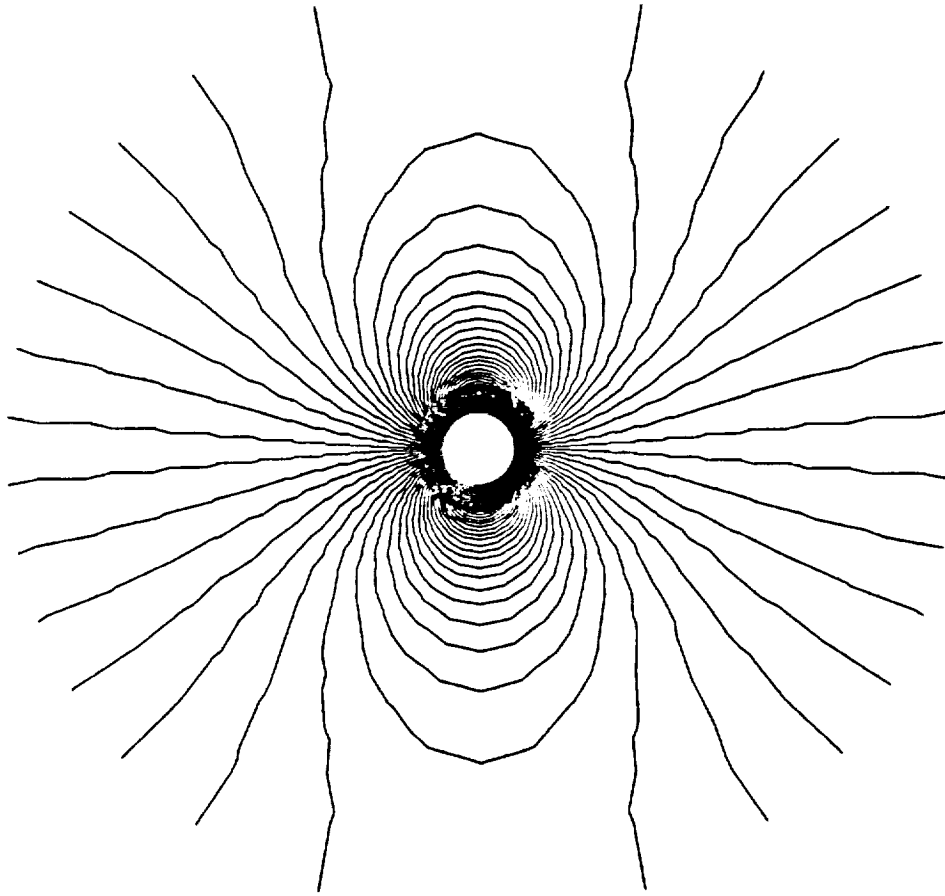


Figure 3.8: Equipotential Contours Beyond the Vicinity of the Two-Wire Conductors
Obtained From the 2DFE Method

Location		MVP(lines/inch)		MVP(Wb/m)		Difference %
r (inch)	θ (deg.)	Analy.	2DFE	Analy.	2DFE	
3.5856	0.0	145.4	142.7	0.5726×10^{-4}	0.5619×10^{-4}	1.9
	10.0	142.7	140.1	0.5620×10^{-4}	0.5514×10^{-4}	1.9
	20.0	134.9	132.4	0.5309×10^{-4}	0.5211×10^{-4}	1.9
	30.0	122.5	120.2	0.4822×10^{-4}	0.4734×10^{-4}	1.8
	40.0	106.5	104.6	0.4192×10^{-4}	0.4119×10^{-4}	1.7
	50.0	87.79	86.35	0.3456×10^{-4}	0.3400×10^{-4}	1.6
	60.0	67.22	66.20	0.2646×10^{-4}	0.2606×10^{-4}	1.5
	70.0	45.41	44.78	0.1788×10^{-4}	0.1763×10^{-4}	1.4
	80.0	22.88	22.58	0.9006×10^{-5}	0.8889×10^{-5}	1.3
	90.0	0.0	-0.006140	0.0	-0.2417×10^{-9}	
6.1959	0.0	82.67	84.11	0.3255×10^{-4}	0.3312×10^{-4}	1.8
	10.0	81.32	82.75	0.3202×10^{-4}	0.3258×10^{-4}	1.8
	20.0	77.35	78.72	0.3045×10^{-4}	0.3099×10^{-4}	1.8
	30.0	70.95	72.22	0.2793×10^{-4}	0.2843×10^{-4}	1.8
	40.0	62.40	63.52	0.2457×10^{-4}	0.2501×10^{-4}	1.8
	50.0	52.05	53.01	0.2049×10^{-4}	0.2087×10^{-4}	1.8
	60.0	40.26	41.02	0.1585×10^{-4}	0.1615×10^{-4}	1.9
	70.0	27.42	27.94	0.1080×10^{-4}	0.1100×10^{-4}	1.9
	80.0	13.88	14.15	0.5465×10^{-5}	0.5571×10^{-5}	1.9
	90.0	0.0	-0.001766	0.0	-0.6952×10^{-10}	
18.501	0.0	27.47	39.65	0.1080×10^{-4}	0.1561×10^{-4}	44.36
	10.0	27.05	39.05	0.1065×10^{-4}	0.1537×10^{-4}	44.37
	20.0	25.80	37.25	0.1016×10^{-4}	0.1467×10^{-4}	44.37
	30.0	23.77	34.32	0.9357×10^{-5}	0.1351×10^{-4}	44.39
	40.0	21.01	30.34	0.8271×10^{-5}	0.1194×10^{-4}	44.42
	50.0	17.62	25.44	0.6935×10^{-5}	0.1002×10^{-4}	44.43
	60.0	13.69	19.78	0.5391×10^{-5}	0.7788×10^{-5}	44.45
	70.0	9.363	13.53	0.3686×10^{-5}	0.5325×10^{-5}	44.47
	80.0	4.752	6.865	0.1871×10^{-5}	0.2703×10^{-5}	44.47
	90.0	0.0	0.0004386	0.0	0.1727×10^{-9}	

Table 3.1: Comparison Between MVP's Obtained from Analytical and 2DFE Methods at Locations Away From the Conductors

Location		Flux Density(Lines/in ²)		Flux Density(Wb/m ²)		Difference %
r (inch)	θ (deg.)	Analy.	2DFE	Analy.	2DFE	
3.9442	5.0	34.84	33.03	0.5400×10^{-3}	0.5119×10^{-3}	5.2
	15.0	34.54	33.16	0.5354×10^{-3}	0.5140×10^{-3}	4.0
	25.0	34.00	32.51	0.5270×10^{-3}	0.5039×10^{-3}	2.4
	35.0	33.31	32.70	0.5163×10^{-3}	0.5069×10^{-3}	1.8
	45.0	32.57	31.80	0.5048×10^{-3}	0.4929×10^{-3}	2.4
	55.0	31.88	31.47	0.4941×10^{-3}	0.4877×10^{-3}	1.3
	65.0	31.31	31.21	0.4852×10^{-3}	0.4837×10^{-3}	0.32
	75.0	30.90	31.25	0.4790×10^{-3}	0.4843×10^{-3}	1.1
	85.0	30.69	31.01	0.4757×10^{-3}	0.4807×10^{-3}	1.0
	95.0	30.69	31.01	0.4757×10^{-3}	0.4807×10^{-3}	1.0
6.8155	5.0	11.17	10.14	0.1731×10^{-3}	0.1571×10^{-3}	9.2
	15.0	11.14	10.28	0.1726×10^{-3}	0.1594×10^{-3}	7.7
	25.0	11.08	10.31	0.1718×10^{-3}	0.1599×10^{-3}	6.9
	35.0	11.01	10.65	0.1706×10^{-3}	0.1708×10^{-3}	3.3
	45.0	10.93	10.69	0.1694×10^{-3}	0.1656×10^{-3}	2.2
	55.0	10.85	11.02	0.1681×10^{-3}	0.1708×10^{-3}	1.6
	65.0	10.78	11.05	0.1671×10^{-3}	0.1713×10^{-3}	2.5
	75.0	10.73	11.25	0.1663×10^{-3}	0.1743×10^{-3}	4.8
	85.0	10.70	11.26	0.1659×10^{-3}	0.1745×10^{-3}	5.2
	95.0	10.70	11.26	0.1659×10^{-3}	0.1745×10^{-3}	5.2
20.351	5.0	1.229	0.5075	0.1905×10^{-4}	0.7866×10^{-5}	58.7
	15.0	1.228	0.6868	0.1904×10^{-4}	0.1065×10^{-4}	44.09
	25.0	1.228	0.9217	0.1903×10^{-4}	0.1429×10^{-4}	24.93
	35.0	1.227	1.178	0.1902×10^{-4}	0.1826×10^{-4}	4.0
	45.0	1.226	1.407	0.1900×10^{-4}	0.2181×10^{-4}	14.8
	55.0	1.225	1.597	0.1898×10^{-4}	0.2476×10^{-4}	30.4
	65.0	1.224	1.752	0.1897×10^{-4}	0.2715×10^{-4}	43.1
	75.0	1.223	1.860	0.1896×10^{-4}	0.2883×10^{-4}	52.1
	85.0	1.223	1.912	0.1895×10^{-4}	0.2964×10^{-4}	56.4
	95.0	1.223	1.912	0.1895×10^{-4}	0.2964×10^{-4}	56.4

Table 3.2: Comparison Between Flux Densities Obtained from Analytical and 2DFE Methods at Locations Away From the Conductors

Location		MVP(lines/inch)		MVP(Wb/m)		Difference %
r (inch)	θ (deg.)	Analy.	2DFE	Analy.	2DFE	
0.6480	8.5	377.40	361.83	0.1486×10^{-3}	0.1425×10^{-3}	4.1
0.5469	36.9	207.45	199.57	0.8167×10^{-4}	0.7857×10^{-4}	3.8
0.6035	68.7	84.38	80.23	0.3322×10^{-4}	0.3159×10^{-4}	4.9
1.7828	20.5	278.48	269.36	0.1096×10^{-3}	0.1060×10^{-3}	3.3
1.6968	41.5	199.21	193.59	0.7843×10^{-4}	0.7622×10^{-4}	2.8
1.5643	63.6	108.51	105.79	0.4272×10^{-4}	0.4165×10^{-4}	2.5

Table 3.3: Comparison Between MVP's Obtained from Analytical and 2DFE Methods at Locations Close to the Conductors

Location		Flux Density(<i>Lines/in</i> ²)		Flux Density(<i>Wb/m</i> ²)		Difference %
<i>r</i> (inch)	<i>θ</i> (deg.)	Analy.	2DFE	Analy.	2DFE	
0.59627	6.1	772.80	703.37	0.1198×10^{-1}	0.1090×10^{-1}	9.0
0.51336	17.0	638.60	591.04	0.9898×10^{-2}	0.9161×10^{-2}	7.4
0.47085	36.0	531.01	485.37	0.8231×10^{-2}	0.7523×10^{-2}	8.6
1.61570	20.3	258.82	235.96	0.4012×10^{-2}	0.3657×10^{-2}	8.8
1.46200	38.4	236.76	236.63	0.3670×10^{-2}	0.3668×10^{-2}	0.05

Table 3.4: Comparison Between Flux Densities Obtained from Analytical and 2DFE Methods at Locations Close to the Conductors

Chapter 4

THE BALLOONING MODEL IN THE 2D MAGNETOSTATIC CASE

Ballooning techniques to simulate infinite boundaries in 2D magnetostatic field solutions using finite elements were developed by earlier investigators in various applications [11]. As seen in chapter 3, it was demonstrated that open boundary 2DFE solution of the field surrounding the two-wire parallel-pair transmission line in open space was inadequate. Hence, in this chapter ballooning techniques for 2DFE codes of the type used by this investigator will be detailed here. That is, in this chapter, a recursion algorithm will be derived using ballooning techniques [2, 3], and then this algorithm will be incorporated into the 2DFE method which was summarized earlier in chapter 2. This 2DFE ballooning model will be applied to an example and its results will be examined by comparison to the analytical solutions. With the 2DFE ballooning model, the study for the effects of the magnetic-type shielding and the effects of defects in such shielding surrounding parallel-pair transmission lines is carried out.

4.1 Ballooning Technique in the Magnetostatic Case

Consider the two round-wire parallel-pair transmission line shown earlier in Figure(3.4), a finite element grid of which is shown here in Figure(4.1). Using conventional finite element techniques, the interior region in this FE grid which has a boundary Γ_0 , may be divided into triangular finite elements as shown in the figure. Hence the node distribution on the surface Γ_0 of the region R , Figure(4.1), is well defined. The FE global matrix equation can be obtained using the conventional 2DFE method for the region, R , and the boundary, Γ_0 , as follows:

$$\underline{S}_{in} \underline{A}_{in} = \begin{bmatrix} S_{RR} & S_{R\Gamma_0} \\ S_{\Gamma_0 R} & S_{\Gamma_0 \Gamma_0} \end{bmatrix} \begin{bmatrix} A_R \\ A_0 \end{bmatrix} = \begin{bmatrix} I_R \\ I_0 \end{bmatrix} \quad (4.1)$$

where the subscript *in* denotes the interior region, the subscript Γ_0 (or 0) denotes the nodes on boundary, Γ_0 , and the subscript R denotes the nodes in the region R .

Assume that the region exterior to R contains only free space, hence the external field is purely Laplacian. The first step in the representation of the exterior region is to define a finite element mesh for an annular region surrounding the region R . This annulus has certain properties which can best be summarized as follows:

- (a) The number of nodes on the inner and outer boundaries are the same and lie on lines radiating from a star point.
- (b) The outer boundary nodes for each successive ballooning annulus have a one-to-one correspondence with those nodes on the original solution region boundary, Γ_0 . This leads to useful geometric similarity properties to the FE triangles in the ballooning region.
- (c) There is a fixed ratio k between the radii of the outer and inner sets of nodes of every annulus, measured from the star point.

Such an exterior annular region with boundary annuli $\Gamma_0, \Gamma_1, \dots$ is shown in Figure(4.2). The exterior region should be matched with the interior region such as shown in Figure(4.3).

Hence, if the points on the inner boundary are denoted:

$$X_n^{(0)} = (x_n, y_n)^{(0)} \quad (4.2)$$

then the outer boundary nodes are given by

$$X_n^{(1)} = (x_n, y_n)^{(1)} = kX_n^{(0)} \quad (4.3)$$

where k is the mapping ratio for the ballooning method at hand.

The FE matrix, \underline{S}_{ext} , for this exterior annular region can now be constructed and a process of matrix condensation is used to remove any equations corresponding internal nodes occurring in the recursive ballooning step.

The FE matrix equation for nodes on Γ_0 and Γ_1 becomes:

$$\underline{S}_{ext}^1 A^{0,1} = \begin{bmatrix} S_{11}^1 & S_{12}^1 \\ S_{21}^1 & S_{22}^1 \end{bmatrix} \begin{bmatrix} A_0 \\ A_1 \end{bmatrix} = \begin{bmatrix} 0 \\ 0 \end{bmatrix} \quad (4.4)$$

where the subscript ext denotes the nodes on the exterior region, the subscript of MVPs, 0, denotes the inner nodes on the Γ_0 and the subscript 1 denotes the nodes on the Γ_1 .

The contributions of each element on this annulus to \underline{S}_{ext} are computed as follows:

$$S_{ij}^e = \frac{\nu}{4\Delta} (r_i r_j + q_i q_j) \quad i, j = l, m, n \quad (4.5)$$

where: Δ is the area of the triangular element, e , and

$$r_l = x_n - x_m, r_m = x_l - x_n, r_n = x_m - x_l$$

$$q_l = y_m - y_n, q_m = y_n - y_l, q_n = y_l - y_m$$

In the same way, a second annulus for the nodes on Γ_1 and Γ_2 can be constructed:

$$\underline{T}^1 A^{1,2} = \begin{bmatrix} T_{11}^1 & T_{12}^1 \\ T_{21}^1 & T_{22}^1 \end{bmatrix} \begin{bmatrix} A_1 \\ A_2 \end{bmatrix} = \begin{bmatrix} 0 \\ 0 \end{bmatrix} \quad (4.6)$$

Because this second annulus is geometrically similar to the first and has the same mapping ratio discussed earlier, it follows that one can write:

$$X_n^{(2)} = kX_n^{(1)} = k^2 X_n^{(0)} \quad (4.7)$$

Applying the geometric similarity given in equation(4.7) yields a set of elemental coefficients, S_{ij}^e , equation(4.5), which remains unchanged as one progresses from one

ballooning annulus to the next. That means the matrix \mathcal{T}^1 in equation(4.6) is equal to the matrix \underline{S}_{ext}^1 in equation(4.4). That is, \underline{S}_{ext}^1 is identical to \mathcal{T}^1 , or

$$\mathcal{T}^1 = \underline{S}_{ext}^1 \quad (4.8)$$

The two annuli may now be combined to yield the following:

$$\begin{bmatrix} S_{11}^1 & S_{12}^1 & 0 \\ S_{21}^1 & S_{22}^1 + T_{11}^1 & T_{12}^1 \\ 0 & T_{21}^1 & T_{22}^1 \end{bmatrix} \begin{bmatrix} A_0 \\ A_1 \\ A_2 \end{bmatrix} = \begin{bmatrix} 0 \\ 0 \\ 0 \end{bmatrix} \quad (4.9)$$

where A_1 are nodal MVPs on the common boundary, Γ_1 , between the two annuli. The equations for A_0 , A_1 , and A_2 may be partially solved to eliminate A_1 , using the fact that

$$A_1 = -(S_{22}^1 + T_{11}^1)^{-1}(S_{21}^1 A_0 + T_{12}^1 A_2) \quad (4.10)$$

Substituting Equation(4.10) into Equation(4.9) leads to the following:

$$\begin{aligned} \underline{S}_{ext}^2 \Delta^{0,2} &= \begin{bmatrix} S_{11}^1 - S_{12}^1(S_{22}^1 + T_{11}^1)^{-1}S_{21}^1 & -S_{12}^1(S_{22}^1 + T_{11}^1)^{-1}T_{12}^1 \\ -T_{21}^1(S_{22}^1 + T_{11}^1)^{-1}S_{21}^1 & T_{22}^1 - T_{21}^1(S_{22}^1 + T_{11}^1)^{-1}T_{12}^1 \end{bmatrix} \begin{bmatrix} A_0 \\ A_2 \end{bmatrix} \\ &= \begin{bmatrix} 0 \\ 0 \end{bmatrix} \end{aligned} \quad (4.11)$$

hence,

$$\begin{aligned} \underline{S}_{ext}^2 &= \begin{bmatrix} S_{11}^1 - S_{12}^1(S_{22}^1 + T_{11}^1)^{-1}S_{21}^1 & -S_{12}^1(S_{22}^1 + T_{11}^1)^{-1}T_{12}^1 \\ -T_{21}^1(S_{22}^1 + T_{11}^1)^{-1}S_{21}^1 & T_{22}^1 - T_{21}^1(S_{22}^1 + T_{11}^1)^{-1}T_{12}^1 \end{bmatrix} \\ &= \begin{bmatrix} S_{11}^2 & S_{12}^2 \\ S_{21}^2 & S_{22}^2 \end{bmatrix} \end{aligned} \quad (4.12)$$

The matrix equation (4.11) has the form of equation(4.4) but relates the two combined annuli, which now has a mapping ratio of k^2 .

From the (i-1)th recursive ballooning step, applying the method given in equation(4.12) recurrssively, one could obtain the following equation:

$$\underline{S}_{ext}^i \Delta^{0,i} = \begin{bmatrix} S_{11}^i & S_{12}^i \\ S_{21}^i & S_{22}^i \end{bmatrix} \begin{bmatrix} A_0 \\ A_i \end{bmatrix} = \begin{bmatrix} 0 \\ 0 \end{bmatrix} \quad (4.13)$$

which relates the MVPs, A_0 and A_i on the boundaries Γ_0 and Γ_i of the ballooned solution region.

For the (i)th application, one can obtain:

$$\mathcal{T}^i \mathcal{A}^{i,i+1} = \begin{bmatrix} T_{11}^i & T_{12}^i \\ T_{21}^i & T_{22}^i \end{bmatrix} \begin{bmatrix} A_i \\ A_{i+1} \end{bmatrix} = \begin{bmatrix} 0 \\ 0 \end{bmatrix} \quad (4.14)$$

which relates the MVPs of the nodes on boundaries Γ_i and Γ_{i+1} . One must recall that the above mentioned geometric similarity property of the successive ballooning layers allow one to write the following:

$$\mathcal{T}^i = \mathcal{S}_{ext}^1 \quad (4.15)$$

Combining equation(4.13) and equation(4.14), and eliminating A_i , one can write the following main recursive relationship for the ballooning technique, which is used here:

$$\begin{aligned} \mathcal{S}_{ext}^{i+1} &= \begin{bmatrix} S_{11}^i - S_{12}^i(S_{22}^i + T_{11}^i)^{-1}S_{21}^i & -S_{12}^i(S_{22}^i + T_{11}^i)^{-1}T_{12}^i \\ -T_{21}^i(S_{22}^i + T_{11}^i)^{-1}S_{21}^i & T_{22}^i - T_{21}^i(S_{22}^i + T_{11}^i)^{-1}T_{12}^i \end{bmatrix} \\ &= \begin{bmatrix} S_{11}^{i+1} & S_{12}^{i+1} \\ S_{21}^{i+1} & S_{22}^{i+1} \end{bmatrix} \end{aligned} \quad (4.16)$$

That is, one can write the following for the ballooned exterior region:

$$\mathcal{S}_{ext}^{i+1} \mathcal{A}^{0,i+1} = \begin{bmatrix} S_{11}^{i+1} & S_{12}^{i+1} \\ S_{21}^{i+1} & S_{22}^{i+1} \end{bmatrix} \begin{bmatrix} A_0 \\ A_{i+1} \end{bmatrix} = \begin{bmatrix} 0 \\ 0 \end{bmatrix} \quad (4.17)$$

which relates the nodal MVPs on the Γ_0 and Γ_{i+1} , and has a mapping ratio of $k^{(i+1)}$.

A new annular region can now be attached to the present outer nodes and the process can be repeated indefinitely. Hence a recursive system has been defined with the outer boundary moving away with the following geometric progression:

$$k^1, k^2, k^3, \dots, k^i, \dots \quad (4.18)$$

The system is rapidly convergent and the S_{12} terms in equation(4.17) (representing the error in the exterior solution) quickly approaches zero. After m applications, one can write:

$$\mathcal{S}_{ext}^m \mathcal{A}^{0,m} = \begin{bmatrix} S_{11}^m & S_{12}^m \\ S_{21}^m & S_{22}^m \end{bmatrix} \begin{bmatrix} A_0 \\ A_m \end{bmatrix} = \begin{bmatrix} 0 \\ 0 \end{bmatrix} \quad (4.19)$$

Finally, the S_{11} terms are attached to the outer nodes of the interior solution region, i.e., the matrix equation(4.1) is combined with the matrix equation(4.19), yielding the following global FE system of equations:

$$\begin{bmatrix} S_{RR} & S_{R\Gamma_0} & 0 \\ S_{\Gamma_0 R} & S_{\Gamma_0 \Gamma_0} + S_{11}^m & S_{12}^m \\ 0 & S_{21}^m & S_{22}^m \end{bmatrix} \begin{bmatrix} A \\ A_0 \\ A_m \end{bmatrix} = \begin{bmatrix} I \\ I_0 \\ 0 \end{bmatrix} \quad (4.20)$$

where A_0 are nodal MVPs on the boundary, Γ_0 , and A_m are the nodal MVPs on the boundary, Γ_m . If Γ_m is far enough, $A_m = A|_{\Gamma_m} \rightarrow 0$ and $S_{21}^m \rightarrow 0$.

If $A_m = 0$, and $S_{21}^m = 0$, the previous equation(4.20) can be rewritten as follows:

$$\begin{bmatrix} S_{RR} & S_{R\Gamma_0} \\ S_{\Gamma_0 R} & S_{\Gamma_0 \Gamma_0} + S_{11}^m \end{bmatrix} \begin{bmatrix} A \\ A_0 \end{bmatrix} = \begin{bmatrix} I \\ I_0 \end{bmatrix} \quad (4.21)$$

In the computer algorithm of the 2DFE ballooning method, m , the number of ballooning layers (or annuli, which from now on will be used interchangeably throughout this thesis), is chosen large enough to lead to negligible coefficients for the matrix, S_{12}^m . Specific values for m will be discussed in the next section, accompanied by some numerical results.

The process of the 2DFE ballooning method can be summarized as follows:

Step(1): Compute the global \underline{S}_{in} matrix of the interior region using the conventional 2DFE method summerized in chapter 2, that is, obtain the FE global matrix \underline{S}_{in} and the global forcing function \underline{I} shown in equation(4.1).

Step(2): Choose a proper m , the number of ballooning layers, and compute the contribution of the exterior annular region Γ_0 and Γ_1 to obtain the FE matrix \underline{S}_{ext}^1 .

Step(3): $i=1$

Step(4): Let $\underline{T}^i = \underline{S}_{ext}^i$.

Step(5): Use the main recursive equation(4.16) to combine the matrices \underline{S}_{ext}^i with \underline{T}^i and therefore, obtain the matrix $\underline{S}_{ext}^{i+1}$.

Step(6): If i is less than m , $i = i + 1$, go to step(4).

Step(7): Incorporate the matrix S_{11}^m into the FE global matrix \underline{S}_{in} as shown in equation(4.21).

Step(8): Solve the FE equation(4.21).

Step(9): End.

4.2 Exploration of the 2DFE Ballooning Model by Test Examples

Now this 2DFE ballooning model will be applied to an example of a two-wire parallel-pair transmission line problem with an infinite boundary, which was shown earlier in Figure(3.1), and its validity should be examined by the comparison of its results with those of the analytical solution whose formulations were given in equations (3.13) through (3.15).

The interior region is shown in Figure(4.4) where the current flowing in the right conductor has a value of 500 amperes and a direction out of the plane of the paper, and the same value of current flows through the left conductor in the opposite direction, that is into the plane of the paper. Its FE mesh is shown in Figure(4.5), where the mapping ratio is $k=1.3$ and the start point is at $P(x_0, y_0) = (0, 0)$.

The equipotentials of the theoretical "true" solution obtained from the analytical method are shown in Figure(4.6). Figures(4.7) through (4.12) show the equipotentials obtained from the 2DFE ballooning method with ballooning layers (annuli), $m=0, 2, 5, 10, 15,$ and 20 , respectively. The quantitative comparisons of the MVP's and flux densities at arbitrarily selected locations shown in Figure(4.13) were carried out. The MVP comparisons between the analytical and 2DFE ballooning solutions in various locations for the ballooning layers, $m=0, 2, 5, 10, 15$ and 20 are listed in Tables(4.1) and (4.2). Also, the flux density comparisons between the solutions obtained from these two methods are also listed in Tables(4.3) through (4.5)

Comparing Figure(4.6), which shows the analytical solution, with Figures(4.7) through (4.12), one can easily find that while the number of ballooning layers, m , is lower ($m=0, 2,$ and 5 , which show various FE ballooning solutions, see Figures(4.7) through (4.9), respectively), the equipotentials obtained from the 2DFE ballooning solutions are obviously distorted, meanwhile when m is increased ($m=10, 15,$ and 20 , see Figures(4.10) through (4.12), respectively), the equipotentials of the 2DFE ballooning solutions are closer and closer to those obtained from the "true" solution. Again, from Tables(4.1) and (4.2), one can find that the errors of the MVPs were reduced while the number of ballooning layers was going up, for example, the errors

of the MVPs are in the range of (20 ~ 70)% with $m=0$, and in the range of (10 ~ 40)% with $m=5$. For $m \geq 10$, the errors are below 10 %. In Tables(4.3) through (4.5), the errors of flux densities bear a similar relationship to the number of ballooning layers, m , to that relationship in the case of the MVP data explained above. Tables(4.1) through (4.5) show one that while the number of ballooning layers, m , is big enough (here, $m \geq 10$), the errors of both MVPs and flux densities are smaller and smaller up to a number of ballooning layers, at which such errors are not further improved by further addition of more ballooning layers. Such lack of continued improvement is due to the inherent numerical errors associated with the FE discretization within the FE grid of the internal region. That is, further improvements can only be obtained by finer FE mesh discretizations in the interior region. Therefore, one can say that this 2DFE ballooning model is useful for magnetostatic problems with infinite boundaries.

4.3 The Effects of the shielding and the Effects of Defects

This 2DFE ballooning model can be used to investigate the effects of the material-type magnetic shielding on the electromagnetic field distributions in a two-wire parallel-pair transmission line case.

Let the cylindrical shell shown in Figure(4.4) surrounding the two-wire parallel-pair transmission line be made of material with relative permeability $\mu_r \geq 1.0$. Finite element magnetic field analysis was applied using the ballooning technique to simulate the infinite free space surrounding the conductors (infinite boundary), with assumed cylindrical shell relative permeabilities of $\mu_r=10, 100, 1000, \text{ and } 5000$. This was done to study the effects of shielding on the magnetic field outside the shield. The equipotentials are shown in Figures(4.14) through (4.17), for $\mu_r=10, 100, 1000, \text{ and } 5000$, respectively. These should be compared with the no shielding case in Figure(4.12) for a qualitative appreciation of the effects of the shield's relative permeability, μ_r , on the field distribution. A quantitative comparison of magnetic flux densities at arbitrarily selected locations outside the shield, shown in Figure(4.18), is given in Table(4.6).

Notice the substantial effect of the shield when $\mu_r \geq 100$, the flux densities outside the shielding are very small because of the magnetic shielding with higher permeabilities.

Also this 2DFE ballooning model can be used to study field distributions resulting from discontinuities in shielding surfaces due to accidental damage or to deliberate hardware design necessities, such as openings for electrical leads. Examples given here assume three possible cylindrical shielding shell discontinuities around the two-wire parallel-pair transmission line under consideration. These defects and their corresponding flux plots for defect angles, $\delta = 10^\circ, 20^\circ$, and 30° , are shown in Figures(4.19) through (4.24), respectively. The effects of the shielding defects were monitored at the arbitrarily chosen locations given in Figure(4.25). The magnetic flux densities are given in Table(4.7). The numerical results show how defects can adversely affect the intended benefits of such shields, which is manifested here in a substantial increase in the flux densities in element # 1305.

Next the combined FE-ballooning technique is developed and applied to the case of shielding involving diffusion type reduced eddy currents in metallic shields for AC type transmission line currents.

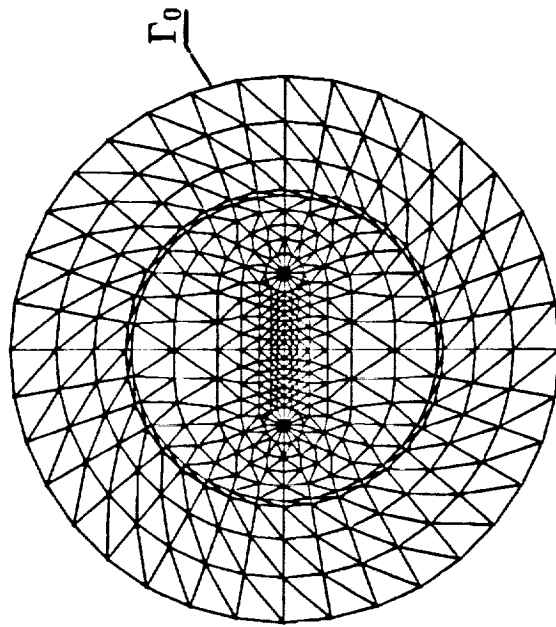


Figure 4.1: Interior FE Grid With Boundary Γ_0 for the Parallel-Pair Transmission Line.

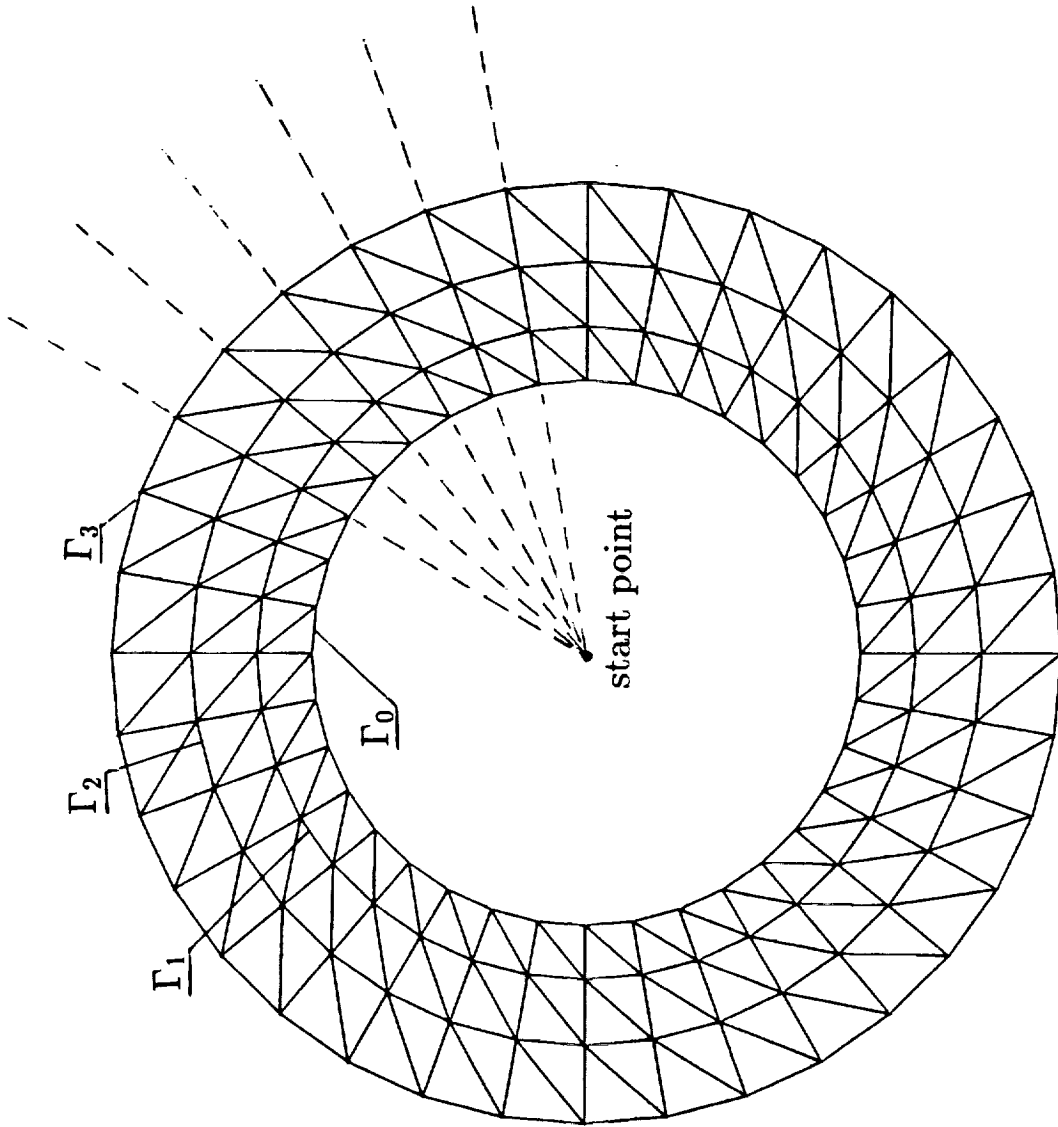
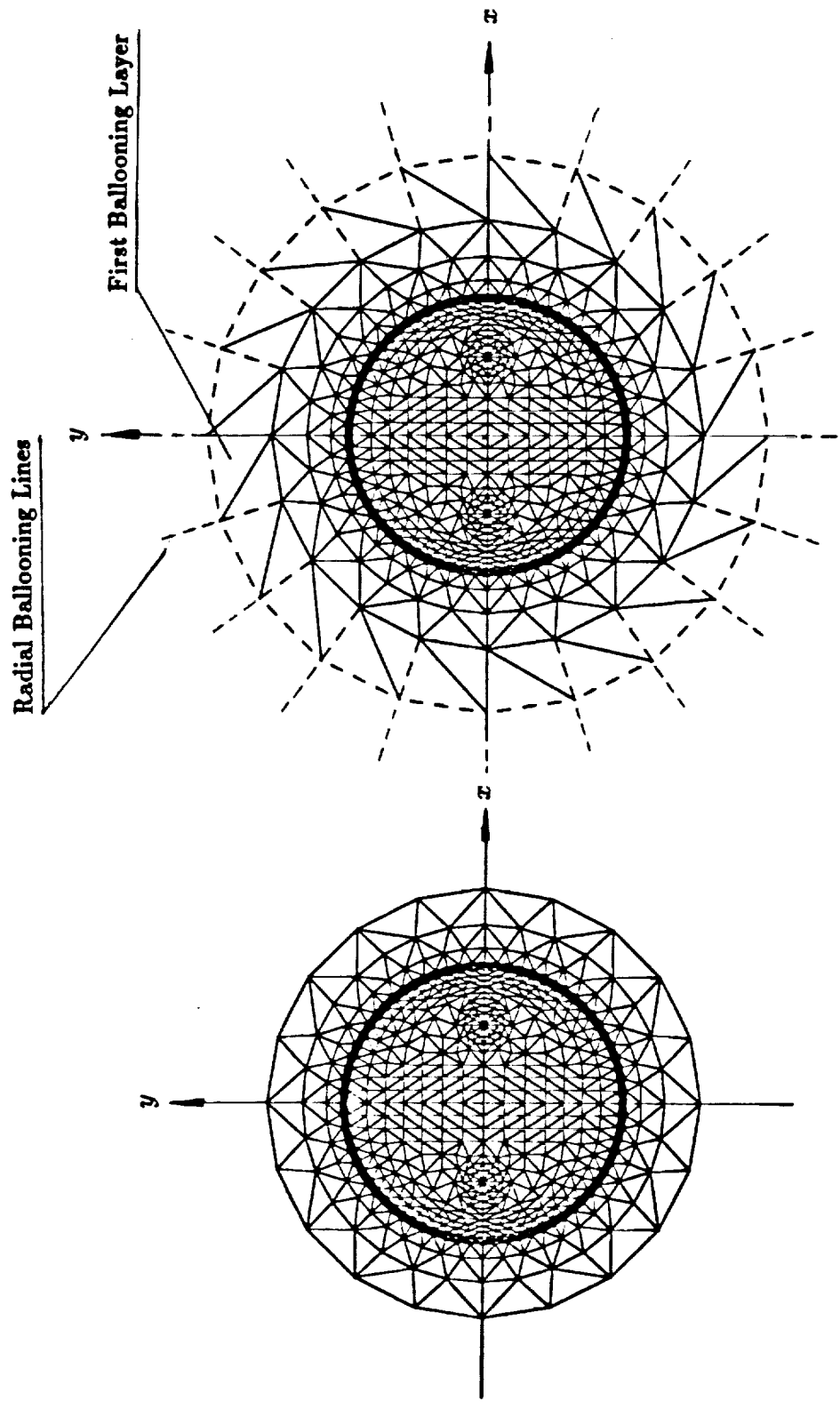


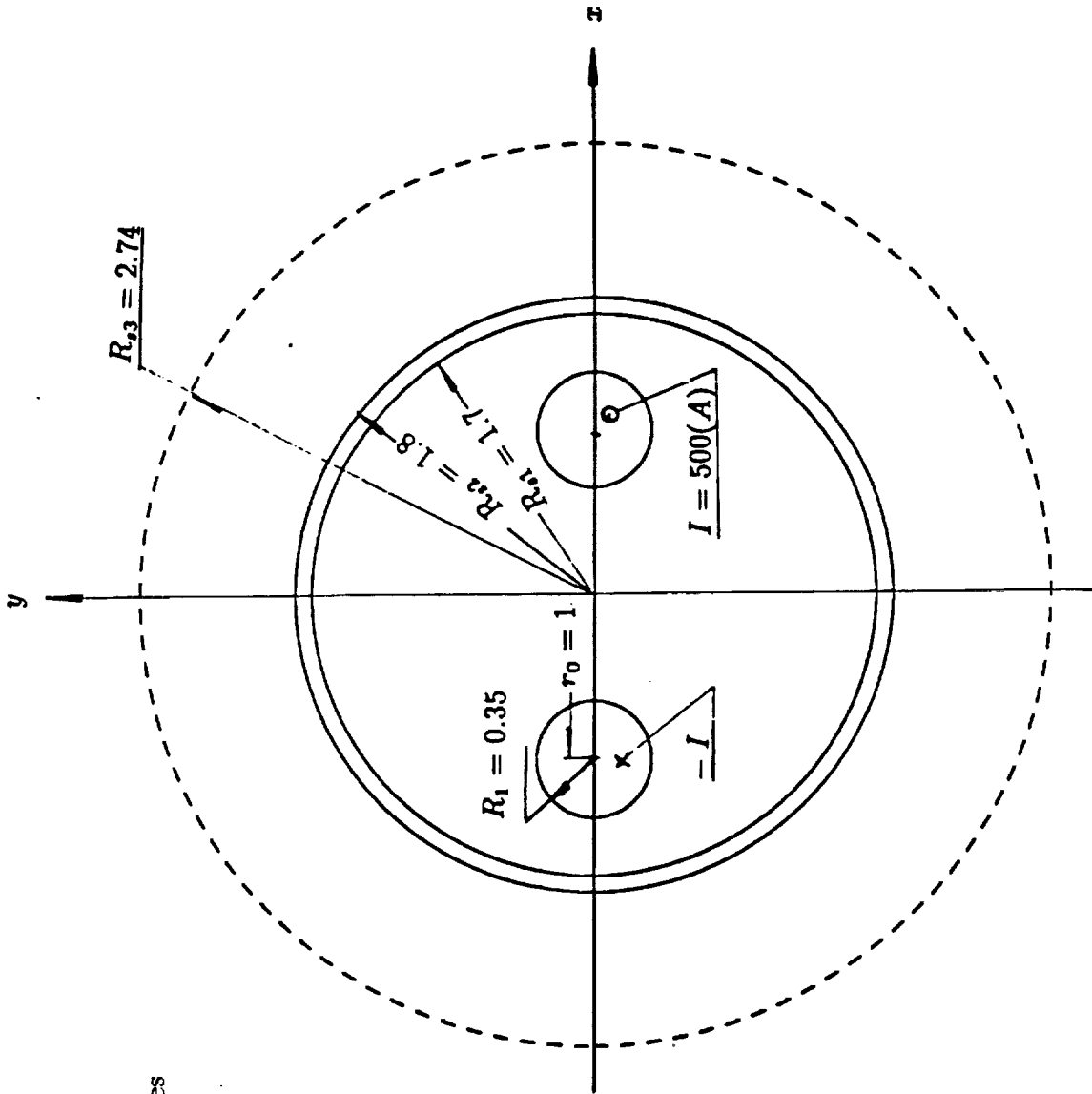
Figure 4.2: The Nature of FE Grids in Bounded Exterior Regions for Ballooning Purposes



(a) 2D-FE Solution Region without Ballooning
 (Open or Naturally Boundary)

(b) 2D-FE Solution Region with Ballooning
 (Infinite Boundary)

Figure 4.3: FE Grids for the Parallel-Pair Transmission Line With and Without Ballooning



Dimensions in inches

1 in = 25.4 mm

Figure 4.4: Geometry of a Two-Wire Parallel-Pair Transmission Line Case

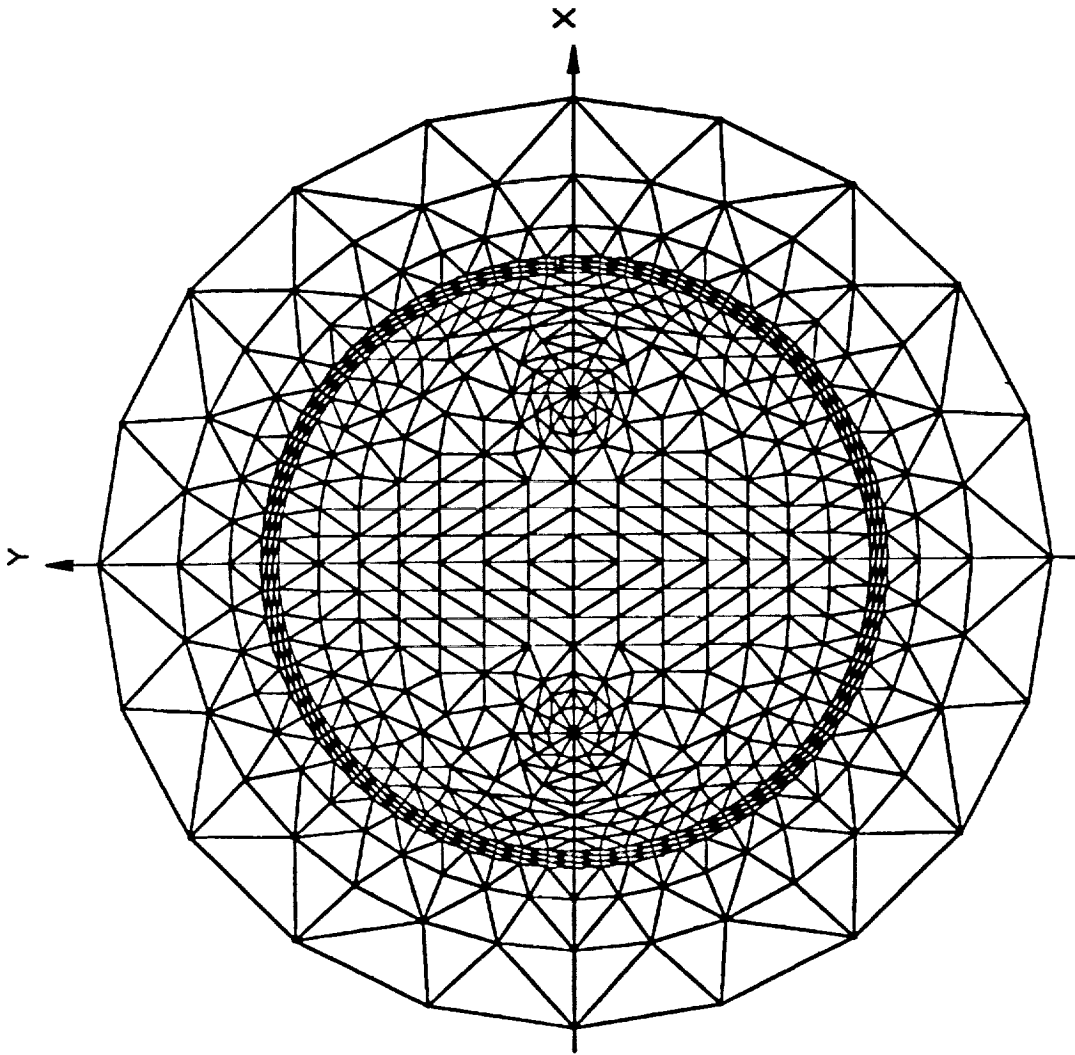


Figure 4.5: FE Grid for the Two-Wire Parallel-Pair Transmission Line Case

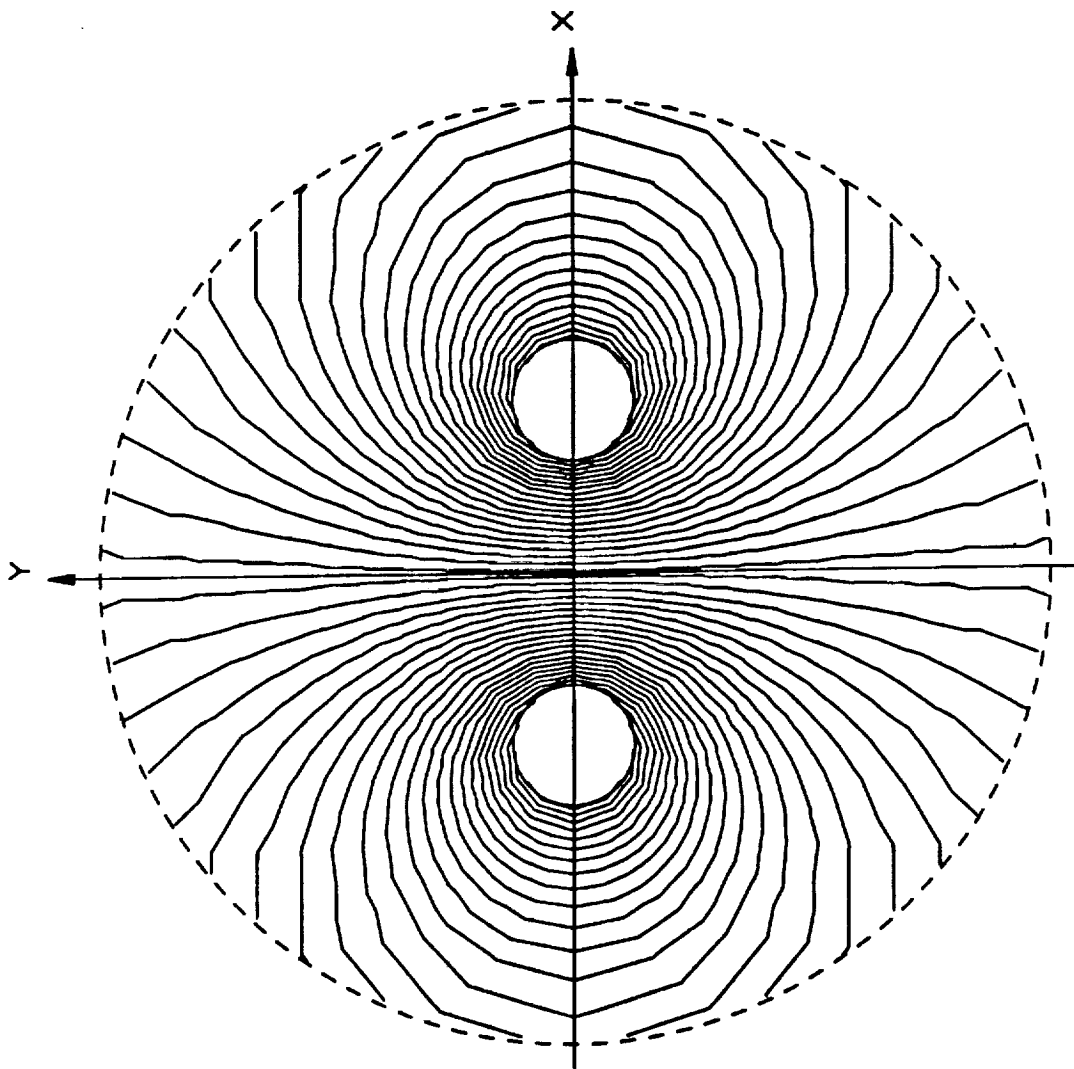


Figure 4.6: MVP Equipotentials for the Parallel-Pair Case Obtained From the Analytical Solution

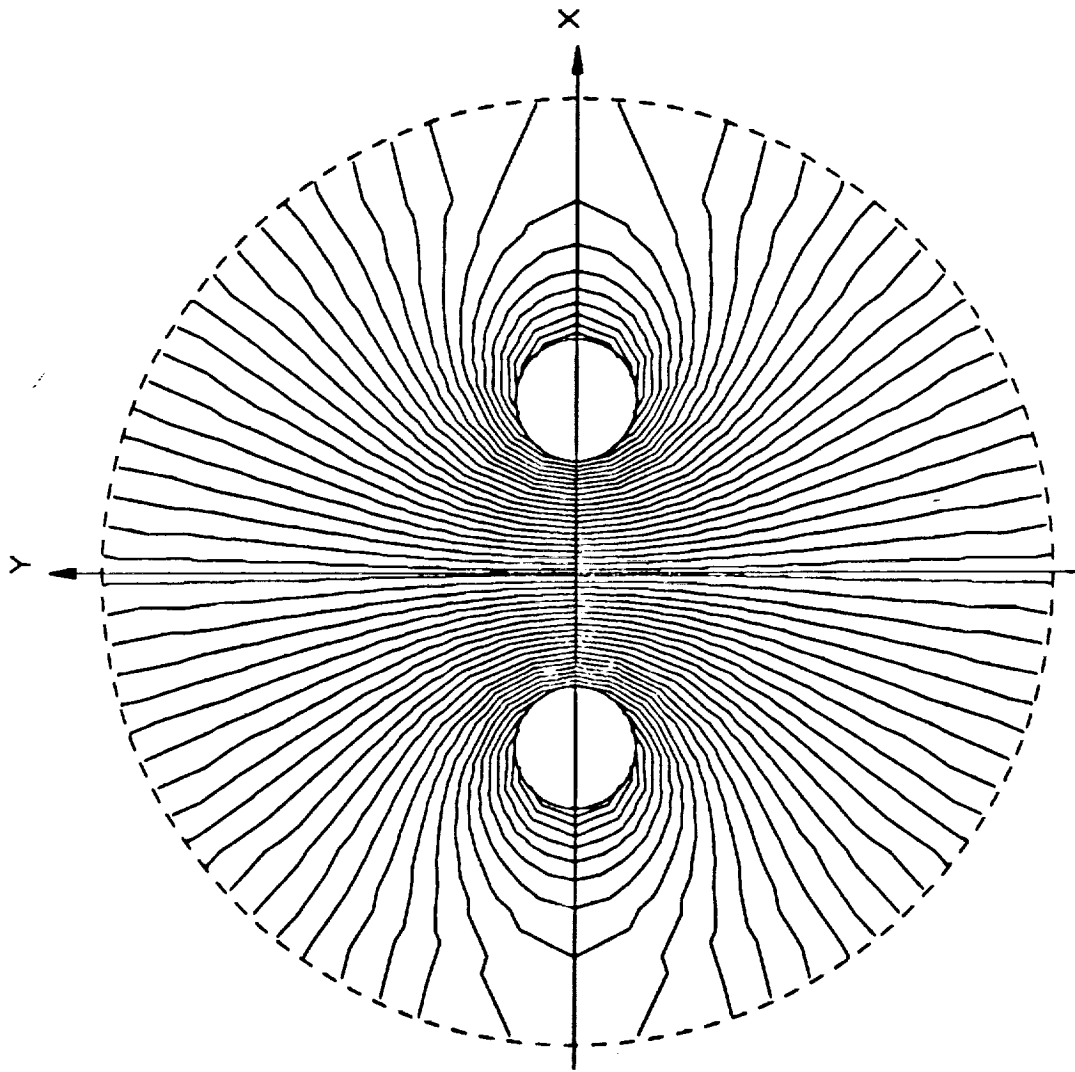


Figure 4.7: MVP Equipotentials Obtained From the FE Solutions With Natural Open Boundary Conditions - No Ballooning

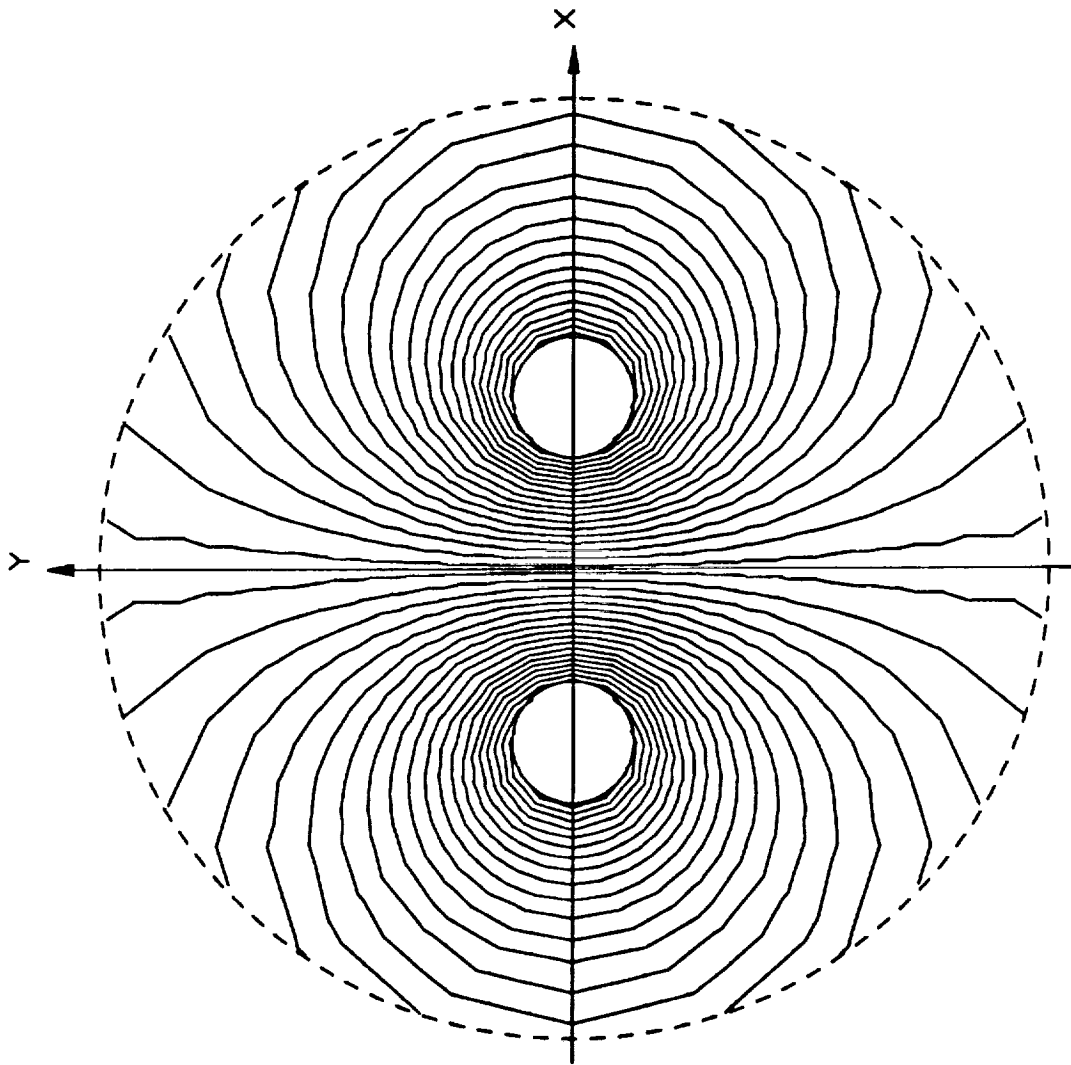


Figure 4.8: MVP Equipotentials Obtained From the FE Solutions With 2 Ballooning Layers

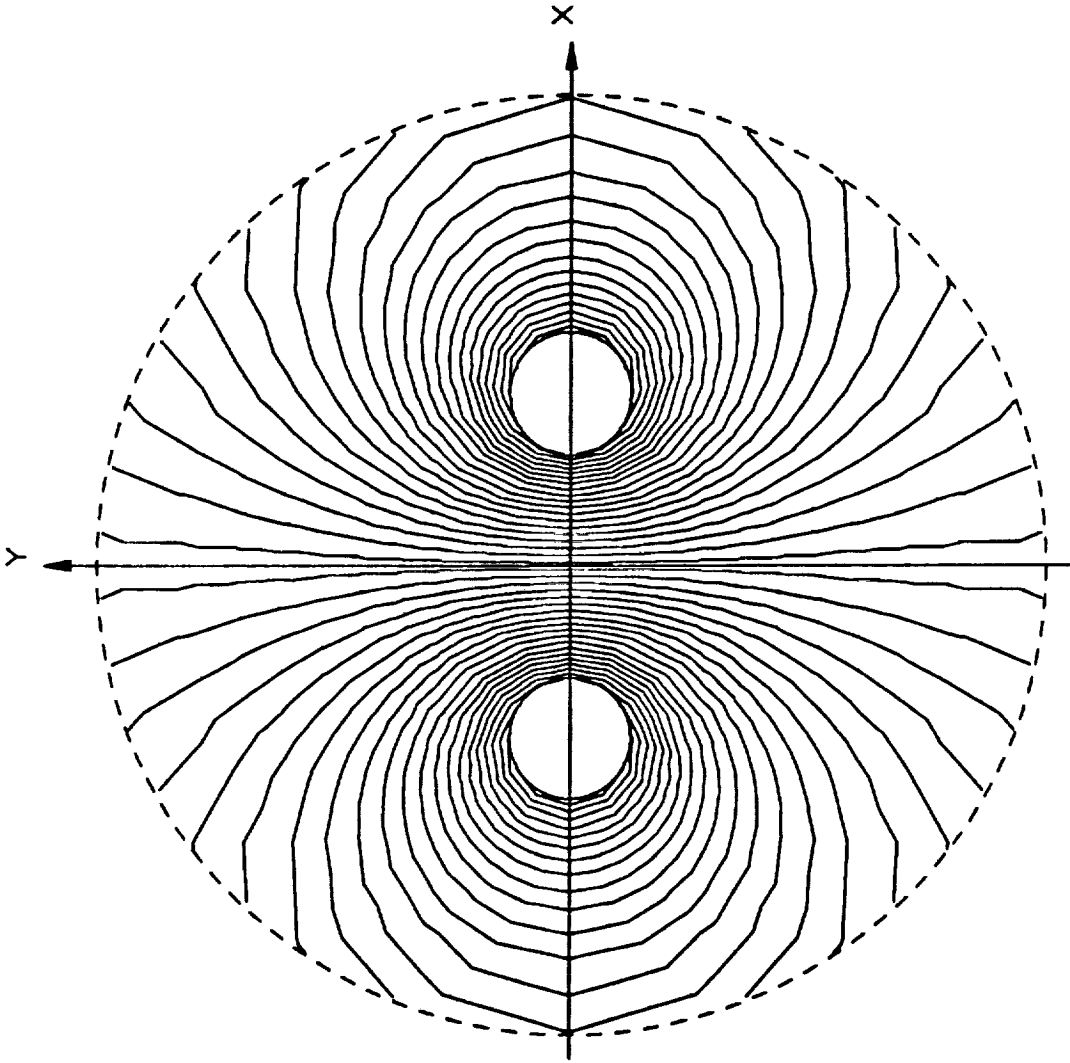


Figure 4.9: MVP Equipotentials Obtained From the FE Solutions With 5 Ballooning Layers

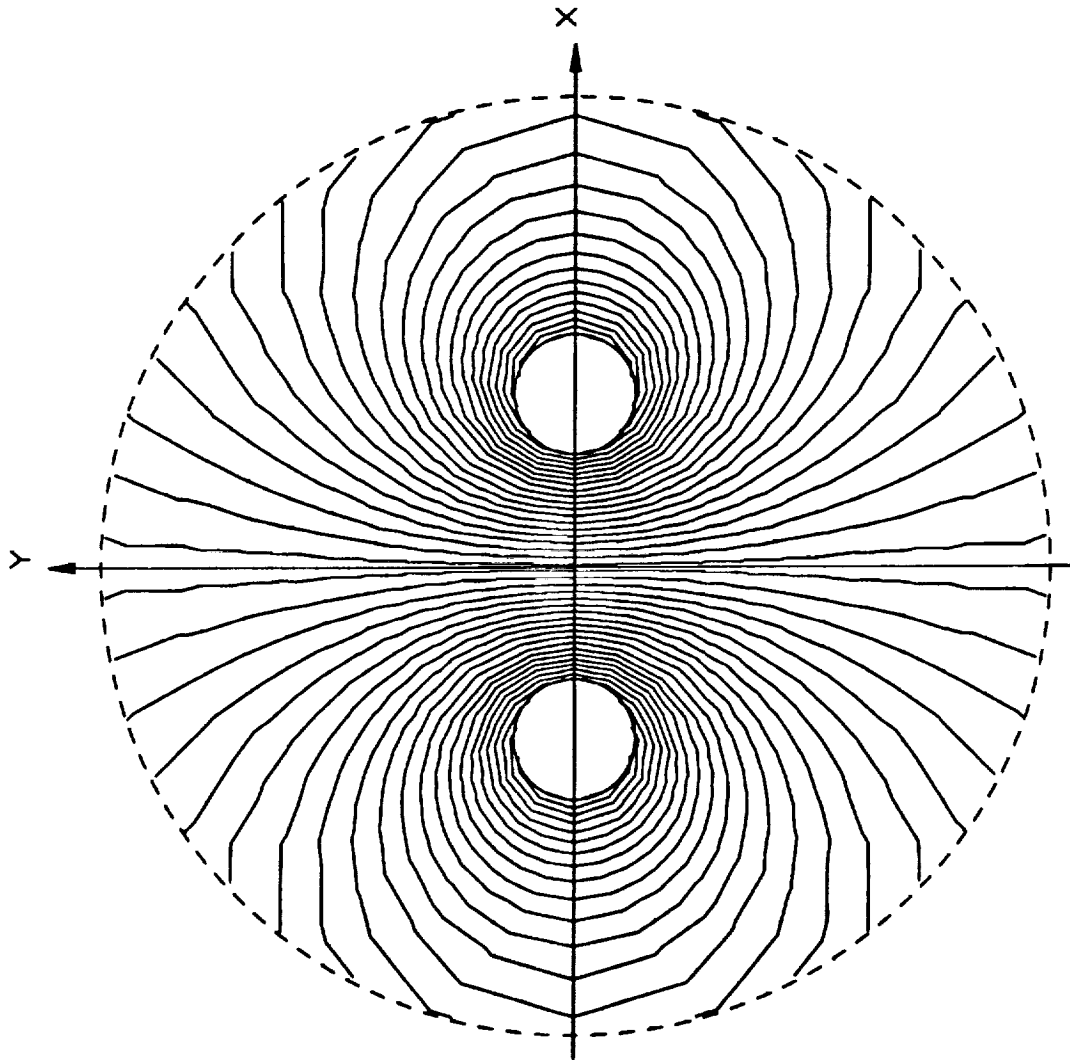


Figure 4.10: MVP Equipotentials Obtained From the FE Solutions With 10 Ballooning Layers

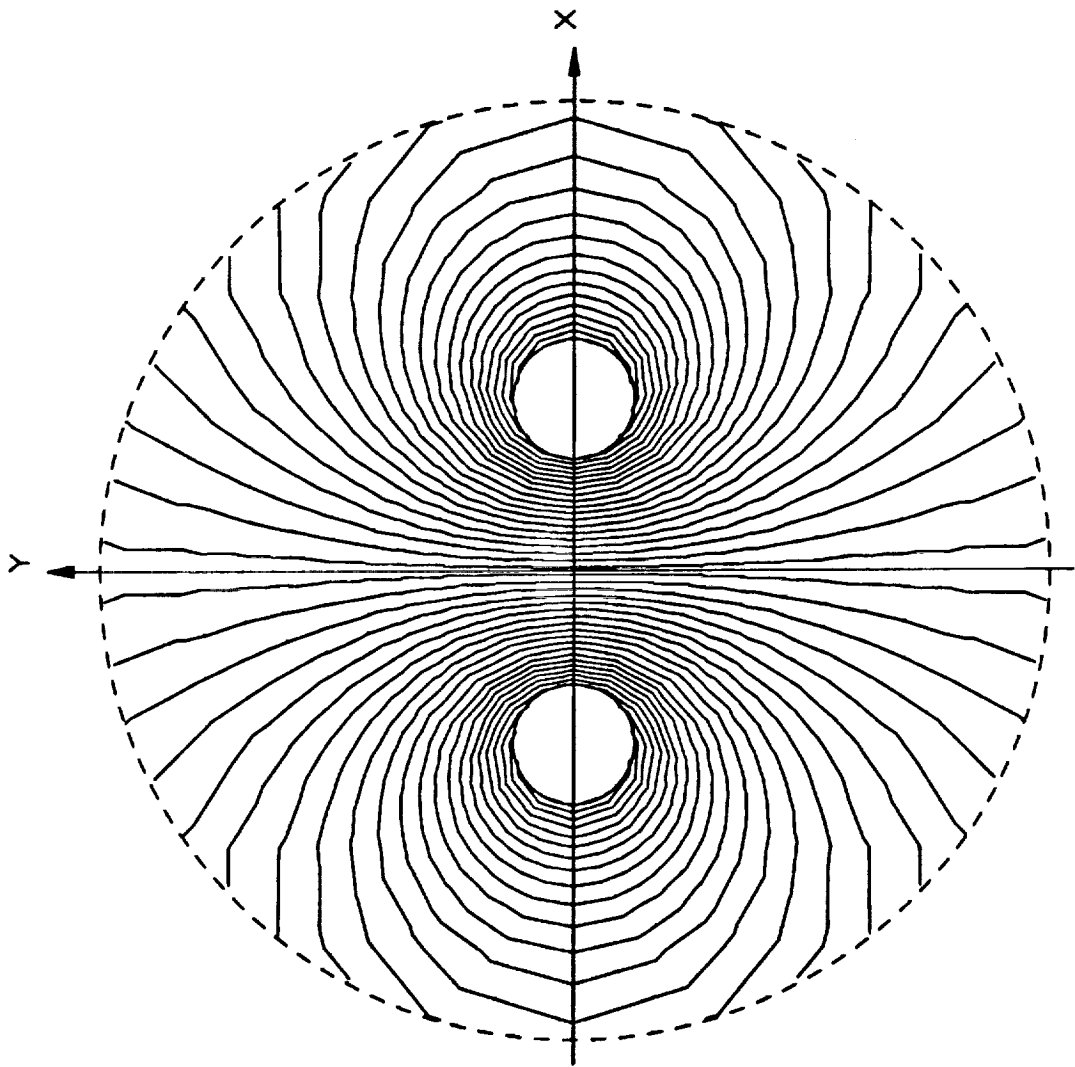


Figure 4.11: MVP Equipotentials Obtained From the FE Solutions With 15 Ballooning Layers

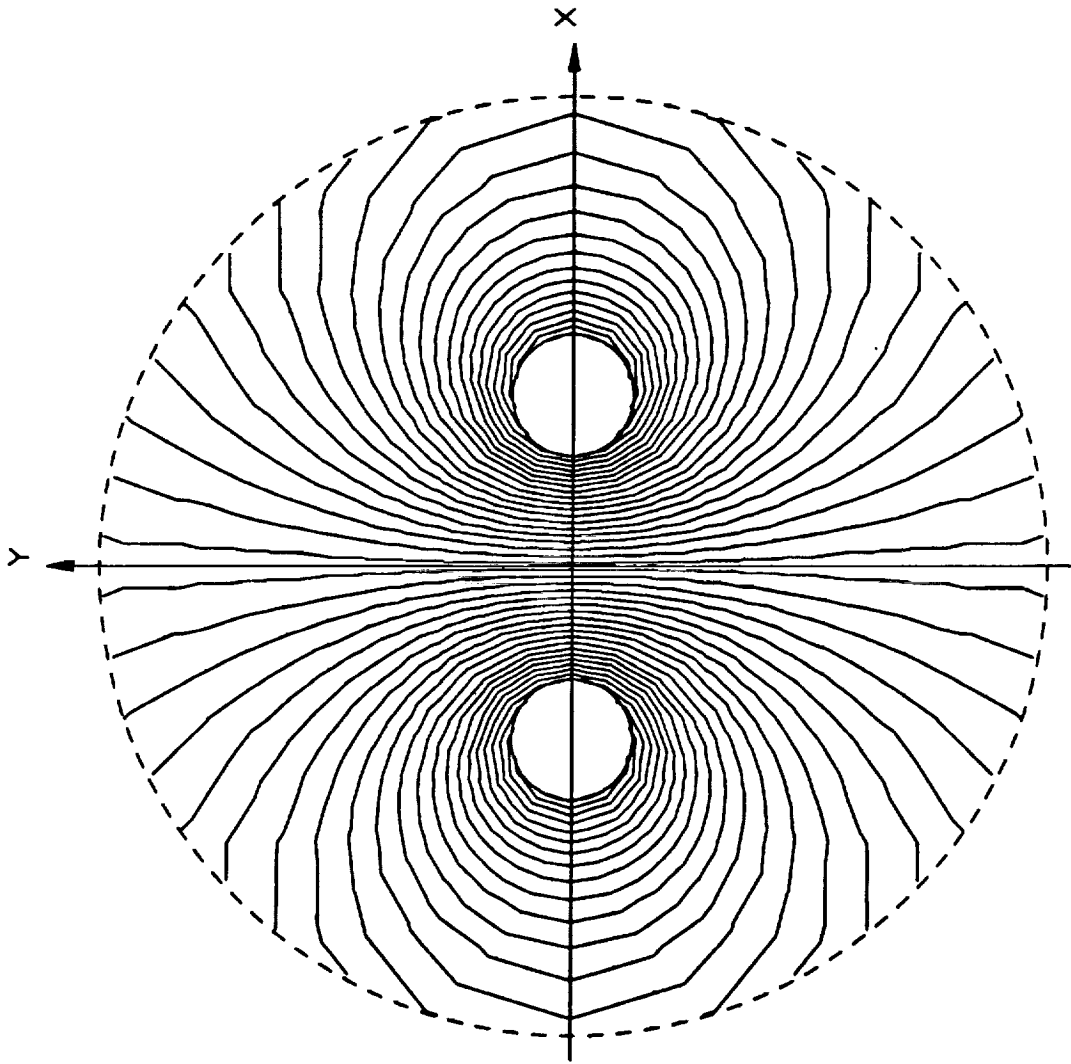


Figure 4.12: MVP Equipotentials Obtained From the FE Solutions With 20 Ballooning Layers

Element	Analytical Solution	FE Solution with Open (neumann) Boundary		FE Solution with Ballooning (Approximation of Infinite Boundary)				
		m=0		m=2		m=5		
		MVP(Lines/in)	Error*(%)	MVP(Lines/in)	Error(%)	MVP(Lines/in)	Error(%)	Error(%)
88	394.4	474.0	20.2	335.1	15.1	362.1	8.21	
92	342.0	417.8	22.2	289.2	15.4	314.3	8.09	
95	273.7	340.0	24.3	229.6	16.1	251.3	8.15	
100	161.3	202.4	25.5	134.6	16.5	148.3	8.03	
105	57.97	71.65	23.6	49.59	14.5	54.34	6.27	
963	315.6	415.4	31.6	253.5	19.7	284.8	9.78	
973	233.2	320.0	37.2	184.1	21.1	210.8	9.59	
988	82.92	118.6	43.0	63.40	23.6	74.83	9.76	
1105	305.1	412.7	35.3	242.6	20.5	275.4	9.73	
1111	262.0	367.3	40.2	202.9	22.6	234.8	10.4	
1118	184.2	267.5	45.3	139.8	24.1	165.2	10.3	
1123	126.3	186.9	48.0	94.45	25.2	113.2	10.4	
1129	61.76	90.61	46.7	46.61	24.5	55.86	9.55	
1133	15.05	20.94	39.1	11.10	26.3	135.1	10.2	
1305	222.6	376.6	69.2	151.9	31.8	194.6	12.6	
1307	207.5	353.6	70.4	141.1	32.0	181.9	12.4	
1310	158.9	272.9	71.7	105.2	33.8	138.6	12.8	
1313	97.10	166.1	71.1	61.43	36.7	83.09	14.4	
1315	54.07	92.91	71.8	34.65	35.9	47.10	12.9	
1317	10.98	18.49	68.3	8.081	26.4	10.64	3.07	

$$* \text{ Error} = \left| \frac{A_{\text{Closed}} - A_{\text{FE}}}{A_{\text{Closed}}} \right| \times 100\% \quad 1 \text{ line/in} = 38.37 \times 10^{-8} \text{ Wb/m}$$

Table 4.1: MVP Comparison Between Analytical and 2D-FE Ballooning Solutions for m=0,2 and 5

Element	Analytical Solution	FE Solution with Ballooning (Approximation of Infinite Boundary)									
		m=10			m=20			m=30			
		MVP(Lines/in)	Error*(%)	MVP(Lines/in)	Error(%)	MVP(Lines/in)	Error(%)	MVP(Lines/in)	Error(%)	MVP(Lines/in)	Error(%)
88	394.4	368.6	6.55	369.1	6.42	369.1	6.42	369.1	6.42	369.1	6.42
92	342.0	320.4	6.31	320.9	6.17	320.9	6.17	320.9	6.17	320.9	6.17
95	273.7	256.6	6.22	257.0	6.07	257.0	6.07	257.0	6.07	257.0	6.07
100	161.3	151.6	5.97	151.9	5.81	151.9	5.81	151.9	5.81	151.9	5.81
105	57.97	55.49	4.28	55.58	4.12	55.58	4.12	55.58	4.12	55.58	4.12
963	315.6	292.3	7.39	292.9	7.20	292.9	7.20	292.9	7.20	292.9	7.20
973	233.2	217.3	6.82	217.8	6.60	217.8	6.60	217.8	6.60	217.8	6.60
988	82.92	77.62	6.40	77.84	6.14	77.84	6.14	77.84	6.14	77.84	6.13
1105	305.1	283.3	7.14	283.9	6.93	283.9	6.93	283.9	6.93	283.9	6.93
1111	262.0	242.5	7.45	243.1	7.22	243.1	7.22	243.1	7.22	243.1	7.22
1118	184.2	171.4	6.94	171.9	6.68	171.9	6.68	171.9	6.68	171.9	6.68
1123	126.3	117.8	6.74	118.2	6.46	118.2	6.46	118.2	6.46	118.2	6.50
1129	61.76	58.12	5.89	58.30	5.61	58.30	5.61	58.30	5.61	58.30	5.61
1133	15.05	14.10	6.33	14.15	6.02	14.15	6.02	14.15	6.02	14.15	6.02
1305	222.6	204.8	7.98	205.6	7.62	205.6	7.62	205.6	7.62	205.6	7.62
1307	207.5	191.8	7.60	192.5	7.23	192.5	7.23	192.5	7.23	192.5	7.23
1310	158.9	146.7	7.72	147.3	7.33	147.3	7.33	147.3	7.33	147.3	7.32
1313	97.10	88.40	8.96	88.82	8.53	88.82	8.53	88.82	8.53	88.82	8.53
1315	54.07	50.16	7.22	50.40	6.78	50.40	6.78	50.40	6.78	50.40	6.78
1317	10.98	11.27	2.67	11.32	3.11	11.32	3.11	11.32	3.11	11.32	3.12

$$* \text{ Error} = \left| \frac{A_{\text{Closed}} - A_{\text{FE}}}{A_{\text{Closed}}} \right| \times 100\% \quad 1 \text{ line/in} = 38.37 \times 10^{-8} \text{ Wb/m}$$

Table 4.2: MVP Comparison Between Analytical and 2D-FE Ballooning Solutions for m=10,20 and 30

Element	Analytical Solution		FE Solution with Open (Neumann) Boundary (m=0)				FE Solution with Ballooning (approximation of Infinite Boundary) (m=2)			
	Flux Density		Flux Density		Flux Density		Flux Density		Flux Density	
	$ \bar{B} $ (Lines/in ²)	θ (°)	$ \bar{B} $ (Lines/in ²)	Error _B [*] (%)	θ (°)	Error _θ ^{**} (%)	$ \bar{B} $ (Lines/in ²)	Error _B (%)	θ (°)	Error _θ (%)
88	374.4	98.36	318.9	14.8	105.5	7.29	410.5	9.64	101.9	3.63
92	319.0	149.6	254.9	20.1	158.0	5.59	300.6	5.76	141.1	5.70
95	266.1	181.7	259.8	2.34	190.8	5.04	256.2	3.73	170.2	6.32
100	221.0	222.8	246.3	11.5	230.4	3.41	184.3	16.6	212.8	4.50
105	215.9	254.5	258.7	19.8	254.5	0.03	174.3	19.3	246.9	2.99
963	227.3	109.3	163.4	28.1	119.9	9.74	250.5	10.2	108.7	.569
973	175.8	171.4	176.9	.605	191.0	11.5	179.4	2.03	160.7	6.21
988	128.8	236.7	181.7	41.1	248.9	5.17	102.9	20.1	232.6	1.73
1105	206.7	94.54	118.6	42.6	104.2	10.2	213.5	3.29	97.68	3.33
1111	171.8	140.4	126.1	26.6	159.0	13.3	180.6	5.14	129.1	8.04
1118	138.4	187.4	151.7	9.54	209.2	11.7	128.2	7.37	172.2	8.12
1123	122.3	214.7	159.4	30.3	231.3	7.76	101.7	16.9	200.5	6.60
1129	117.4	244.1	176.8	50.6	254.6	4.31	94.39	19.6	241.9	.902
1133	108.8	263.5	159.5	46.7	264.6	.438	74.62	31.4	259.1	1.67
1305	104.5	98.46	30.18	71.1	159.0	61.5	115.3	10.4	103.2	4.77
1307	100.1	131.0	69.53	30.6	197.4	50.6	99.58	.523	128.8	1.73
1310	89.01	176.0	122.7	37.9	214.4	21.8	96.18	8.06	167.1	5.08
1313	79.75	215.8	134.7	68.9	234.1	8.47	76.09	4.59	197.8	8.35
1315	75.66	240.3	140.7	86.0	251.6	4.72	62.55	17.3	231.4	3.70
1317	74.18	264.0	138.8	87.1	90.00	134.	54.58	26.4	270.0	2.27

$$* \text{ Error}_{|\bar{B}|} = \left| \frac{|\bar{B}|_{\text{Closed}} - |\bar{B}|_{\text{FE}}}{|\bar{B}|_{\text{Closed}}} \right| \times 100\%$$

$$** \text{ Error}_{\theta} = \left| \frac{\theta_{\text{Closed}} - \theta_{\text{FE}}}{\theta_{\text{Closed}}} \right| \times 100\%$$

$$1 \text{ line/in}^2 = 1550 \times 10^{-8} \text{ Wb/m}^2$$

Table 4.3: Flux Density Comparison Between Analytical and 2D-FE Ballooning Solutions for m=0 and 2

Element	Analytical Solution		FE Solution with Ballooning (Approximation of Infinite Boundary)										
	Flux Density		Flux Density (m=5)					Flux Density (m=10)					
	$ B (Lines/in^2)$	$\theta(^{\circ})$	$ B (Lines/in^2)$	$Error_B^*(\%)$	$\theta(^{\circ})$	$Error_{\theta}^{**}(\%)$	$ B (Lines/in^2)$	$Error_B^*(\%)$	$\theta(^{\circ})$	$Error_{\theta}^{**}(\%)$	$ B (Lines/in^2)$	$Error_B^*(\%)$	$\theta(^{\circ})$
88	374.4	98.36	393.2	5.02	102.5	4.17	389.0	3.91	102.6	4.31			
92	319.0	149.6	289.9	9.11	143.8	3.88	287.5	9.90	144.5	3.42			
95	266.1	181.7	253.8	4.60	174.1	4.16	253.4	4.75	175.1	3.63			
100	221.0	222.8	194.4	12.0	217.1	2.55	197.0	10.9	218.1	2.11			
105	215.9	254.5	190.6	11.7	249.0	2.19	194.5	9.90	249.4	2.01			
963	227.3	109.3	233.8	2.86	110.1	.714	229.8	1.10	110.4	1.05			
973	175.8	171.4	174.5	.748	166.2	3.00	173.5	1.30	167.6	2.20			
988	128.8	236.7	117.3	8.90	237.8	.445	120.9	6.09	238.8	.899			
1105	206.7	94.54	195.9	5.22	98.38	4.07	191.7	7.26	98.57	4.27			
1111	171.8	140.4	167.3	2.60	133.0	5.29	164.2	4.40	134.0	4.57			
1118	138.4	187.4	127.2	8.09	180.0	3.91	127.3	8.04	182.0	2.89			
1123	122.3	214.7	109.2	10.7	209.1	2.59	111.4	8.97	211.0	1.70			
1129	117.4	244.1	110.1	6.20	246.1	.834	114.0	2.87	247.0	1.19			
1133	108.8	263.5	91.74	15.7	261.1	.901	95.94	11.8	261.5	.752			
1305	104.5	98.46	97.96	6.24	105.6	7.24	93.86	10.2	106.3	7.95			
1307	100.1	131.0	86.49	13.6	136.2	3.99	83.60	16.5	138.4	5.60			
1310	89.01	176.0	94.09	5.70	177.6	.912	94.01	5.61	180.2	2.39			
1313	79.75	215.8	83.30	4.45	209.2	3.06	85.46	7.16	211.7	1.91			
1315	75.66	240.3	76.97	1.73	239.3	.391	80.66	6.61	240.9	.251			
1317	74.18	264.0	71.88	3.10	270.0	2.27	76.14	2.64	270.0	.227			

$$* Error_B = \left| \frac{\bar{B}|_{Closed} - \bar{B}|_{FE}}{\bar{B}|_{Closed}} \right| \times 100\%$$

$$** Error_{\theta} = \left| \frac{\theta_{Closed} - \theta_{FE}}{\theta_{Closed}} \right| \times 100\%$$

$$1 line/in^2 = 1550 \times 10^{-8} Wb/m^2$$

Table 4.4: Flux Density Comparison Between Analytical and 2D-FE Ballooning Solutions for m=5 and 10

Element	FE Solution with Ballooning (Approximation of Infinite Boundary)																	
	Analytical Solution						(m=20)						(m=30)					
	Flux Density		$\theta(^{\circ})$	Flux Density		$\theta(^{\circ})$	Flux Density		$\theta(^{\circ})$	Flux Density		$\theta(^{\circ})$	Flux Density		$\theta(^{\circ})$	Flux Density		$\theta(^{\circ})$
$ B (Lines/in^2)$	$ B (Lines/in^2)$		$ B (Lines/in^2)$	$Error_B(\%)$	$\theta(^{\circ})$													
88	374.4	98.36	388.7	3.82	102.6	388.7	4.32	102.6	388.7	3.82	102.6	388.7	3.82	102.6	388.7	3.82	102.6	4.32
92	319.0	149.6	287.3	9.96	144.6	287.3	3.39	144.6	287.3	9.96	144.6	287.3	9.96	144.6	287.3	9.96	144.6	3.39
95	266.1	181.7	253.4	4.76	175.1	253.4	3.59	175.1	253.4	4.76	175.1	253.4	4.76	175.1	253.4	4.76	175.1	3.59
100	221.0	222.8	197.2	10.8	218.2	197.2	2.08	218.2	197.2	10.8	218.2	197.2	10.8	218.2	197.2	10.8	218.2	2.08
105	215.9	254.5	194.8	9.75	249.5	194.8	2.00	249.5	194.8	9.75	249.5	194.8	9.75	249.5	194.8	9.75	249.5	2.00
963	227.3	109.3	229.5	.964	110.5	229.5	1.07	110.5	229.5	.964	110.5	229.5	.964	110.5	229.5	.964	110.5	1.07
973	175.8	171.4	173.5	1.34	167.7	173.5	2.14	167.7	173.5	1.34	167.7	173.5	1.34	167.7	173.5	1.34	167.7	2.14
988	128.8	236.7	121.2	5.87	238.9	121.2	.933	238.9	121.2	5.87	238.9	121.2	5.87	238.9	121.2	5.87	238.9	.934
1105	206.7	94.54	191.4	7.42	98.58	191.4	4.28	98.58	191.4	7.42	98.58	191.4	7.42	98.58	191.4	7.42	98.58	4.28
1111	171.8	140.4	164.0	4.54	134.1	164.0	4.51	134.1	164.0	4.54	134.1	164.0	4.54	134.1	164.0	4.54	134.1	4.51
1118	138.4	187.4	127.3	8.03	182.1	127.3	2.81	182.1	127.3	8.03	182.1	127.3	8.03	182.1	127.3	8.03	182.1	2.81
1123	122.3	214.7	111.5	8.83	211.2	111.5	1.63	211.2	111.5	8.83	211.2	111.5	8.83	211.2	111.5	8.83	211.2	1.63
1129	117.4	244.1	114.3	2.61	247.0	114.3	1.22	247.0	114.3	2.61	247.0	114.3	2.61	247.0	114.3	2.61	247.0	1.22
1133	108.8	263.5	96.27	11.5	261.5	96.27	.741	261.5	96.27	11.5	261.5	96.27	11.5	261.5	96.27	11.5	261.5	.741
1305	104.5	98.46	93.54	10.5	106.3	93.54	8.00	106.3	93.54	10.5	106.3	93.54	10.5	106.3	93.54	10.5	106.3	8.00
1307	100.1	131.0	83.38	16.7	138.5	83.38	5.73	138.5	83.38	16.7	138.5	83.38	16.7	138.5	83.38	16.7	138.5	5.73
1310	89.01	176.0	94.01	5.62	180.4	94.01	2.50	180.4	94.01	5.62	180.4	94.01	5.62	180.4	94.01	5.62	180.4	2.50
1313	79.75	215.8	85.64	7.38	211.9	85.64	1.82	211.9	85.64	7.38	211.9	85.64	7.38	211.9	85.64	7.38	211.9	1.82
1315	75.66	240.3	80.95	6.99	241.0	80.95	.299	241.0	80.95	6.99	241.0	80.95	6.99	241.0	80.95	6.99	241.0	.299
1317	74.18	264.0	76.47	3.08	270.0	76.47	2.27	270.0	76.47	3.08	270.0	76.47	3.08	270.0	76.47	3.08	270.0	2.27

$$* \text{ Error}_{|B|} = \left| \frac{|B|_{\text{Closed}} - |B|_{\text{FE}}}{|B|_{\text{Closed}}} \right| \times 100\%$$

$$** \text{ Error}_{\theta} = \left| \frac{\theta_{\text{Closed}} - \theta_{\text{FE}}}{\theta_{\text{Closed}}} \right| \times 100\%$$

$$1 \text{ line}/in^2 = 1550 \times 10^{-8} \text{ Wb}/m^2$$

Table 4.5: Flux Density Comparison Between Analytical and 2D-FE Ballooning Solutions for m=20 and 30

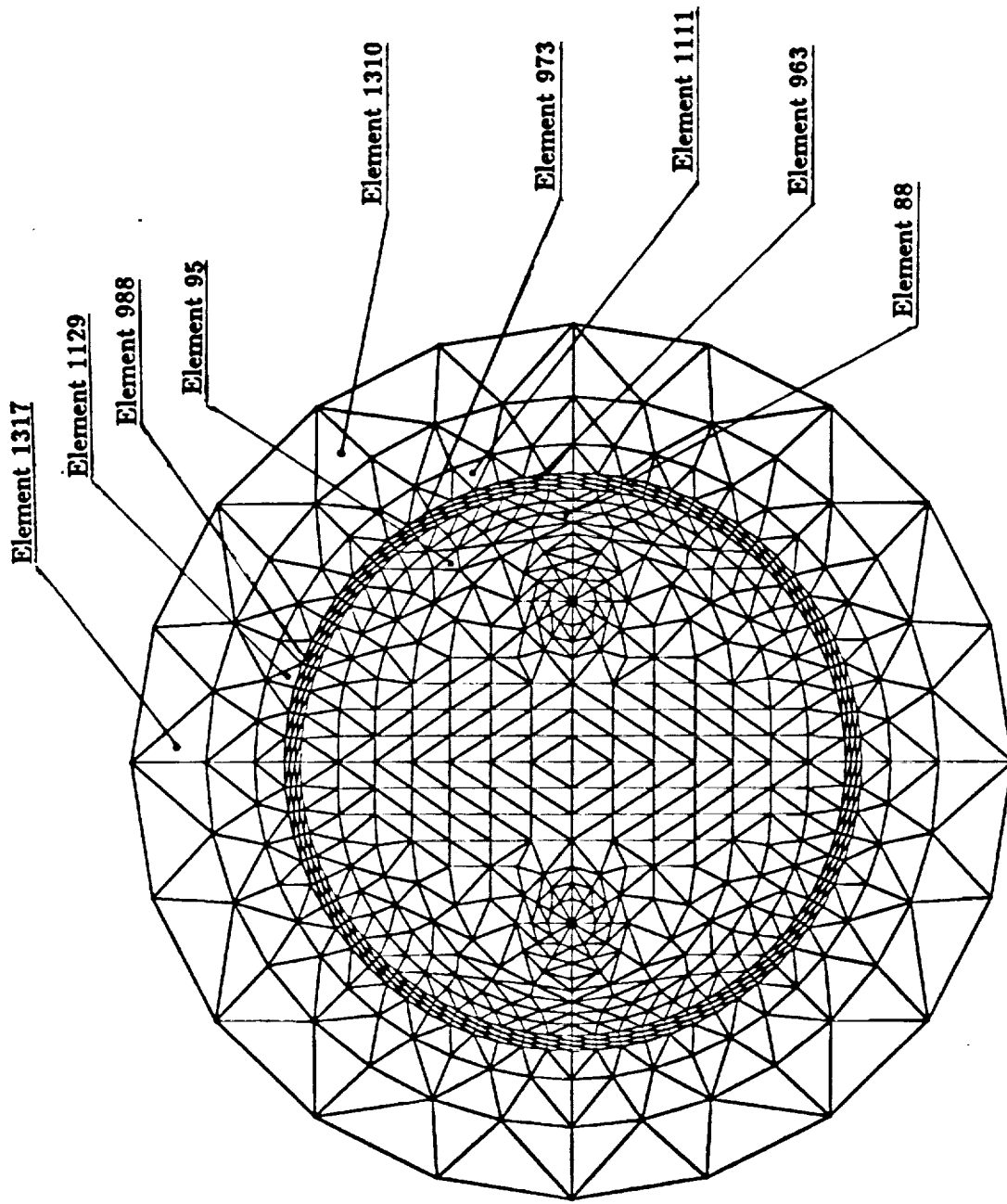


Figure 4.13: Finite Elements Chosen for MVP and Flux Density Data Comparisons in Tables (4.1) Through (4.5)

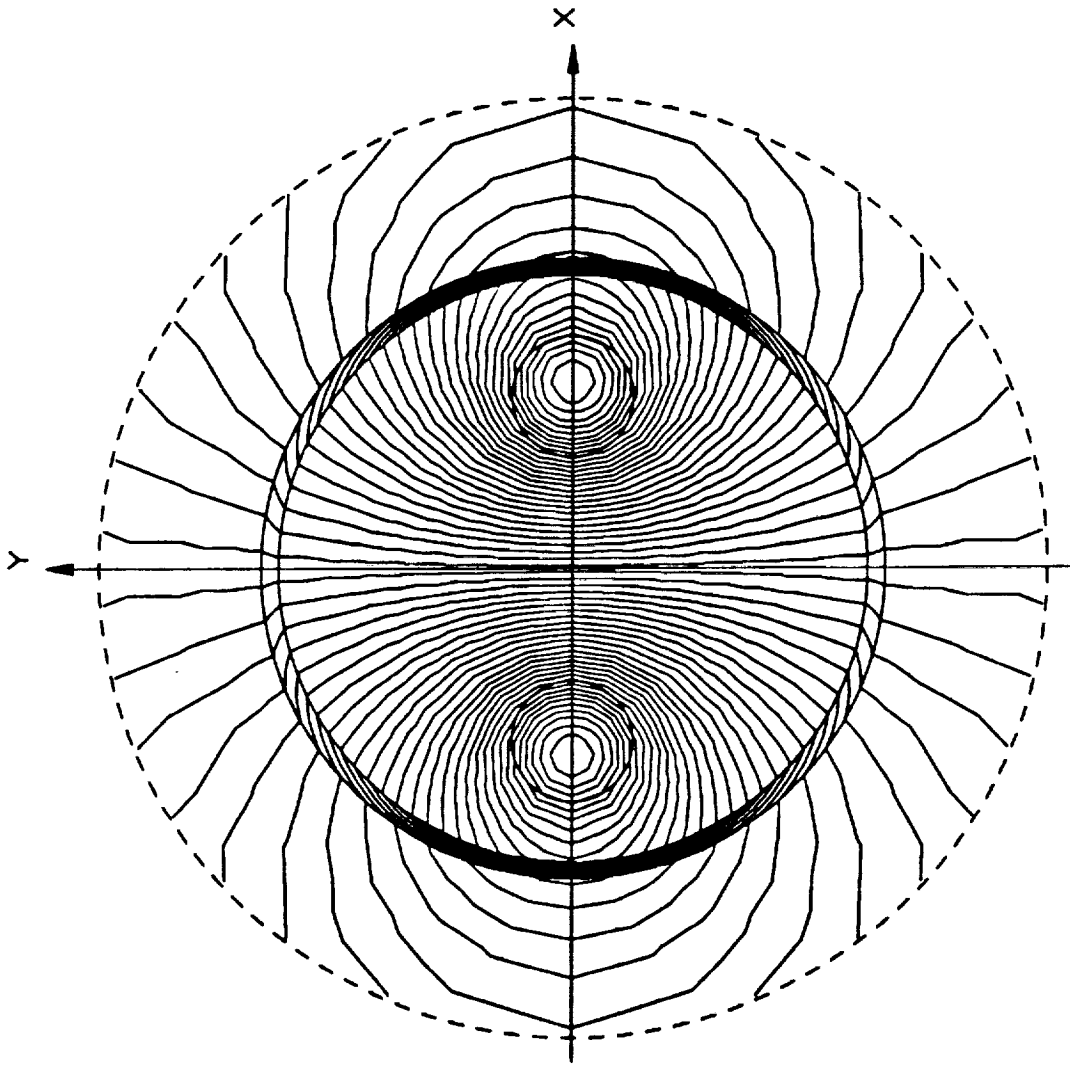


Figure 4.14: The Parallel-Pair MVP equipotentials Obtained From FE Solutions With Ballooning ($m=15$) Including Shielding ($\mu_r = 10$)

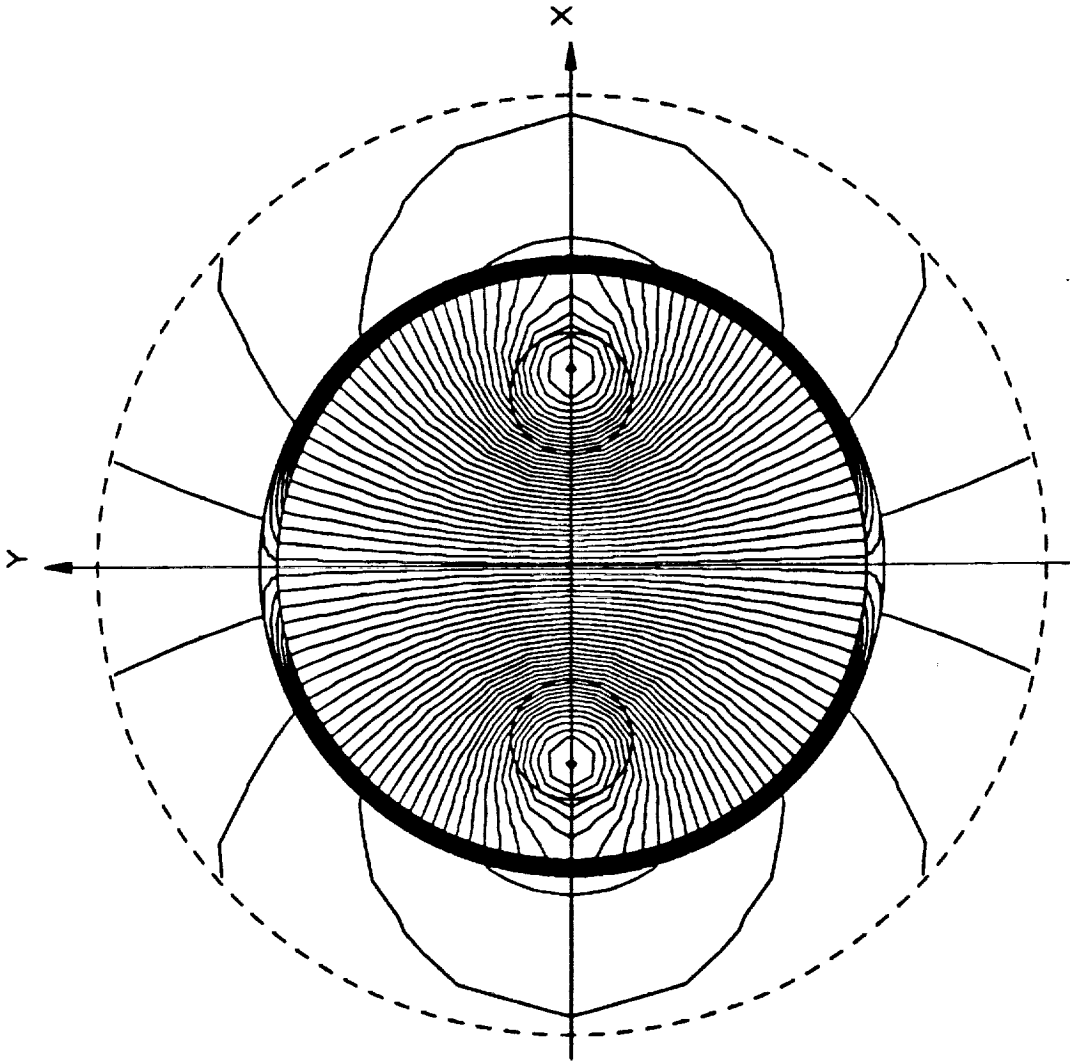


Figure 4.15: The Parallel-Pair MVP Equipotentials Obtained From FE Solutions With Ballooning ($m=15$) Including Shielding ($\mu_r = 100$)

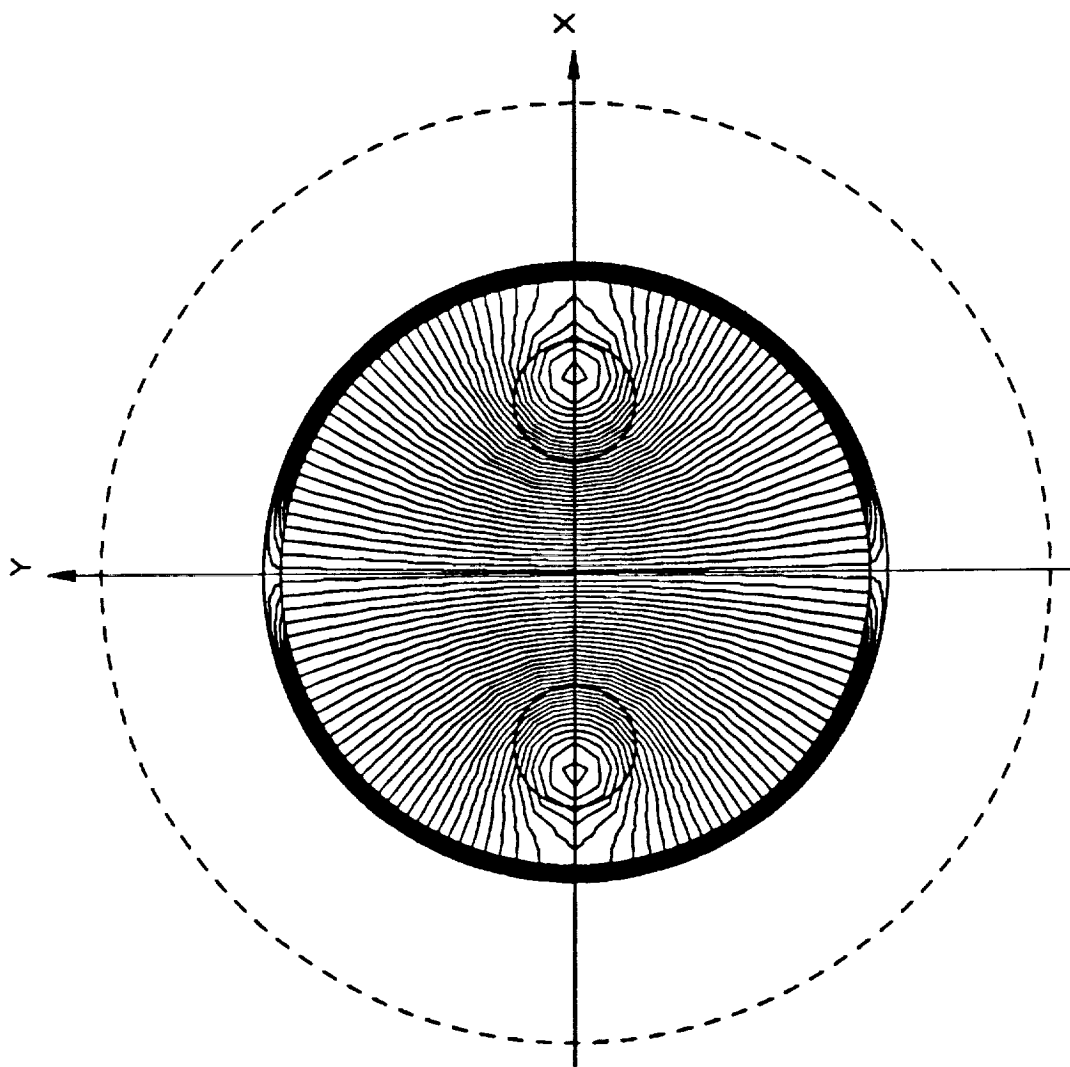


Figure 4.16: The Parallel-Pair MVP Equipotentials Obtained From FE Solutions With Ballooning ($m=15$) Including Shielding ($\mu_r = 1000$).

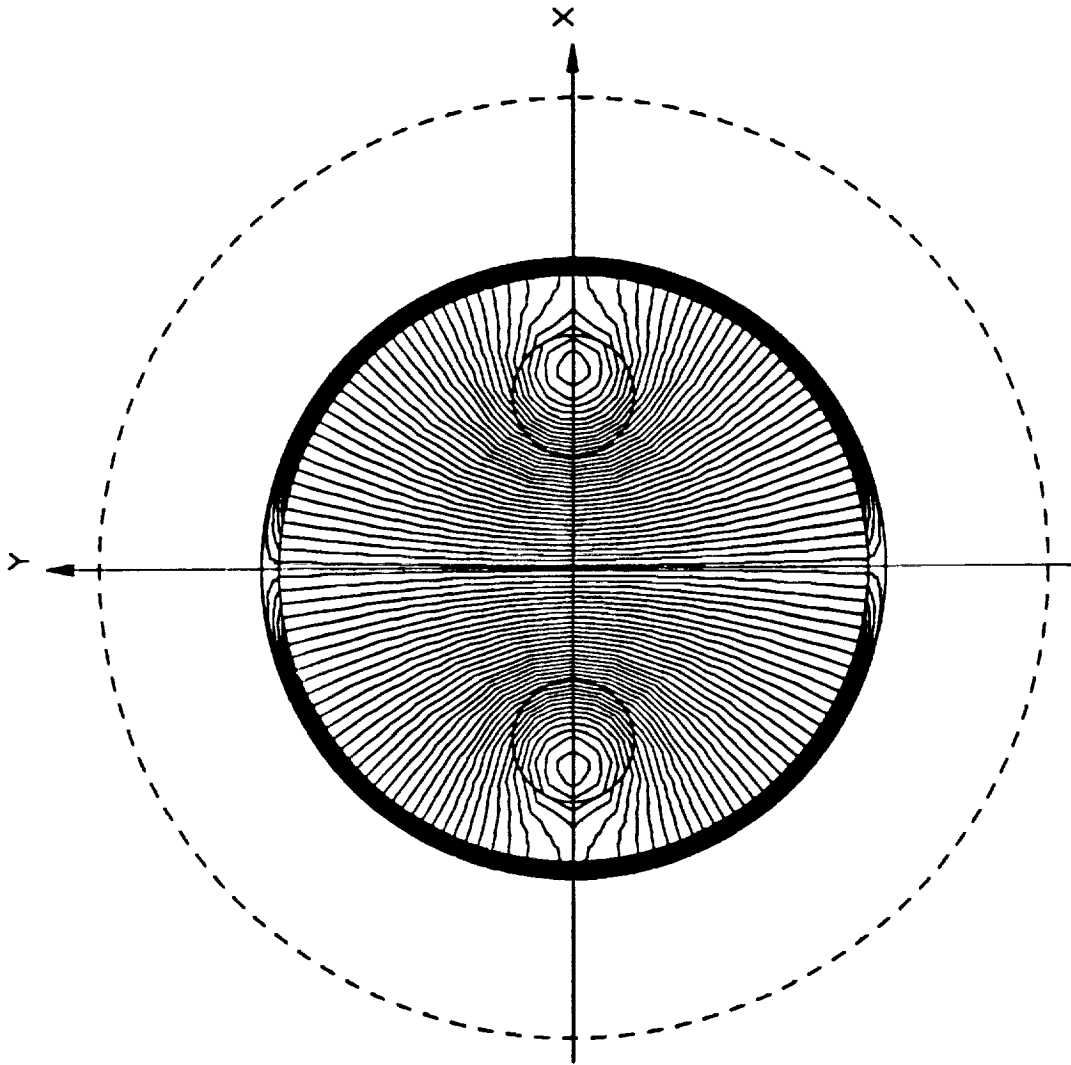


Figure 4.17: The Parallel-Pair MVP Equipotentials Obtained From FE Solutions With Ballooning ($m=15$) Including Shielding ($\mu_r = 5000$).

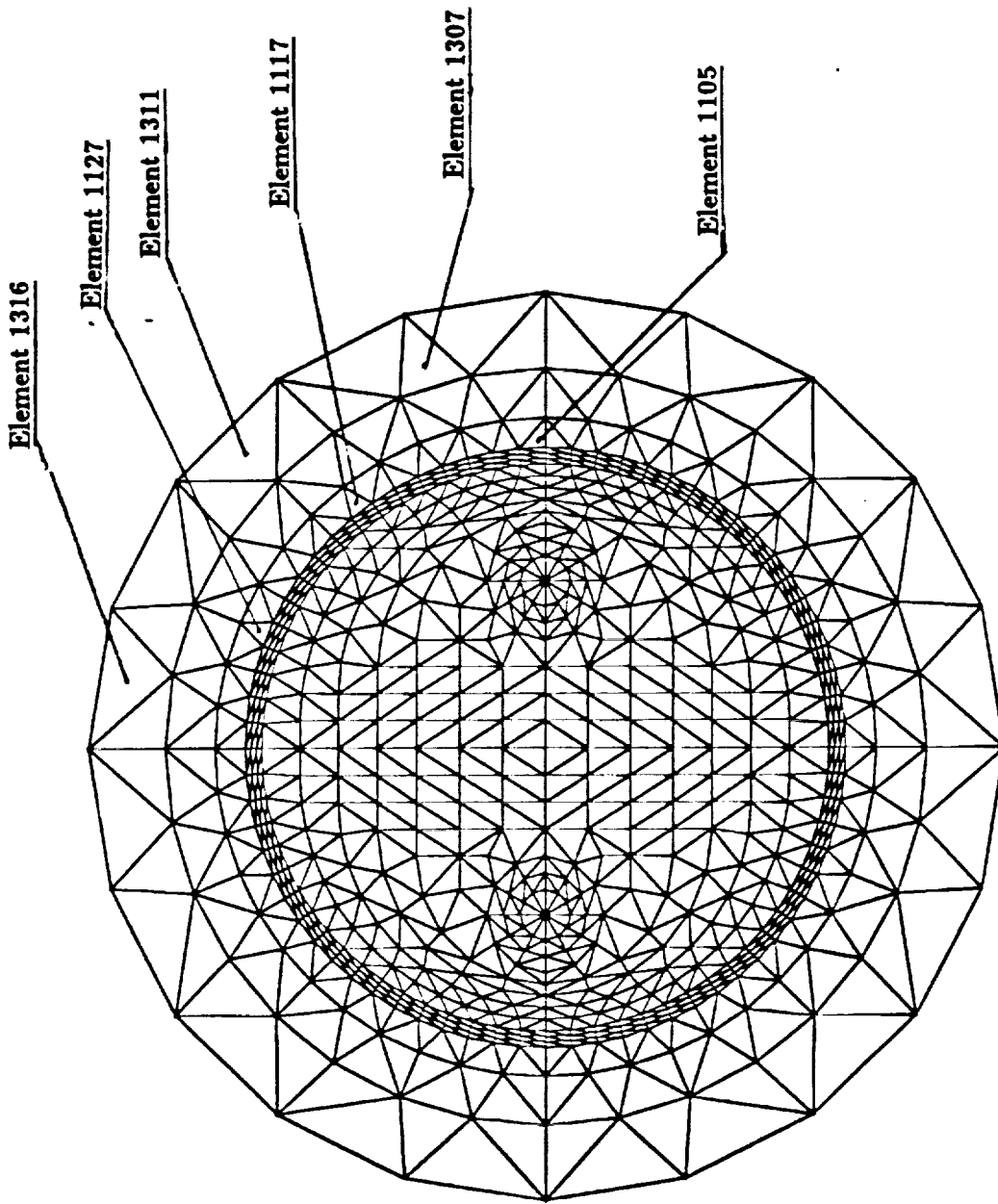


Figure 4.18: Finite Elements at Which the Effects of Shielding on Flux Densities are Given in Table(4.6) i

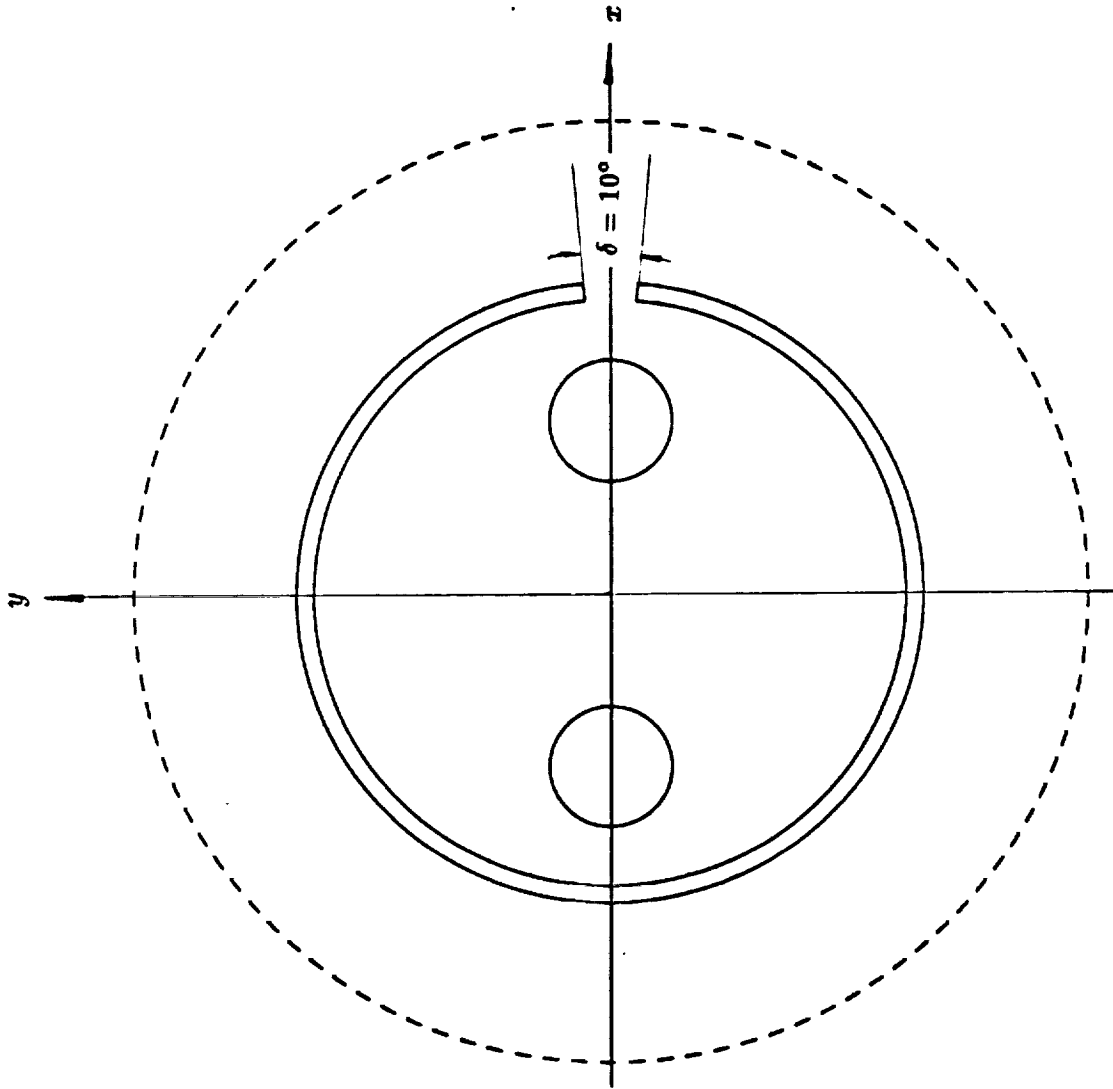


Figure 4.19: Geometry of a Defective Shield Case ($\delta = 10^\circ$)

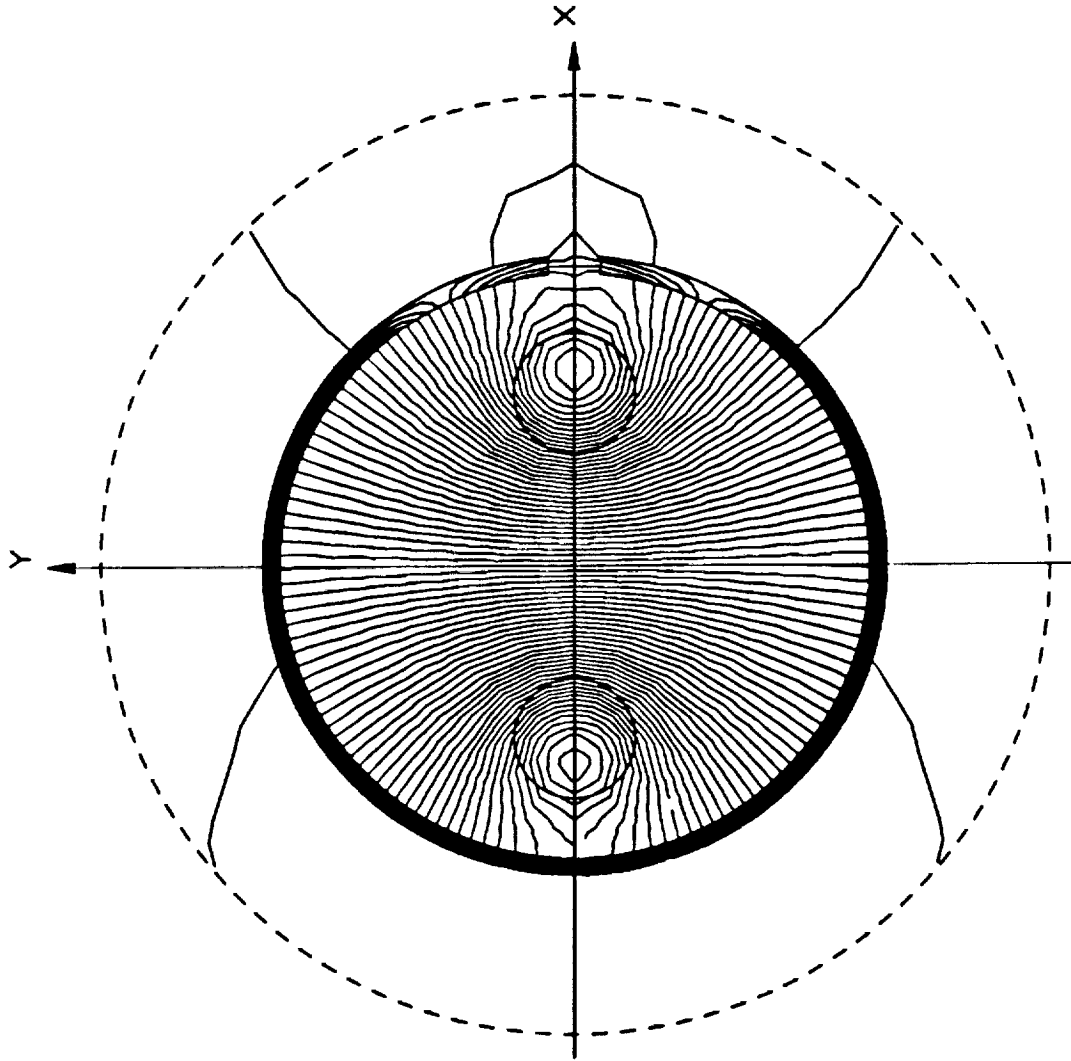


Figure 4.20: The Parallel-Pair MVP Equipotentials Obtained With Ballooning
($m=15$) Including a Defective Shielding Case ($\mu_r = 1000, \delta = 10^\circ$)

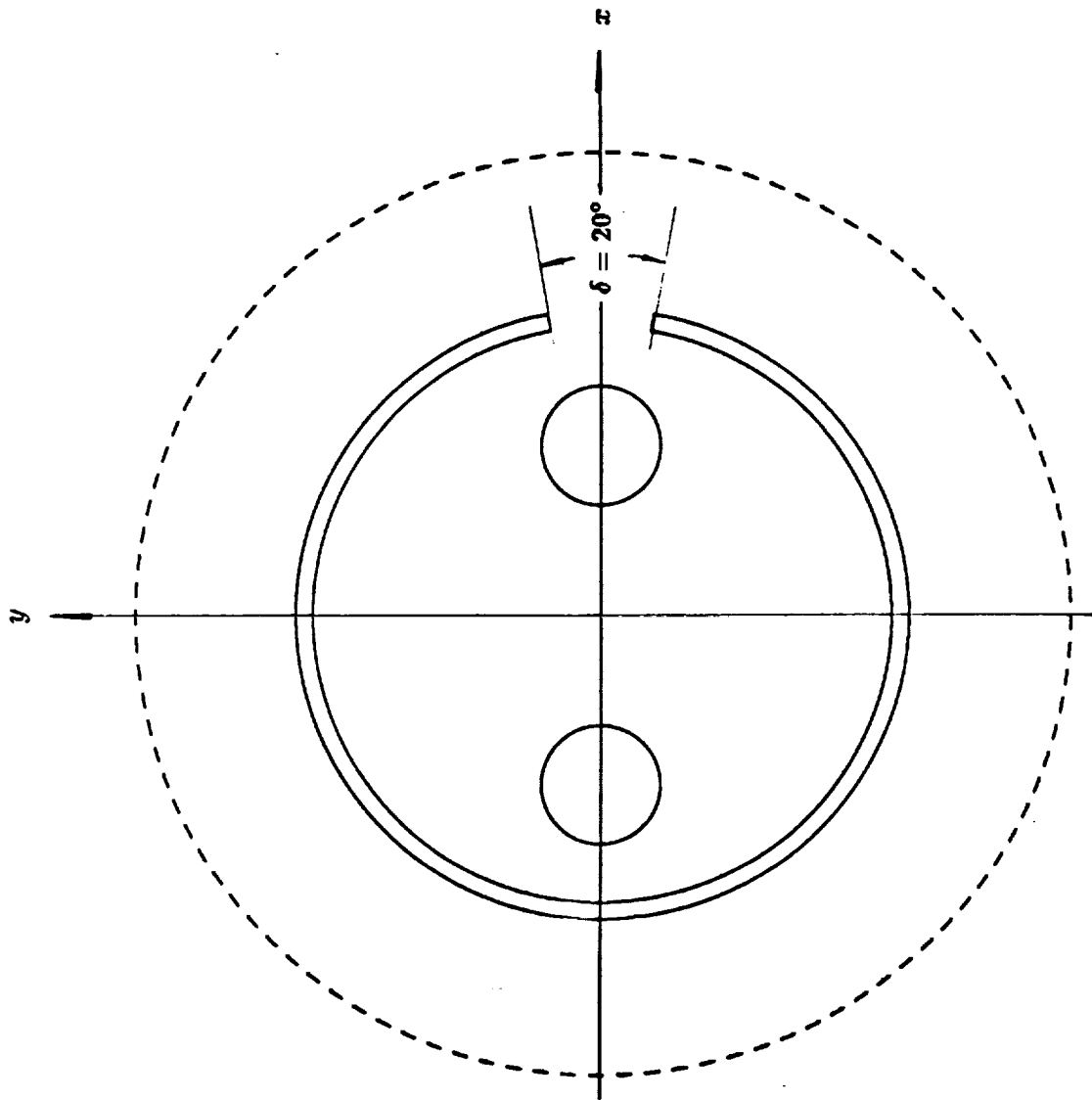


Figure 4.21: Geometry of a Defective Shield Case ($\delta = 20^\circ$)

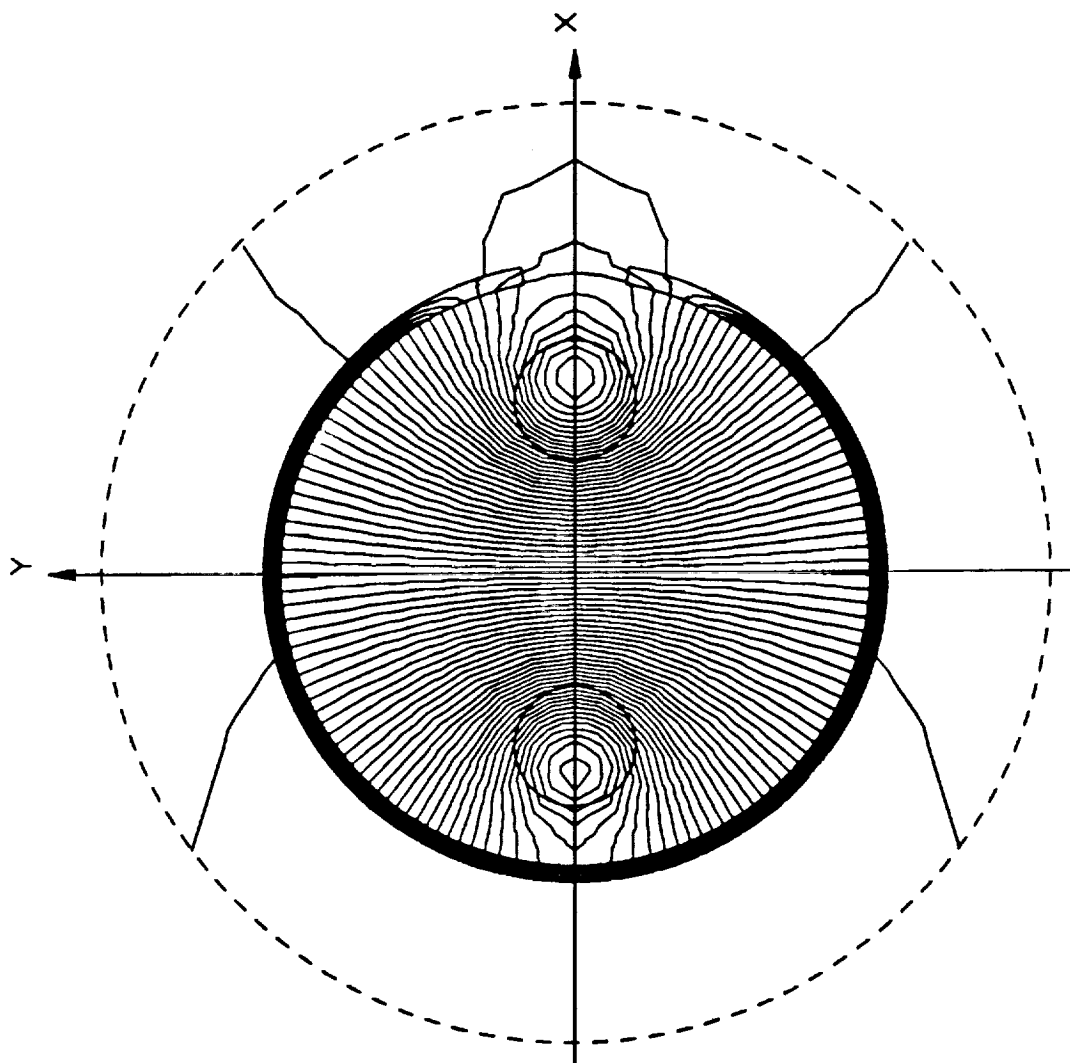


Figure 4.22: The Parallel-Pair MVP Equipotentials Obtained With Ballooning
($m=15$) Including a Defective Shielding Case ($\mu_r = 1000, \delta = 20^\circ$)

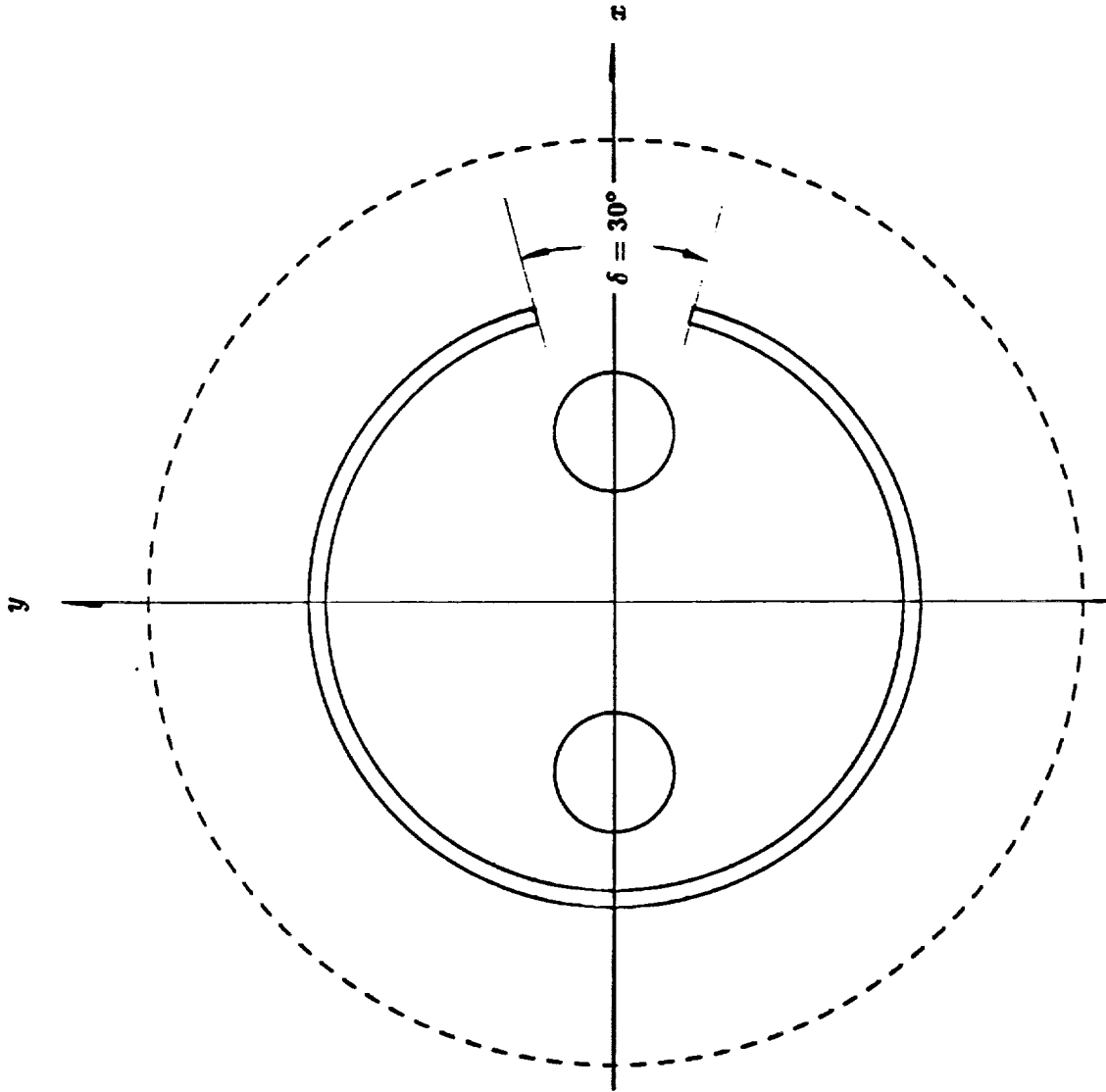


Figure 4.23: Geometry of a Defective Shield Case ($\delta = 30^\circ$)

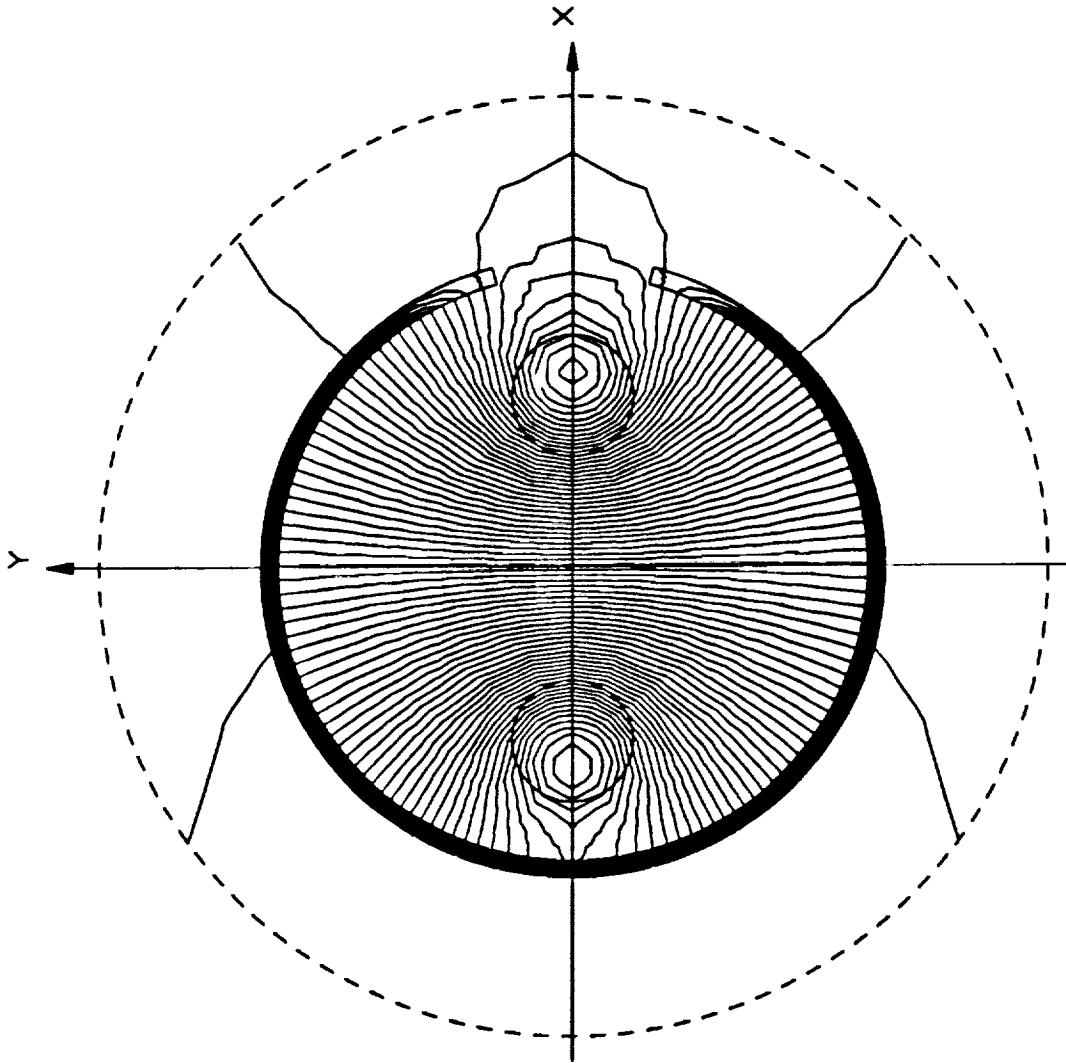


Figure 4.24: The Parallel-Pair MVP Equipotentials Obtained With Ballooning
($m=15$) Including a Defective Shielding Case ($\mu_r = 1000, \delta = 30^\circ$)

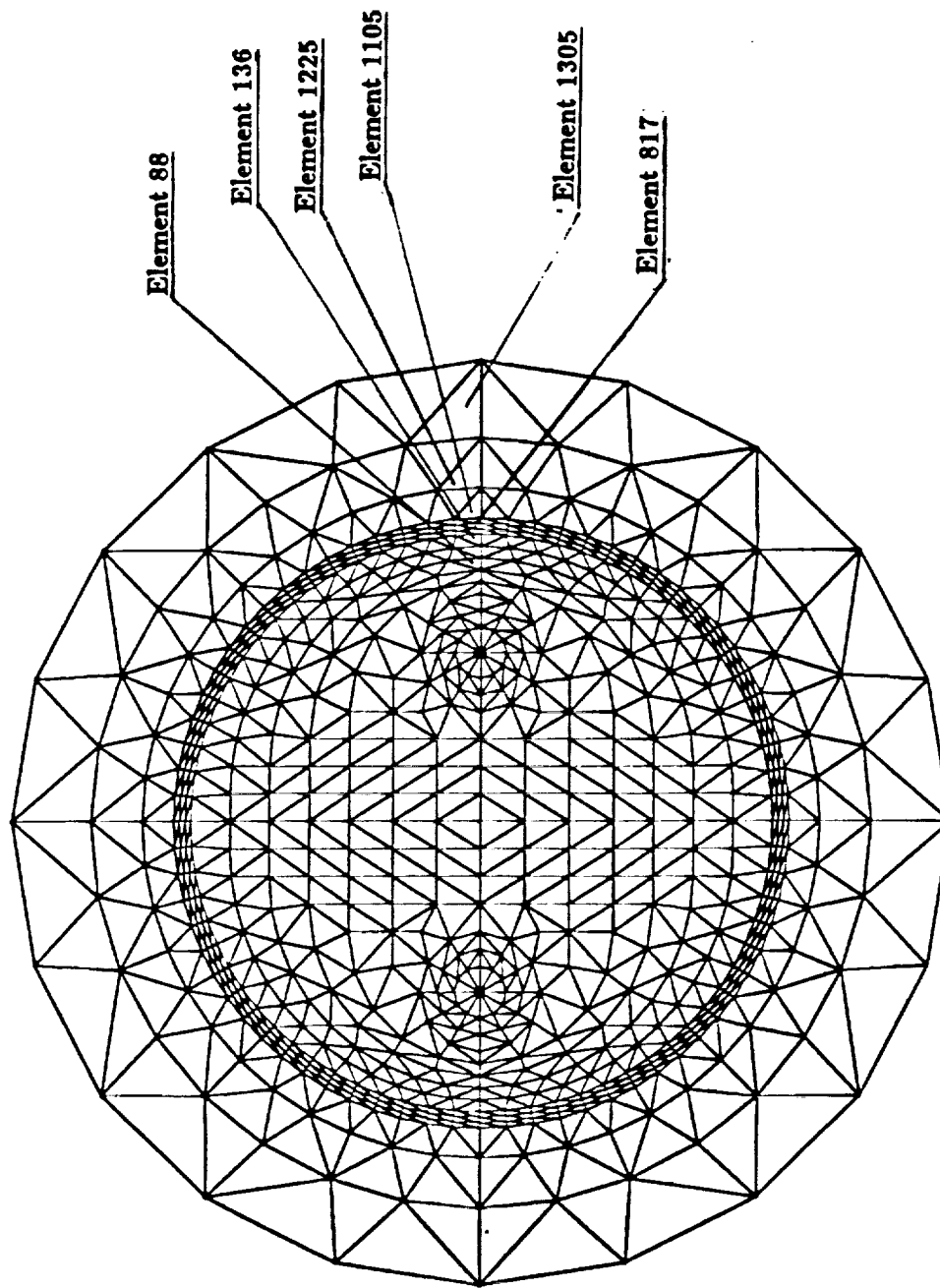


Figure 4.25: Finite Elements at Which the Effects of Defective Shielding on Flux Densities are Given in Table (4.7)

Location	$\mu_r = 1$	$\mu_r = 10$	$\mu_r = 100$	$\mu_r = 1000$
Element	$ B (Lines/in^2)$	$ B (Lines/in^2)$	$ B (Lines/in^2)$	$ B (Lines/in^2)$
1105	191.4	143.8	42.83	5.440
1117	150.8	121.8	39.19	5.056
1127	119.0	102.4	36.06	4.744
1307	83.39	65.34	20.51	2.635
1311	68.95	57.39	19.42	2.533
1316	57.28	48.17	16.56	2.168
the ballooning layers $m=15$				

Table 4.6: Flux Density Values in Cases of Shielding Materials

With Various Relative Permeabilities Without Defects

Location	$\delta = 0^\circ$	$\delta = 10^\circ$	$\delta = 20^\circ$	$\delta = 30^\circ$
Element	$ B (Lines/in^2)$	$ B (Lines/in^2)$	$ B (Lines/in^2)$	$ B (Lines/in^2)$
88	178.3	248.7	236.1	234.6
136	66.10	312.4	168.6	154.3
817	6366.	341.9	159.5	125.5
1105	5.440	199.6	98.76	84.56
1225	4.140	56.11	47.73	45.54
1305	2.911	22.21	22.13	21.87
the ballooning layers $m=15$				

Table 4.7: Flux Density With Defective Shielding for Various Defect Angles δ ,
for a Shielding Material With $\mu_r=1000$

Chapter 5

THE BALLOONING MODEL IN THE 2D DIFFUSION QUASI-STATIC CASE

The 2DFE ballooning model derived in the previous chapter can be used to solve the magnetic field problems with open boundaries only in the static case. For the space station applications of interest here, many field problems with infinite boundaries should be dealt with in the quasi static case, so that an AC 2DFE ballooning model is needed for the AC eddy current problems with open boundaries. In this chapter, the previous ballooning 2DFE model will be developed further in the frequency domain for use with the quasi static cases at hand. The new model will be applied to the study of electromagnetic field distributions surrounding a two-wire parallel-pair transmission line with conductive shielding in the (Hz to kHz) frequency range. The effects of shielding thickness and the effects of defects are also investigated.

5.1 The 2DFE Ballooning Model in the Quasi Static Case

5.1.1 The 2DFE Model in the Quasi Static Case

From chapter 2, one should use Equation(2.14) as the governing differential equation in the 2D quasi static case in the frequency domain. Phasor vectors and phasor matrices should be used. The corresponding MVP boundary value problem can be formulated as follows [11]:

$$\begin{cases} \nu\left(\frac{\partial^2 \tilde{A}}{\partial x^2} + \frac{\partial^2 \tilde{A}}{\partial y^2}\right) = -\tilde{J}_s + j\omega\sigma\tilde{A} & \text{(the governing p.d.e.)} \\ \tilde{A} = 0 & \text{(Dirichlet condition on boundary } C_1) \\ \nu \cdot \frac{\partial \tilde{A}}{\partial n} = 0 & \text{(Neumann condition on boundary } C_2) \end{cases} \quad (5.1)$$

The energy functional for the above problem is given by the following [11]:

$$F(\tilde{A}) = \int \int_R \left[\frac{1}{2} \left\{ \frac{1}{\mu} \left(\frac{\partial \tilde{A}}{\partial y} \right)^2 + \frac{1}{\mu} \left(\frac{\partial \tilde{A}}{\partial x} \right)^2 \right\} - \tilde{J}_s \cdot \tilde{A} + \frac{1}{2} j\omega\sigma \tilde{A}^2 \right] dx dy \quad (5.2)$$

Minimizing the functional in equation(5.2) is equivalent to solving the partial differential equation (p.d.e.) with Dirichlet and/or Neumann boundary conditions, equation(5.1). Using the FE method summarized in chapter 2, equation(5.2) can be discretized and minimized. Consequently, a complex matrix equation can be obtained for every triangular element as follows [11]:

$$\tilde{S}^e \tilde{A}^e = (\tilde{V}^e + \tilde{W}^e) \tilde{A}^e = \tilde{I}^e \quad (5.3)$$

where:

$$\tilde{V}^e = \begin{bmatrix} \tilde{V}_{ll}^e & \tilde{V}_{lm}^e & \tilde{V}_{ln}^e \\ \tilde{V}_{ml}^e & \tilde{V}_{mm}^e & \tilde{V}_{mn}^e \\ \tilde{V}_{nl}^e & \tilde{V}_{nm}^e & \tilde{V}_{nn}^e \end{bmatrix} \quad (5.4)$$

$$\tilde{V}_{ij}^e = \frac{\nu}{4\Delta} (r_i r_j + q_i q_j) \quad i, j = l, m, n \quad (5.5)$$

$$\tilde{W}^e = \begin{bmatrix} \tilde{W}_{ll}^e & \tilde{W}_{lm}^e & \tilde{W}_{ln}^e \\ \tilde{W}_{ml}^e & \tilde{W}_{mm}^e & \tilde{W}_{mn}^e \\ \tilde{W}_{nl}^e & \tilde{W}_{nm}^e & \tilde{W}_{nn}^e \end{bmatrix} = j\omega\sigma \frac{\Delta}{12} \begin{bmatrix} 2 & 1 & 1 \\ 1 & 2 & 1 \\ 1 & 1 & 2 \end{bmatrix} \quad (5.6)$$

$$\tilde{I}^e = \begin{bmatrix} \tilde{I}_l \\ \tilde{I}_m \\ \tilde{I}_n \end{bmatrix} = \frac{\Delta \tilde{J}_s}{3} \begin{bmatrix} 1 \\ 1 \\ 1 \end{bmatrix} \quad i = l, m, n \quad (5.7)$$

$$\begin{aligned}
r_l &= x_n - x_m, & q_l &= y_m - y_n \\
r_m &= x_l - x_n, & q_m &= y_n - y_l \\
r_n &= x_m - x_l, & q_n &= y_l - y_m
\end{aligned}
\tag{5.8}$$

and,

$$\Delta = \frac{1}{2} \begin{vmatrix} 1 & 1 & 1 \\ x_l & x_m & x_n \\ y_l & y_m & y_n \end{vmatrix}
\tag{5.9}$$

Assembling the element matrices $\tilde{\mathcal{A}}^e$ and forcing function vectors $\tilde{\mathcal{I}}^e$ given in Equation(5.3) for all elements, one can obtain an FE complex global matrix equation as follows:

$$\tilde{\mathcal{A}} \tilde{\mathcal{A}} = \tilde{\mathcal{I}}
\tag{5.10}$$

where:

$$\tilde{\mathcal{A}} = \sum_{e=1}^{ne} \tilde{\mathcal{A}}^e = \sum_{e=1}^{ne} (\tilde{\mathcal{V}}^e + \tilde{\mathcal{W}}^e)
\tag{5.11}$$

where symbol ne denotes the total number of elements.

5.1.2 The Ballooning Technique in the Quasi Static Case

In [4], Brauer presented a ballooning model to compute eddy current problems with open boundaries. In that model, eddy currents and all sources should be included in the interior region, hence the exterior region must be free space. In this thesis, a new AC 2DFE ballooning model will be derived for the diffusion type case in which the eddy currents can exist everywhere. In this new model, the total region is also divided into two subregions: the interior region which includes eddy currents and all sources ,and the exterior region which includes eddy currents only. The exterior region still consists of many annuli which have the same properties as in the previous chapter such as the start point, the fixed mapping ratio, and the same number of nodes on every boundary and the geometry similarity property to the FE triangular elements in the ballooning region of the magnetostatic case of chapter 4.

This 2DFE ballooning model for the quasi static case is very similar to that for the static case discussed in the previous chapter. However, the difference between

these two models should be highlighted as given next. In the ballooning model for the static case, every annular matrix is the same, that is, $\underline{T}^i = \underline{S}_{ext}^1$, which leads to the simple recursive algorithm discussed earlier. In the quasi static case, the element matrices have imaginary components which are proportional to the element area, Δ . Therefore, one should compute the annular matrix $\tilde{\underline{T}}^i$ for every annular region bounded by Γ_i and Γ_{i+1} . This annular FE contribution can be written as follows:

$$\tilde{\underline{T}}^i \tilde{\underline{A}}^{i,i+1} = 0 \quad (5.12)$$

where:

$$\tilde{\underline{T}}^i = \sum_{e=1}^{na} (\tilde{\underline{V}}^e + \tilde{\underline{W}}^{ei}) \quad (5.13)$$

where the symbol na denotes the number of elements in the annular region. The real components of the matrix $\tilde{\underline{T}}^i$ are unchanged from one annular region to the next. Hence, one can obtain the following:

$$\tilde{\underline{V}}^i = \tilde{\underline{V}}^{i-1} = \tilde{\underline{V}}^{i-2} = \dots = \tilde{\underline{V}}^1 \quad (5.14)$$

However, the imaginary components of the matrix $\tilde{\underline{T}}^i$ are not constant, that is:

$$\tilde{\underline{W}}^{ei} = j\omega\sigma \frac{\Delta_i}{12} \begin{bmatrix} 2 & 1 & 1 \\ 1 & 2 & 1 \\ 1 & 1 & 2 \end{bmatrix} = j\omega\sigma \frac{\Delta_1 k^{2i}}{12} \begin{bmatrix} 2 & 1 & 1 \\ 1 & 2 & 1 \\ 1 & 1 & 2 \end{bmatrix} \quad (5.15)$$

where, k is the mapping ratio between any two adjacent annuli.

Now, the FE matrix, $\tilde{\underline{S}}_{ext}$, for the exterior region can be constructed and any internal nodal MVPs can be removed by a similar process of matrix condensation as shown in the last chapter. Combining the AC ballooning model and the AC 2DFE model, one can obtain the process of this AC 2DFE ballooning model as follows:

Step(1): Using Equations(5.3) through (5.6) and (5.11), compute the complex FE global matrix $\tilde{\underline{S}}_{in}$ and the forcing function $\tilde{\underline{I}}$ in the interior region R , Figure(4.5).

Step(2): Choose a proper m , the number of ballooning layers, and using equations(5.12) through (5.15), compute the matrix $\tilde{\underline{S}}_{ext}^1$ which is the contribution of the exterior annular region Γ_0 and Γ_1 .

Step(3): $i=1$.

Step(4): Using Equations(5.12) through (5.15), compute the matrix \tilde{T}^i which is the contribution of the exterior annular region Γ_i and Γ_{i+1} .

Step(5) Using the relationship between the matrices \tilde{S}_{ext}^i and \tilde{T}^i shown in equation(4.16), obtain the matrix \tilde{S}_{ext}^{i+1} , where:

$$\tilde{S}_{ext}^{i+1} = \begin{bmatrix} \tilde{S}_{11}^{i+1} & \tilde{S}_{12}^{i+1} \\ \tilde{S}_{21}^{i+1} & \tilde{S}_{22}^{i+1} \end{bmatrix} \quad (5.16)$$

Step(6): Repeat step(4) and step(5) until $i > m$.

Step(7): Incorporate the ballooning matrix \tilde{S}_{11}^m into the FE global equation (5.3), that is:

$$\begin{bmatrix} \tilde{S}_{RR} & \tilde{S}_{R\Gamma_0} \\ \tilde{S}_{\Gamma_0 R} & \tilde{S}_{\Gamma_0 \Gamma_0} + \tilde{S}_{11}^m \end{bmatrix} \begin{bmatrix} \tilde{A} \\ \tilde{A}_{\Gamma_0} \end{bmatrix} = \begin{bmatrix} \tilde{I} \\ \tilde{I}_{\Gamma_0} \end{bmatrix} \quad (5.17)$$

Step(8): Solve for the complex MVPs from the equation(5.17).

Step(9): End.

5.2 The 2DFE Solution Using Ballooning Techniques with Conductive Shielding

The AC 2DFE ballooning model for the eddy current case has been obtained in the last section. Now it can be applied to a two-wire parallel-pair transmission line problem with a conductive shield and an infinite boundary. The geometry of the interior region was shown in Figure(5.1), where a current which varies sinusoidally with a peak value $I=500$ A flows through the right conductor and in the direction out of the plane of the paper, and the same value of current flows through the left conductor in the opposite direction, that is, into the plane of the paper. Eddy currents exist in the copper shielding and elsewhere is free space. For the ballooning model, here the start point is chosen at $(x_0, y_0) = (0, 0)$, and $k = 1.3$ is chosen as the mapping ratio. The FE grid of the interior region is the same as shown in Figure(4.5).

The computations were carried out using the AC 2DFE ballooning model derived in the previous section for the eddy current case in various chosen frequencies ($f=0$

Hz, 400 Hz, 2 kHz, and 20 kHz). Figures(5.2) through (5.6) show the equipotentials in the case of frequency $f=0$ Hz, that is the magnetostatic case, and with ballooning layers, $m=0, 2, 5, 10,$ and $20,$ respectively. Figures(5.7) through (5.11) show those case with $m=0, 2, 5, 10,$ and $20,$ when $f=400$ Hz, respectively. Figures(5.12) through (5.16) show those in the case of $f=2$ kHz and with ballooning layers, $m=0, 2, 5, 10,$ and $20,$ respectively. Figures(5.17) through (5.21) show those in the case of $f=20$ kHz and with the ballooning layers, $m=0, 2, 5, 10,$ and $20,$ respectively. The magnitudes of flux densities at some selected locations shown in Figure(5.22) are plotted in Figures(5.23) through (5.25) for various conductive shielding thicknesses.

Comparing Figures(5.2) through (5.21), one can arrive at some conclusions as follows:

- (1) In a certain frequency (here, in any one of the frequencies, $f=0$ Hz, 400 Hz, 2 kHz, and 20 kHz), while the number of ballooning layers, $m,$ is larger and larger, the variation in the contours of the equipotentials is smaller and smaller, which means that when m is large enough, the equipotentials may almost converge to those of the “true” solution.
- (2) In lower frequency cases, such as $f=0$ Hz, and $f=400$ Hz, whenever m is greater than 10, the equipotentials are almost unchangeable. In higher frequency cases, less ballooning layers are sufficient to obtain more accuracy of the equipotential contours. For example, in the case of $f=2$ kHz, it was found that a number of ballooning layers, $m=5,$ is quite sufficient. It is interesting to point out that in the case of $f=20$ kHz, no ballooning layers are needed. These results reveal that the higher the frequency, the strong the weakening effects of eddy currents in the shielding on fields outside that shielding. That is, at higher frequencies the fields outside the shielding are effectively diminished.
- (3) In Figures(5.23) through (5.25), three shielding thicknesses are used. Those figures show the effects of varying the conductive shielding thickness, from which one can find that the thicker the conductive shielding the more effective it is reducing the outer fields. That is, the weaker the fields outside the shielding.

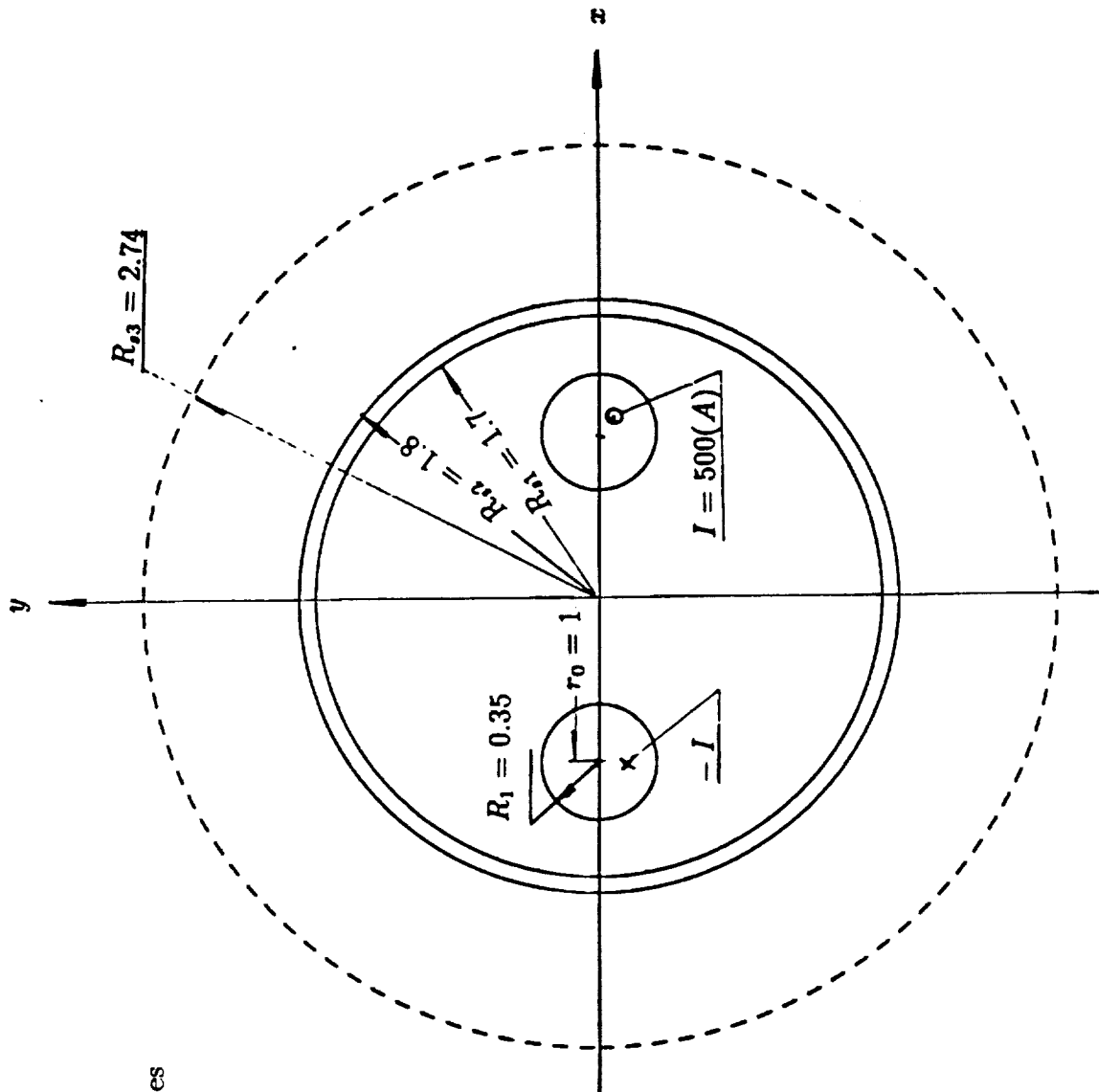
5.3 The 2DFE Solution Using Ballooning Techniques with Defects of the Conductive Shielding

In this section, the AC 2DFE ballooning model is used to study the field distributions resulting from various defects in the conductive shielding. For shielding defect angles, $\delta = 10^\circ$, 20° , and 30° , the corresponding FE solution regions are shown in Figures(4.19), (4.21), and (4.23), respectively. In the case of a frequency, $f=400$ Hz, the shielding thickness, $\Delta_s = 0.025$ in, the number of ballooning layers, $m=10$, and an AC current with a peak value, $I=500$ A is assumed to pass through the two conductors in the directions shown in the figures. The corresponding equipotential plots for angular defects, $\delta = 10^\circ$, 20° , and 30° , are shown in Figures(5.26) through (5.28), respectively. The effects of the defects were monitored at the arbitrarily chosen locations given in Figure(5.29). In the case of a frequency, $f=400$ Hz, an angular defect, $\delta = 20^\circ$, and a shield thickness, $\Delta_s = 0.025$ in, the magnitudes of magnetic flux densities at the locations shown in Figure(5.29) are given in Figure(5.30).

In the case of a frequency, $f=400$ Hz, comparing Figures(5.26) through (5.28) which show the equipotentials for defect angles, $\delta = 10^\circ$, 20° , and 30° , respectively, with Figure(5.11) which shows those with no defects in the shielding, leads one to conclude that the larger the defect angle, δ , the greater and greater the magnetic flux densities leaking in the neighbourhood of the defect area. Comparing Figure(5.30) which shows the effects of defects in the case of an angular defect, $\delta = 20^\circ$, and a shielding thickness, $\Delta_s = 0.025$ in, with Figures(5.23) through (5.25), which show the effects of the shielding thickness without defects, one can see the slight degradation of the effectiveness of the magnetic field shielding near the defect region.

The AC 2DFE ballooning model can be used to solve parallel-pair transmission line problems with infinite boundaries. However, in space station applications, there are potential situations which might involve twisted-pair type transmission lines, as well as other configurations not available yet, for which the above model is not suitable. One of the simplest methods to solve the simplest twisted-pair transmission line

problem is the closed-form analytical method using the *Biot – Savart Law* in conjunction with 3D integral type method. These will be discussed in the next chapter.



Dimensions in inches
 1 in = 25.4 mm

Figure 5.1: Geometry of a Two-Wire Parallel-Pair Transmission Line Case

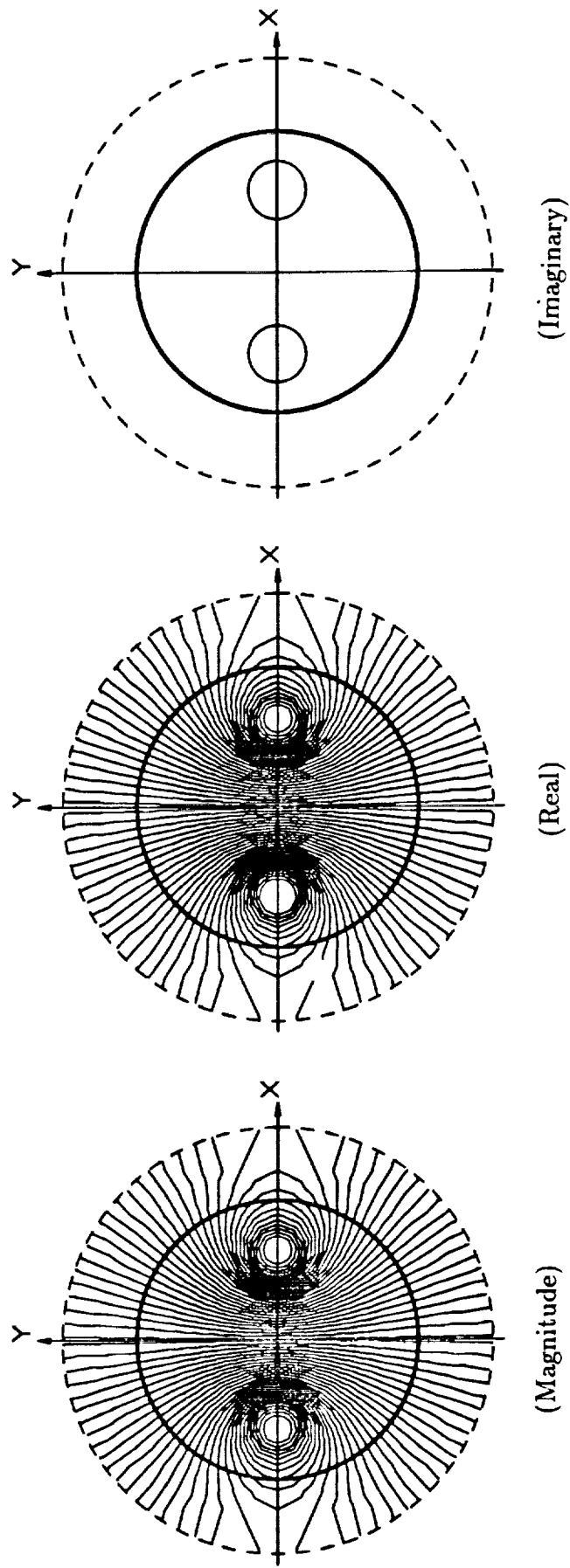


Figure 5.2: The Parallel-Pair MVP Equipotentials Obtained From FE Solutions for $f = 0Hz$ With Conductive Shielding Without Ballooning - The Natural Open Boundary

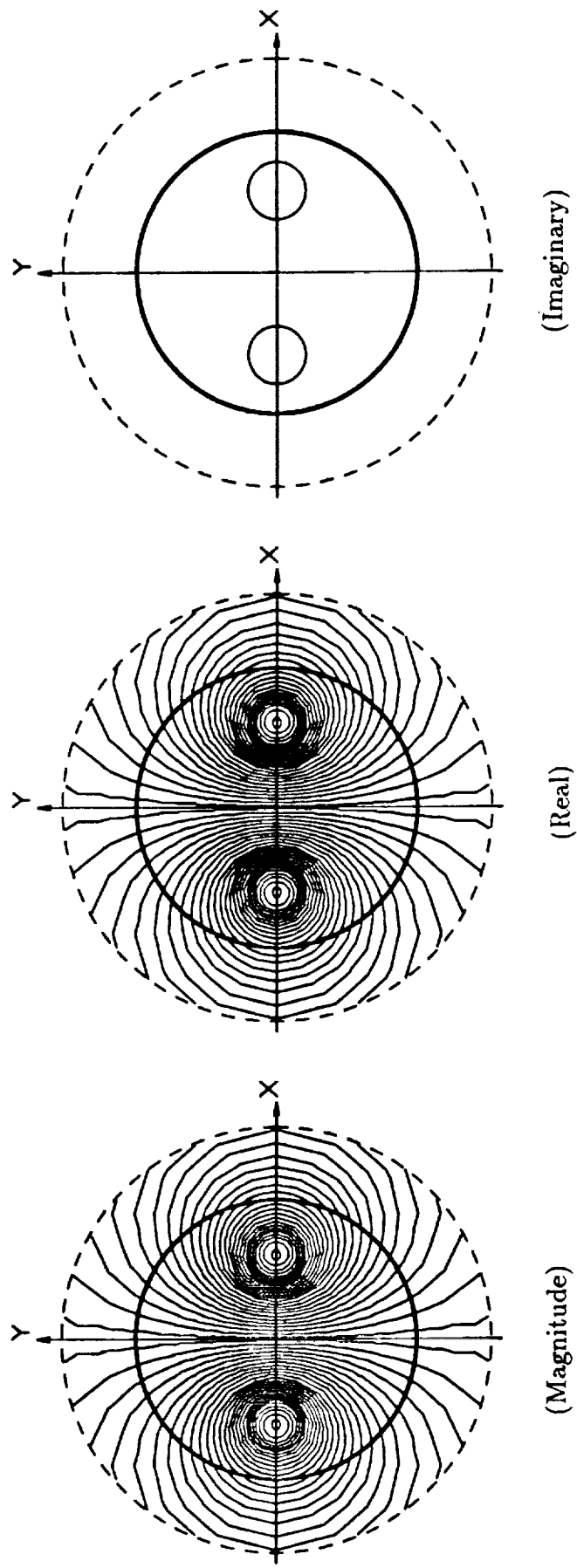


Figure 5.3: The Parallel-Pair MVP Equipotentials Obtained From FE Solutions With Ballooning ($m=2$) for $f = 0Hz$ With Conductive Shielding

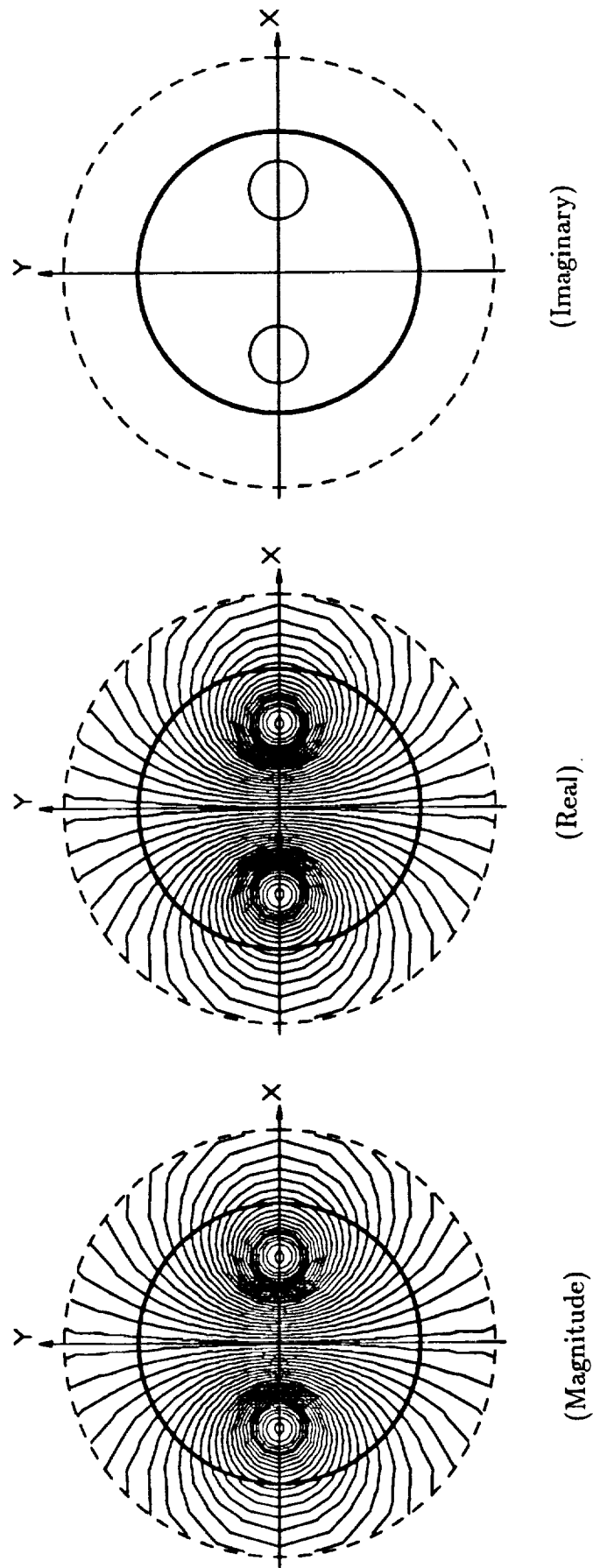


Figure 5.4: The Parallel-Pair MVP Equipotentials Obtained From FE Solutions With Ballooning ($m=5$) for $f = 0Hz$ With Conductive Shielding

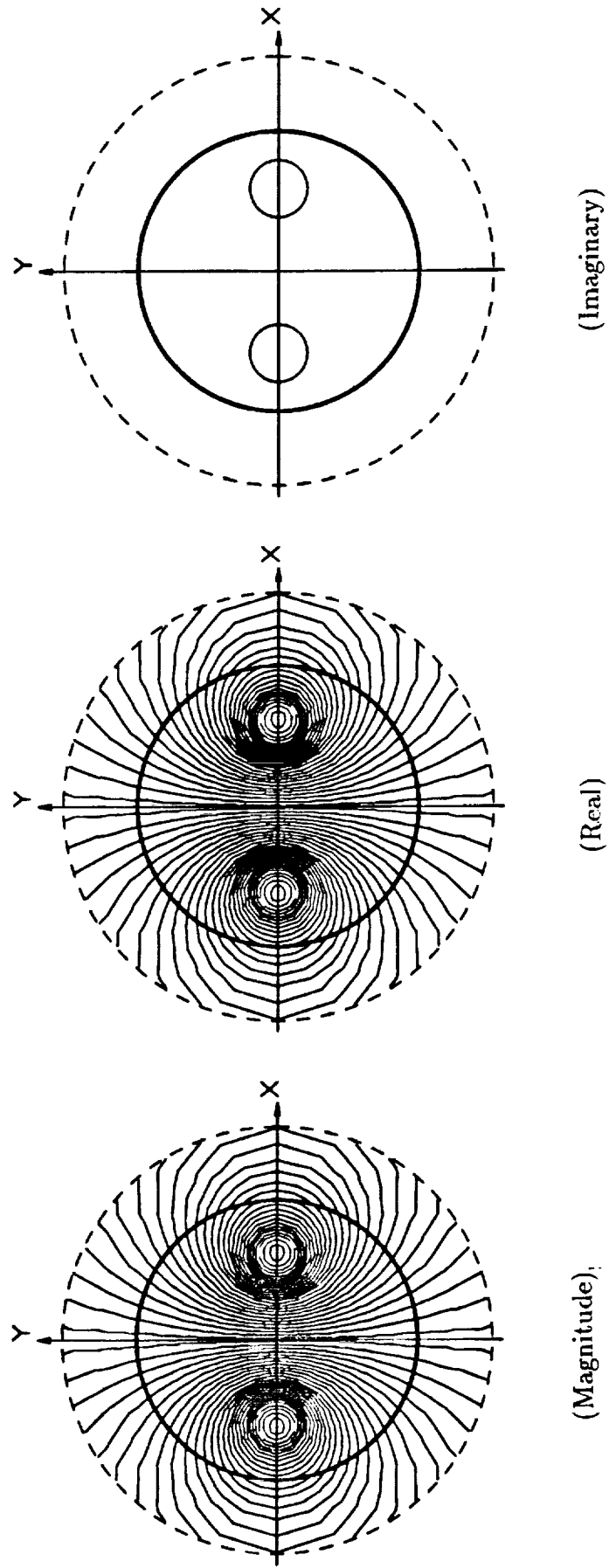
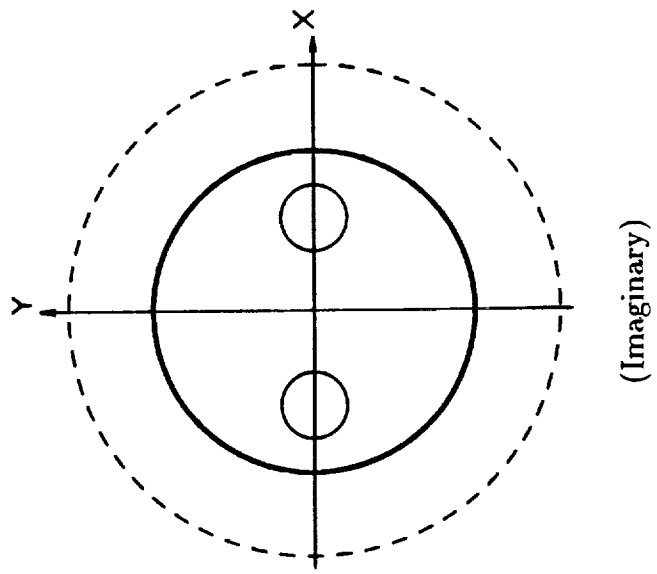
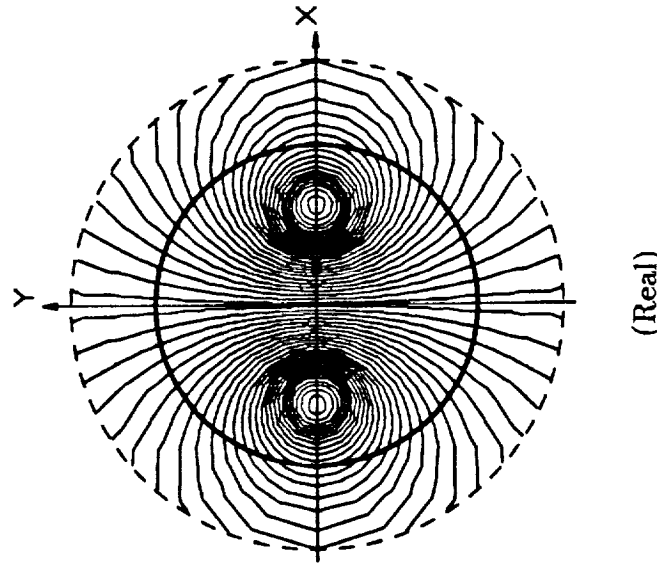


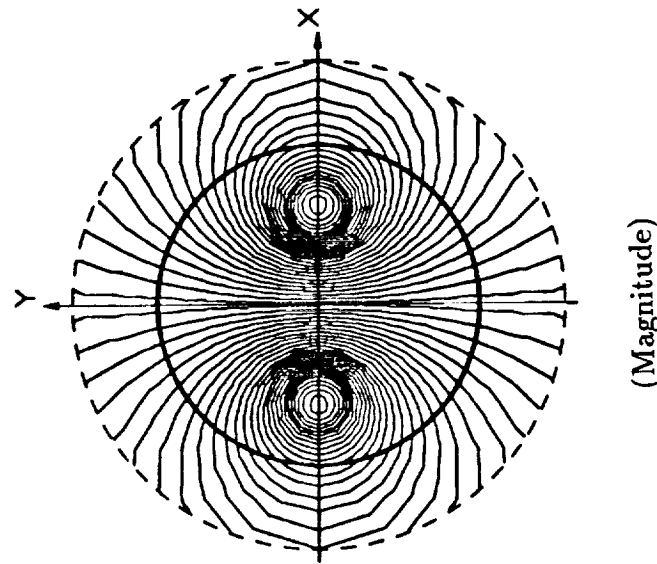
Figure 5.5: The Parallel-Pair MVP Equipotentials Obtained From FE Solutions With Ballooning ($m=10$) for $f = 0Hz$ With Conductive Shielding



(Imaginary)



(Real)



(Magnitude)

Figure 5.6: The Parallel-Pair MVP Equipotentials Obtained From FE Solutions With Ballooning ($m=20$) for $f = 0H_z$ With Conductive Shielding

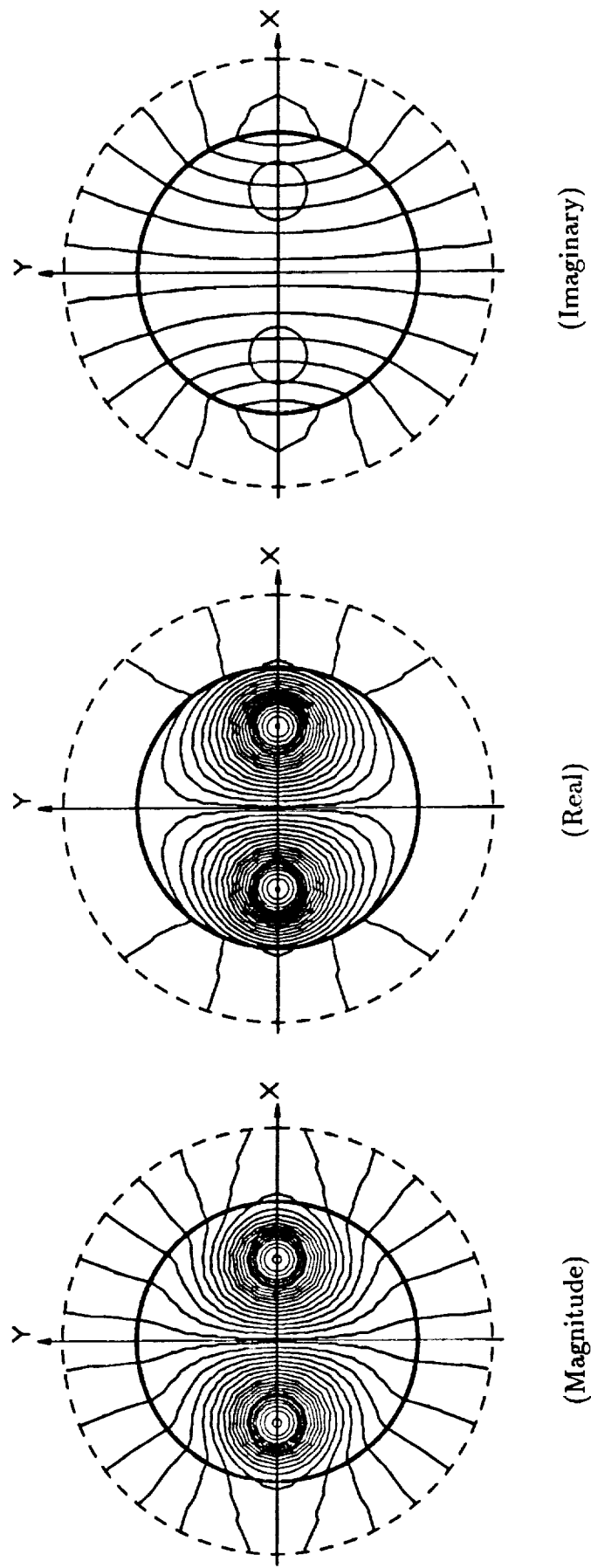


Figure 5.7: The Parallel-Pair MVP Equipotentials Obtained From FE Solutions for:
 $f = 400Hz$ With Conductive Shielding Without Ballooning -
 The Natural Open Boundary

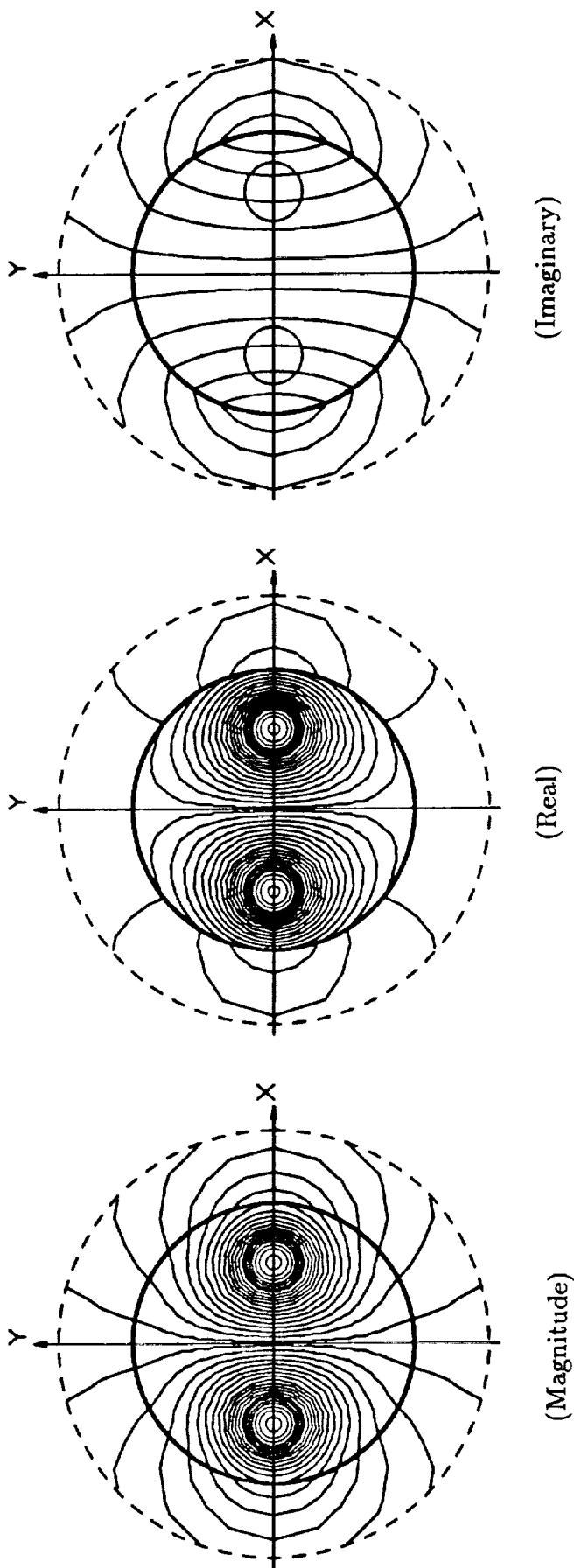


Figure 5.8: The Parallel-Pair MVP Equipotentials Obtained From FE Solutions With Ballooning ($m=2$) for $f = 400Hz$ With Conductive Shielding

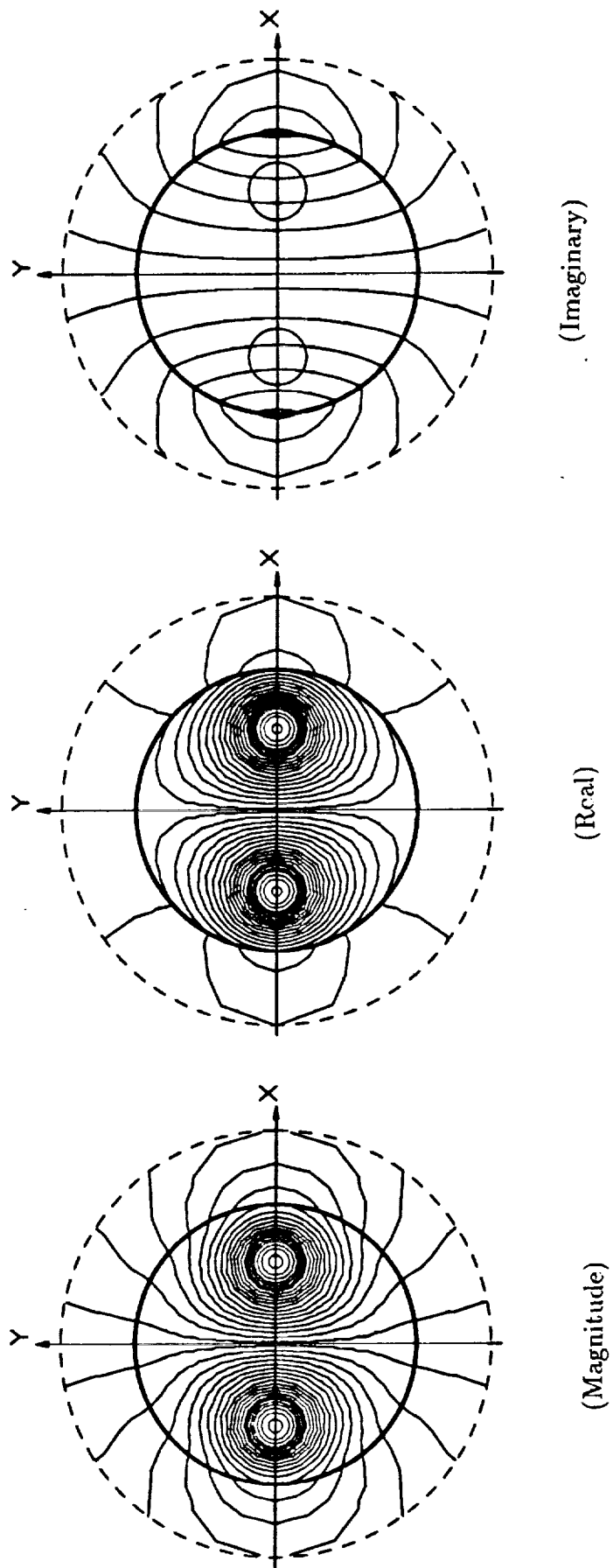


Figure 5.9: The Parallel-Pair MVP Equipotentials Obtained From FE Solutions With Ballooning ($m=5$) for $f = 400Hz$ With Conductive Shielding

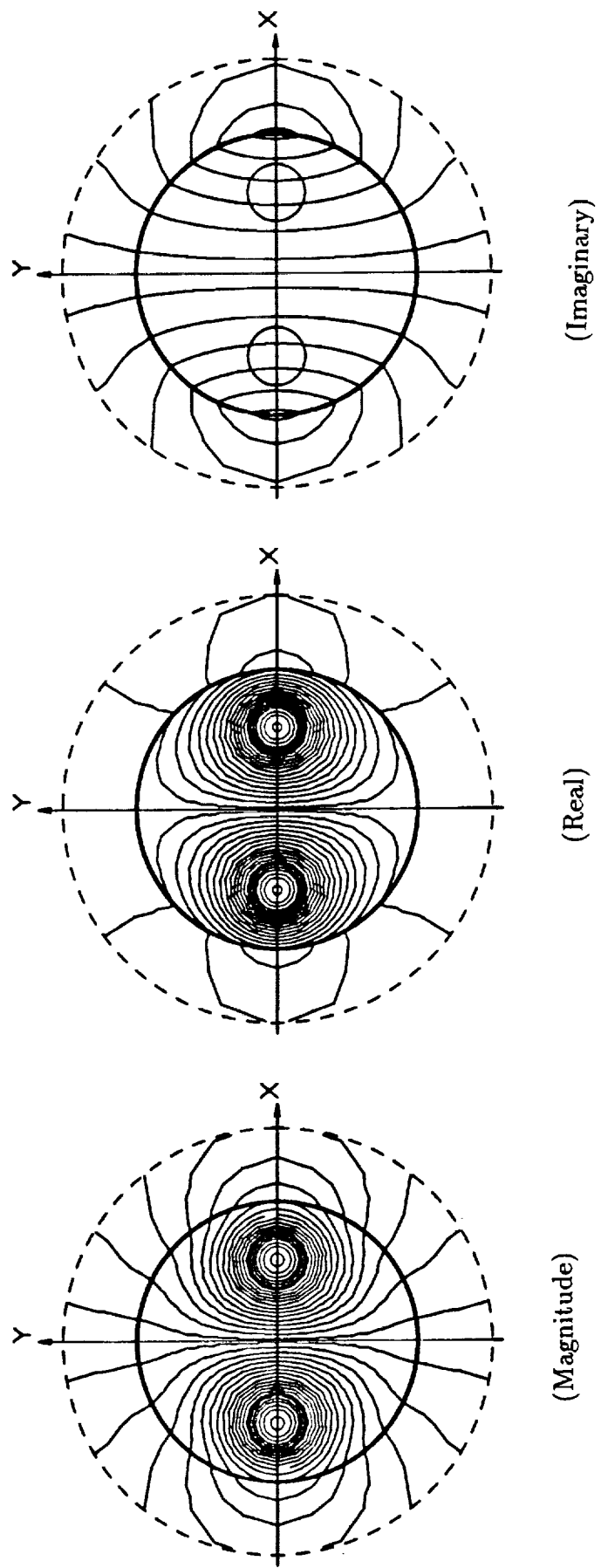
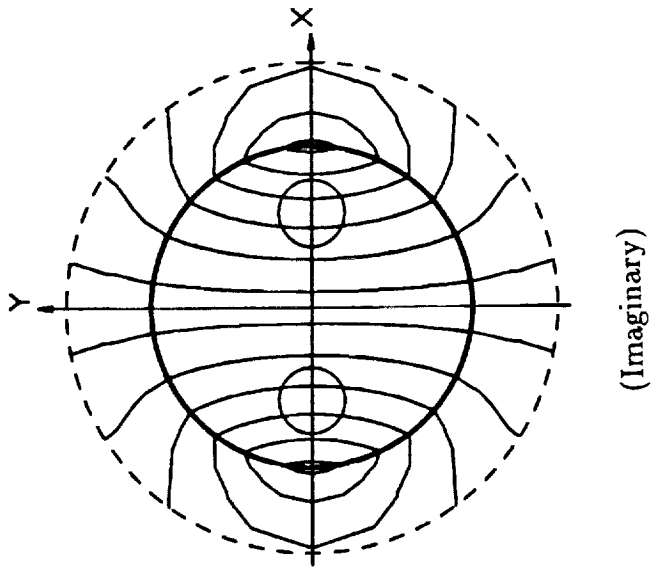
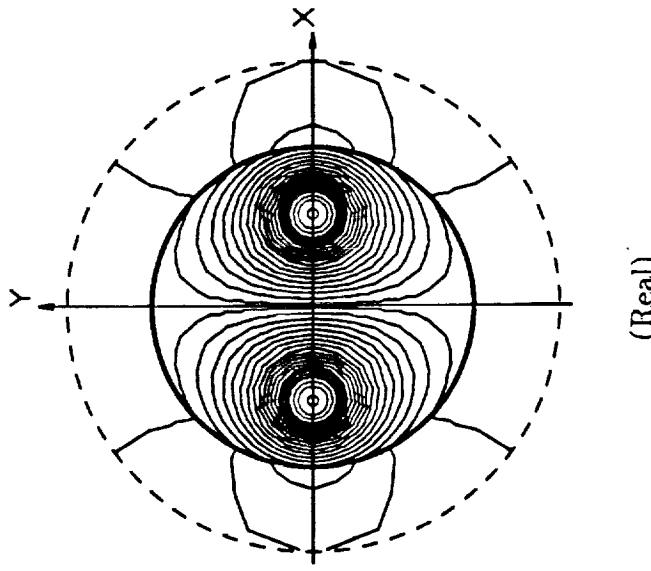


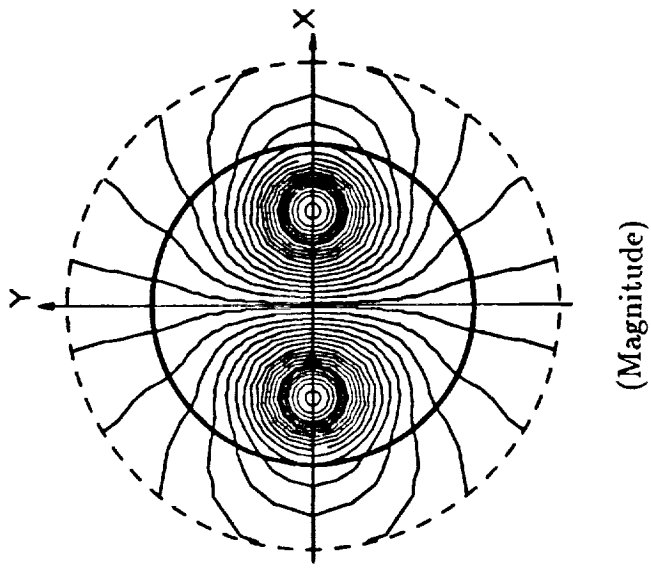
Figure 5.10: The Parallel-Pair MVP Equipotentials Obtained From FE Solutions With Ballooning ($m=10$) for $f = 400Hz$ With Conductive Shielding



(Imaginary)



(Real)



(Magnitude)

Figure 5.11: The Parallel-Pair MVP Equipotentials Obtained From FE Solutions With Ballooning ($m=20$) for $f = 400Hz$ With Conductive Shielding

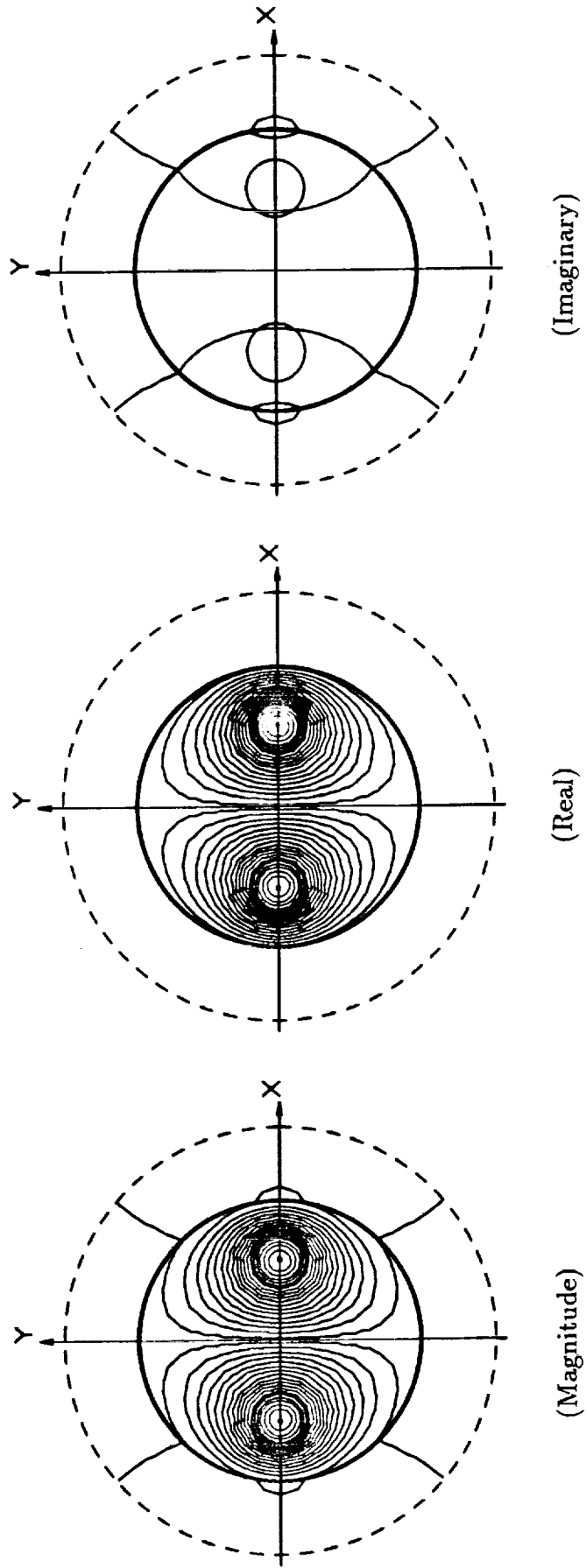


Figure 5.12: The Parallel-Pair MVP Equipotentials Obtained From FE Solutions for $f = 2kH/z$ With Conductive Shielding Without Ballooning - The Natural Open Boundary

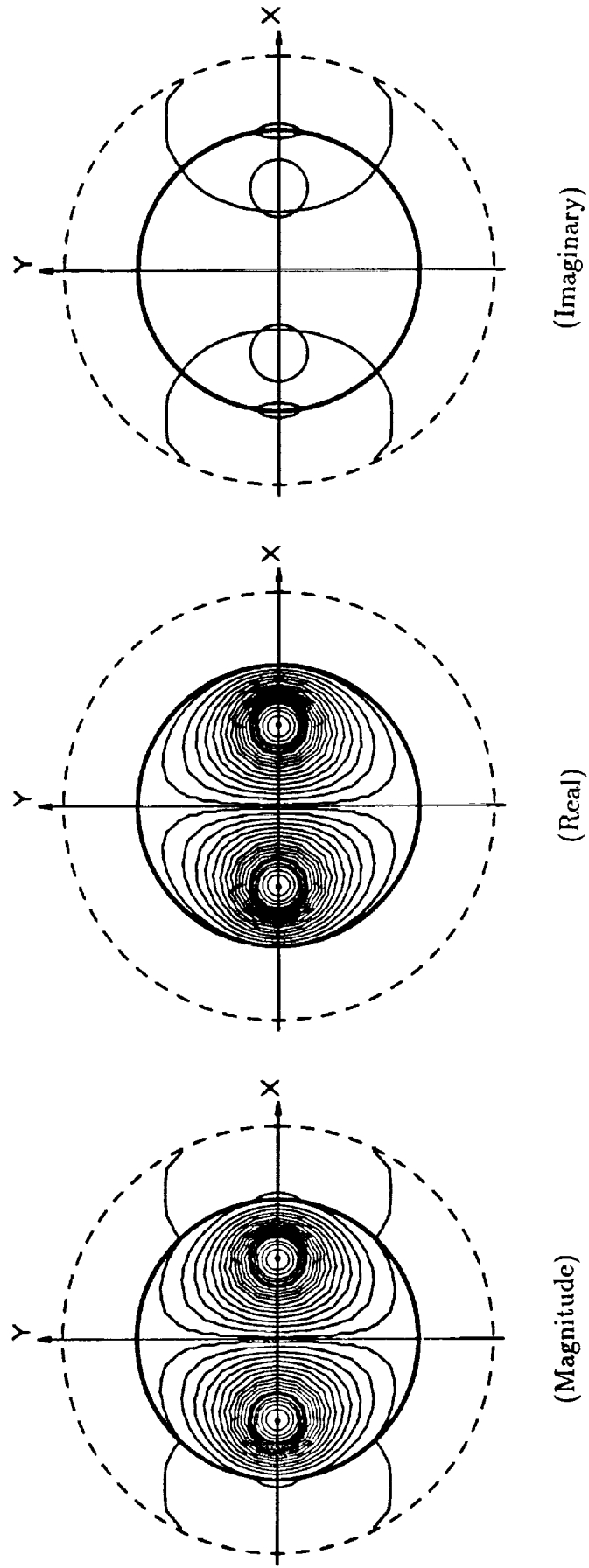


Figure 5.13: The Parallel-Pair MVP Equipotentials Obtained From FE Solutions With Ballooning ($m=2$) for $f = 2kHz$ With Conductive Shielding

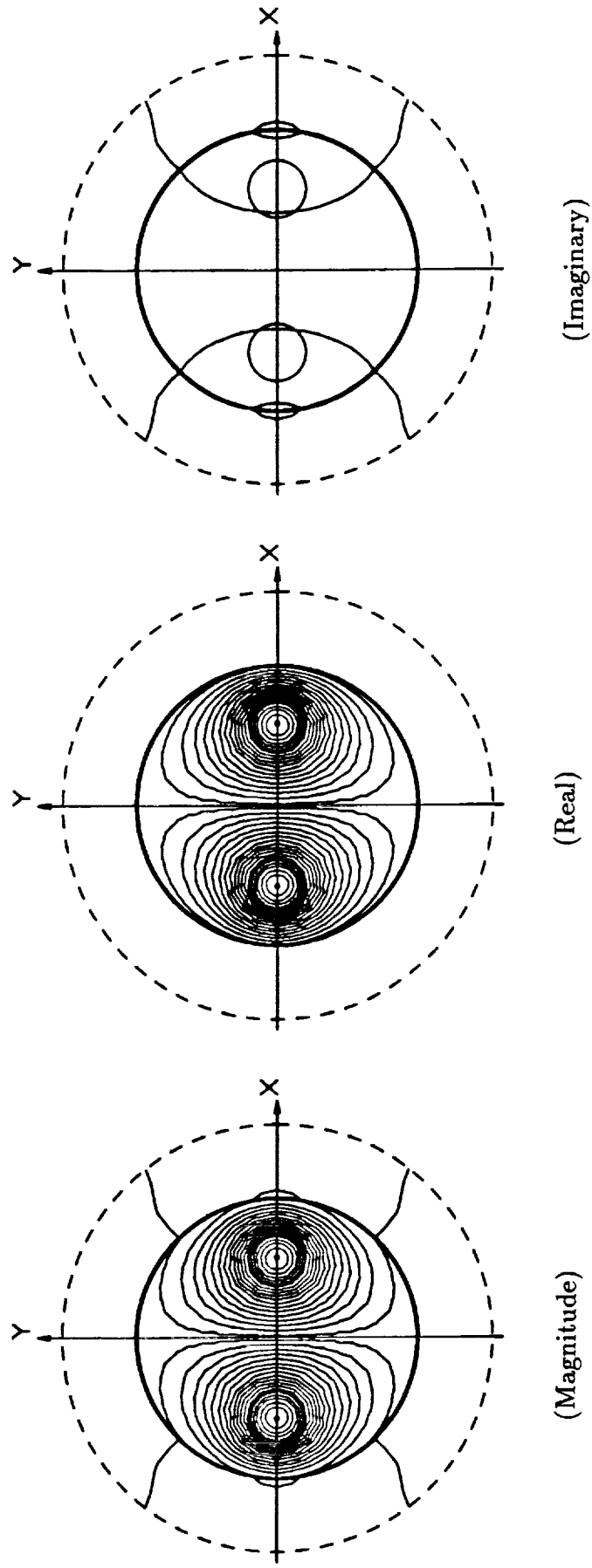


Figure 5.14: The Parallel-Pair MVP Equipotentials Obtained From FE Solutions With Ballooning ($m=5$) for $f = 2kH_z$ With Conductive Shielding

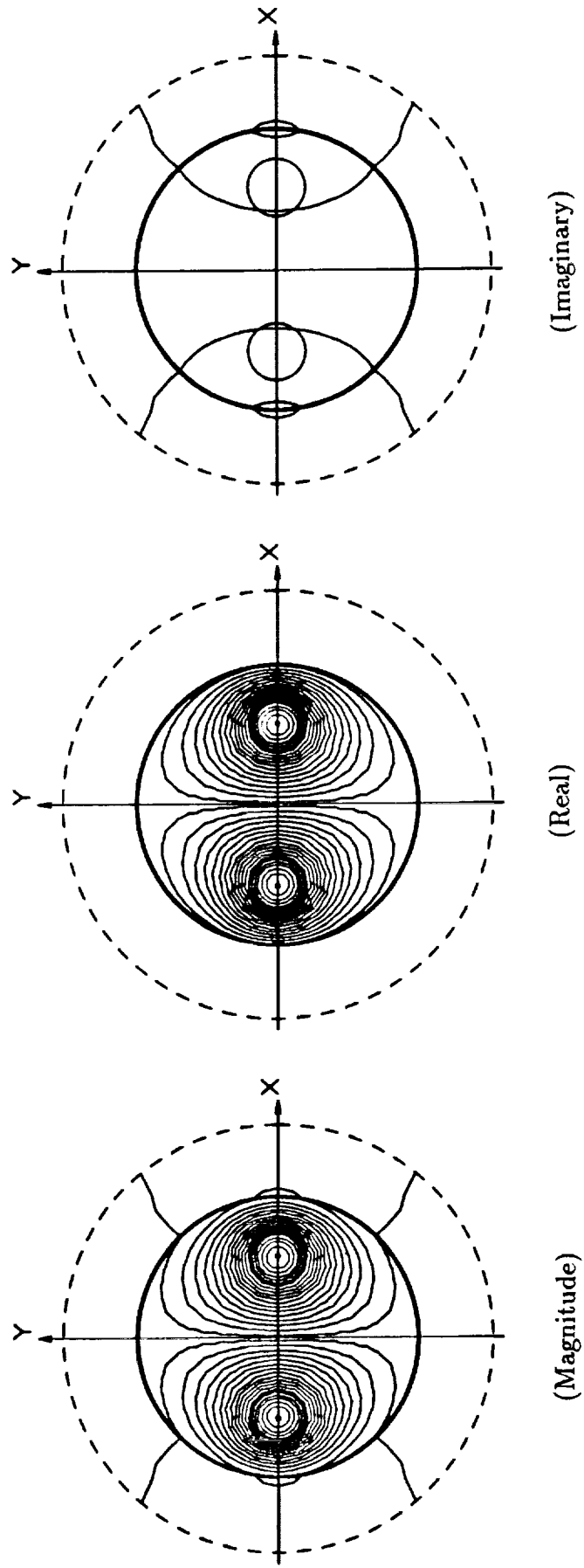


Figure 5.15: The Parallel-Pair MVP Equipotentials Obtained From FE Solutions ' With Ballooning ($m=10$) for $f = 2kHz$ With Conductive Shielding

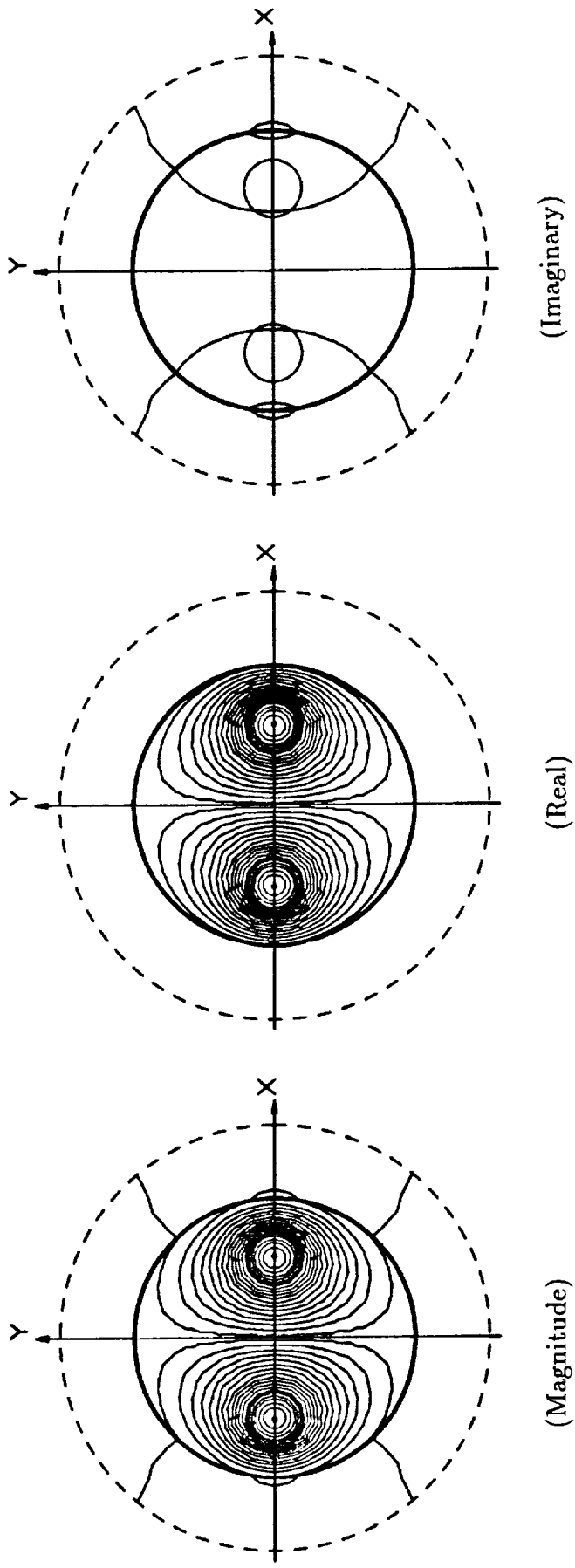


Figure 5.16: The Parallel-Pair MVP Equipotentials Obtained From FE Solutions With Ballooning ($m=20$) for $f = 2kH_z$ With Conductive Shielding

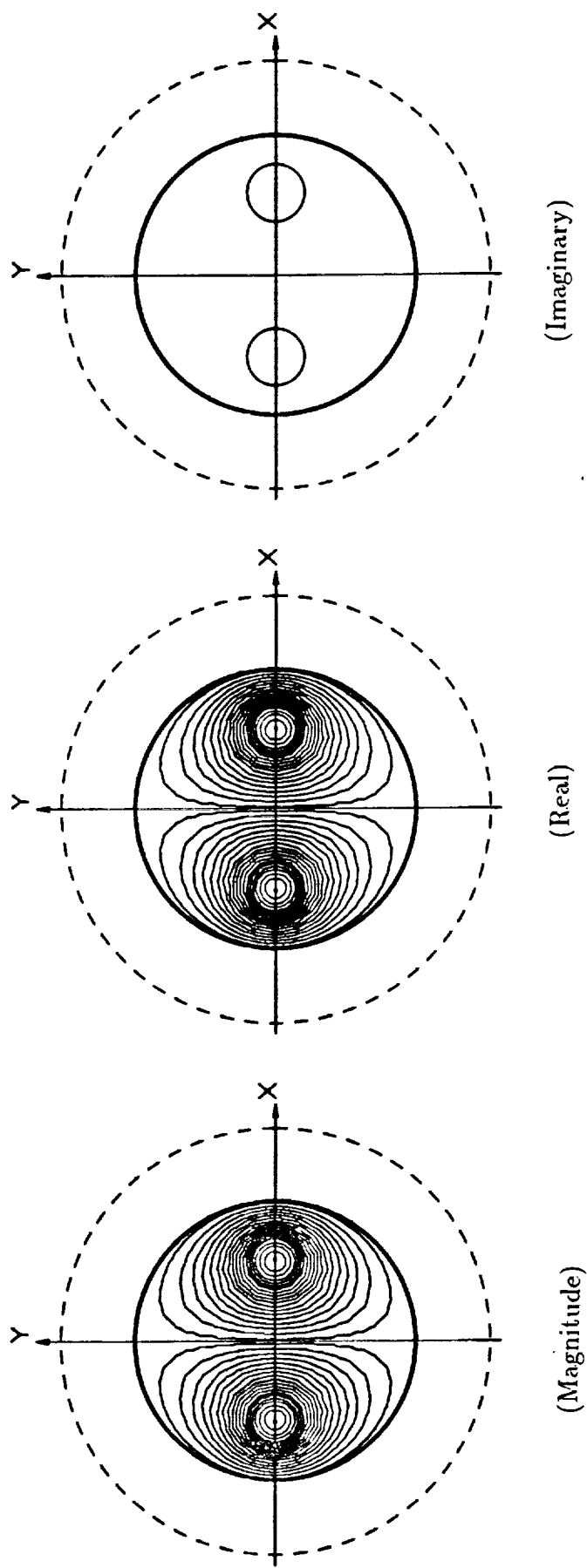


Figure 5.17: The Parallel-Pair MVP Equipotentials Obtained From FE Solutions for

$f = 20kHz$ With Conductive Shielding Without Ballooning -

The Natural Open Boundary

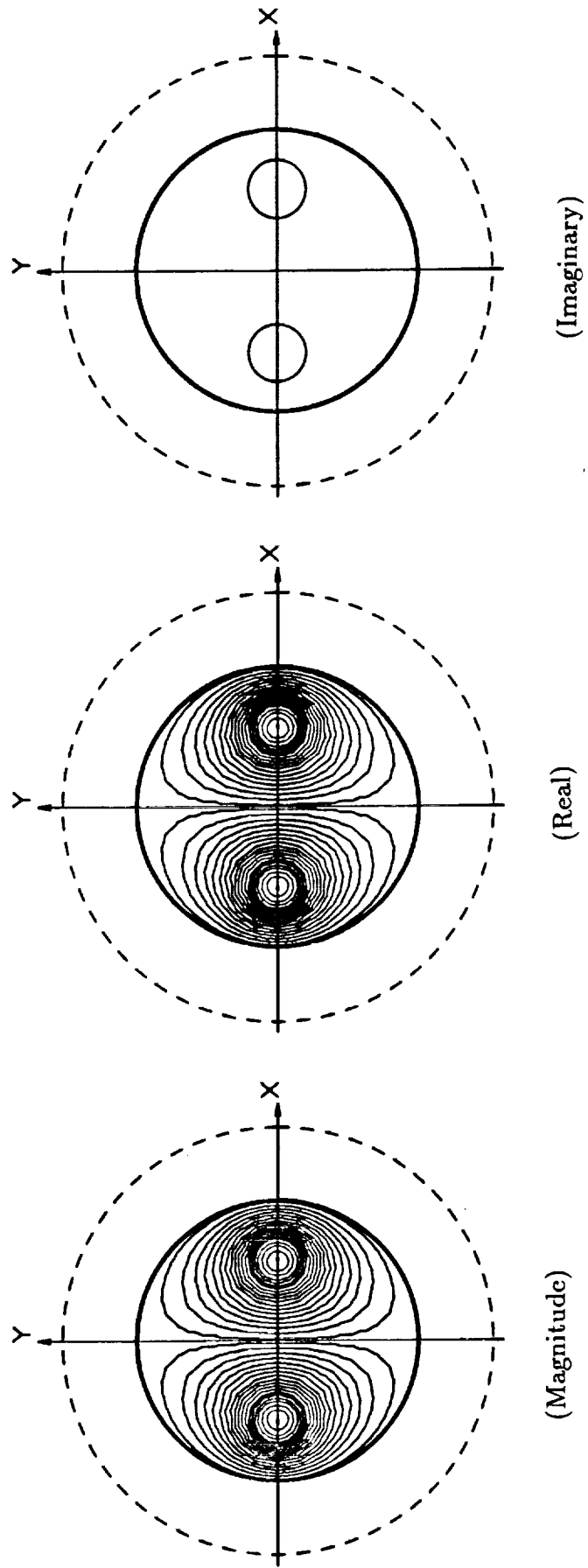


Figure 5.18: The Parallel-Pair MVP Equipotentials Obtained From FE Solutions:
 With Ballooning ($m=2$) for $f = 20kH z$ With Conductive Shielding

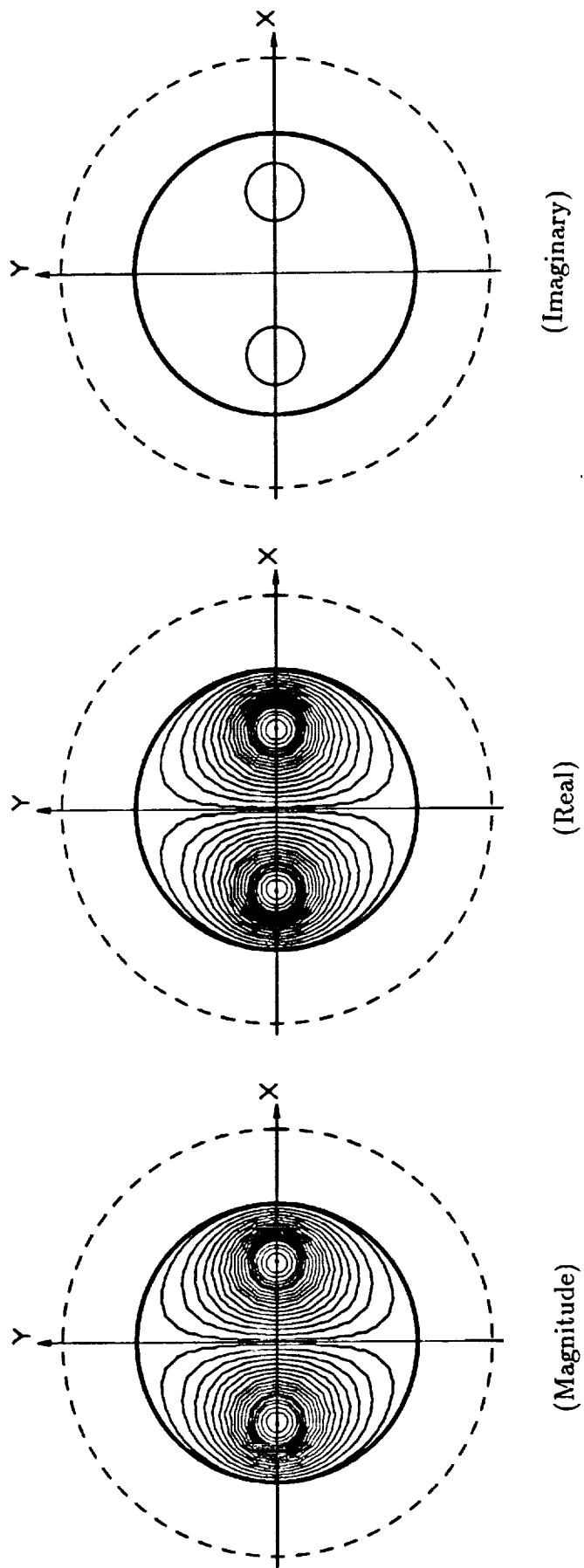


Figure 5.19: The Parallel-Pair MVP Equipotentials Obtained From FE Solutions With Ballooning ($m=5$) for $f = 20kH_z$ With Conductive Shielding

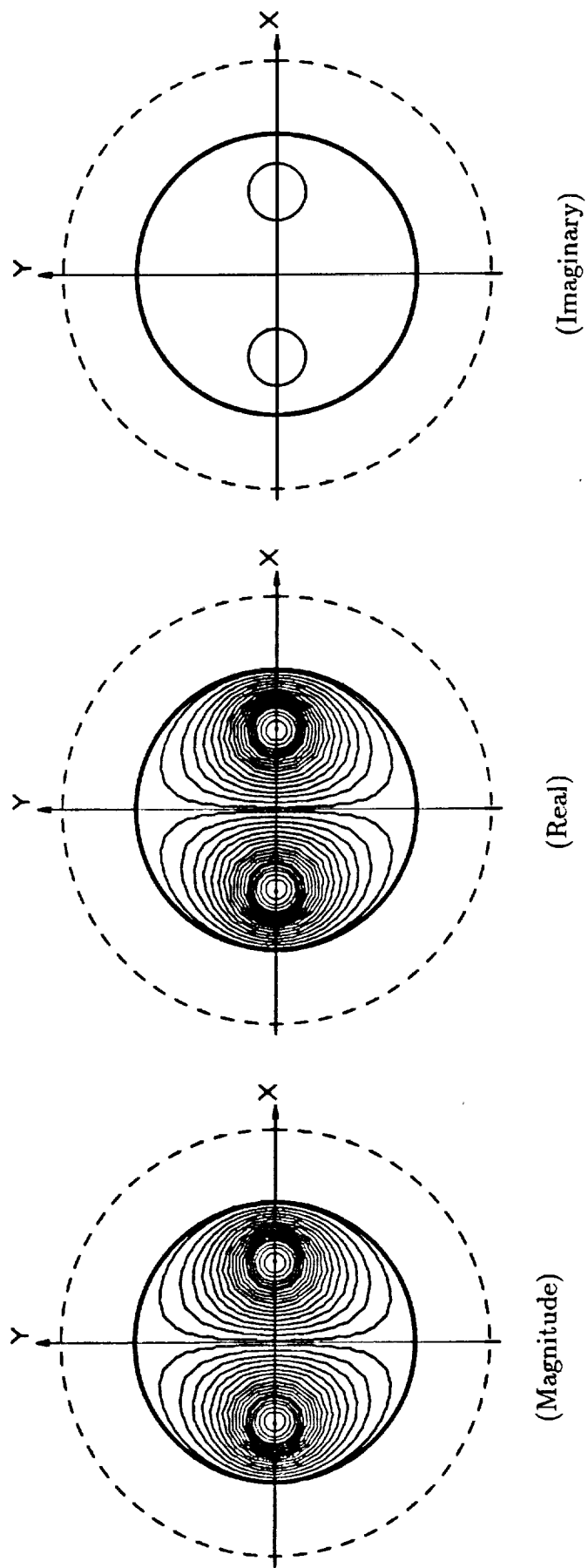


Figure 5.20: The Parallel-Pair MVP Equipotentials Obtained From FE Solutions With Ballooning ($m=10$) for $f = 20kH_z$ With Conductive Shielding.

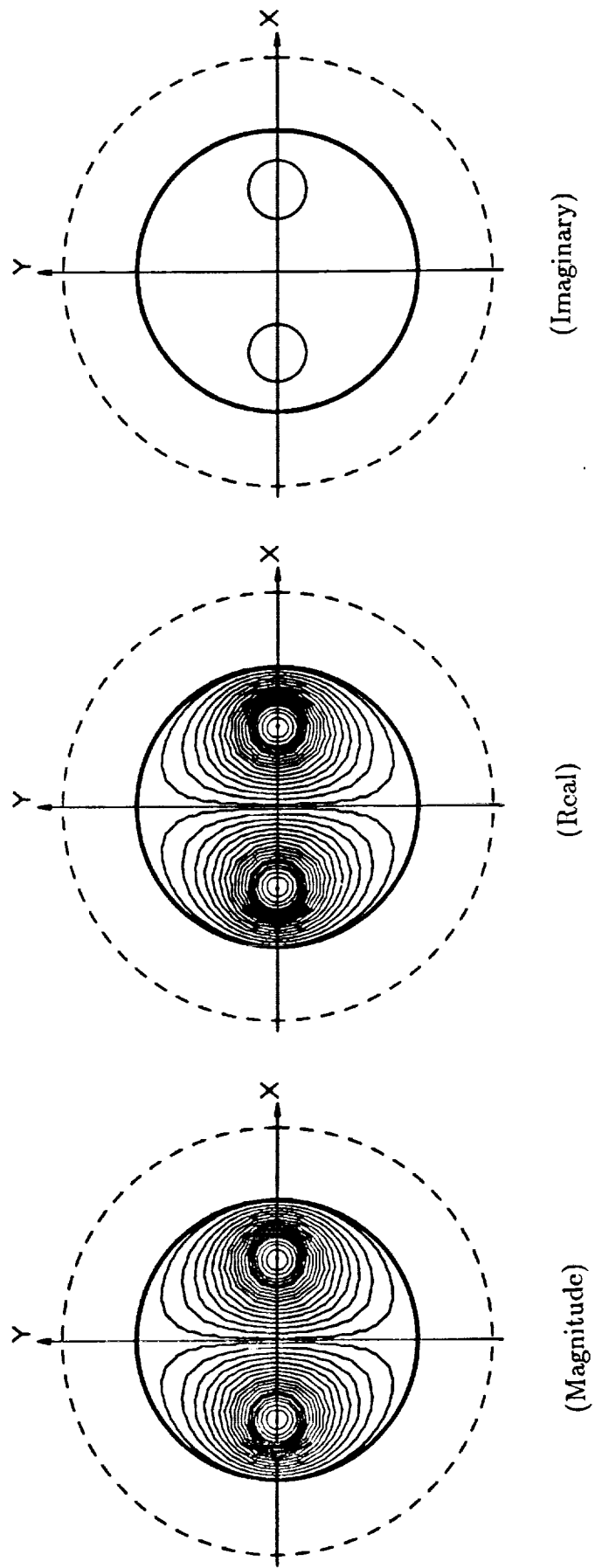


Figure 5.21: The Parallel-Pair MVP Equipotentials Obtained From FE Solutions With Ballooning ($m=20$) for $f = 20kH_z$ With Conductive Shielding

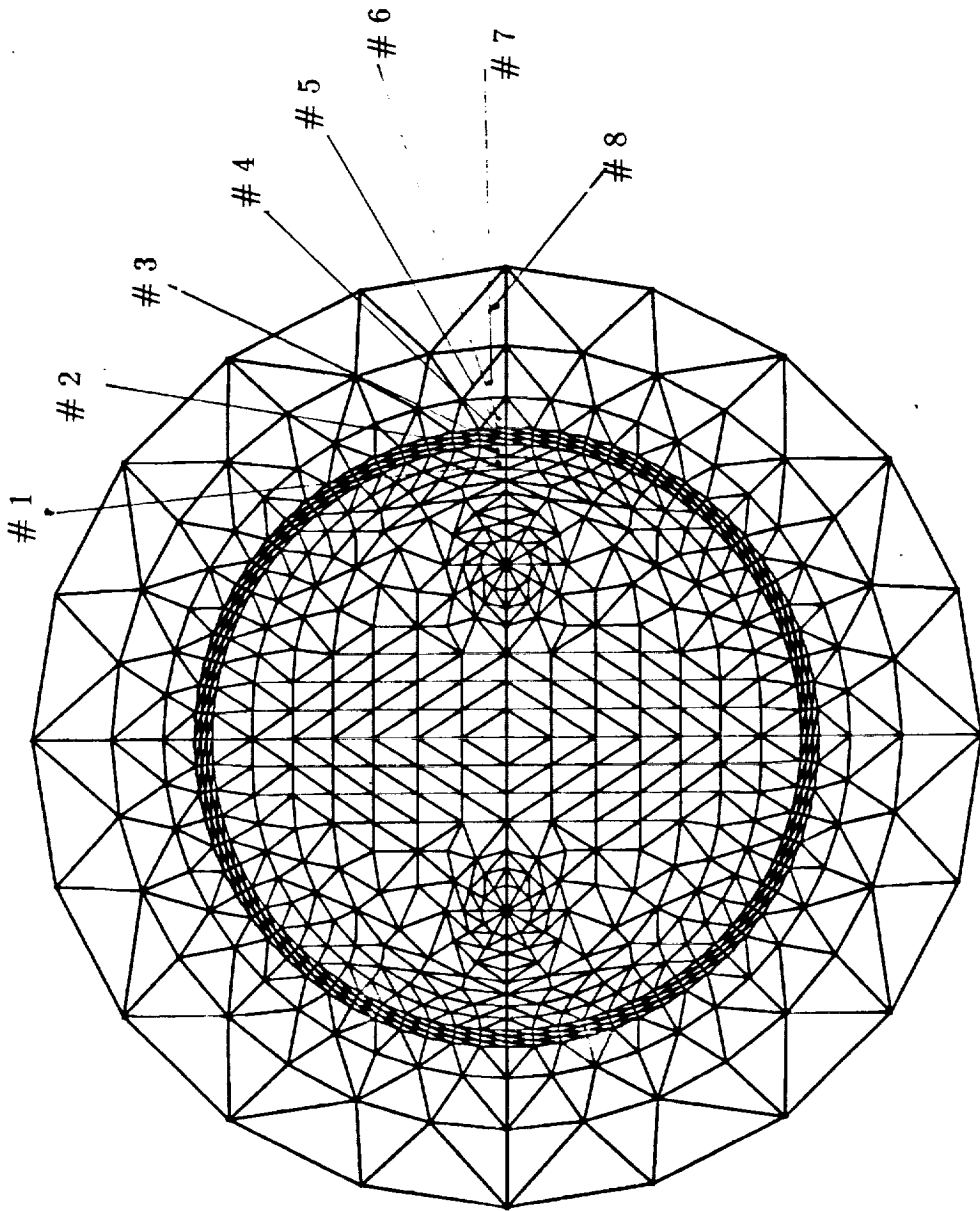


Figure 5.22: Finite Elements at Which the Effects of Shielding Thickness on Flux
 Densities are Given in Figures(5.23) Through (5.25)

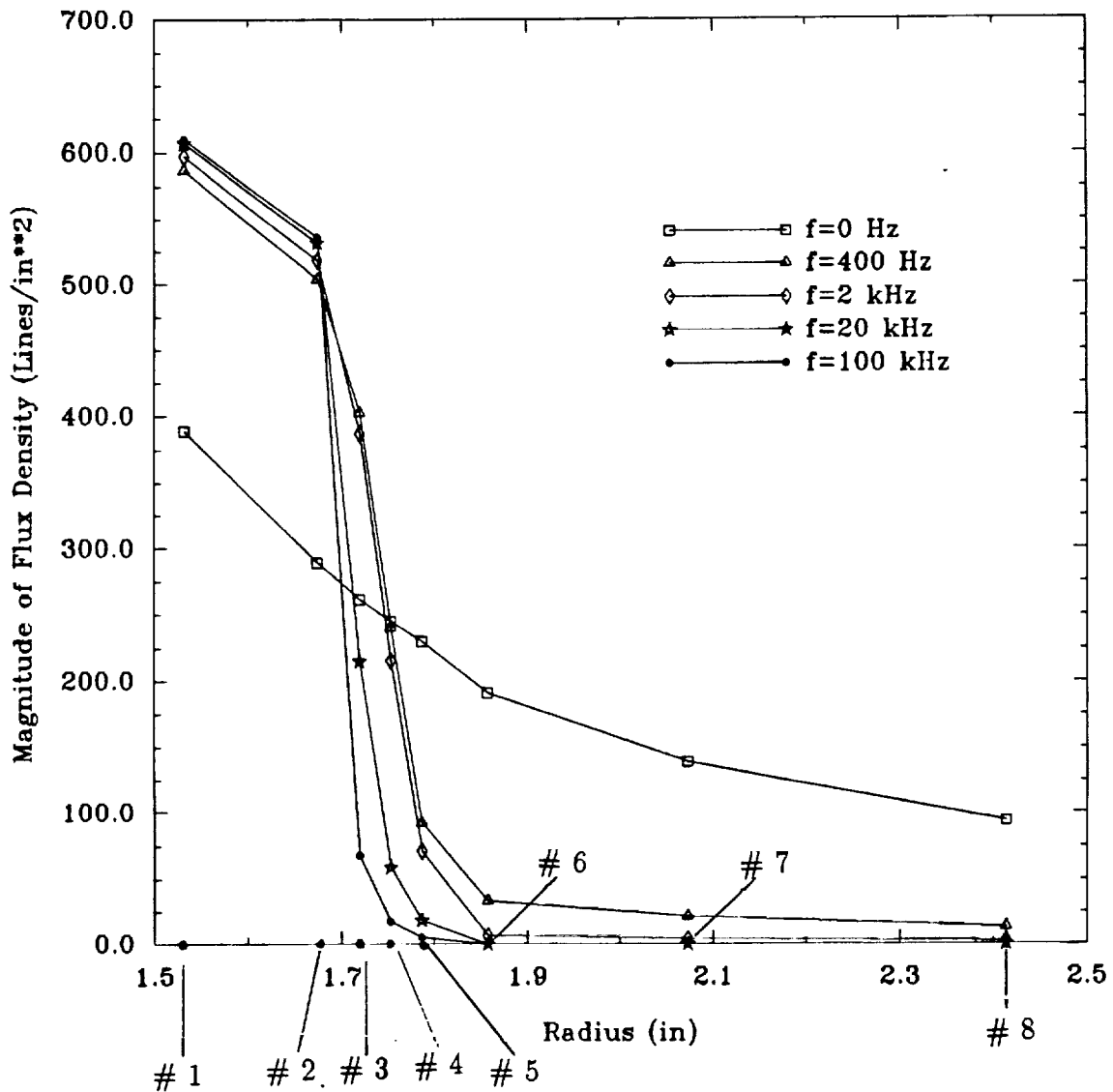


Figure 5.23: Flux Density Magnitudes With Ballooning ($m=10$) and no Defects With a Conductive Shield Thickness, $\Delta_s=0.1$ in, for $f=0$ Hz, 400 Hz, 2 kHz, 20 kHz and 100 kHz, for a Current $I=500$ A

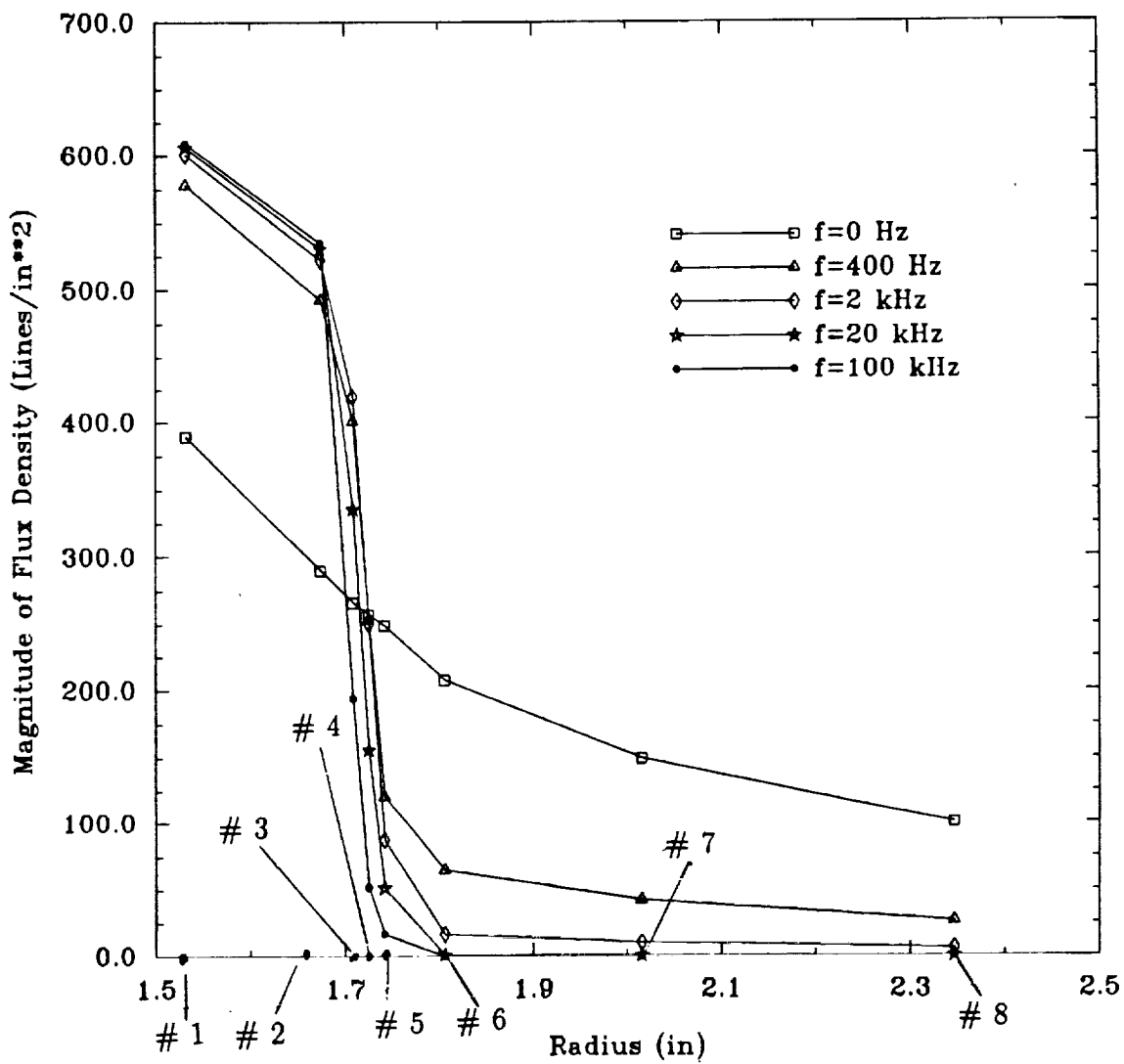


Figure 5.24: Flux Density Magnitudes With Ballooning ($m=10$) and no Defects With a Conductive Shield Thickness, $\Delta_s=0.05$ in, for $f=0$ Hz, 400 Hz, 2 kHz, 20 kHz and 100 kHz, for a Current $I=500$ A

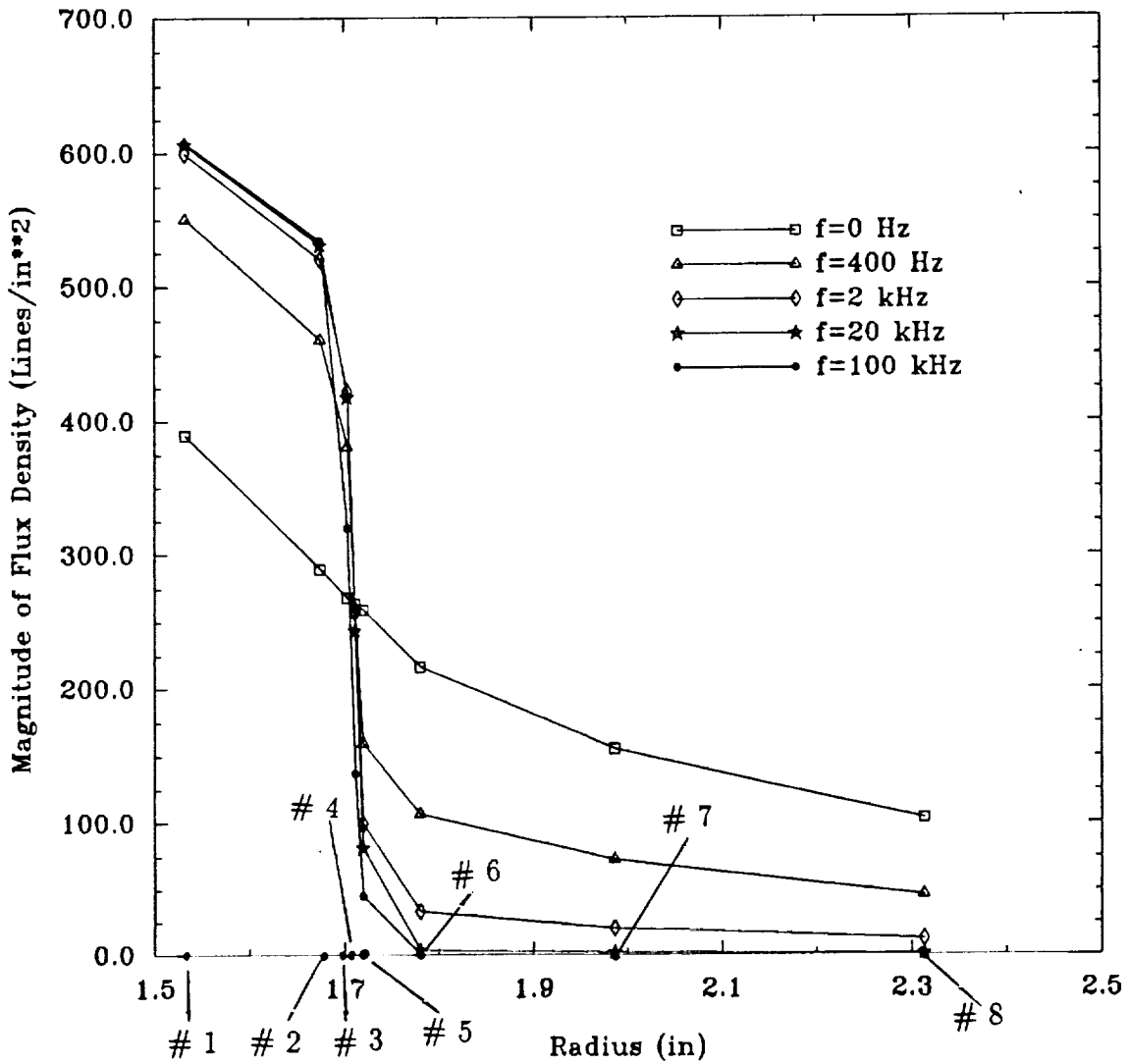


Figure 5.25: Flux Density Magnitudes With Ballooning ($m=10$) and no Defects With a Conductive Shield Thickness, $\Delta_s=0.025$ in, for $f=0$ Hz, 400 Hz, 2 kHz, 20 kHz and 100 kHz, for a Current $I=500$ A

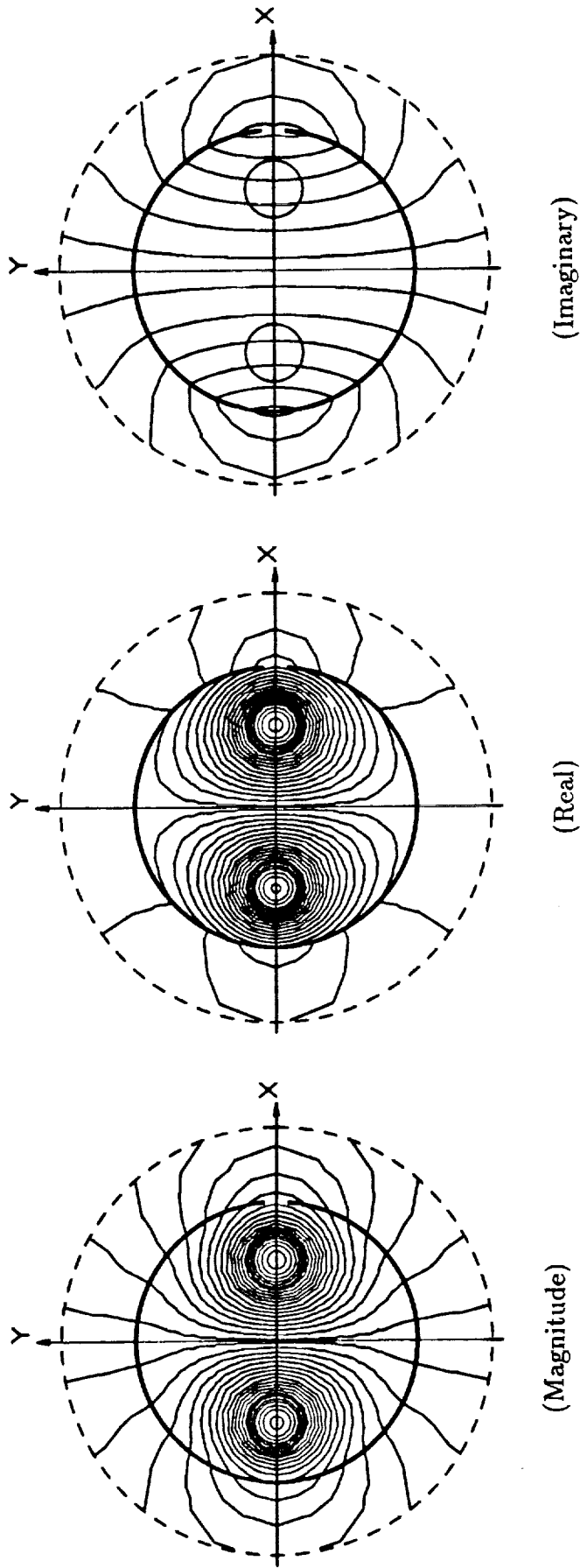


Figure 5.26: The Parallel-Pair MVP Equipotentials Obtained From FE Solutions With Ballooning ($m=10$)

for $f = 400Hz$ - the Case of a Conductive Shield With an Angular Defect, $\delta = 10^\circ$ Shield Thickness, $\Delta_s = 0.025$ in, for a Current $I=500$ A.

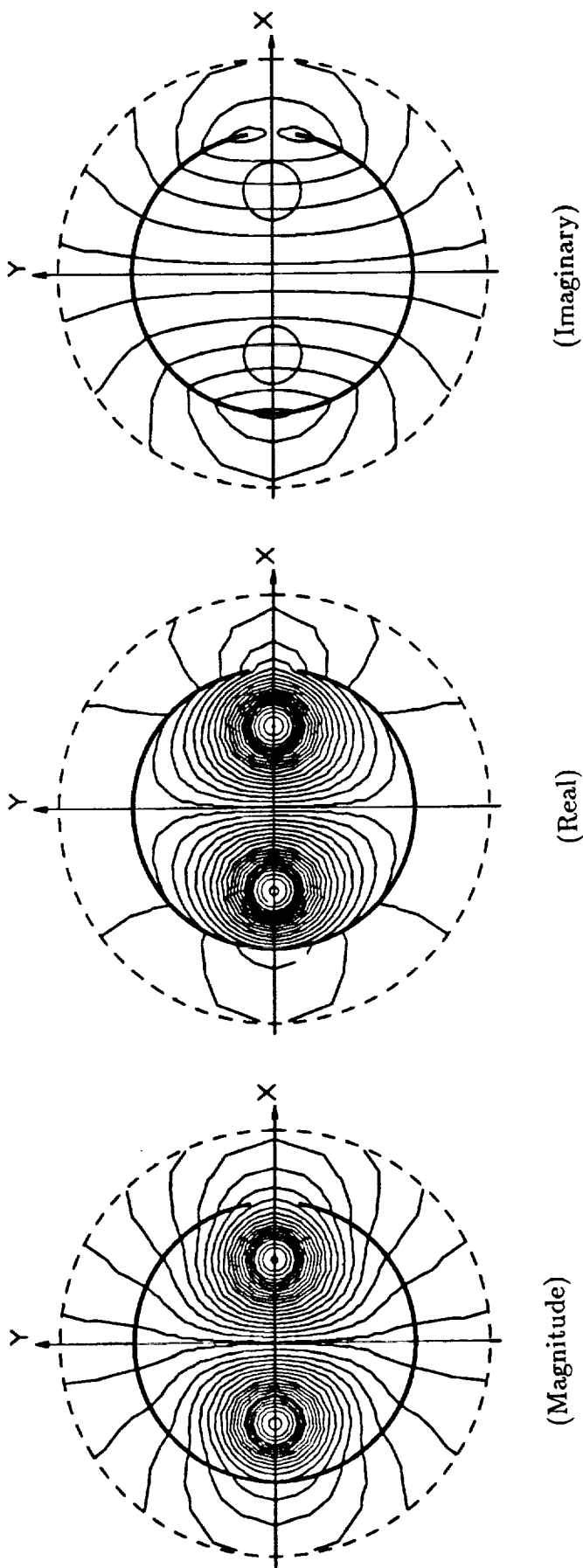


Figure 5.27: The Parallel-Pair MVP Equipotentials Obtained From FE Solutions With Ballooning ($m=10$) for $f = 400Hz$ - the Case of a Conductive Shield With an Angular Defect, $\delta = 20^\circ$ Shield Thickness, $\Delta_s=0.025$ in, for a Current $I=500$ A

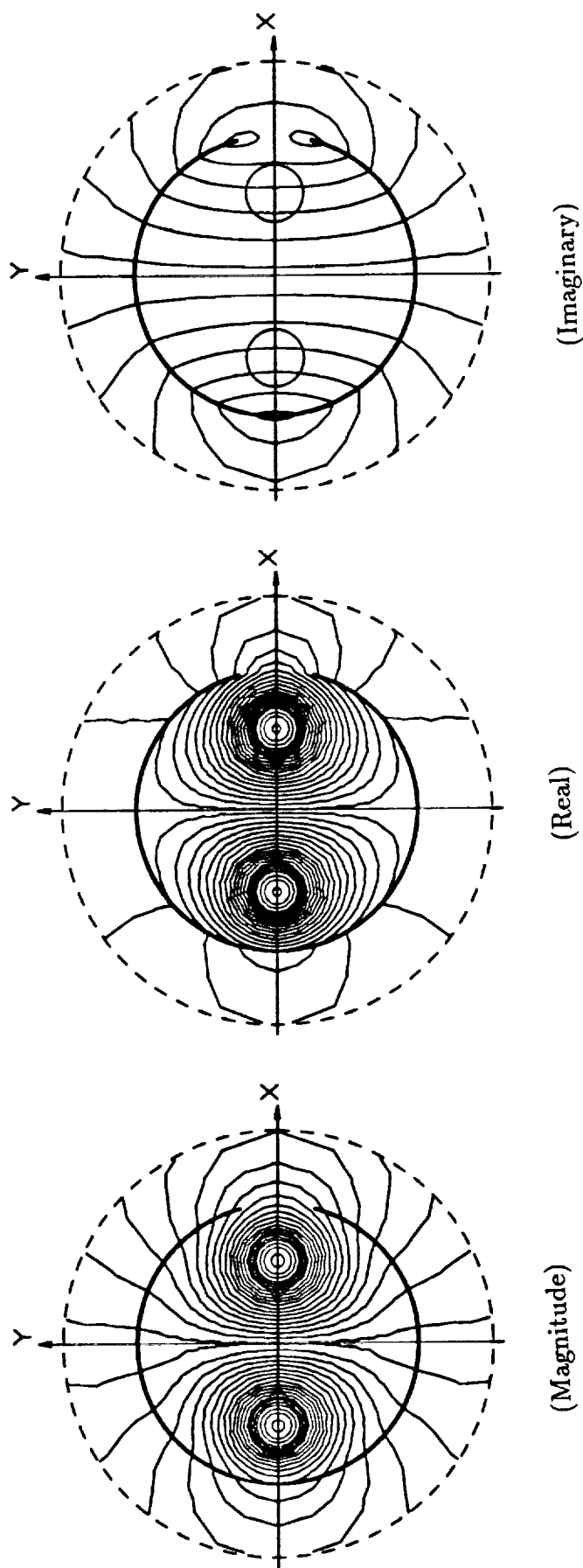


Figure 5.28: The Parallel-Pair MVP Equipotentials Obtained From FE Solutions With Ballooning ($m=10$) for $f = 400\text{ Hz}$ - the Case of a Conductive Shield With an Angular Defect, $\delta = 30^\circ$, Shield Thickness, $\Delta_s = 0.025$ in, for a Current $I=500$ A :

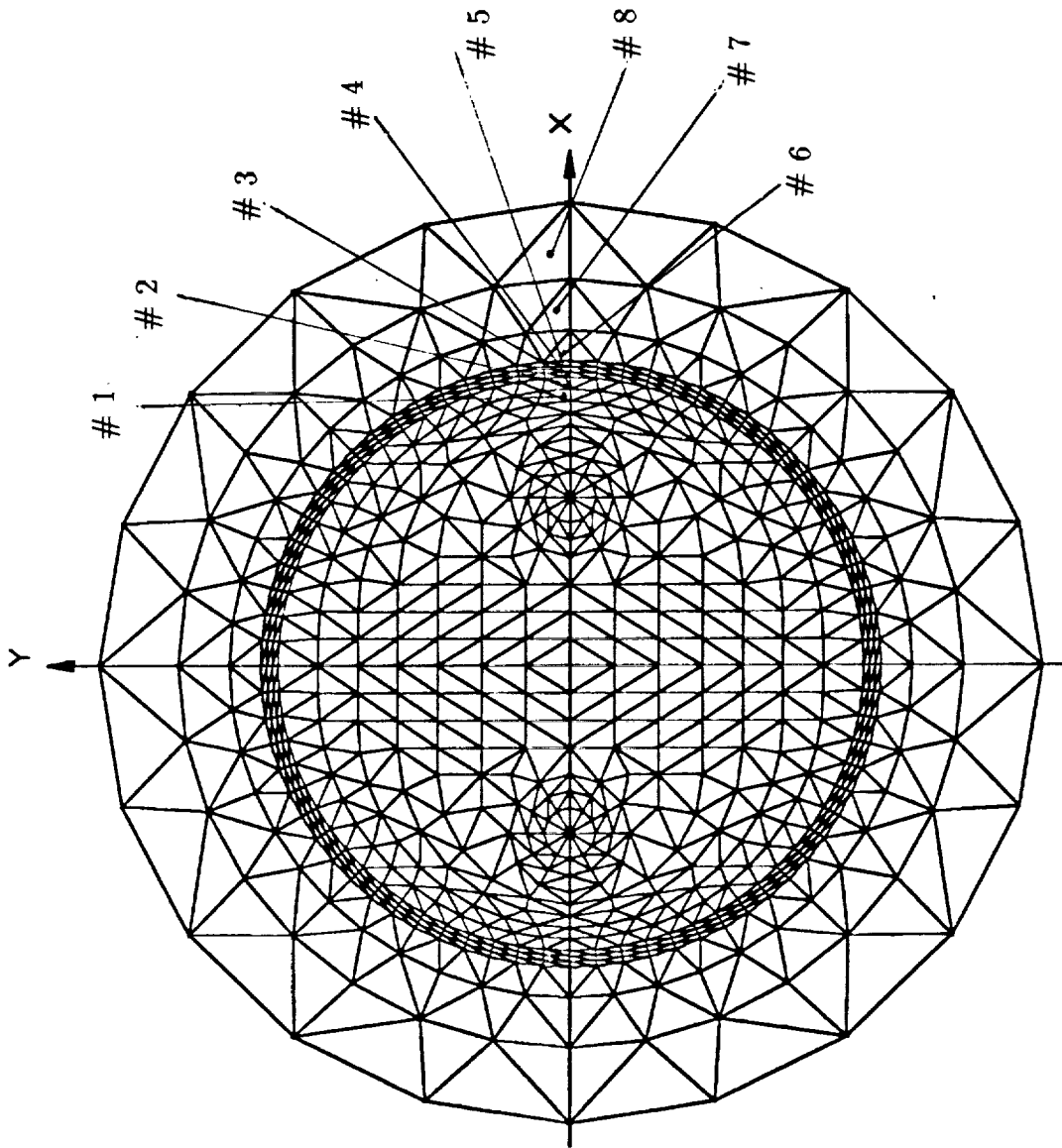


Figure 5.29: Finite Elements at Which the Effects of Defective Shielding on Flux

Densities are Given in Figure(5.30)

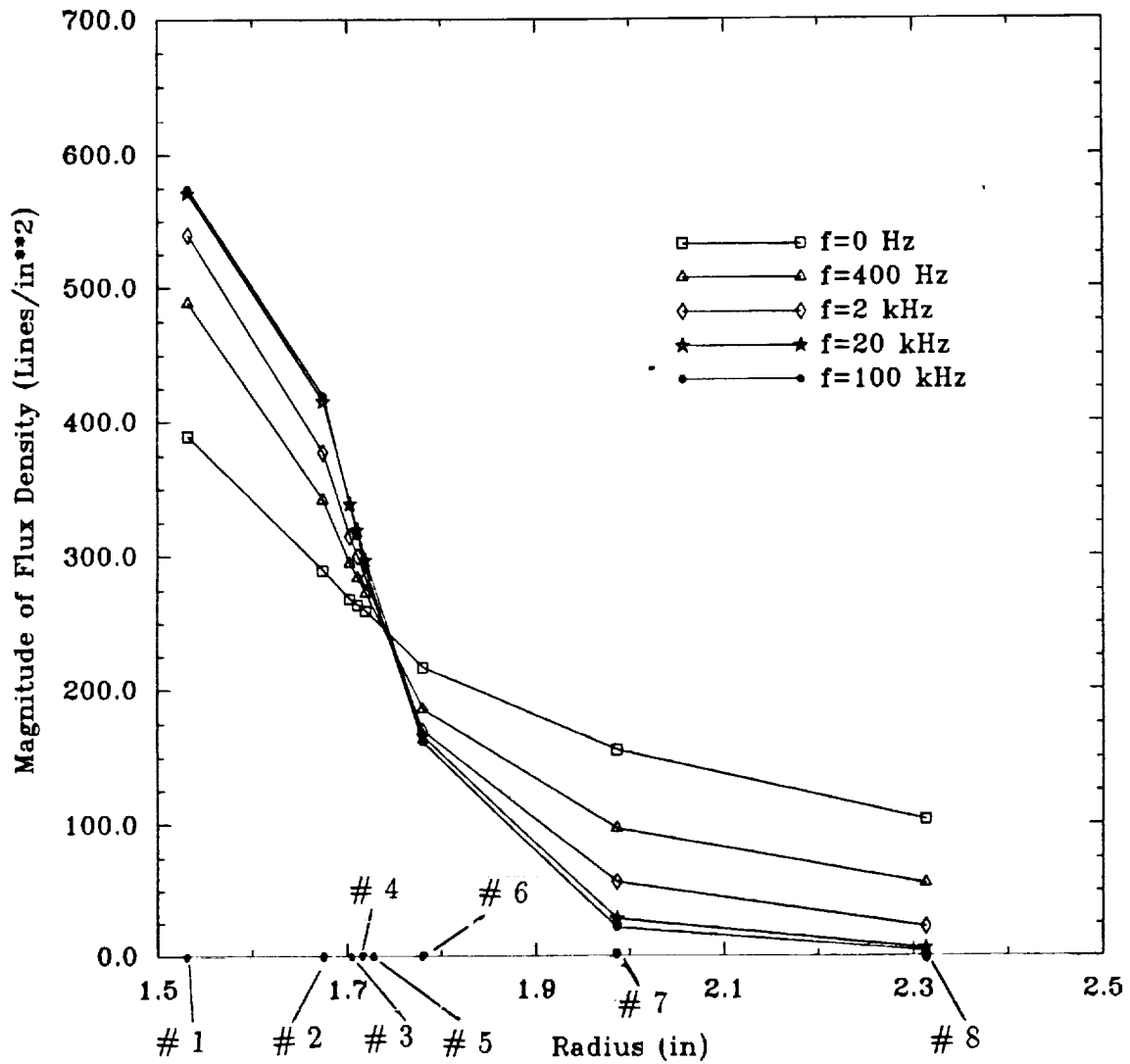


Figure 5.30: Flux Density Magnitudes With Ballooning ($m=10$) and a Conductive Shield With an Angular Defect, $\delta = 20^\circ$, Shield Thickness, $\Delta_s=0.025$ in, for $f=0$ Hz, 400 Hz, 2 kHz, 20 kHz and 100 kHz, for a Current $I=500$ A

Chapter 6

CLOSED FORM SOLUTION OF THE TWISTED-PAIR TRANSMISSION LINE

In chapter 4 and chapter 5, the 2DFE ballooning models have been developed in the DC case and AC case and applied to the two-wire parallel-pair transmission line problems with infinite boundaries which might become one of the common problems in the space station power transmission line applications. Another potential problem is that of the magnetic field surrounding twisted-pair transmission lines, again with infinite boundaries. This will be shown here not to be amenable to solution by the 2DFE ballooning models. Therefore, some new methods are needed for those twisted-pair problems. In this thesis, only the simplest twisted-pair case is considered so that closed-form formulations can be derived by the *Biot – Savart Law* coupled with integral methods. From the results of these closed-form solutions, some useful insight into the nature of the magnetic field surrounding such transmission lines will be obtained.

6.1 The Derivation of the Formulation

6.1.1 *Biot – Savart Law*

The magnetostatic field may be described by the magnetic vector potential (MVP) \bar{A} , which, in a homogeneous uniform linear medium, is governed by [11]:

$$\nabla^2 \bar{A} = -\mu \bar{J} \quad (6.1)$$

Equation(6.1) is called the MVP's Poisson equation and may be solved by the well known integral formulation as follows:

$$\bar{A} = \frac{\mu}{4\pi} \int \frac{\bar{J} dv}{r} \quad (6.2)$$

where, the symbol r denotes the distance from the field (or observation) point to the source point. The relationship between the MVP and the flux density is given by

$$\nabla \times \bar{A} = \bar{B} \quad (6.3)$$

Premultiplying both side of equation(6.2) by the operator $\nabla \times$, and using the definition in equation(6.3), one could obtain an expression for the flux density as follows:

$$\bar{B} = \frac{\mu}{4\pi} \int \nabla \times \left(\frac{\bar{J} dv}{r} \right) \quad (6.4)$$

Consider the following useful vector identity:

$$\nabla \times \left(\frac{\bar{J}}{r} \right) = \frac{1}{r} \nabla \times \bar{J} - \bar{J} \times \nabla \left(\frac{1}{r} \right) \quad (6.5)$$

where, \bar{J} is only a function of the position of the source point, which leads to $\nabla \times \bar{J} = 0$, and $\nabla \left(\frac{1}{r} \right) = -\frac{\bar{r}}{r^3}$. Equation(6.4) can therefore be rewritten as follows:

$$\bar{B} = \frac{\mu}{4\pi} \int \frac{\bar{J} \times \bar{r}}{r} dv \quad (6.6)$$

that is known as the *Biot – Savart Law*.

If the cross section of the conductor is very small, the following relationship could be obtained:

$$\bar{J} dv = \bar{J} ds dl = I d\bar{l} \quad (6.7)$$

Using equation(6.7), one can rewrite equation(6.2) and equation(6.6) respectively, as follows:

$$\bar{A} = \frac{\mu I}{4\pi} \int \frac{d\bar{l}}{r} \quad (6.8)$$

and

$$\vec{B} = \frac{\mu I}{4\pi} \int \frac{d\vec{l} \times \vec{r}}{r} \quad (6.9)$$

6.1.2 Analytical solutions for a two-wire twisted-pair transmission line by the *Biot – Savart Law*

Now, consider a two-wire twisted-pair transmission line which consists of many pitches in free space shown in Figure(6.1). The details of the geometry in one pitch are shown in Figure(6.2), where a pair of DC currents ($I=500$ A) flow through the pair of spiralling conductors, that is, one is spinning along the positive z axis and the other along the negative z axis.

Now, consider the MVP formulation. Using the integral MVP method, equation(6.8), one can compute the MVP at any arbitrary point, $P(x, y, z)$, shown in Figure(6.2), as follows:

$$\vec{A}(x, y, z) = \frac{\mu_0 I}{4\pi} \int_s \frac{d\vec{l}_1}{r_1} - \frac{\mu_0 I}{4\pi} \int_s \frac{d\vec{l}_2}{r_2} = \frac{\mu_0 I}{4\pi} \sum_{i=0}^{NP-1} \int_{s_i} \left(\frac{d\vec{l}_1}{r_1} - \frac{d\vec{l}_2}{r_2} \right) \quad (6.10)$$

where: the symbol NP denotes the number of pitches, the subscript, s , denotes the line source, \vec{r}_1 denotes the space vector from the source point on conductor #1 to the field (observation) point, \vec{r}_2 denotes the space vector from the source point on conductor #2 to the field (observation) point.

From the geometry shown in Figure(6.2), some useful relationships can be written as follows:

$$\begin{cases} x_1 = r_0 \cos \theta_1 \\ y_1 = r_0 \sin \theta_1 \\ z_1 = \frac{h}{2\pi} \theta_1 \\ \theta_1 : (-\pi NP, \pi NP) \end{cases} \quad (6.11)$$

$$\begin{cases} x_2 = r_0 \cos \theta_2 = -r_0 \cos \theta_1 \\ y_2 = r_0 \sin \theta_2 = -r_0 \sin \theta_1 \\ z_2 = \frac{h}{2\pi} (\theta_2 - \pi) = \frac{h}{2\pi} \theta_1 \\ \theta_2 = \theta_1 + \pi \end{cases} \quad (6.12)$$

$$r_1 = [(x - r_0 \cos \theta_1)^2 + (y - r_0 \sin \theta_1)^2 + (z - \frac{h}{2\pi} \theta_1)^2]^{\frac{1}{2}} \quad (6.13)$$

$$r_2 = [(x + r_0 \cos \theta_1)^2 + (y + r_0 \sin \theta_1)^2 + (z - \frac{h}{2\pi} \theta_1)^2]^{\frac{1}{2}} \quad (6.14)$$

$$d\bar{l}_1 = -r_0 \sin \theta_1 d\theta_1 \hat{a}_x + r_0 \cos \theta_1 d\theta_1 \hat{a}_y + \frac{h}{2\pi} d\theta_1 \hat{a}_z \quad (6.15)$$

$$d\bar{l}_2 = r_0 \sin \theta_1 d\theta_1 \hat{a}_x - r_0 \cos \theta_1 d\theta_1 \hat{a}_y + \frac{h}{2\pi} d\theta_1 \hat{a}_z \quad (6.16)$$

Substituting equations(6.11) through (6.16) into equation(6.10), one may obtain the MVP as follows:

$$\bar{A} = \frac{\mu_0 I}{4\pi} \sum_{i=-NP/2}^{NP/2-1} \int_{2\pi i}^{2\pi(i+1)} \left[\begin{array}{c} -\frac{r_0 \sin \theta_1 d\theta_1}{r_1} - \frac{r_0 \sin \theta_1 d\theta_1}{r_2} \\ \frac{r_0 \cos \theta_1 d\theta_1}{r_1} + \frac{r_0 \cos \theta_1 d\theta_1}{r_2} \\ \frac{\frac{h}{2\pi} d\theta_1}{r_1} - \frac{\frac{h}{2\pi} d\theta_1}{r_2} \end{array} \right] \quad (6.17)$$

Now, consider the flux density formulation. Using the *Biot – Savart Law*, equation(6.9), one can compute the flux density at any arbitrary point, $P(x, y, z)$, shown in Figure(6.2), as follows:

$$\begin{aligned} \bar{B} &= \frac{\mu_0 I}{4\pi} \int_0^l \frac{d\bar{l}_1 \times \bar{r}_1^0}{r_1^2} - \frac{\mu_0 I}{4\pi} \int_0^l \frac{d\bar{l}_2 \times \bar{r}_2^0}{r_2^2} \\ &= \frac{\mu_0 I}{4\pi} \sum_{i=-NP/2}^{NP/2-1} \int_{l_i}^{l_{i+1}} \left(\frac{d\bar{l}_1 \times \bar{r}_1^0}{r_1^2} - \frac{d\bar{l}_2 \times \bar{r}_2^0}{r_2^2} \right) \\ &= \frac{\mu_0 I}{4\pi} \sum_{i=-NP/2}^{NP/2-1} \int_{l_i}^{l_{i+1}} \left(\frac{d\bar{l}_1 \times \bar{r}_1}{r_1^3} - \frac{d\bar{l}_2 \times \bar{r}_2}{r_2^3} \right) \end{aligned} \quad (6.18)$$

where \bar{r}_1^0 and \bar{r}_2^0 are the unit space vectors from the source points, P_1 and P_2 , on conductor #1 and conductor #2 to the field (observation) point, P , which are given as follows:

$$\bar{r}_1^0 = \frac{1}{r_1} [(x - r_0 \cos \theta_1) \hat{a}_x + (y - r_0 \sin \theta_1) \hat{a}_y + (z - \frac{h}{2\pi} \theta_1) \hat{a}_z] = \frac{\bar{r}_1}{r_1} \quad (6.19)$$

$$\bar{r}_2^0 = \frac{1}{r_2} [(x + r_0 \cos \theta_1) \hat{a}_x + (y + r_0 \sin \theta_1) \hat{a}_y + (z - \frac{h}{2\pi} \theta_1) \hat{a}_z] = \frac{\bar{r}_2}{r_2} \quad (6.20)$$

Using vector operation rules, one may obtain the following:

$$\begin{aligned}
 d\vec{l}_1 \times \vec{r}_1 &= \begin{vmatrix} \hat{a}_x & \hat{a}_y & \hat{a}_z \\ -r_0 \sin \theta_1 d\theta_1 & r_0 \cos \theta_1 d\theta_1 & \frac{h}{2\pi} d\theta_1 \\ x - r_0 \cos \theta_1 & y - r_0 \sin \theta_1 & z - \frac{h}{2\pi} \theta_1 \end{vmatrix} \\
 &= \begin{bmatrix} r_0 \cos \theta_1 d\theta_1 (z - \frac{h}{2\pi} \theta_1) - (y - r_0 \sin \theta_1) \frac{h}{2\pi} d\theta_1 \\ (x - r_0 \cos \theta_1) \frac{h}{2\pi} d\theta_1 + r_0 \sin \theta_1 d\theta_1 (z - \frac{h}{2\pi} \theta_1) \\ -r_0 \sin \theta_1 d\theta_1 (y - r_0 \sin \theta_1) - r_0 \cos \theta_1 d\theta_1 (x - r_0 \cos \theta_1) \end{bmatrix} \quad (6.21)
 \end{aligned}$$

and,

$$\begin{aligned}
 -d\vec{l}_2 \times \vec{r}_2 &= \begin{vmatrix} \hat{a}_x & \hat{a}_y & \hat{a}_z \\ -r_0 \sin \theta_1 d\theta_1 & r_0 \cos \theta_1 d\theta_1 & -\frac{h}{2\pi} d\theta_1 \\ x + r_0 \cos \theta_1 & y + r_0 \sin \theta_1 & z - \frac{h}{2\pi} \theta_1 \end{vmatrix} \\
 &= \begin{bmatrix} r_0 \cos \theta_1 d\theta_1 (z - \frac{h}{2\pi} \theta_1) + (y + r_0 \sin \theta_1) \frac{h}{2\pi} d\theta_1 \\ -(x + r_0 \cos \theta_1) \frac{h}{2\pi} d\theta_1 + r_0 \sin \theta_1 d\theta_1 (z - \frac{h}{2\pi} \theta_1) \\ -r_0 \sin \theta_1 d\theta_1 (y + r_0 \sin \theta_1) - r_0 \cos \theta_1 d\theta_1 (x + r_0 \cos \theta_1) \end{bmatrix} \quad (6.22)
 \end{aligned}$$

Substituting equation(6.21) and equation(6.22) into equation(6.18), one can obtain the formulation of the flux density as follows:

$$\begin{aligned}
 \vec{B} &= \frac{\mu_0 I}{4\pi} \sum_{i=-NP/2}^{NP/2-1} \int_{2\pi i}^{2\pi(i+1)} \left(\frac{1}{r_1^3} \begin{bmatrix} r_0 \cos \theta_1 (z - \frac{h}{2\pi} \theta_1) - (y - r_0 \sin \theta_1) \frac{h}{2\pi} \\ (x - r_0 \cos \theta_1) \frac{h}{2\pi} + r_0 \sin \theta_1 (z - \frac{h}{2\pi} \theta_1) \\ -r_0 \sin \theta_1 (y - r_0 \sin \theta_1) - r_0 \cos \theta_1 (x - r_0 \cos \theta_1) \end{bmatrix} \right. \\
 &\quad \left. + \frac{1}{r_2^3} \begin{bmatrix} r_0 \cos \theta_1 (z - \frac{h}{2\pi} \theta_1) + (y + r_0 \sin \theta_1) \frac{h}{2\pi} \\ -(x + r_0 \cos \theta_1) \frac{h}{2\pi} + r_0 \sin \theta_1 (z - \frac{h}{2\pi} \theta_1) \\ -r_0 \sin \theta_1 (y + r_0 \sin \theta_1) - r_0 \cos \theta_1 (x + r_0 \cos \theta_1) \end{bmatrix} \right) d\theta_1 \quad (6.23)
 \end{aligned}$$

6.2 The Computation of Flux Densities

The closed-form analytical formulations of the magnetic field surrounding the two-wire twisted-pair transmission line, which is depicted schematically in Figure(6.2), was derived in the previous section. Those formulations can be programmed with the numerical integral method (see Appendix B) for use on computers. The magnetic flux density, \overline{B} , specifically the B_x and B_y components, can be computed at any cross-section and at any angle, θ , shown in Figure(6.2). Here, in this thesis, this calculation was performed at locations along the three concentric circles shown by the dotted lines in Figure(6.3). The resulting \overline{B} field at various points along the three dotted circles is shown by the \overline{B} vector arrow displays, whose direction indicates the orientation of the \overline{B} field in the $x - y$ plane or the z direction, and whose length is proportional to the magnitude of the resultant \overline{B} field along the $x - y$ plane or along the z axis.

These \overline{B} field results are shown in Figure(6.4) for the parallel-wire case discussed in chapter 4, and in Figure(6.5) and (6.6) for the twisted-pair case for a pitch, $h = 5''$, and a plane with $\theta = 0^\circ$. There are no z -component \overline{B} fields resulting from the parallel-pair case as shown in Figure(6.4), while there are z -component \overline{B} fields resulting from the twisted-pair case as shown in Figure(6.6). These \overline{B} field calculations were repeated for a plane with $\theta = 90^\circ$, and the results are shown in Figures(6.7) and (6.8).

The effects of the choice of the pitch, h , shown in Figure(6.2), on the flux density components, B_x , B_y , B_z and resultant magnitudes, $\|\overline{B}\|$, are documented in Figures(6.9) through (6.12) at the mid-plane point for a transmission line of length 20000 inches. For all these cases, in Figure(6.2), r_0 is equal to 1.0 inch, and the DC current flowing in each conductor is equal to 500 A.

Figures(6.5) through (6.8) demonstrate the 3D nature of the \overline{B} field surrounding a two-wire twisted-pair transmission line. Figures(6.9) through (6.12) show that shorter lengths of the twist pitch make the \overline{B} fields outside the transmission line decay more quickly in the radially outward direction. That is, at locations far away from the transmission line, the z -component of the fields, B_z , is of the same order of magnitudes of the x , and y components, B_x , and B_y . Accordingly, the z -component, B_z , could not be neglected in comparison to the B_x and B_y . That is, the twisted-pair

problem should be dealt with using 3D magnetic field computation methods.

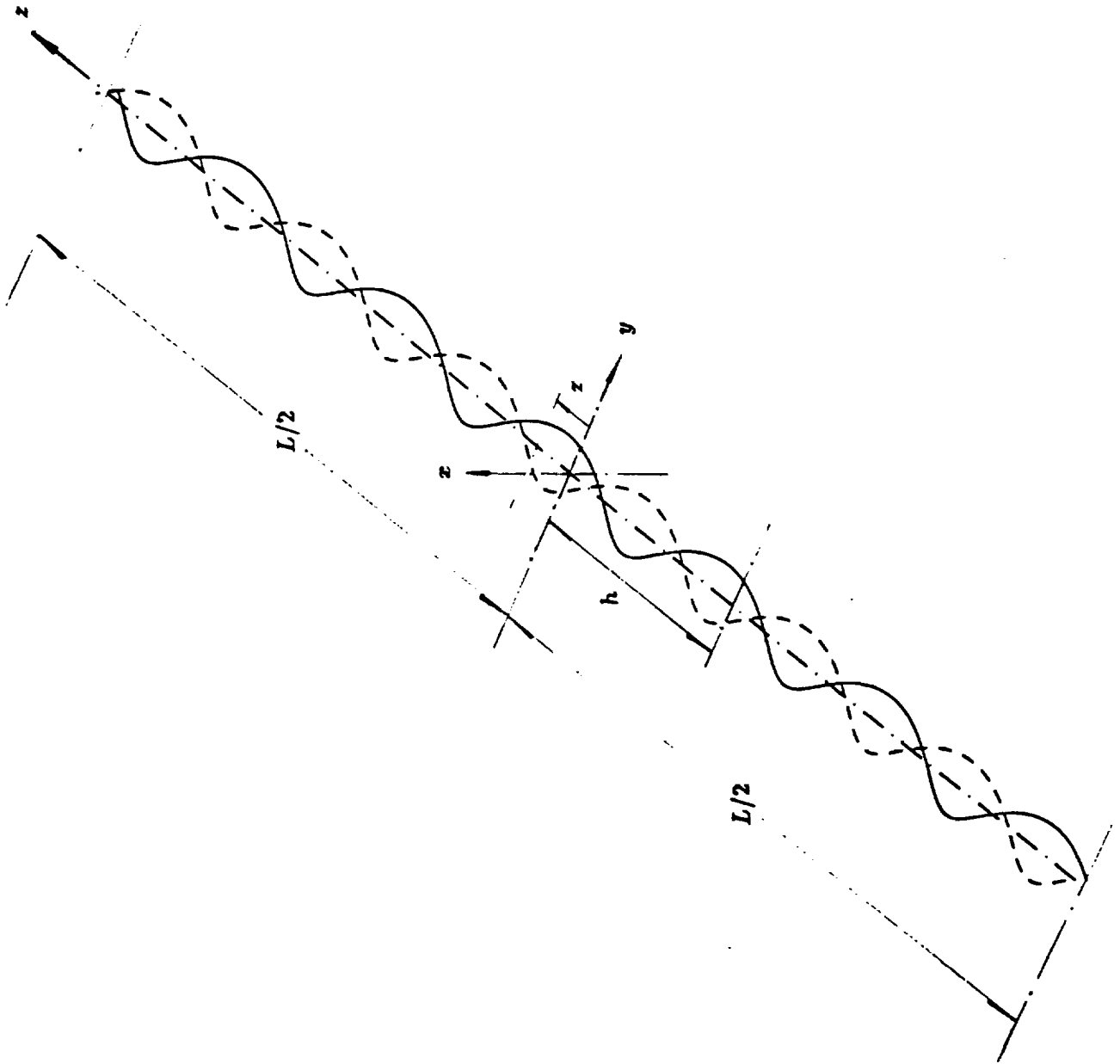


Figure 6.1: Isometric View of the Twisted-Pair Geometry and Locations Where the \mathbf{B} Fields are Computed

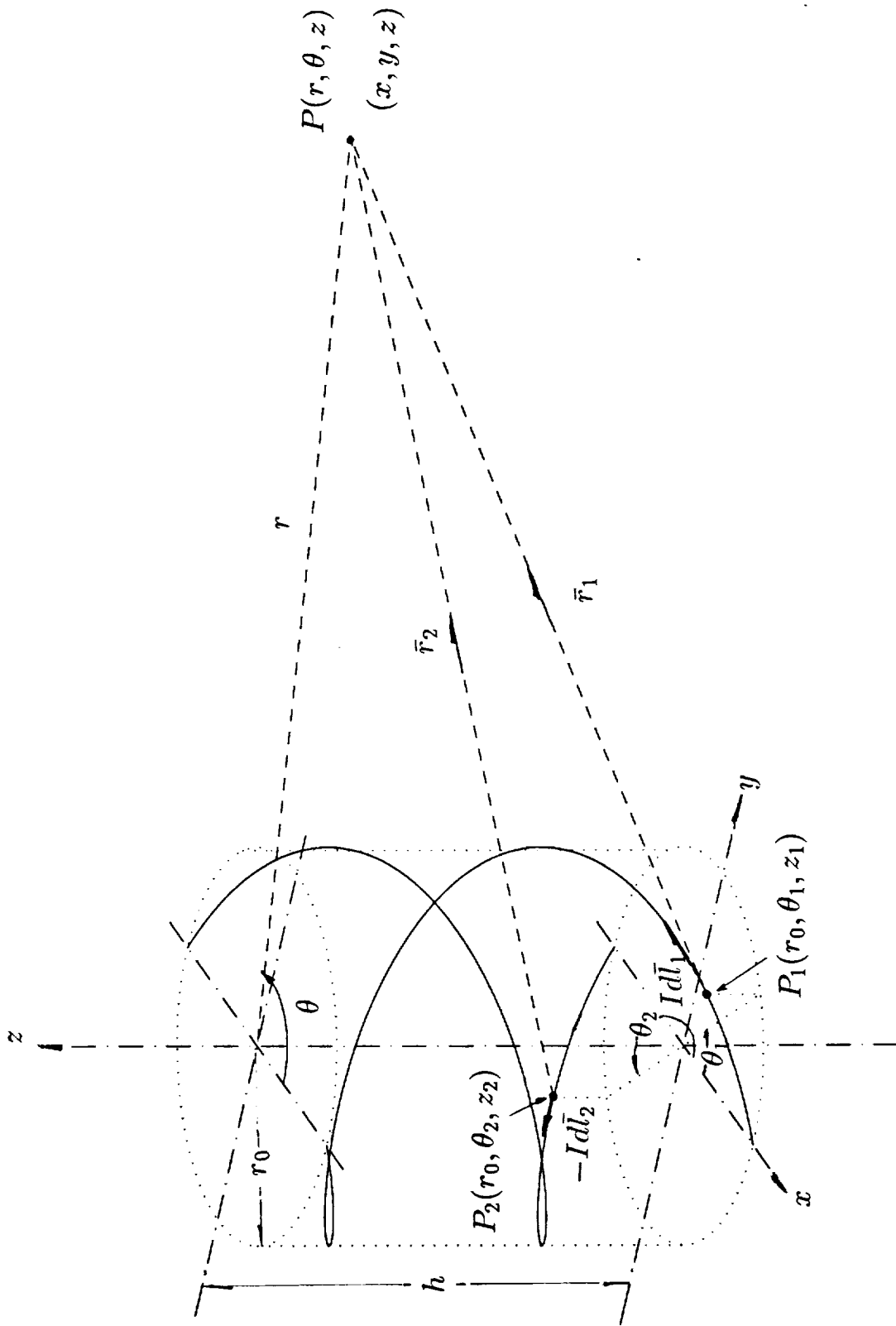


Figure 6.2: Two-Wire (Twisted-Pair) Transmission Line

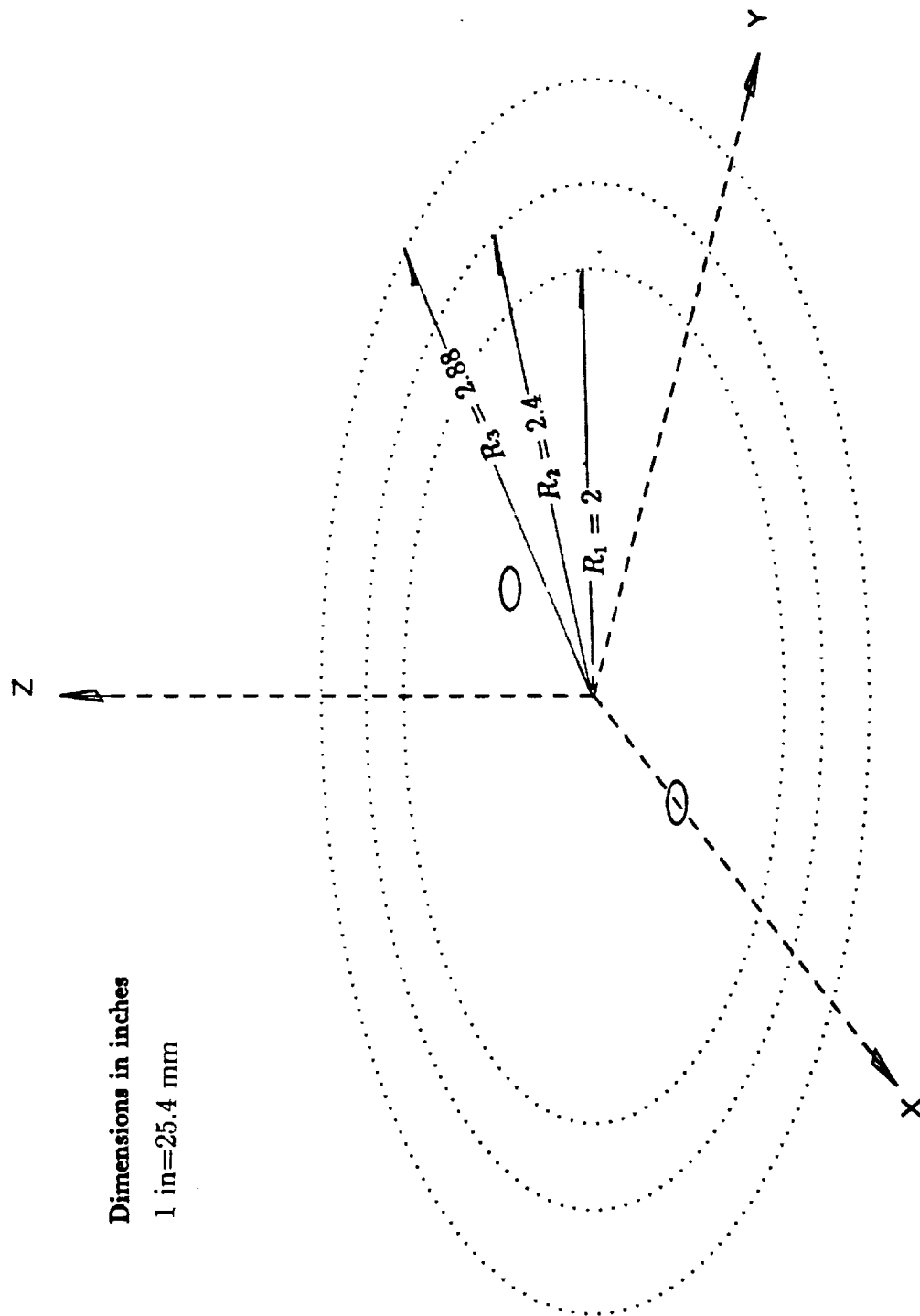


Figure 6.3: Twisted-Pair Cross Section at $\theta = 0^\circ$

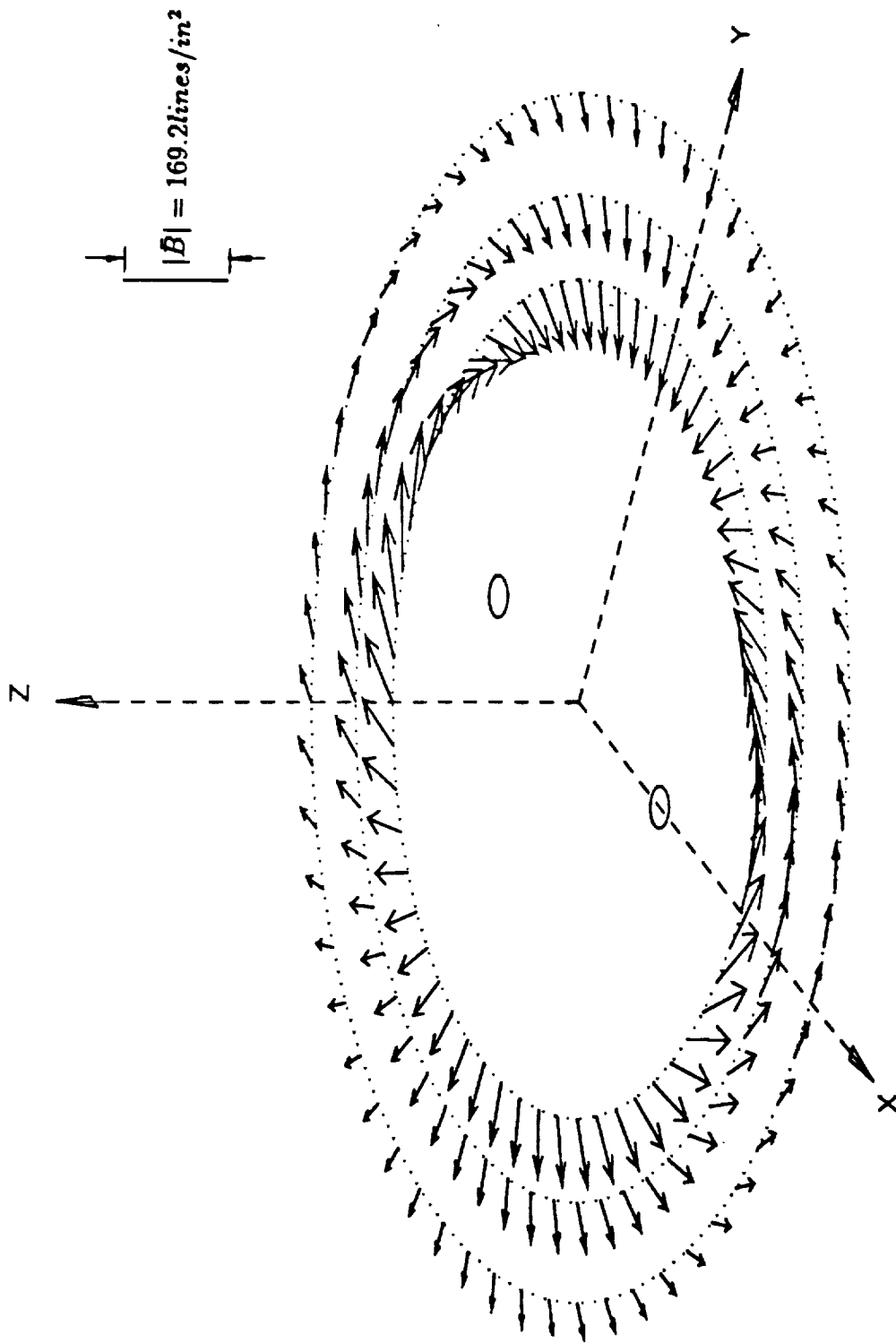


Figure 6.4: Flux Density Components B_x and B_y for the Parallel-Pair in the $x - y$ Plane ($I = 500A$)
 (No z -Component of Flux Density in This Case)

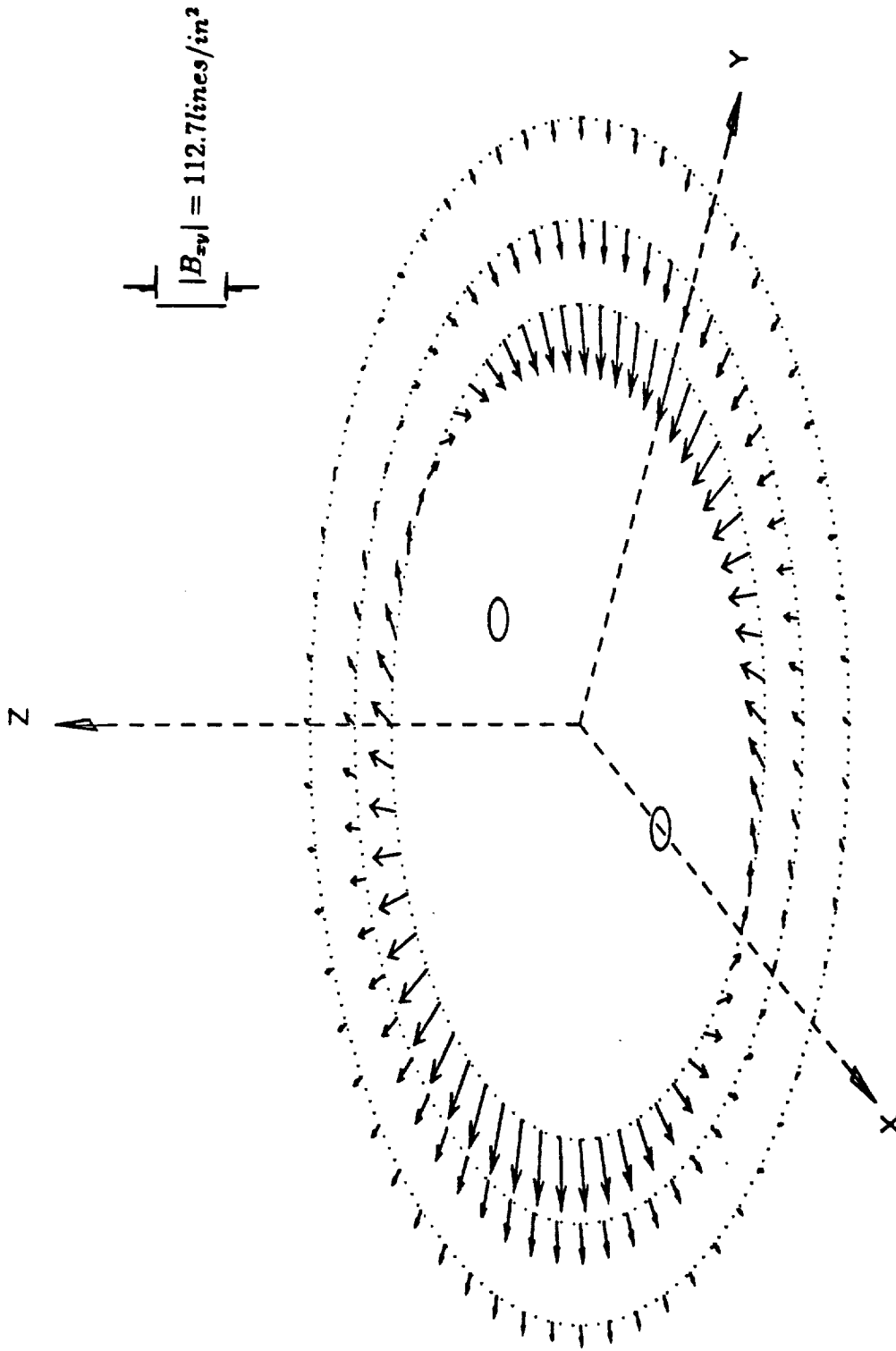


Figure 6.5: Flux Density Components B_r and B_y for the Twisted-Pair for a Pitch, $h \approx 5''$ ($=12.7 \text{ cm}$) in the $\theta = 0^\circ$ Plane ($I = 500A$)

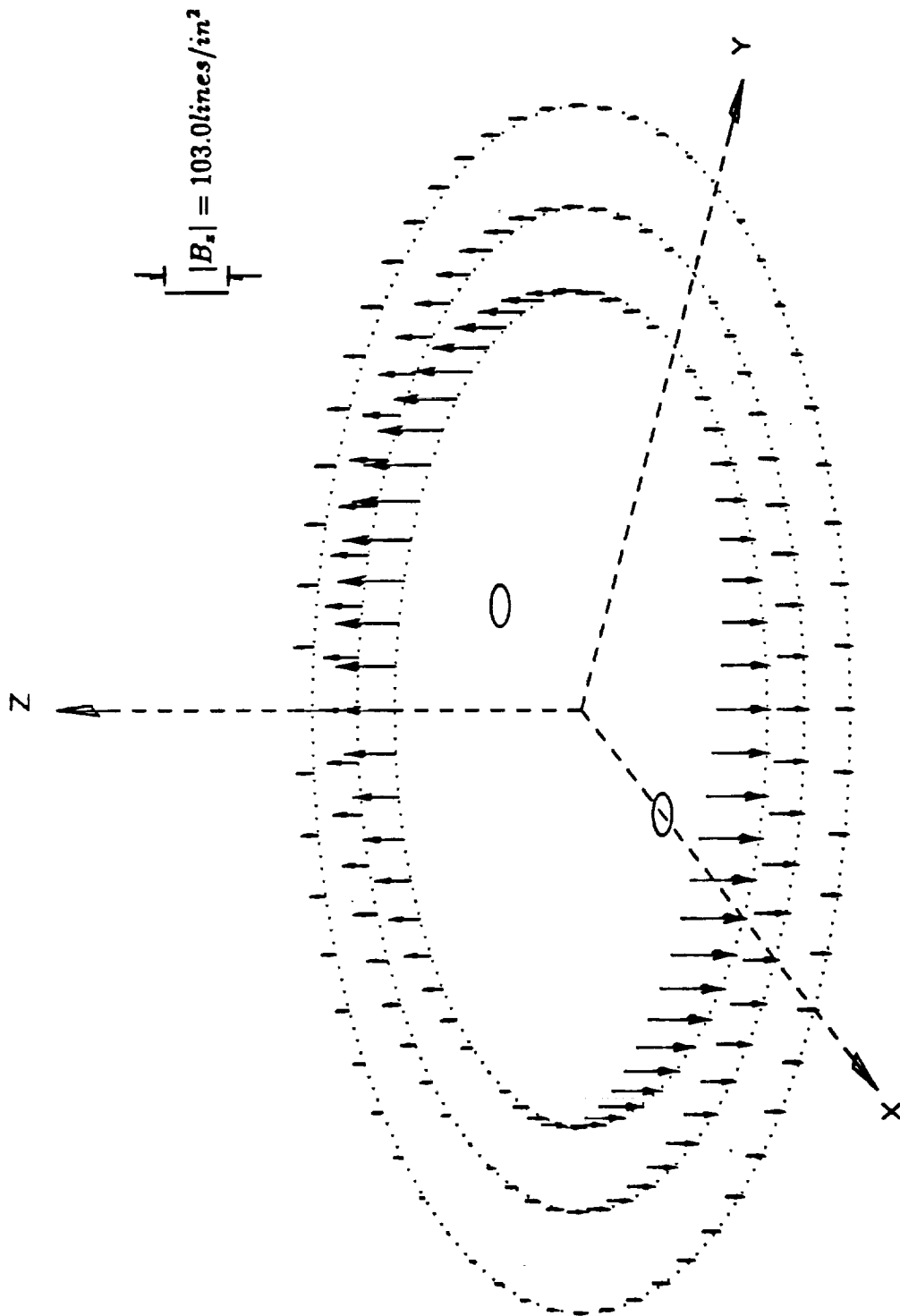


Figure 6.6: Flux Density Component B_z for the Twisted-Pair for a Pitch, $h = 5'' (=12.7 \text{ cm})$ in the $\theta = 0^\circ$ Plane ($I = 500A$)

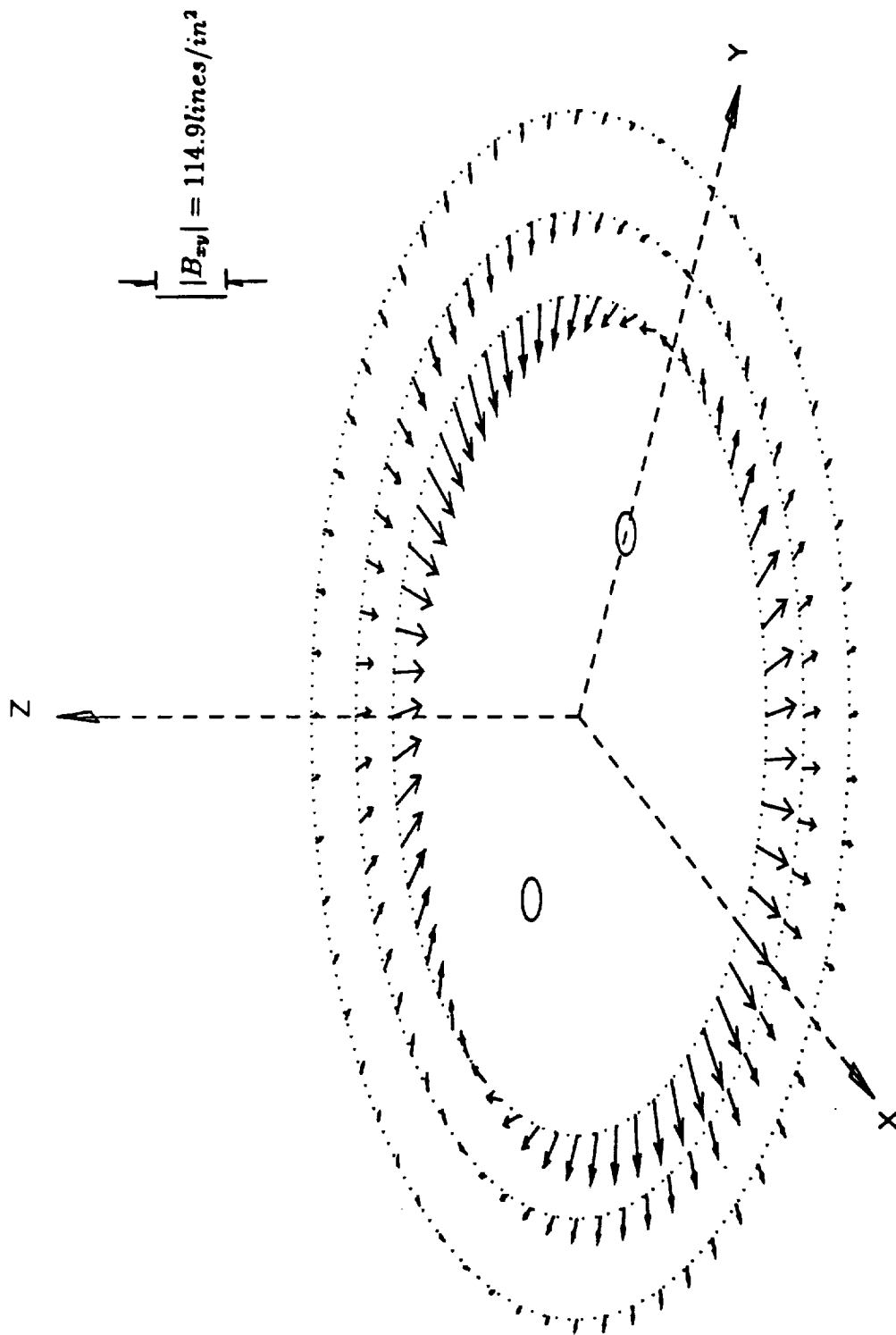


Figure 6.7: Flux Density Components B_x and B_y for the Twisted-Pair for a Pitch, $h = 5'' (=12.7 \text{ cm})$ in the $\theta = 90^\circ$ Plane ($I = 500A$)

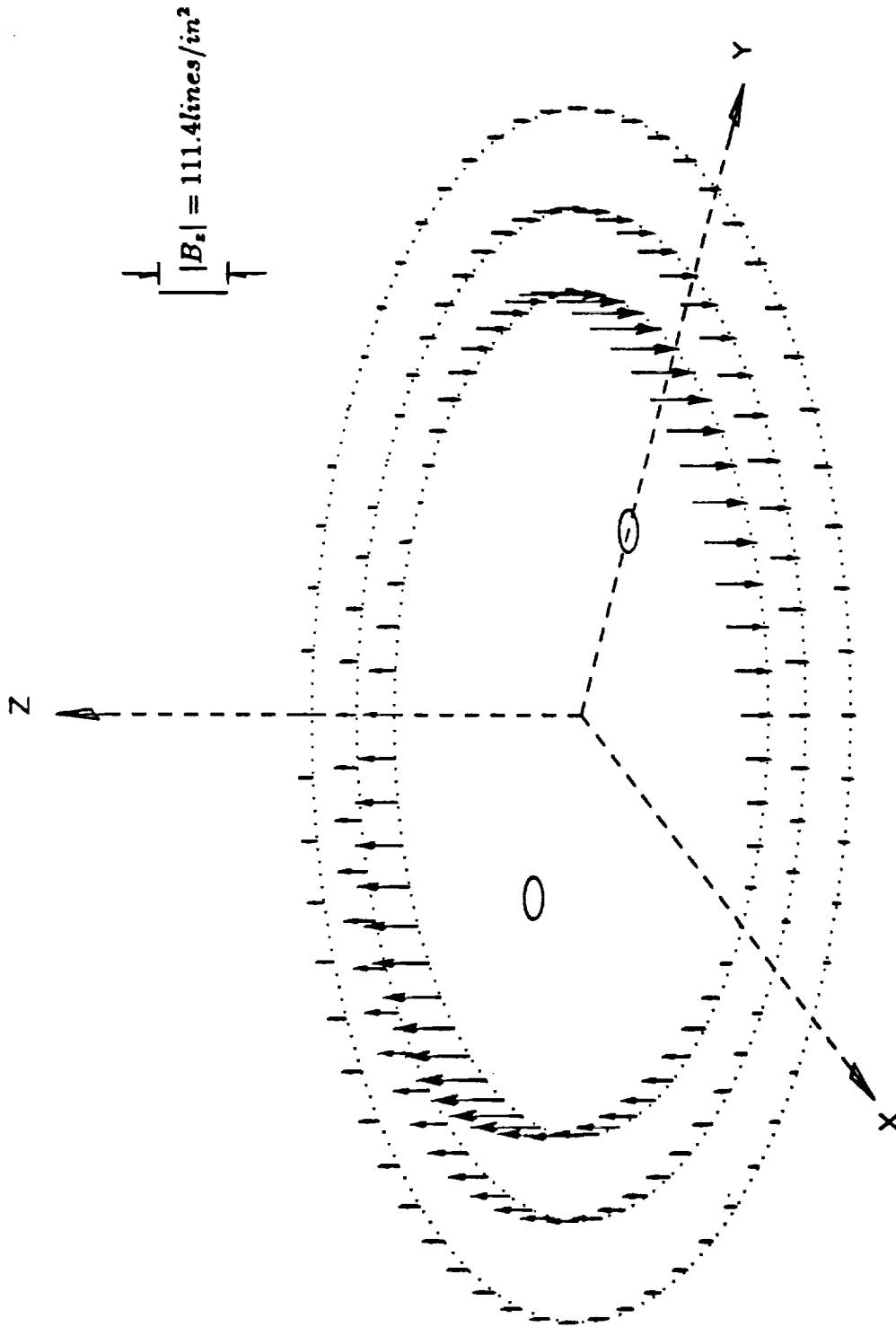


Figure 6.8: Flux Density Component B_z for the Twisted-Pair for a Pitch, $h = 5'' (=12.7 \text{ cm})$ in the $\theta = 90^\circ$ Plane ($I = 500A$)

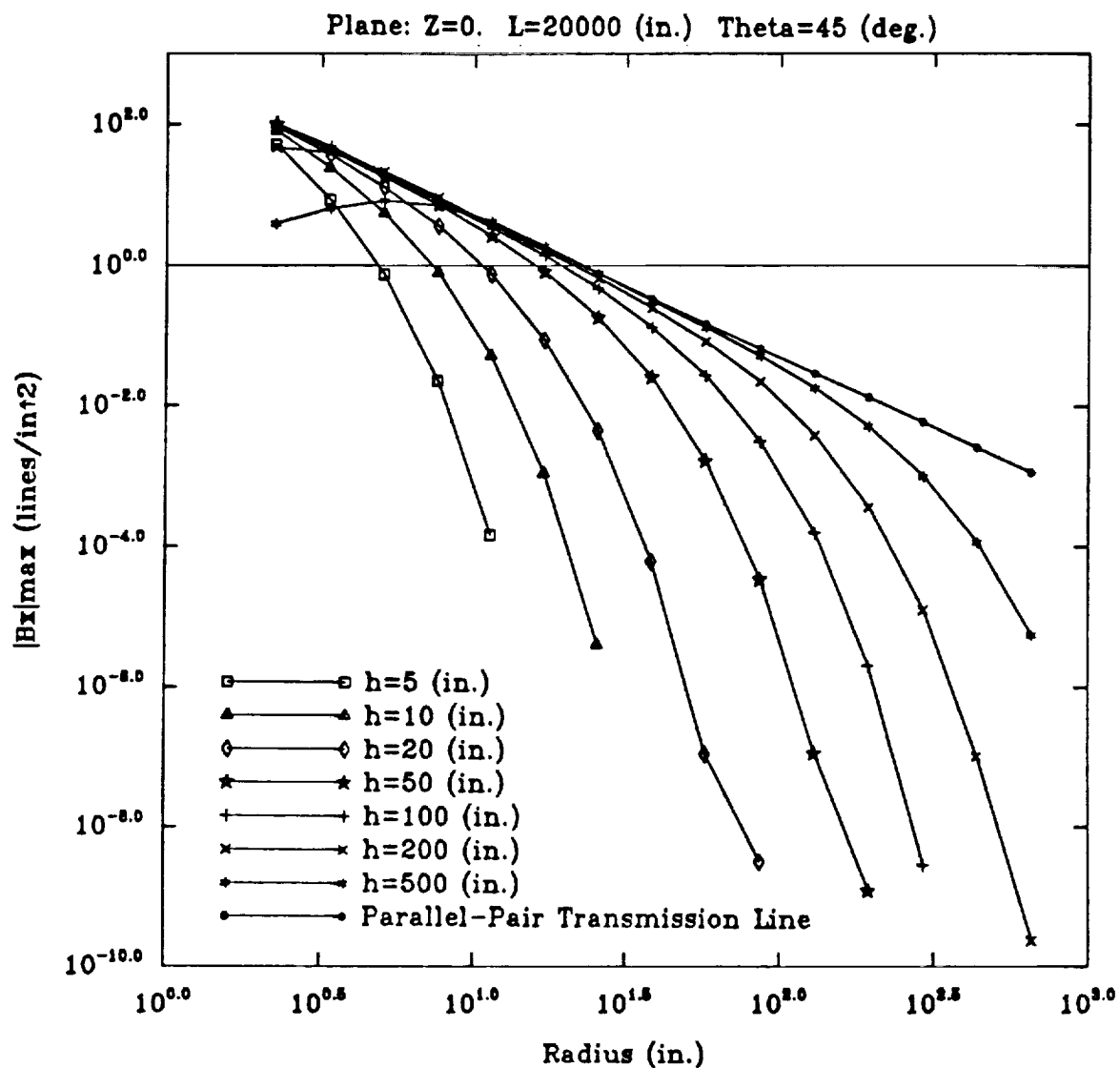


Figure 6.9: Magnitude of Flux Density Component $|B_x|_{max}$ for Different Pitch Lengths ($I = 500A$)

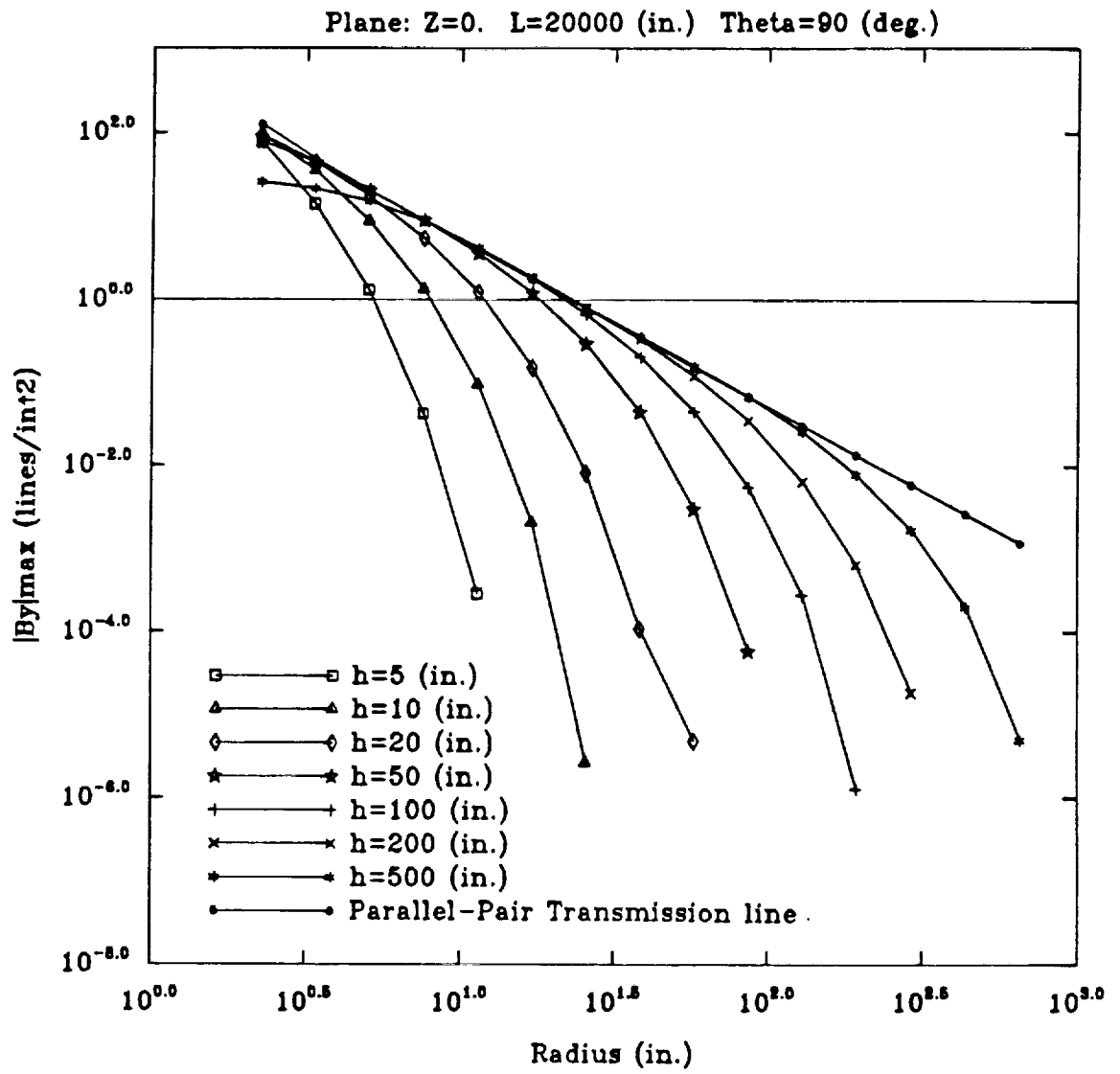


Figure 6.10: Magnitude of Flux Density Component $|B_y|_{max}$ for Different Pitch Lengths ($I = 500A$)

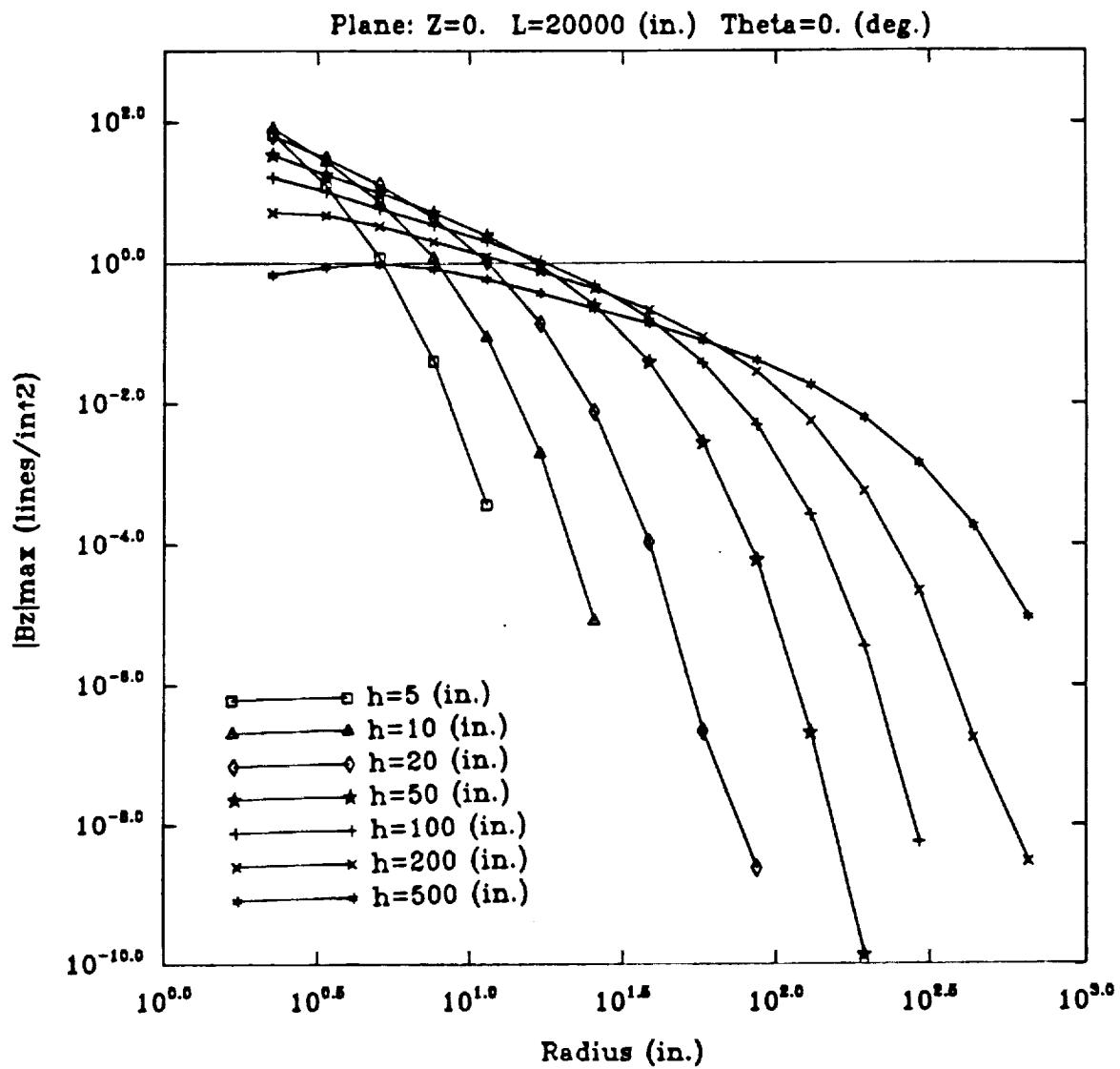


Figure 6.11: Magnitude of Flux Density Component $|B_z|_{max}$ for Different Pitch Lengths ($I = 500A$)

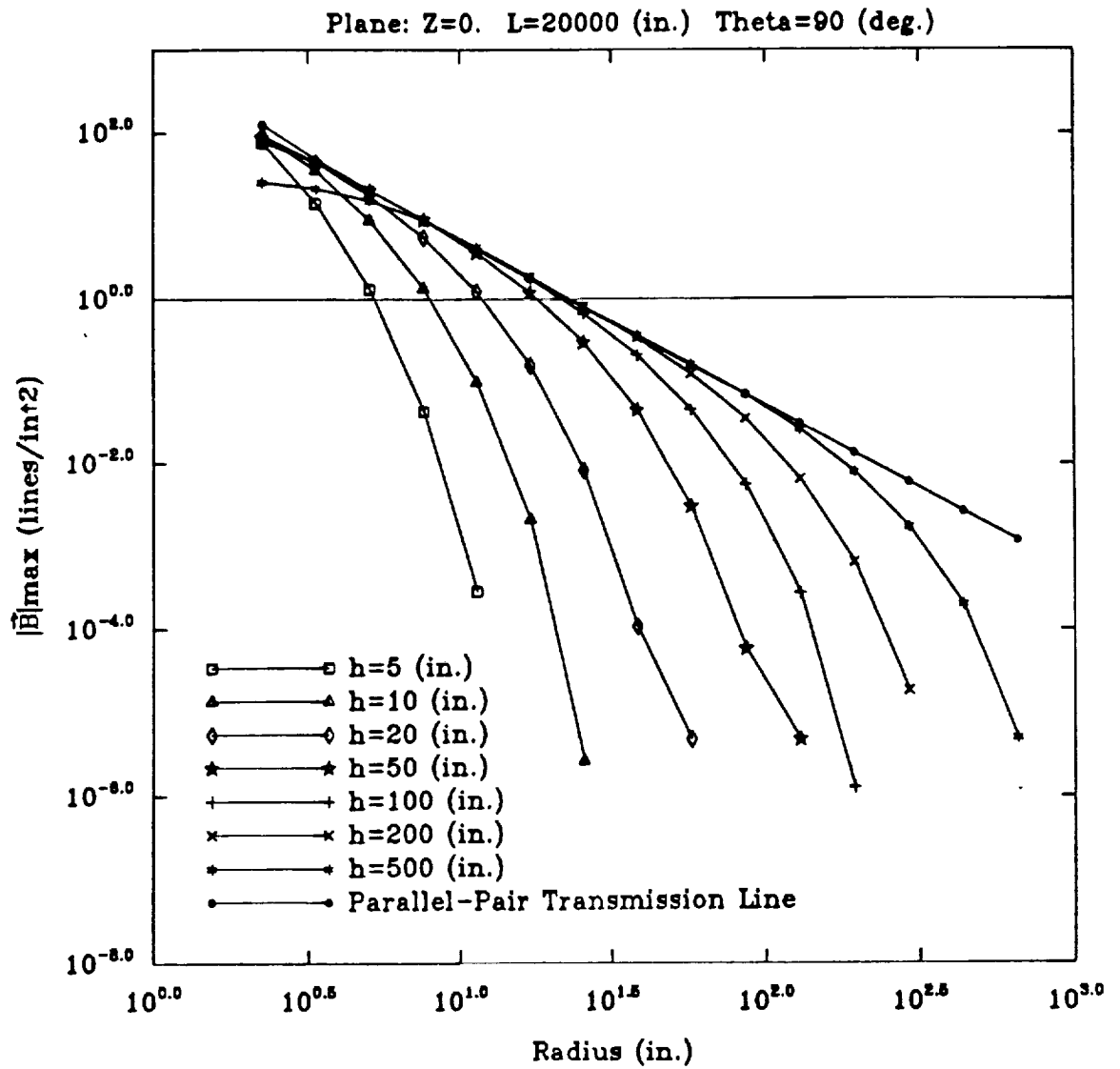


Figure 6.12: Magnitude of Flux Density $|B|_{\max}$ for Different Pitch Lengths
 ($I = 500A$)

Chapter 7

CONCLUSIONS AND FUTURE WORK

7.1 Conclusions

In this thesis, the ballooning methods incorporated into the 2DFE model have been presented to solve the 2D electromagnetic problems with infinite boundaries in the DC case and the quasi static (AC) case. The verification of this model was carried out by comparison of the results with those of the analytical solution in the magnetostatic case for a two-wire parallel-pair transmission line problem with no shielding and with an infinite boundary. This is because there exists a closed-form solution for that type of problem. Studies of the field distributions resulting from the magnetic shielding in the DC case and the conductive shielding in the AC case were performed. and the effects of possible defects in such shields were considered in both cases.

In the application to solve two-wire parallel-pair transmission line problems with infinite boundaries, an interior region, R , including eddy currents and all sources, with a circular boundary and an exterior annular region only representing free space were chosen. Usually, in this 2DFE ballooning model, not only the free space but the eddy current can be included in the exterior region, and because the field solution is limited to the interior region, R , the consideration in choosing the contour Γ_0 is that all regions of interest should be included in the interior region, R . This

2DFE ballooning model is applicable to complicated as well as simple shapes of the boundary, Γ_0 , which must satisfy the criterion that no radial line from the start point P_0 intersects such a boundary more than once.

Recalling the procedure of the AC 2DFE ballooning method, after modeling the interior region, R , by the FE method, it is necessary to form only one additional FE matrix, for an annulus one element wide which shares interface nodes with R , and then the FE matrix for the any other annulus is just the linear combination of the real components and complex components of the first one. With this performance of the annular matrices, the recursive computation to form the FE matrix for the exterior region becomes quicker and simpler. Having developed the recursive algorithm and obtained the FE matrix for the total exterior region, the only terms of interest in the matrix are those associated with the interface nodes on Γ_0 , so that the size of the matrix which has to be solved to compute the field in the interior region, R , is unaffected by the addition of the exterior region.

According to ballooning theory, the accuracy of the solution can be improved by increasing the number of ballooning layers, m . Recalling the results shown in chapter 4 and chapter 5, one may find that the lower the number of ballooning layers, m , the more improvement can be achieved by increasing m . However, if m is already large, little improvement could be obtained by increasing its value. Actually, there are three facts which would affect the accuracy of the solution: (1) the number of ballooning layers, m ; (2) the density of finite elements both in the interior region and the annuli; (3) the order of the interpolation polynomials (shape functions) used in the finite element formulation. Therefore, when the 2DFE ballooning model is applied to the magnetic field problems with infinite boundaries, the number of ballooning layers, m , should be chosen judiciously, and if further improvements of the results are required, finer FE mesh discretizations such as smaller finite elements, or high order finite elements will have to be adopted.

A closed-form solution for the magnetic fields surrounding a two-wire twisted-pair transmission line in the static case was presented in the previous chapter. The results show that the shorter the pitch of the twist, the weaker the magnetic fields surrounding that twisted-pair transmission line. Comparing these results, one may find that three

components of the flux densities are in the same order of magnitude, hence, for near field effects none of them can be neglected. In other words, the twisted-pair problem is a 3D problem.

7.2 Future Work

According to the conclusions in the previous section, the 3D nature of the field surrounding a twisted-pair transmission line means that it will be necessary to use 3DFE analysis or some equivalent method to evaluate the effects of magnetic material-type shielding or eddy current-type electromagnetic field shielding in association with such twisted pairs. It may be possible and necessary to develop 3D ballooning models for twisted-pair problems or some other space station problems with infinite boundaries, which is one of the possible future works stemming from this research.

In the space station applications, a future space station can be modeled as a long wire structure (with a diameter of 1 m and a length of 100 m approximately). In some cases, the space station orbits the earth at an altitude of 300 km with a velocity of approximately 8 km/s. The motion of the space station through the geomagnetic field results in an electromotive force $\mathbf{v} \times \mathbf{B}$ along its length. This electromotive force (emf) causes a potential drop across the space station and a current existing between the space station and the space plasma.

A 3DFE method and a 3D ballooning method may be adopted to compute the electromagnetic field distribution for this problem. This may be accomplished as follows:

- (1) Choose a sphere as an interior region enclosing the space station.
- (2) Use a conventional 3DFE method to build up the global matrix system on the interior region where the $\mathbf{v} \times \mathbf{B}$ components are considered.
- (3) Divide the exterior region outside the interior region into many layers which are concentric with the interior region.
- (4) Compute the FE matrix for each layer and use ballooning techniques to obtain the contribution matrix for the exterior region.
- (5) Incorporate the contribution matrix of the exterior region into the global system

including the interior region to solve the problem.

It seems possible to obtain the local electromagnetic field distribution in detail using such a 3DFE ballooning model. These fields can be used to calculate the currents, as well as physical quantities and phenomena of interest.

Bibliography

- [1] P.Silvester, M.V.K. Chari, *IEEE Trans.* Vol. PAS-89, pp 1642, 1970.
- [2] C.F.R.L.Antunes, E.M.Freeman D.Lowther and P.Silvester, "A static ballooning technique for 2-D open boundary problems." *J. Appl. Phys.*, Vol.53, No.11, pp 8360-8362, 1982.
- [3] D.A.Lowther, C.B.Rajanathan and P.P.Silvester, "A Finite Element for Solving 2-D Open Boundary Problems" *IEEE Trans.* Vol. MAG-14, pp.467-469, 1978.
- [4] John R. Brauer, "Open Boundary Finite Elements for Axisymmetric Magnetic and Skin Effect Problems." *J. Appl. Phys.*, Vol.53, No.11, pp 8366-8368, 1982.
- [5] Lee,J.F., and Cendes,Z.J.,"Transfinite Elements: A Highly Efficient Procedure for Modeling Open Field Problems." *J. Appl. Phys.*, Vol.16, No.8, pp.3913-3915. 1987
- [6] M.V.K. Chari, "Electromagnetic Field Computation of Open Boundary Problems by a Semi-Analytic Approach." *IEEE Trans.* Vol. MAG-23, pp.3566-3568, 1987.
- [7] M.V.K. Chari, G. Bedrosian, "Hybrid Harmonic/Finite Element Method for Two-Dimensional Open Boundary Problems." *IEEE Trans.* Vol. MAG-23, pp.3572-3574, 1987.
- [8] M.V.K. Chari, G. Bedrosian,"A Hybrid Method for Eddy Current Open-Boundary Field Computation." *J. Appl. Phys.*, Vol.63, No.8, pp. 3019-3021, 1988.

- [9] P.W.Barber, N.A.O.Demerdash, R.Wang, B.Hurysz, and Z.Luo, "Analysis of Electromagnetic Interference From Power System Processing and Transmission Components for Space Station Freedom." *First Interim Progress Report for the Period January 1-June 30,1990*. Grant No. NAG3-1126, Submitted to NASA Lewis Research Center, January 1991.
- [10] P.W.Barber, N.A.O.Demerdash, R.Wang, B.Hurysz, and Z.Luo, "Analysis of Electromagnetic Interference From Power System Processing and Transmission Components for Space Station Freedom." *Interim Progress Report for the Period July 1-December 31,1990*. Grant No. NAG3-1126, Submitted to NASA Lewis Research Center, January 1991.
- [11] S.Ratnajeevan H.Hoole, " Computer-Aided Analysis and Design of Electromagnetic Devices." Elsevier Science Publishing Co., Inc. 1989.
- [12] W. Cheney, D. Kincaid, "Numerical Mathematics and Computing." Brooks/Cole Publishing Co., 1985.

APPENDIX A

List of Symbols

A_x, A_y, A_z	The x, y and z components of the magnetic vector potential
\bar{A}	Magnetic vector potential
B_x, B_y, B_z	The x, y and z components of the flux density
\bar{B}	Magnetic flux density
\bar{D}	Electric flux density
\bar{E}	The electric field intensity
$F(A)$	Energy functional
H_x, H_y, H_z	The x, y and z components of the field intensity
\bar{H}	Magnetic field intensity
J_x, J_y, J_z	The x, y and z components of the source current density
\bar{J}_s	The source current density
\bar{J}_e	The eddy current density
I	Source current
ν	Material reluctivity
μ	Material permeability
σ	Conductivity of medium
ρ	Charge density
ϵ	Permittivity of medium
ω	Angular speed
\mathbb{S}	Global FE coefficient matrix
\mathbf{I}	Forcing function vector
\mathbf{A}	Vector of MVP components
MVP	Magnetic vector potential
p.d.e.	Partial differential equation

AC Alternate current
DC Direct current
2DFE Two dimensional finite element
3DFE Three dimensional finite element

APPENDIX B

Gaussian Quadrature Integral Method

There is a large family of numerical integration formulas that conform to the following pattern:

$$\int_{-1}^1 f(x)dx \approx A_1f(x_1) + A_2f(x_2) + \dots + A_nf(x_n)$$

In using such a formula, it is only necessary to know the “nodes” x_1, x_2, \dots, x_n and the “weights” A_1, A_2, \dots, A_n .

One major source of the previous formula is in the theory of polynomial interpolation. If the nodes have been fixed, then there is a corresponding Lagrange interpolation formula:

$$p(x) = \sum_{i=1}^n f(x_i)l_i(x)$$

$$\text{where } l_i(x) = \prod_{j=1, j \neq i}^n \left(\frac{x - x_j}{x_i - x_j} \right).$$

This formula provides a polynomial p of degree $\leq n - 1$ that interpolate f at the nodes; that is, $p(x_i) = f(x_i)$ for $1 \leq i \leq n$. If the circumstances are favorable, p will be a good approximation to f , and $\int_a^b f(x)dx$ will be a good approximation to

$\int_a^b p(x)dx$. Therefore

$$\int_a^b f(x)dx \approx \int_a^b p(x)dx = \sum_{i=1}^n f(x_i) \int_a^b l_i(x)dx = \sum_{i=1}^n A_i f(x_i).$$

where we have put $A_i = \int_a^b l_i(x)dx$. From the way in which the previous formula has been derived, we know that it will give correct values for the integral of every polynomial of degree $\leq n - 1$.

In the preceding discussion, the nodes have been arbitrary, although for practical reasons they should belong to the interval in which the integration is to be carried out. Gauss discovered that by a special placement of the nodes, the accuracy of the numerical integration process could be greatly increased. There exist tables in which the numerical values of the nodes and weights are listed for the formula

$$\int_{-1}^1 f(x) \approx \sum_{i=1}^n A_i f(x_i)$$

Those nodes x_1, x_2, \dots, x_n are called the Gaussian nodes with which the previous formula will be exact for all polynomials of degree $\leq 2n - 1$.

Here the table for $n = 10$ is given.

	$x_k^{(n)}$	$A_k^{(n)}$
n=10	$\pm 0.14887\ 43390$	0.29552 42247
	$\pm 0.43389\ 53941$	0.26926 67193
	$\pm 0.67940\ 95683$	0.21908 63625
	$\pm 0.86506\ 33667$	0.14945 13492
	$\pm 0.97390\ 65285$	0.06667 13443

Usually, the integral interval of function $f(x)$ is on $[a, b]$. In order to use the Gaussian quadrature formula, one should transfer interval $[a, b]$ to interval $[-1, 1]$ using a linear transformation, for example, for the twisted-pair case in section 6.1, the following linear transformation can be carried out:

$$\int_{2\pi i}^{2\pi(i+1)} f(\theta) d\theta = \pi \int_{-1}^1 f(\pi t + (2i+1)\pi) dt$$

where,

$$\theta = \pi t + (2i+1)\pi$$

$$\text{if } \theta = 2\pi i, \text{ then } t = -1$$

$$\text{if } \theta = 2\pi(i+1), \text{ then } t = 1$$

$$d\theta = \pi dt.$$

Now, one can use the Gaussian quadrature formula as follows:

$$\int_{2\pi i}^{2\pi(i+1)} f(\theta) d\theta = \pi \sum_{k=1}^n A_k^{(n)} f(\pi x_k^{(n)} + (2i+1)\pi)$$

For further details reference [12] should be consulted.

Appendix B

Modeling and Analysis of Near-Field Radiation from
Electromagnetic Sources on NASA Space Station
Freedom

CLARKSON UNIVERSITY

**Modeling and Analysis of Near-Field Radiation From
Electromagnetic Sources on NASA Space Station Freedom**

A Thesis

by

Brian J. Hurysz

Department of Electrical and Computer Engineering

Submitted in partial fulfillment of the requirements

for the degree of

Master of Science

Electrical Engineering

May 1991

Accepted by the Graduate School

Date

Dean

The undersigned have examined the thesis entitled

*Modeling and Analysis of Near-Field Radiation From Electromagnetic Sources on
NASA Space Station Freedom,*

presented by **Brian J. Hurysz**, a candidate for the degree of Master of Science,
and hereby certify that it is worthy of acceptance.

May 14, 1991

Date

Peter W. Barber

Peter W. Barber, Advisor

Nabeel A.O. Demerdash

Nabeel A.O. Demerdash, Examining Committee

Said Ahmed-Zaid

Said Ahmed-Zaid, Examining Committee

Hossein Salehfar

Hossein Salehfar, Examining Committee

Abstract

A method is developed for modeling and analyzing electric fields from radiating sources on a structure in the ionosphere. The ionosphere is approximated as a zero-order plasma (zero magnetic field) with all sources radiating below the characteristic plasma frequency, where electromagnetic waves are evanescent. The moment-method numerical technique is modified to incorporate a zero-order plasma and is shown to compare very well with analytical solutions for a dipole. Simulations are performed on a wire structure with a radiating source in unbounded free space and a zero-order plasma environment for comparison purposes. The conclusion is that the ionosphere serves to attenuate electromagnetic waves and thus reduces potential electromagnetic interference problems.

Acknowledgements

The author wishes to express his sincere gratitude to Professor Peter W. Barber whose guidance, encouragement, and time throughout this research have made this work possible. The support and patience of Professor Barber were very much appreciated, and will always be remembered for the positive effects they had and will have on the author's life.

The author also wishes to acknowledge Professor Nabeel A.O. Demerdash for his support throughout this work and for the professional guidance he bestowed.

In addition, the author wishes to extend gratitude to the other members of his examining committee, Professor Said Ahmed-Zaid and Professor Hossein Salehfar, for their concerns and support in this work.

The author recognizes the support received under NASA Lewis Research Center's Grant No. NAG3-1126 which made this research possible.

Contents

1	Introduction	1
1.1	Ionospheric Modeling	2
1.2	Electromagnetic Analysis	6
1.3	Overview of the Thesis	8
2	Theory	9
2.1	Radiating Sources – Analytical Solution	9
2.2	Radiating Sources – Moment Method	17
2.3	Ionosphere – Zero-Order Plasma	22
3	Results – Analytical Solution	27
3.1	Attenuation Factor	27
3.2	Computer Simulation	31

3.3	Zero-Order Plasma Compared to Free Space	32
3.4	Summary	34
4	Results – Numerical Solution	37
4.1	Input Impedance	38
4.2	Current Distribution	41
4.3	Comparison of Far-Field Results	42
4.4	Comparison of Near-Field Results	43
4.5	Electric Field Contour Plots for Space Station Structure	46
4.6	Summary	50
5	Conclusions and Further Research	52
5.1	Future Work	55
A	Evaluating Partial Derivatives and Simplifying	58

List of Tables

4.1	Input impedance of an isolated dipole, in ohms.	38
4.2	Input impedance of dipole 1 in the presence of dipole 2, in ohms. . .	39
4.3	Input impedance of $\lambda/2$ dipole, in ohms.	39

List of Figures

1.1	Atmospheric molecular density versus altitude [1].	2
1.2	Time of day variations of electron density versus altitude [2].	3
1.3	Simple examples of ionospheric impact on radiowave systems [3].	4
1.4	Observed and predicted sunspot numbers for several solar cycles [3].	4
1.5	Wire-grid model of F-16 aircraft [9].	7
2.1	An elemental dipole (a) and its equivalent (b) [14].	10
2.2	Electric field radiation of elemental dipole in a spherical coordinate system [14].	11
2.3	(a) E_θ and (b) E_r for an elemental dipole source on the z -axis [14].	16
2.4	(a) Cylindrical conductor model of elemental dipole. (b) Current filament model used to replace the cylindrical conductor [14].	19
2.5	Current filament Idz' with field $E_z(z)$ at a distance r	20

3.1	Ionospheric charge density as a function of altitude [5].	28
3.2	Plasma frequency versus electron density.	29
3.3	Attenuation versus frequency for specified electron densities	30
3.4	Comparison of electric field magnitude versus distance for free space and a zero-order plasma environment.	33
3.5	Comparison of electric field intensity for different frequencies, FS=free space, P=plasma.	35
3.6	The effect of varying the electron density on the electric field. . . .	36
4.1	Simple wire model of the space station with a short monopole an- tenna located at one end.	41
4.2	Current distribution along a 100 m wire divided into 34 pulse seg- ments with a monopole source on one end at 20 KHz, 100 KHz, 1 MHz, and 5 MHz.	42
4.3	Calculated far-field radiation pattern for $\lambda/2$ dipole antenna for an increasing number of segments using MININEC3 and analytical so- lution.	43
4.4	x -component of electric field calculated analytically and numerically for unbounded free space and zero-order plasma.	45
4.5	z -component of electric field calculated analytically and numerically for unbounded free space and zero-order plasma.	45

4.6	Wire model of NASA Space Station Freedom.	46
4.7	Electric field intensity in $dB\mu V/m$ from radiating source on space station model in a free space environment.	48
4.8	Electric field intensity in $dB\mu V/m$ from radiating source on space station model in a zero-order plasma environment.	49

Chapter 1

Introduction

The goal of this research work is to analyze the potential effects of electromagnetic interference (EMI) originating from power system processing and transmission components for NASA Space Station Freedom. Particular emphasis is given to EMI sources radiating in a plasma environment, i.e., the ionosphere. The approach consists of three sequential steps:

1. Determine the characteristics of the ionospheric plasma and formulate a working model for purposes of EMI analysis.
2. Develop analytical tools (models and computer programs) to predict the electromagnetic fields from isolated sources radiating in unbounded free space or a plasma environment.
3. Develop numerical tools (moment-method formulation) to predict the electromagnetic fields from radiating sources on a simple space station structure in free space or a plasma environment.

1.1 Ionospheric Modeling

There is considerable information on the properties of the ionosphere and the different natural phenomena that affect its electromagnetic characteristics. To start with, the ionosphere is a region of the earth's atmosphere composed of molecules that are ionized by solar radiation. Figure 1.1 shows the molecular content of

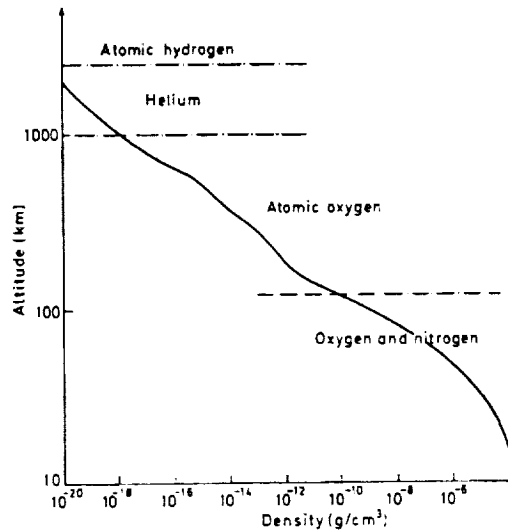


Figure 1.1: Atmospheric molecular density versus altitude [1].

the atmosphere as a function of altitude. Due to gravity, the heaviest molecules (N_2, O_2) are at the lowest altitude and the lighter molecules (He, H) are at higher altitudes. In the middle region, where the space station will be located, atomic oxygen (O) is the most prevalent.

The degree of ionization of these molecules depends on many different factors. The two strongest contributors are time of day and altitude. During the nighttime, solar radiation does not reach the ionosphere and ions recombine resulting in the electron density, N , decreasing. Figure 1.2 shows this effect and also the altitude

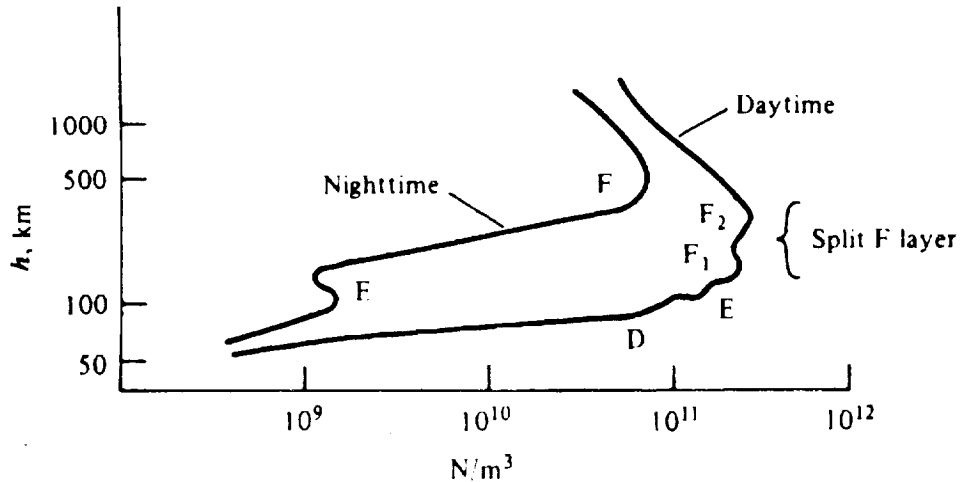


Figure 1.2: Time of day variations of electron density versus altitude [2].

variation. The envelope can be qualitatively explained in simple terms. At higher altitudes the solar radiation is very intense but there are few molecules. As the altitude decreases, the molecular concentration increases and more solar radiation is absorbed. Eventually, a point is reached where the high molecular concentration absorbs most of the remaining solar energy and the ionization reaches a maximum. Continuing to lower altitudes the electron density decreases. Since the atmosphere is composed of many different gases with different ionization and recombination characteristics, different layers and peaks in the electron density form [2]. These have been labeled the D, E, and F layers. An important consequence of the layering is that radio waves in certain frequency ranges can be bounced off of the ionosphere to improve communication distances. Figure 1.3 shows how some of the properties of the ionosphere are exploited in today's world for useful means.

Another important contributor to the electron density is sunspot activity. Figure 1.4 shows sunspot activity observed for the past few cycles, and the predicted activity using the Lincoln-McNish method [3]. Increased sunspot activity increases solar radiation which leads to increased ionization of the atmosphere. This of-

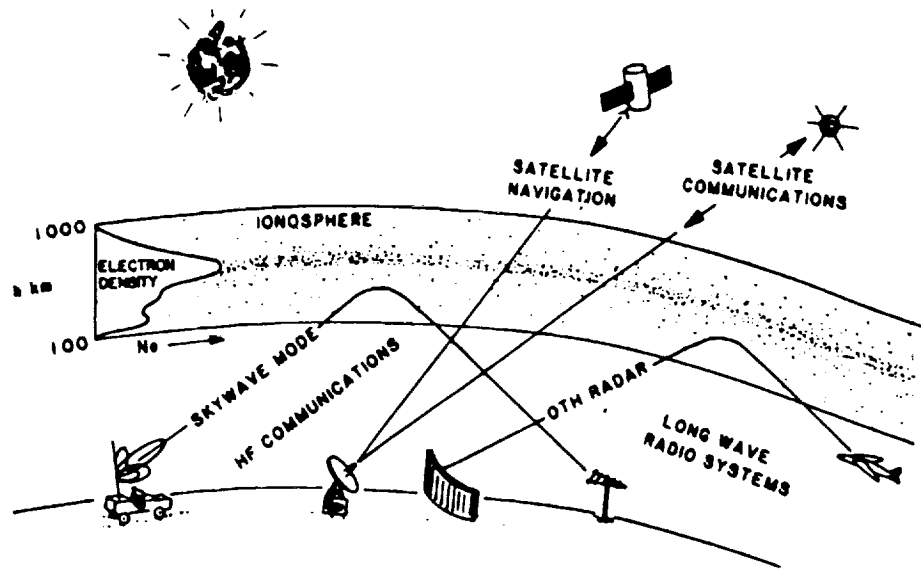


Figure 1.3: Simple examples of ionospheric impact on radiowave systems [3].

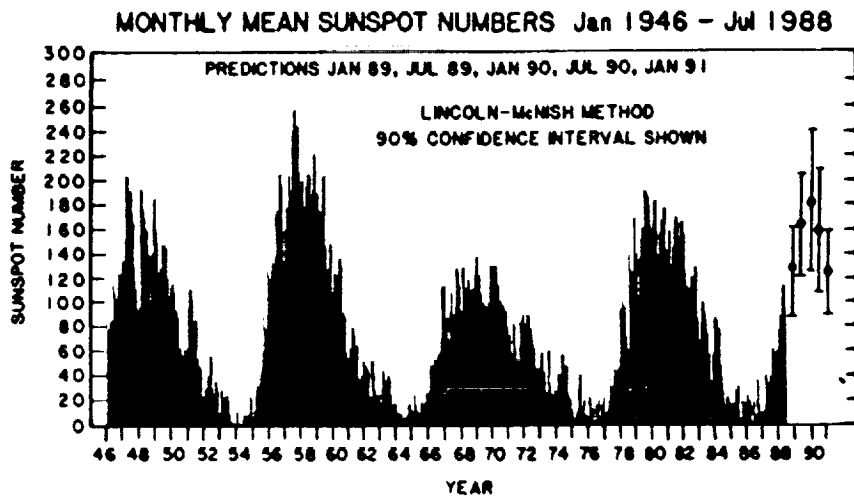


Figure 1.4: Observed and predicted sunspot numbers for several solar cycles [3].

ten disrupts the normal communication schemes in positive and negative ways. On one hand, the layers become more pronounced which increases reception and transmission distances in radio communications. On the other hand, satellite communications can deteriorate if the frequencies are not high enough.

At the space-station altitude range of 450 to 550 km, the ionosphere is considered fully ionized. It is a neutral region of mobile positive ions (predominantly O^+) and electrons (e^-) that form a plasma. Plasmas are considered the fourth and most energetic state of matter. They are also the most abundant state in the universe [1], and occur in everyday life in fluorescent lighting, vacuum tubes, video display terminals, and lasers.

A unique feature of the ionospheric plasma is the presence of the earth's magnetic field. This makes the ionosphere an anisotropic plasma, where the polarization of the medium, \mathbf{P} , and the electric field, \mathbf{E} , are not in the same direction [4]. The Lorentz formula, $\mathbf{F} = q(\mathbf{E} + \mathbf{v} \times \mathbf{B})$, states that a free electron traveling with a velocity, \mathbf{v} , perpendicular to a constant magnetic field, \mathbf{B} , will travel in a circular orbit. This leads to an angular (cyclotron) frequency for an electron in the earth's magnetic field of $5 \times 10^{-5} \text{ Wb/m}$ equal to 1.4 MHz . A consequence of this is that radiowaves close to 1.4 MHz are highly attenuated [2]. Also, the current density, \mathbf{J} , and the electric field, \mathbf{E} , are related by a tensor (matrix) quantity. It will become evident from the formulations in the next chapter that a tensor permittivity instead of a scalar value severely complicates the analysis of wave propagation in a plasma medium.

In order to solve EMI type problems, the ionospheric plasma is usually discussed in simpler terms. The zero-order plasma model is used, where the effects of the magnetic field of the earth are neglected. The theoretical formulation of

electromagnetic wave propagation is then based on a scalar permittivity. With this approximation, electromagnetic wave propagation in a plasma becomes similar to wave propagation in a waveguide. The zero-order plasma model also assumes a homogeneous plasma. Although the ionosphere is locally homogeneous, motion of the space station through the plasma creates ram/wake effects [5, 6] similar to that of an aircraft passing through air. Thus the ion and electron densities are increased in front of the space station and decreased behind the space station.

1.2 Electromagnetic Analysis

Computer analysis of EMI is a widely-used technique and sophisticated computer programs are available to simulate the EMI for complex systems involving hundreds of sources and susceptors [7]. Built into these programs are different types of models for sources and susceptors and transfer functions for various forms of coupling. To use the programs for analysis, a system must first be described in terms of sources and susceptors and their geometrical arrangement. This is then entered as parametric data into computerized data sheets. This procedure simplifies EMI analysis on major aircraft and weapons systems, where the programs have been developed and proven effective. However, the complex procedure is not appropriate for modeling electromagnetic radiation in the ionospheric plasma. For this reason, attention turned to finding a general numerical code that could be easily worked with, understood, and modified to predict EMI in a plasma environment.

The moment method is a numerical technique for solving electromagnetic field problems. It was first unified into a general procedure by Roger F. Harrington in 1968 [8]. Since then it has been utilized on powerful computers to solve complex

electromagnetic radiation and scattering problems. The moment method utilizes a few assumptions that increases its ability to handle a problem as large as the space station. The primary assumption is that all current flows in thin wires and is axially directed. Both radiating sources and the space station structure are then modeled with wires, like the airplane in Figure 1.5. The result is that the radiated

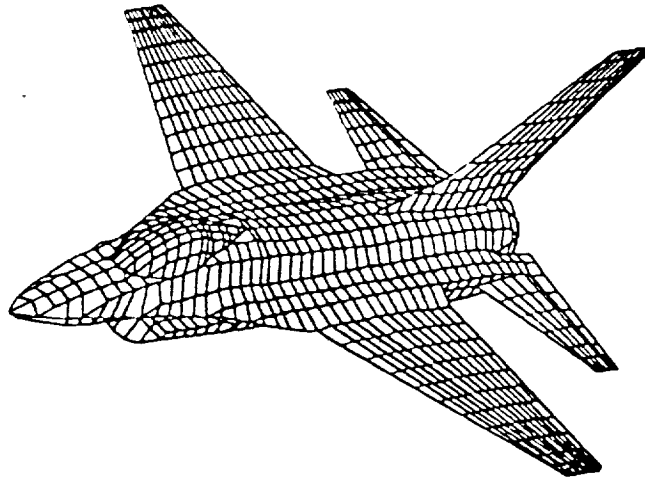


Figure 1.5: Wire-grid model of F-16 aircraft [9].

electromagnetic fields can be calculated anywhere in space relative to the structure. This shows what effect variations in the amplitude and location of sources on the space-station structure have on potential EMI problems. It should be pointed out that a parallel effort is under way to use the finite-element method for specific source modeling [10, 11] that will lead to the development of equivalent sources that can be input into the moment-method analysis. But, at this time, tools are being developed that are more general in their source modeling to allow for flexibility in design parameters.

MININEC3 was the selected moment-method code [12] to be modified for two reasons. The first is that it is proven and well documented. It runs on a personal

computer, but it is limited by the size of the problem it can handle and by the speed at which it runs. This makes it ideal for the analysis of simple models, but not practical for more complicated and defined structures. The second reason is that MININEC3 is a scaled-down version of NEC, numerical electromagnetic code [13], which is one of the most advanced computer codes available. If MININEC3 can be modified for a plasma environment to accurately predict EMI for small problems, then the same methodology may be applied to NEC (or other moment-method codes) to handle more complicated problems.

1.3 Overview of the Thesis

Many steps are required before the electric fields in the ionospheric plasma medium can be predicted. Chapter 2 starts the work with theoretical formulations. First, the analytical solution for a radiating source is derived. Then the moment-method numerical technique is explained. Lastly, the zero-order plasma model is discussed. In chapter 3 analytical results are compared for the radiating source in free-space and a zero-order plasma. Chapter 4 starts with verification of the moment-method code in free space and zero-order plasma. Then the simple space station structure is explained and electric fields in free space and a zero-order plasma are presented and compared. Chapter 5 contains the conclusions which were based on the research and gives some suggestions for further work in this area.

Chapter 2

Theory

This chapter has three goals. The first is to derive the analytical solution for the electric fields from a radiating elemental dipole. The elemental dipole was chosen because its analytical solution is well understood and the theory behind the moment method is closely related to that of the elemental dipole. The second goal is to formulate and explain the moment method. The moment method is a numerical approximation for determining electromagnetic fields from complex thin-wire geometries. The final goal is to explain the zero-order plasma approximation. This includes a consideration of electromagnetic wave propagation and incorporation of the plasma into the moment method.

2.1 Radiating Sources – Analytical Solution

The formulation for determining the electric fields generated from an elemental (short) dipole are documented in many textbooks [4, 14, 15]. The following for-

mulation serves two important purposes. First, the analytical solution is used to formulate the moment method. Second, a closed-form solution is developed for the dipole radiating in a zero-order plasma. Since the elemental dipole is the fundamental building block of this research, a brief description of it precedes the formulation of its fields.

An elemental dipole is a short linear conductor. By definition, its length, L , is much less than the wavelength, λ ($L \ll \lambda$), and the radius, a ($d = 2a$), is small compared to the length ($a \ll L$). The current, I , can then be assumed constant over its length. Figure 2.1(a) shows an elemental dipole and Figure 2.1(b) represents its equivalent. The transmission lines are balanced and shielded to provided the

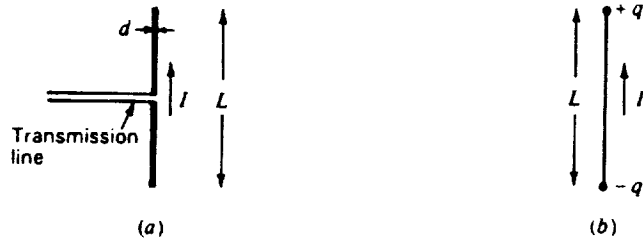


Figure 2.1: An elemental dipole (a) and its equivalent (b) [14].

uniform current and no radiation. They are therefore, excluded in the equivalent model. The elemental dipole can then be described as a thin linear conductor with a constant current. The electric field components E_r , E_θ , and E_ϕ , at an observation point, P , from a dipole coincident with the z -axis and at the origin, are defined in a spherical coordinate system as shown in Figure 2.2.

The formulation for the electric field components begins with Maxwell's equations relating the electric field intensity, \mathbf{E} , to the magnetic field intensity, \mathbf{H} ,

$$\nabla \times \mathbf{E} = -j\omega\mu\mathbf{H}, \quad (2.1)$$

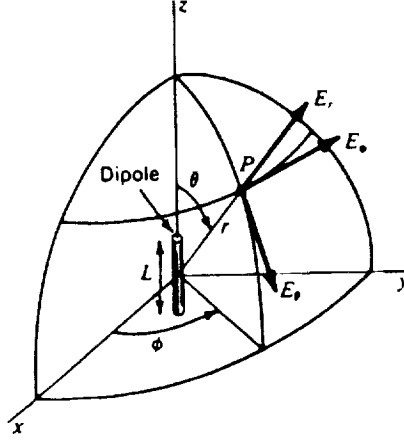


Figure 2.2: Electric field radiation of elemental dipole in a spherical coordinate system [14].

$$\nabla \times \mathbf{H} = j\omega\epsilon\mathbf{E} + \mathbf{J}, \quad (2.2)$$

where \mathbf{J} is the source current density, ω is the angular frequency, μ is the permeability of the medium, and ϵ is the permittivity of the medium. Using the identity $\nabla \cdot \nabla \times (\cdot) = 0$ on (2.1),

$$\nabla \cdot \nabla \times \mathbf{E} = -j\omega\mu(\nabla \cdot \mathbf{H}) = 0. \quad (2.3)$$

Since a vector with zero divergence can be expressed as the curl of some other vector, \mathbf{H} can be written as the curl of \mathbf{A} ,

$$\mathbf{H} = \nabla \times \mathbf{A}, \quad (2.4)$$

where \mathbf{A} is defined as the magnetic vector potential, MVP. Substituting (2.4) into (2.1) gives

$$\nabla \times \mathbf{E} = -j\omega\mu\nabla \times \mathbf{A}, \quad (2.5)$$

$$\nabla \times \mathbf{E} + \nabla \times j\omega\mu\mathbf{A} = \nabla \times (\mathbf{E} + j\omega\mu\mathbf{A}) = 0. \quad (2.6)$$

Since any curl-free vector is the gradient of some scalar,

$$\mathbf{E} + j\omega\mu\mathbf{A} = -\nabla V, \quad (2.7)$$

where V is the electric scalar potential. Substituting (2.4) and (2.7) into (2.2) yields

$$\nabla \times \nabla \times \mathbf{A} = -j\omega\epsilon\nabla V + k^2\mathbf{A} + \mathbf{J}, \quad (2.8)$$

where k is the wave number, $\omega\sqrt{\mu\epsilon}$. Using the vector identity $\nabla \times \nabla \times \mathbf{A} = \nabla(\nabla \cdot \mathbf{A}) - \nabla^2\mathbf{A}$, (2.8) reduces to

$$\nabla(\nabla \cdot \mathbf{A}) - \nabla^2\mathbf{A} - k^2\mathbf{A} = -j\omega\epsilon\nabla V + \mathbf{J}. \quad (2.9)$$

Since only the curl of the MVP has been specified, its divergence can be chosen to simplify (2.9). Common choices are the Coulomb Gauge and the Lorentz Gauge. In this case the Lorentz Gauge

$$\nabla \cdot \mathbf{A} = -j\omega\epsilon V \quad (2.10)$$

is used to eliminate the electric potential term. Substituting this into (2.9) reduces the formulation to

$$\nabla^2\mathbf{A} + k^2\mathbf{A} = -\mathbf{J}, \quad (2.11)$$

which is the Helmholtz equation or the complex wave equation. It relates the MVP to the source current density. Substituting (2.10) into (2.7) relates the electric field to the MVP. The result is

$$\mathbf{E} = -j\omega\mu\mathbf{A} + \frac{1}{j\omega\epsilon}\nabla(\nabla \cdot \mathbf{A}). \quad (2.12)$$

The electric field resulting from a source current density can be determined by simultaneously solving (2.11) and (2.12). But this can be simplified further for an elemental dipole, by solving for the MVP and combining the two equations. As

previously stated, the elemental dipole is centered at the origin, and is coincident with the z -axis as shown in Figure 2.2. Since the current on the wire is in the z direction, the source current density and MVP are also in the z direction. At points away from the origin (not on the wire), $\mathbf{J} = 0$ and (2.11) reduces to

$$\nabla^2 A_z + k^2 A_z = 0, \quad (2.13)$$

where A_z denotes the (scalar) MVP in the z direction. For observation points sufficiently far enough away from the dipole, the source looks like a point. The resulting A_z from a point source, $I dz'$, is spherically symmetric (a function of the radius only), $A_z = A_z(r)$. Evaluating the Laplacian of the MVP with the radial dependence only and substituting into (2.13) gives

$$\frac{1}{r^2} \frac{\partial}{\partial r} \left(r^2 \frac{\partial A_z}{\partial r} \right) + k^2 A_z = 0 \quad (2.14)$$

in spherical coordinates, where r is the distance between the source and observation points. The two solutions for the MVP from (2.14) with $r \neq 0$ (not at the origin) are

$$A_z = \frac{C_1}{r} e^{-jkr} \quad (2.15)$$

and

$$A_z = \frac{C_2}{r} e^{jkr}. \quad (2.16)$$

Since (2.15) represents an outward traveling wave and (2.16) represents an inward traveling wave, (2.15) is the appropriate solution for the radiating dipole. In order to find the constant C_1 , let $\omega \rightarrow 0$. Then (2.15) becomes

$$A_z = \frac{C_1}{r} \quad (2.17)$$

and Helmholtz's equation (2.11) becomes

$$\nabla^2 A_z = -J_z. \quad (2.18)$$

Helmholtz's equation for the case $\omega = 0$ is solved by noting its resemblance to Poisson's equation,

$$\nabla^2 V = -\frac{\rho_v}{\epsilon}, \quad (2.19)$$

where ρ_v is the charge density. The solution of (2.19) is known to be

$$V(\mathbf{r}) = \int_{vol} \frac{\rho_v(\mathbf{r}') dv'}{4\pi\epsilon r}, \quad (2.20)$$

where \mathbf{r}' , the source point, is the location of ρ_v and \mathbf{r} , the field point, is where V is observed. The volume of the source region is vol , and $r = |\mathbf{r} - \mathbf{r}'|$ is the distance between the source and field points. Noting the mathematical analogy between (2.18) and (2.19), A_z is determined to be

$$A_z(\mathbf{r}) = \int_{vol} \frac{J_z(\mathbf{r}') dv'}{4\pi r}. \quad (2.21)$$

Since the volume of the dipole can be written in terms of its cross sectional area times its length, L , and the cross sectional area times the source current density, J_z , equals the source current, I , (2.21) becomes

$$A_z = \int_L \frac{I dz'}{4\pi r}. \quad (2.22)$$

Equating (2.22) and (2.17), results in

$$C_1 = \int_L \frac{I dz'}{4\pi}. \quad (2.23)$$

Substituting back into (2.15) leads to the solution

$$A_z = \int_L \frac{I dz'}{4\pi r} e^{-jkr}. \quad (2.24)$$

Performing the integration for the elemental dipole,

$$A_z = \frac{IL}{4\pi r} e^{-jkr}. \quad (2.25)$$

This shows that the MVP can be determined at a specified distance from an elemental dipole current source. If the magnetic field intensity were desired, it would

be determined by taking the del cross product (or curl) of the MVP, (2.4). This is the point from which the moment-method formulation will be started in the next section.

Since it is common for the analytical solution of \mathbf{E} from an elemental dipole to be expressed in spherical coordinates, the MVP in the z direction is transformed into spherical coordinates using

$$A_r = \hat{z}A_z \cdot \hat{r} = \hat{z}A_z \cdot \hat{z} \cos \theta = A_z \cos \theta \quad (2.26)$$

and

$$A_\theta = \hat{z}A_z \cdot \hat{\theta} = \hat{z}A_z \cdot \hat{z} (-\sin \theta) = -A_z \sin \theta, \quad (2.27)$$

where A_r is the radial component of the MVP, and A_θ is the theta component of the MVP. The electric field expressed by (2.12) is now

$$\mathbf{E} = -j\omega\mu (\hat{r}A_r + \hat{\theta}A_\theta) + \frac{1}{j\omega\epsilon} \nabla (\nabla \cdot (\hat{r}A_r + \hat{\theta}A_\theta)). \quad (2.28)$$

Evaluating $\nabla (\nabla \cdot \mathbf{A})$ in (2.28) and reducing \mathbf{E} to the radial, E_r , and theta, E_θ , components yields

$$E_r = -j\omega\mu A_r + \frac{1}{j\omega\epsilon} \frac{\partial}{\partial r} \left(\frac{1}{r^2} \frac{\partial}{\partial r} r^2 A_r + \frac{1}{r \sin \theta} \frac{\partial}{\partial \theta} A_\theta \sin \theta \right) \quad (2.29)$$

and

$$E_\theta = -j\omega\mu A_\theta + \frac{1}{j\omega\epsilon r} \frac{\partial}{\partial \theta} \left(\frac{1}{r^2} \frac{\partial}{\partial r} r^2 A_r + \frac{1}{r \sin \theta} \frac{\partial}{\partial \theta} A_\theta \sin \theta \right). \quad (2.30)$$

The phi component, E_ϕ , shown in Figure 2.2 is not present. Substituting (2.26) and (2.27) into (2.29) and (2.30), and simplifying the expressions yields

$$E_r = -j\omega\mu A_z \cos \theta + \frac{\cos \theta}{j\omega\epsilon} \frac{\partial}{\partial r} \left(\frac{1}{r^2} \frac{\partial}{\partial r} (r^2 A_z) \right) - \frac{2 \cos \theta}{j\omega\epsilon} \frac{\partial}{\partial r} \left(\frac{A_z}{r} \right) \quad (2.31)$$

and

$$E_\theta = j\omega\mu A_z \sin \theta - \frac{\sin \theta}{j\omega\epsilon r^3} \frac{\partial}{\partial r} (r^2 A_z) + \frac{2A_z \sin \theta}{j\omega\epsilon r^2}. \quad (2.32)$$

Substituting (2.25) into (2.31) and (2.32) and simplifying the expressions results in the final analytical solutions for the electric field intensities,

$$E_r = \frac{IL}{2\pi} e^{-jkr} \left(\frac{1}{r^2} \sqrt{\frac{\mu}{\epsilon}} + \frac{1}{j\omega\epsilon r^3} \right) \cos \theta \quad (2.33)$$

and

$$E_\theta = \frac{IL}{4\pi} e^{-jkr} \left(\frac{j\omega\mu}{r} + \frac{1}{r^2} \sqrt{\frac{\mu}{\epsilon}} + \frac{1}{j\omega\epsilon r^3} \right) \sin \theta. \quad (2.34)$$

Figure 2.3(a) shows E_θ and Figure 2.3(b) shows E_r . In three dimensions, E_θ has

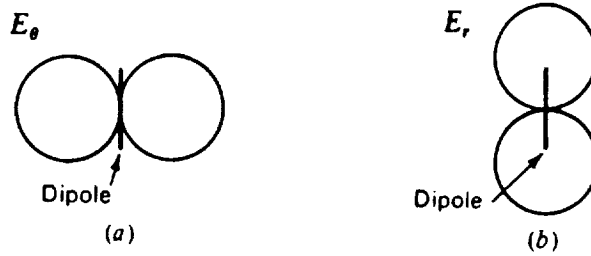


Figure 2.3: (a) E_θ and (b) E_r for an elemental dipole source on the z -axis [14].

a characteristic donut shape around the dipole and E_r appears as equally sized spheres on the top and bottom of the dipole.

Equations (2.33) and (2.34) are often referred to as the near-field patterns for radiation from an elemental dipole. This is because, near the dipole E_r and E_θ are similar in magnitude. But far away from the dipole $E_\theta \gg E_r$, so that E_r can be neglected. How far away is determined by examining the $1/r$, $1/r^2$, and $1/r^3$ terms in (2.33) and (2.34). The three terms are equal at $r = \lambda/2\pi$ in free space, where λ is the wavelength. For $r \gg \lambda/2\pi$, the $1/r$ term is dominant and the electric field reduces to

$$E_\theta = \frac{IL}{4\pi} e^{-jkr} \frac{j\omega\mu}{r} \sin \theta. \quad (2.35)$$

If a frequency of 1 *MHz* ($\lambda \simeq 300 \text{ m}$) is used as an example, the far field approximation could be used if $r \gg 50 \text{ m}$. Since the maximum dimension of the space station is about 100 *m*, the far field approximation cannot be used at this frequency. The attention now turns to formulating the moment method.

2.2 Radiating Sources – Moment Method

The moment method is a numerical tool for predicting fields from thin-wire structures for which there are no analytical solutions. It is a numerical method capable of connecting a large number of small wire segments and determining field patterns by enforcing electromagnetic boundary conditions on and between the segments. Since it is based on current segments and the elemental dipole approximates a current segment, the analytical solution developed in the previous section for the elemental dipole is utilized. This explanation of the moment method is similar to that in Kraus [14].

In the previous section, the MVP was related to the electric field \mathbf{E} in (2.12). For an elemental dipole along the z -axis, it was shown that the MVP is in the z direction only. Substituting A_z into (2.12) and evaluating $\nabla(\nabla \cdot \hat{z}A_z)$ yields

$$E_z = \frac{1}{j\omega\epsilon} \left(\frac{\partial^2 A_z}{\partial z^2} \right) - j\omega\mu A_z, \quad (2.36)$$

which reduces to

$$E_z = \frac{1}{j\omega\epsilon} \left(\frac{\partial^2 A_z}{\partial z^2} + k^2 A_z \right). \quad (2.37)$$

From the solution of the Helmholtz equation, the MVP was related to a current pulse segment in (2.24). Substituting the value for A_z into (2.37) yields Pockling-

ton's equation [14],

$$E_z(\mathbf{r}) = \frac{1}{4\pi j\omega\epsilon} \int_l \left(\frac{\partial^2}{\partial z^2} \left(\frac{e^{-jkr}}{r} \right) + \frac{k^2}{r} e^{-jkr} \right) I(z') dz', \quad (2.38)$$

where $E_z(\mathbf{r})$ is the radiated electric field at an observation point \mathbf{r} from a current source at z' and r is the distance between the two points, $r = |\mathbf{r} - \mathbf{r}'|$.

In the moment method, the solution in (2.38) is used twice. Obviously, the formulation may be used to calculate the radiated electric fields from current sources. But this is not chronologically the first time that it is used in the moment-method solution. First, (2.38) is used to obtain the current in the wire from the voltage applied across the dipole terminals. Then the radiated fields can be calculated. To explain this, a closer look at the dipole source is needed.

The dipole source is physically a cylindrical current-carrying perfect conductor as shown in Figure 2.4(a). Assuming that the conductivity of the wire is high, the current is located entirely on the surface of the cylinder. For the dipole centered at the z -axis, all of the current is then at a wire radius a from the z -axis. This is shown in Figure 2.4(a). Since all of the current is equidistant from the center of the cylinder (z -axis), the current density will be considered to flow in a thin filament a distance a from and parallel to the z -axis. This is shown in Figure 2.4(b).

In any electromagnetic radiation or scattering problem involving a conductor, there are two components of electric field, \mathbf{E}_{app} , which creates the current on the conductor, and \mathbf{E}_{rad} , which is the electric field radiated by the current carrying conductor. In the case of the elemental dipole antenna, \mathbf{E}_{app} results from a voltage applied across the antenna terminals (see Figure 2.1(a)). The total electric field

$$\mathbf{E}_{\text{app}} + \mathbf{E}_{\text{rad}} = \mathbf{E}_{\text{obs}}, \quad (2.39)$$

where \mathbf{E}_{obs} is the total observed electric field intensity. Since the skin depth is zero

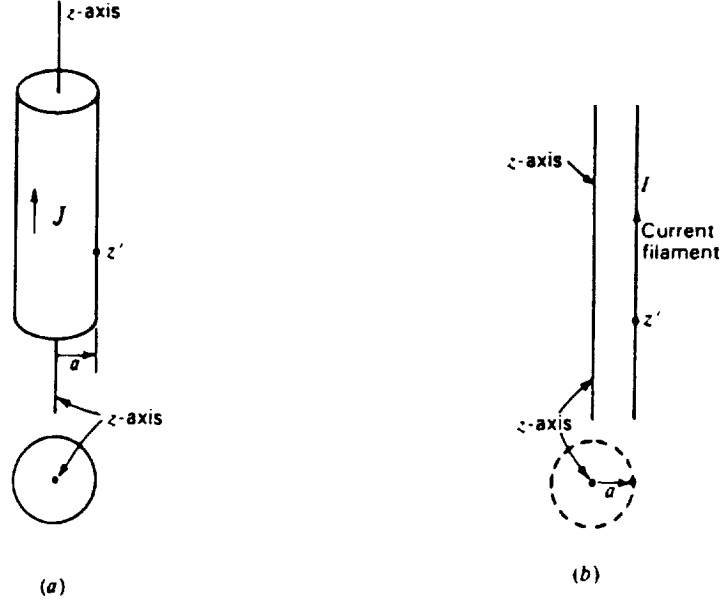


Figure 2.4: (a) Cylindrical conductor model of elemental dipole. (b) Current filament model used to replace the cylindrical conductor [14].

for a perfect conductor, the observed internal electric field, \mathbf{E}_{obs} , is zero and

$$\mathbf{E}_{\text{rad}} = -\mathbf{E}_{\text{app}}. \quad (2.40)$$

For the special case of the radiated electric field within the elemental dipole, (2.38) becomes

$$-E_{\text{app}}(z) = \frac{1}{4\pi j\omega\epsilon} \int_l \left(\frac{\partial^2}{\partial z^2} \left(\frac{e^{-jkr}}{r} \right) + \frac{k^2}{r} e^{-jkr} \right) I(z') dz', \quad (2.41)$$

where $r = [(z - z')^2 + a^2]^{1/2}$ as shown in Figure 2.5. Since \mathbf{E}_{app} is known, (2.41) is an integral equation which can be solved for $I(z')$. Then $I(z')$ can be substituted into (2.38) to obtain the electric field everywhere.

The electric field formulation is made more concise by substituting the Green's function notation,

$$G_{zz'} = \frac{e^{-jkr}}{r}, \quad (2.42)$$

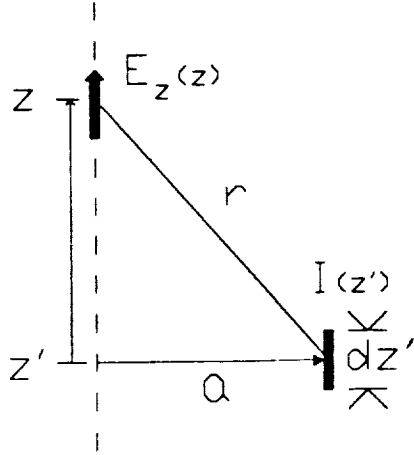


Figure 2.5: Current filament Idz' with field $E_z(z)$ at a distance r .

into (2.41). The result is

$$-E_{app}(z) = \frac{1}{4\pi j\omega\epsilon} \int_l \left(\frac{\partial^2}{\partial z^2} G_{zz'} + k^2 G_{zz'} \right) I(z') dz'. \quad (2.43)$$

It is shown in the Appendix that evaluation of the partial derivatives in (2.43) gives

$$-E_{app}(z) = \frac{1}{4\pi j\omega\epsilon} \int_l \frac{e^{-jkr}}{r^3} \left((1 + jkr) \left(2 - 3 \left(\frac{a}{r} \right)^2 \right) + k^2 a^2 \right) I(z') dz'. \quad (2.44)$$

Substituting $\omega = \frac{k}{\sqrt{\mu\epsilon}}$ and the intrinsic impedance of the medium $\eta = \sqrt{\frac{\mu}{\epsilon}}$, yields

$$-E_{app}(z) = \frac{-j\eta}{4\pi k} \int_l \frac{e^{-jkr}}{r^3} \left((1 + jkr) \left(2 - 3 \left(\frac{a}{r} \right)^2 \right) + k^2 a^2 \right) I(z') dz'. \quad (2.45)$$

The relationships in (2.38) and (2.45) form the theory behind the moment method. They are the relationships between applied electric fields, radiated electric fields, and current sources. They have come directly from Maxwell's equations with no assumptions about the medium that the radiation is traveling in. They are therefore, valid for free space or a plasma, using the proper permittivity and permeability. The remaining part of this section incorporates the methodology behind the evaluation of (2.45).

The first transformation is to let observation points be denoted by subscript m and source points by subscript n . This will be done gradually over several steps starting with (2.45). It can be written as

$$-E_{app}(z) = \int_l I(z') G(r_{mn}) dz', \quad (2.46)$$

where

$$G(r_{mn}) = \frac{-j\eta e^{-jkr}}{4\pi k r^3} \left((1 + jkr) \left(2 - 3 \left(\frac{a}{r} \right)^2 \right) + k^2 a^2 \right), \quad (2.47)$$

and r_{mn} is substituted for r , where r_{mn} is the distance between source point n and field (observation) point m . The function, $G(r_{mn})$, consists of terms forming a geometry matrix of source and observation points that are used in the moment method. In any problem there are two of these matrices formed. One for the applied field to calculate currents in filaments, and another to calculate radiated electric fields from the currents. Although $G(r_{mn})$ may seem like a complicated term, in the moment-method formulation it is often simple compared to the current term. The environmental parameters are also contained in $G(r_{mn})$, but they do not vary from source to observation point.

The current term in (2.46) can be approximated by the current series

$$I(z') = \sum_{n=1}^N I_n F_n(z'), \quad (2.48)$$

where I_n is a constant magnitude and $F_n(z')$ is a pulse function (equal to zero or unity) for incremental segments $\Delta z'_n$. In other words, the current is constant over a segment n in the same manner as with the elemental dipole. There are more complicated current series using overlapping segments with piecewise sinusoidal or triangular current distributions [14], but in MININEC3 the current pulse is used.

The contribution from each current pulse segment n can then be summed to obtain the electric field at m . Incorporating this into (2.46) for the m^{th} segment

results in

$$-E_{app}(z_m) = \sum_{n=1}^N \int_{\Delta z'_n} I_n F_n(z') G(r_{mn}) dz', \quad (2.49)$$

where the integral and the summation have been interchanged and $\Delta z'_n$ is the length of the n^{th} segment. The current portion can be pulled outside of the integral because its magnitude does not vary over a given segment. The result is

$$-E_{app}(z_m) = \sum_{n=1}^N I_n \int_{\Delta z'_n} G(r_{mn}) dz'. \quad (2.50)$$

Letting

$$G_{mn} = \int_{\Delta z'_n} G(r_{mn}) dz', \quad (2.51)$$

and assuming $G(r_{mn})$ is constant over the small interval $\Delta z'_n$, (2.51) becomes

$$G_{mn} = G(r_{mn}) \Delta z'_n. \quad (2.52)$$

(2.50) can now be reduced to a matrix form.

$$-[E_m] = [G_{mn}] [I_n], \quad (2.53)$$

where $[E_m]$ is the matrix of electric fields from the matrix of current segments, $[I_n]$. Multiplying both sides by the segment length Δz ,

$$-[V_m] = [Z_{mn}] [I_n], \quad (2.54)$$

where V_m is the applied voltage at the m^{th} segment, and Z_{mn} is the impedance matrix. This equation can be solved for the vector of current amplitudes $[I_n]$. These can then be substituted into (2.38) to obtain the radiated electric field anywhere.

2.3 Ionosphere – Zero-Order Plasma

The ionosphere is approximated by neglecting the earth's magnetic field. This is the zero-order plasma approximation. In this section, electromagnetic waves

radiating from an elemental dipole in a plasma will be shown to behave like an electromagnetic wave propagating in a waveguide. The formulation parallels the explanation given by Collin [2]. At the end, the zero-order plasma model is incorporated into the moment-method formulation.

It seems appropriate to start the formulation for the zero-order plasma in simple terms. Considering a moving electron point charge in the presence of an electric field, \mathbf{E} , the force on the particle is given as

$$m_e \frac{d\mathbf{v}}{dt} = -e\mathbf{E}, \quad (2.55)$$

where m_e is the mass of the electron, \mathbf{v} its velocity, and $-e$ its charge. For the sinusoidal case, (2.55) becomes

$$j\omega m_e \mathbf{v} = -e\mathbf{E}. \quad (2.56)$$

Since the current density, \mathbf{J} , equals $eN\mathbf{v}$, substituting this into (2.56) yields

$$\mathbf{J} = -eN\mathbf{v} = \frac{Ne^2}{j\omega m_e} \mathbf{E}. \quad (2.57)$$

This current density can then be substituted into Maxwell's equation (2.1),

$$\nabla \times \mathbf{H} = j\omega\epsilon_o \mathbf{E} + \mathbf{J} = j\omega\epsilon_o \left(1 - \frac{Ne^2}{\omega m_e}\right) \mathbf{E}, \quad (2.58)$$

where ϵ_o is the permittivity of free space, 8.854×10^{-12} (F/m). The equivalent permittivity of the zero-order plasma is then

$$\epsilon = \epsilon_o \left(1 - \frac{Ne^2}{\omega m_e}\right), \quad (2.59)$$

which is the scalar quantity times ϵ_o mentioned in chapter 1.

Plasma models can be discussed in more useful terms using their characteristic plasma frequency. It is defined as

$$\omega_p = \sqrt{\frac{Ne^2}{m_e \epsilon_o}}. \quad (2.60)$$

Writing ϵ in terms of ω_p yields

$$\epsilon = \epsilon_o \left(1 - \left(\frac{\omega_p}{\omega} \right)^2 \right). \quad (2.61)$$

Since the wave number, k , is defined as $\omega\sqrt{\epsilon\mu}$, k becomes

$$k = \omega\sqrt{\epsilon_o\mu_o} \sqrt{1 - \left(\frac{\omega_p}{\omega} \right)^2}. \quad (2.62)$$

The permeability of free space, μ_o , is introduced since the plasma is not a magnetic material. Writing k in terms of wavelength, λ ,

$$k = \frac{2\pi}{\lambda} \sqrt{1 - \left(\frac{\omega_p}{\omega} \right)^2}. \quad (2.63)$$

In section 2.1, the analytical solutions for the electric field components from the elemental dipole were shown to be

$$E_r = \frac{IL}{2\pi} e^{-jkr} \left(\frac{1}{r^2} \sqrt{\frac{\mu}{\epsilon}} + \frac{1}{j\omega\epsilon r^3} \right) \cos \theta, \quad (2.64)$$

and

$$E_\theta = \frac{IL}{4\pi} e^{-jkr} \left(\frac{j\omega\mu}{r} + \frac{1}{r^2} \sqrt{\frac{\mu}{\epsilon}} + \frac{1}{j\omega\epsilon r^3} \right) \sin \theta, \quad (2.65)$$

in (2.33) and (2.34). Substituting the expression for k from (2.63) into the exponential term yields

$$e^{-jkr} = e^{-jr \frac{2\pi}{\lambda} \sqrt{1 - \left(\frac{\omega_p}{\omega} \right)^2}}. \quad (2.66)$$

In the zero-order plasma approximation, k is either a real or an imaginary term depending on the frequency ratio. Then for $k = \beta - j\alpha$, where α equals the attenuation constant and β equals the propagation constant, either $\beta = 0$ or $\alpha = 0$. Therefore, for $\omega > \omega_p$, the wave propagates, and for $\omega < \omega_p$, the wave does not propagate, but decays exponentially as an evanescent wave,

$$e^{-\alpha r}, \quad (2.67)$$

where

$$\alpha = \frac{2\pi}{\lambda} \sqrt{\left(\frac{\omega_p}{\omega}\right)^2 - 1}. \quad (2.68)$$

This behavior in the zero-order plasma is similar to electromagnetic waves in a waveguide, where waves below a cutoff frequency become evanescent.

It will be shown in the following chapter that the plasma frequency of the ionosphere is typically in the 2 to 10 MHz range. Since the frequencies and harmonics from the space station power system processing and transmission components are below this, the radiated electromagnetic waves are evanescent. Electric field intensities in a zero-order plasma can then be determined by multiplying the electric field intensities in free space by an attenuation factor, $e^{-\alpha r}$, where α is the real number obtained from (2.66) when $\omega < \omega_p$. The free space phase term can simply be neglected since it does not effect the magnitude of the intensity. For the moment-method formulation, $e^{-\alpha r}$ can replace the e^{-jkr} term in (2.38).

It is important to summarize the approximations that have been made in accounting for the plasma:

1. the earth's magnetic field has been neglected, therefore the ionospheric plasma is assumed to be isotropic (the zero-order plasma approximation);
2. the frequencies of interest are assumed to be below the (electron) plasma frequency, hence evanescent rather than propagating fields result;
3. the attenuation of the near-field evanescent fields is assumed to occur in the same manner as for the far fields;
4. the attenuation factor, $e^{-\alpha r}$, is incorporated into the moment-method solution only in the calculation of the radiated fields and not in the calculation of the currents which produce the fields.

The approximations listed here simplified the development of a basic framework for EMI analysis using the moment method in the ionospheric plasma. Continuing work will improve the sophistication of the model by removing the first, third, and fourth approximations, thereby resulting in a more realistic simulation of the radiation problem.

Chapter 3

Results – Analytical Solution

In Chapter 2, the analytical formulations for E_r and E_θ from an elemental dipole were given in (2.33) and (2.34). In the last section of the chapter, the zero-order plasma model was incorporated into the formulations. In this chapter, the electric fields are calculated and then compared for unbounded free space and the zero-order plasma. But first, some input conditions are discussed as they relate to the space station and the ionosphere. Then computerized simulations are performed for different circumstances.

3.1 Attenuation Factor

The distinguishing property of the ionosphere was determined in Chapter 1 to be the electron density. In order to determine the electron density, curves for the maximum and minimum charge density N , $\#/m^3$, as functions of altitude are shown in Figure 3.1 [5]. For a given altitude the maximum electron density occurs

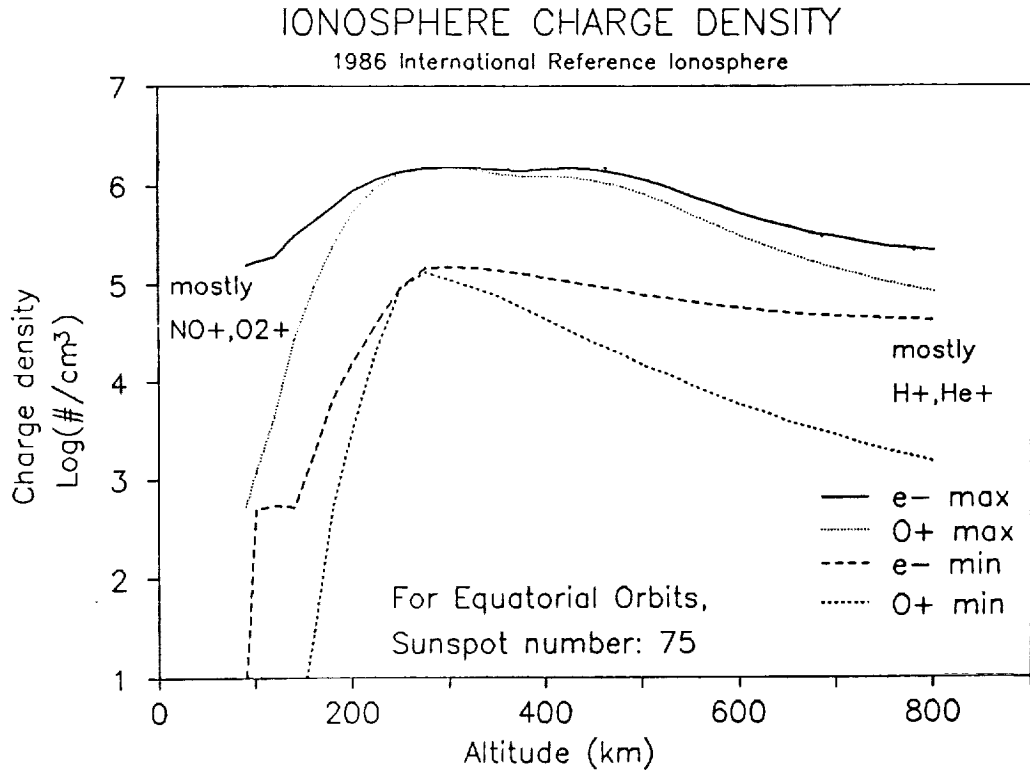


Figure 3.1: Ionospheric charge density as a function of altitude [5].

during the daytime and the minimum occurs at nighttime (also see Figure 1.2). The two electron density curves in Figure 3.1 were digitized by approximating them with linear equations and entering them into the computer program. For a given altitude, a value is entered and used to interpolate between the minimum and maximum electron density values, i.e., unity corresponds to maximum N . In a more specific application, the program IRI-86 [6] could be used to give a more accurate value of N based on all the parameters that influence the ionosphere. Since the plasma serves to attenuate EMI, the worst case is for minimum N or free space. Meanwhile, it should be pointed out that overdesigning EMI protection for the free space case could be costly.

The space station is being designed to operate between an altitude of 450 and

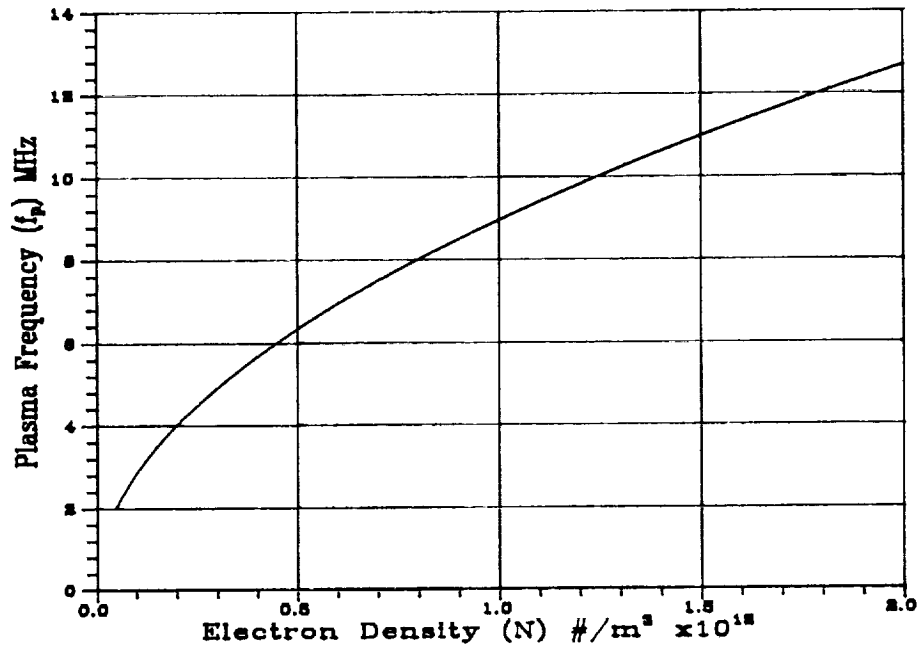


Figure 3.2: Plasma frequency versus electron density.

550 km. A conservative range for N would then be between 5×10^{10} and 2×10^{12} electrons per cubic meter [5]. Figure 3.2 shows the plasma frequency versus the electron density for the desired altitude range calculated from (2.60). Similar to a waveguide, propagation occurs for frequencies above the plasma frequency and attenuation below the plasma frequency. From the graph, it can be seen that the minimum plasma frequency of 2 MHz corresponds to the minimum electron density. As stated in Chapter 1, this analysis concentrates on frequencies below the plasma frequency. Figure 3.3 shows this by plotting the attenuation versus frequency (2.68) up to the plasma frequency for given electron densities. The attenuation in dB/m is calculated from $20 \log_{10} e^{\alpha}$. The graph also shows that the dB/m attenuation is fairly constant over frequency variations up to near the plasma frequency.

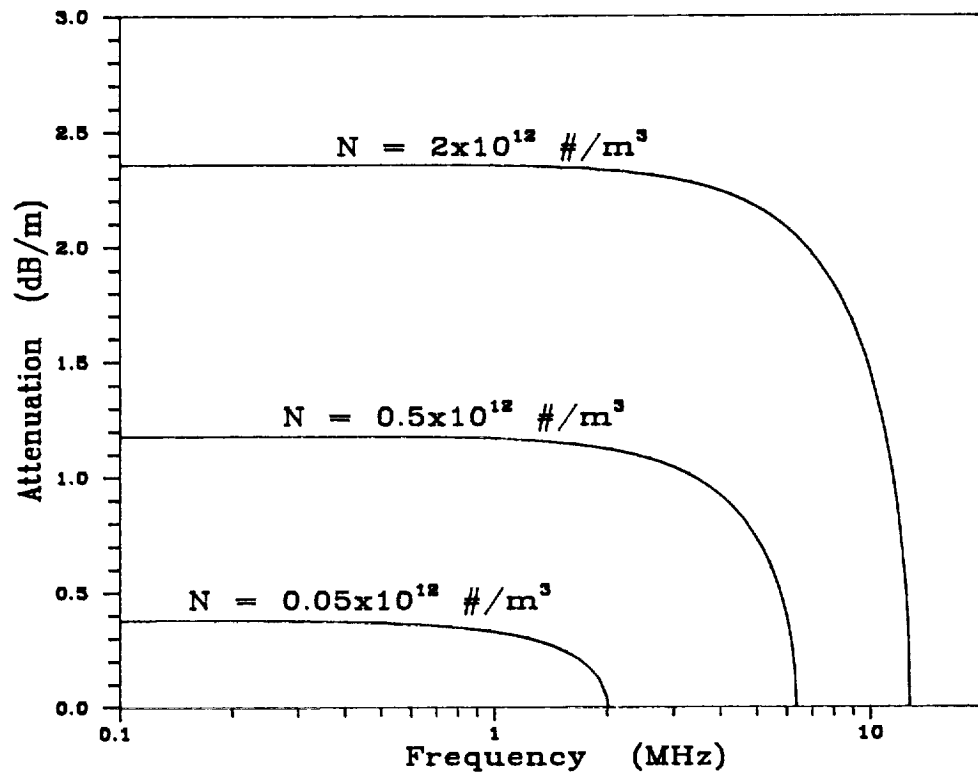


Figure 3.3: Attenuation versus frequency for specified electron densities

3.2 Computer Simulation

The computer program was written to calculate the analytical solutions for the elemental dipole in unbounded free space and the zero-order plasma. A quick review of the equations and parameters follows:

$$E_r = \frac{Il}{2\pi} e^{-jkr} \left(\frac{1}{r^2} \sqrt{\frac{\mu_o}{\epsilon_o}} + \frac{1}{j\omega\epsilon_o r^3} \right) \cos \theta \quad (3.1)$$

and

$$E_\theta = \frac{Il}{4\pi} e^{-jkr} \left(\frac{j\omega\mu_o}{r} + \frac{1}{r^2} \sqrt{\frac{\mu_o}{\epsilon_o}} + \frac{1}{j\omega\epsilon_o r^3} \right) \sin \theta \quad (3.2)$$

As discussed in section 2.3, the free space permittivity and permeability are used in the formulation. The remaining parameter, k , was determined to be equal to $\omega\sqrt{\mu_o\epsilon_o}$ for unbounded free space and $\omega\sqrt{\mu_o\epsilon_o}\sqrt{1 - \left(\frac{\omega_p}{\omega}\right)^2}$ for the zero-order plasma approximation. For the plasma, k is either real or imaginary, giving propagation or attenuation, depending on whether the frequency, ω , is above or below the plasma frequency, ω_p , respectively.

By substituting the parameters into E_r and E_θ , the electric fields are obtained as functions of (ω, N, r, θ) . The current, I , and length, l , were set equal to unity, and for free space the phase term is neglected since only the magnitude of the electric field is desired in the case of the elemental dipole. The final result of the simulation is the electric field intensities for an elemental dipole in free space and a zero-order plasma at given points.

3.3 Zero-Order Plasma Compared to Free Space

The following simulations look at the distinguishing characteristics of the electric field in the zero-order plasma compared to free space. The first case examines the electric field components as the distance from the source increases. The next case looks at the effect of changing the frequency. The final case addresses the issue of variations in the electron density. Before any calculations can be made, the parameters that do not vary for a particular simulation need to be set. The first two are the length of and current through the elemental dipole. It was previously mentioned that these are set equal to unity to normalize the electric fields. In the next chapter when MININEC3 is compared to analytical solutions, the current and length will be adjusted to physical values. The next consideration is choosing a value for θ . Since the effect of θ on field components is given in (3.1) and (3.2), its value was set to 45° to normalize its contribution to E_r and E_θ .

To examine the plasma's effect on the electric field as the distance from the source increases, it seemed appropriate to start the calculations at 1 *m*, and extend out to the present design length of the space station, 100 *m*. Figure 3.4 shows the fields over this distance for free space and the zero-order plasma. The frequency was chosen to be 20 *kHz* because it corresponds to the switching frequency of converters on the solar panels. The initial electron density, 10^{11} $\#/m^3$, was chosen because it is in the middle of the specified range. As expected, the electric field components in the plasma are attenuated. The electric field is expressed in *dB* $\mu V/m$ to conform to NASA's EMI documentation requirements [16]. This is calculated by expressing E in $\mu V/m$, and taking $20 \log_{10} E$. It is effectively a comparison of the field compared to a unit value of 1 $\mu V/m$.

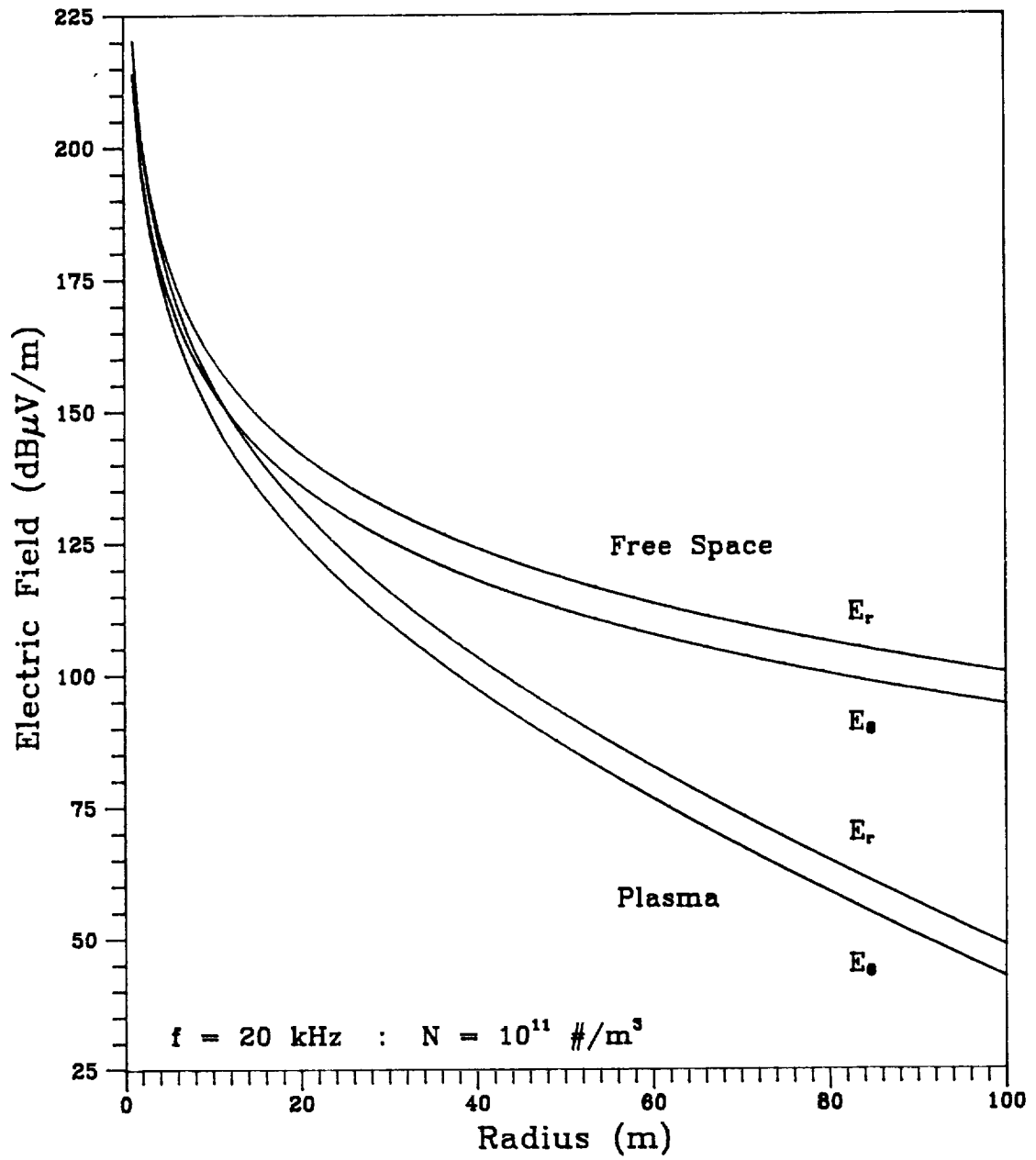


Figure 3.4: Comparison of electric field magnitude versus distance for free space and a zero-order plasma environment.

To examine the plasma's effect on the electric fields at different frequencies, a range must be set. Remembering that waves propagate above the plasma frequency and are evanescent below, it wouldn't make any sense to choose a value above the plasma frequency. What is known is that only values in the kHz range have ever been mentioned by NASA for some of the power system components. With this in mind, $1 MHz$ is established as the maximum test point. For the lower limit, the $20 kHz$ switching frequency is chosen. Figure 3.5 compares E_θ for the different frequencies in both free space and zero order plasma. For both mediums, as the frequency increases the magnitude decreases. This was also noticed in the E_r component. As was predicted in Figure 3.3, the dB attenuation in the plasma is similar for both frequencies.

The final issue looked at is to vary the electron density. From Figure 3.3, an increase in N should increase the attenuation. Figure 3.6 shows E_θ for a typical range of free space, $N = 0$, up to a maximum $N = 10^{12} \# / m^3$. As expected, an increase in N increases the attenuation.

3.4 Summary

In this chapter, a method was presented for determining the attenuation factor from measured charge density curves. The dB/m attenuation from the zero-order plasma was shown to be constant up to approximately one-half the plasma frequency. The electric field components for the elemental dipole in free space and the zero-order plasma were compared as functions of distance, frequency, and electron density.

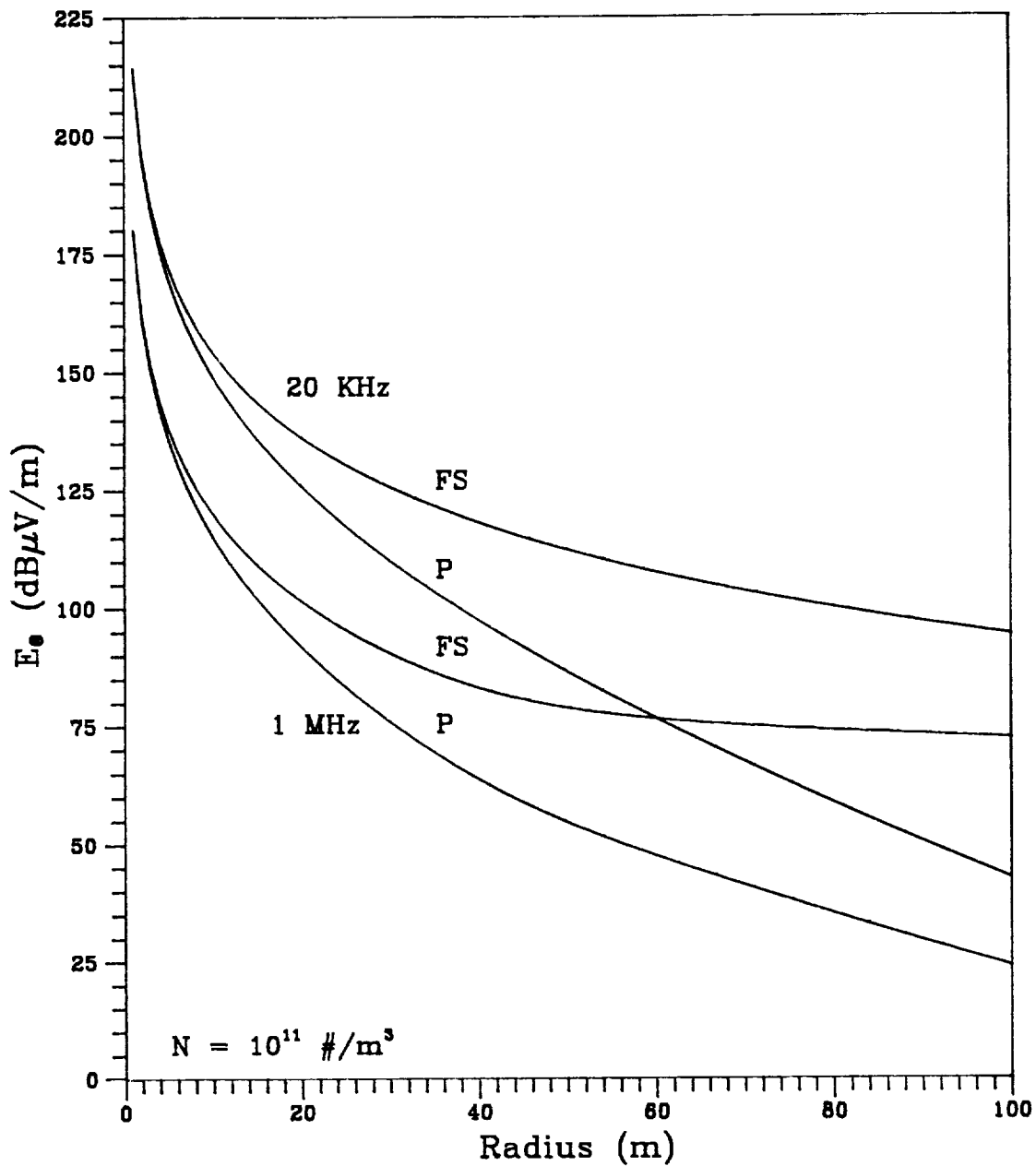


Figure 3.5: Comparison of electric field intensity for different frequencies, FS=free space, P=plasma.

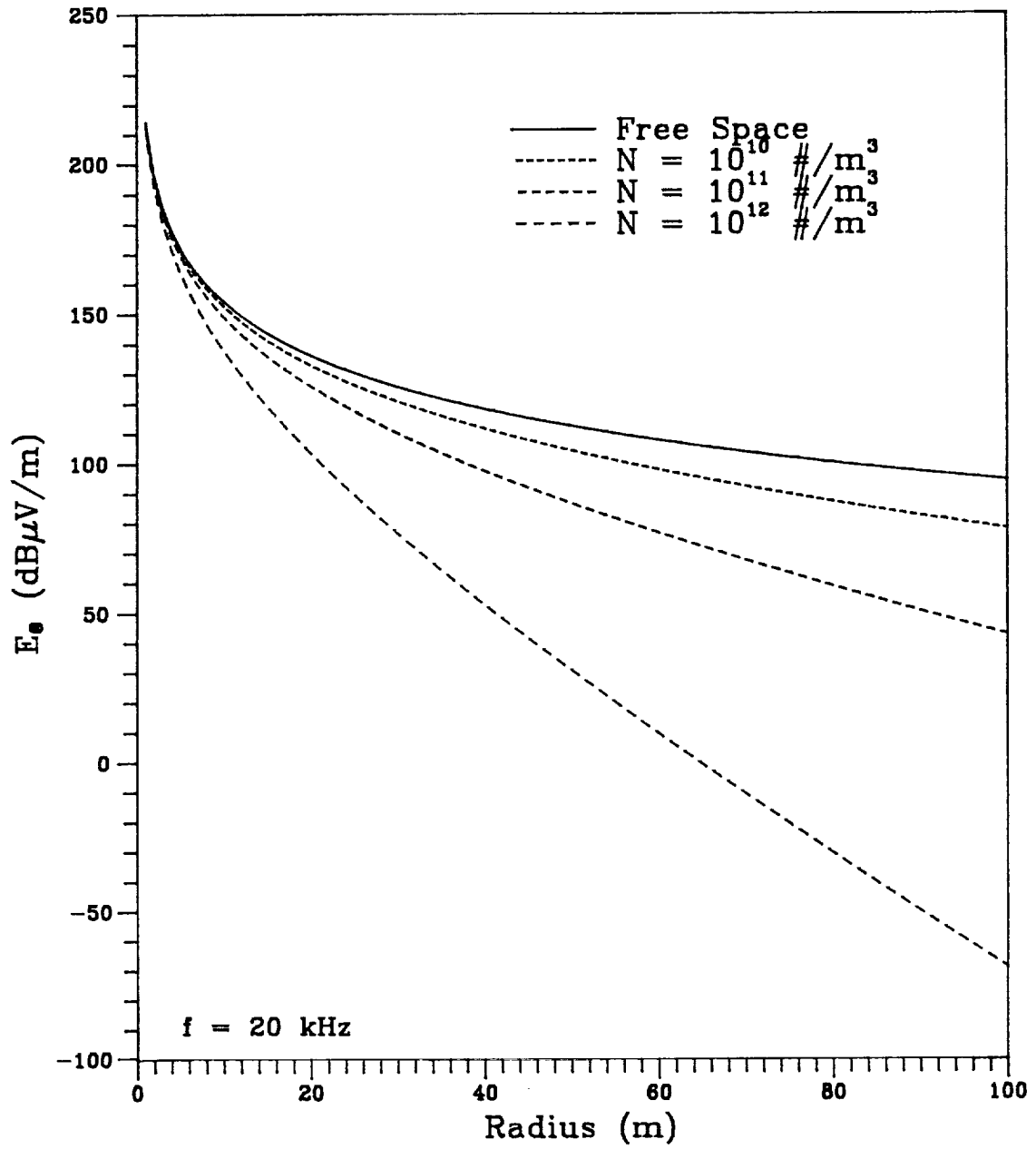


Figure 3.6: The effect of varying the electron density on the electric field.

Chapter 4

Results – Numerical Solution

In Chapter 3, the electric field for an elemental dipole was compared for free space and a zero-order plasma environment. The goal of which was to obtain preliminary results for some simple cases. However, the analytical approach is only applicable to isolated sources, i.e., sources that radiate in unbounded space without the presence of other structures. In this chapter, results for a more realistic space station configurations are discussed. But first, a verification procedure for MININEC3 is presented. This is done to insure that the program produces correct results in both mediums, and to gain experience with choosing proper convergence parameters.

MININEC3 is by no means a complex implementation of the moment method like NEC is. It is small, runs on a PC, is written in BASIC, is not cluttered with built in functions or designs, is well documented, and is easy to work with. It provides a good test bed for ideas. As MININEC3 is a widely accepted code, the validation procedures used to make sure the program produces correct results

center around the type of models needed for the space station structure, instead of complex antenna designs. This means taking simple dipole and monopole sources on simple wire structures and at relatively low frequencies in the KHz range. This way the results can be qualitatively understood and provide proof of concept for modifying a larger program like NEC.

MININEC3 is validated using two techniques. How accurate are MININEC3 results compared to analytical solutions? For problems where there are no analytical solutions, how does MININEC3 results compare to more complex moment-method solutions? Four tests were used to answer these concerns. The first test compares solutions for the input impedance for some simple antenna configurations. The second test looks at currents on a long-wire structure for different frequencies. A third test looks at the numerical accuracy for determining far fields in free space from dipoles of different numbers of segments. The final validation technique compares MININEC3 and the analytical solution for near field radiation in free space and the zero-order plasma. In all four cases, convergence of the solutions is obtained by paying strict attention to the number of wire segments that are used to discretize a structure. A general rule of thumb is 10 segments per wavelength. This allows for accurate representation of the current waveform on the wire.

4.1 Input Impedance

The input impedance is a particularly sensitive measure of the numerical accuracy of MININEC3 [14]. The reason for this is the use of pulse functions for the current instead of more complicated functions (explained in section 2.2). In the first two input impedance cases, MININEC3 is compared to solutions using

Table 4.1: Input impedance of an isolated dipole, in ohms.

<i>N, Modes</i>	<i>MININEC</i>	<i>King's Solution*</i>
1	N/A	2.000-j1921
3	1.927-j1980	1.892-j1916
5	1.902-j1970	1.864-j1905
7	1.887-j1957	1.856-j1899
15	1.856-j1922	N/A

* King calculated the solutions using piecewise sinusoidal functions [14].

$$\text{length} = \lambda/10, \text{ wire radius} = \lambda/10000$$

piecewise sinusoidal functions. In the third test, the analytical solution is known. Table 4.1 shows the input impedance for an isolated dipole antenna of length $\lambda/10$. For convergence, the results show that approximating the antenna by only three segments is sufficient to obtain the correct input impedance. Table 4.2 shows the antenna impedance when another identical wire is located parallel to and at a distance of $\lambda/100$ from the first antenna. The wire coupling configuration is more representative of the type of problem that would be of concern for an EMI analysis on the space station. Once again, only a few segments are required to adequately approximate the antenna input impedance. Table 4.3 completes the study of input impedance by calculating it for a longer antenna, a $\lambda/2$ dipole. Again, only a few segments are required to accurately approximate the input impedance. The rule of thumb dictated 10 segments/ λ for accurate results. For this dipole, 5 segments would then be needed, so these results justify the rule of thumb.

Table 4.2: Input impedance of dipole 1 in the presence of dipole 2, in ohms.

<i>N, Modes</i>	<i>MININEC</i>	<i>King'sSolution*</i>
1	1.264-j1908	1.382-j1822
3	1.281-j1918	N/A
15	1.256-j1868	N/A

* King calculated the solution using piecewise sinusoidal functions [14].

d=dipole separation distance= $\lambda/100$

length = $\lambda/10$, wire radius = $\lambda/10000$

Table 4.3: Input impedance of $\lambda/2$ dipole, in ohms.

<i>N, Modes</i>	<i>MININEC</i>	<i>Known[14]</i>
3	72.39+j60.75	73.0+j42.5
5	75.90+j41.88	
9	78.05+j41.88	
19	79.28+j42.09	

length = $\lambda/2$, wire radius = $\lambda/10000$

4.2 Current Distribution

Another method used in validating MININEC3 was solving for the induced currents in the wire structure. These currents form a special type of conducted EMI, i.e., currents induced in the space station structure by EMI sources. As a test case, Figure 4.1 shows a 100 m wire (divided into 34, 3 m pulse segments)

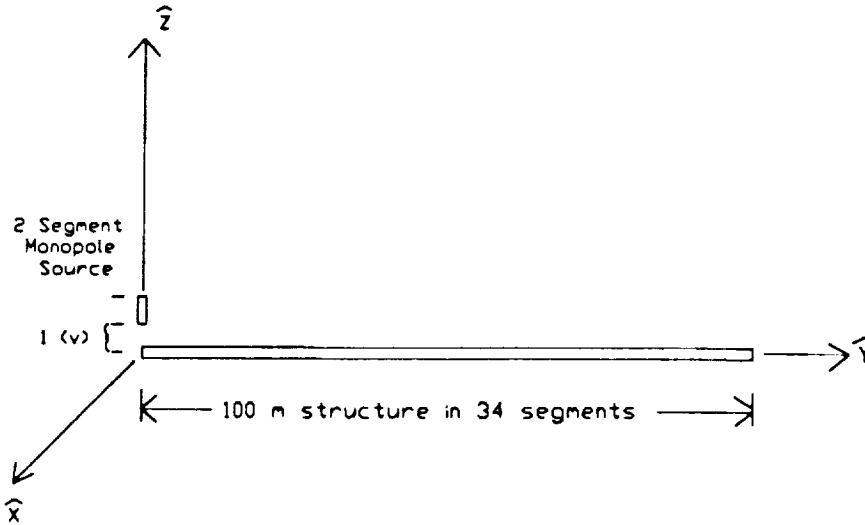


Figure 4.1: Simple wire model of the space station with a short monopole antenna located at one end.

excited by a short monopole antenna at one end. The current distribution along the simple structure is then calculated for a 20 KHz, 100 KHz, 1 MHz, and 5 MHz source and shown in Figure 4.2. At the lower frequencies of 20 and 100 KHz, the normalized current distribution is identical. This is attributed to the length of the structure being less than 3 % of the wavelength. As the frequency increases to 1 MHz, the distribution changes only slightly as the structure is then 1/3 of a wavelength. At 5 MHz, which is higher than the maximum frequencies discussed, the structure is 5/3 wavelengths. This higher frequency was used because it provides nice qualitative results since the current standing wave pattern shows a wire length

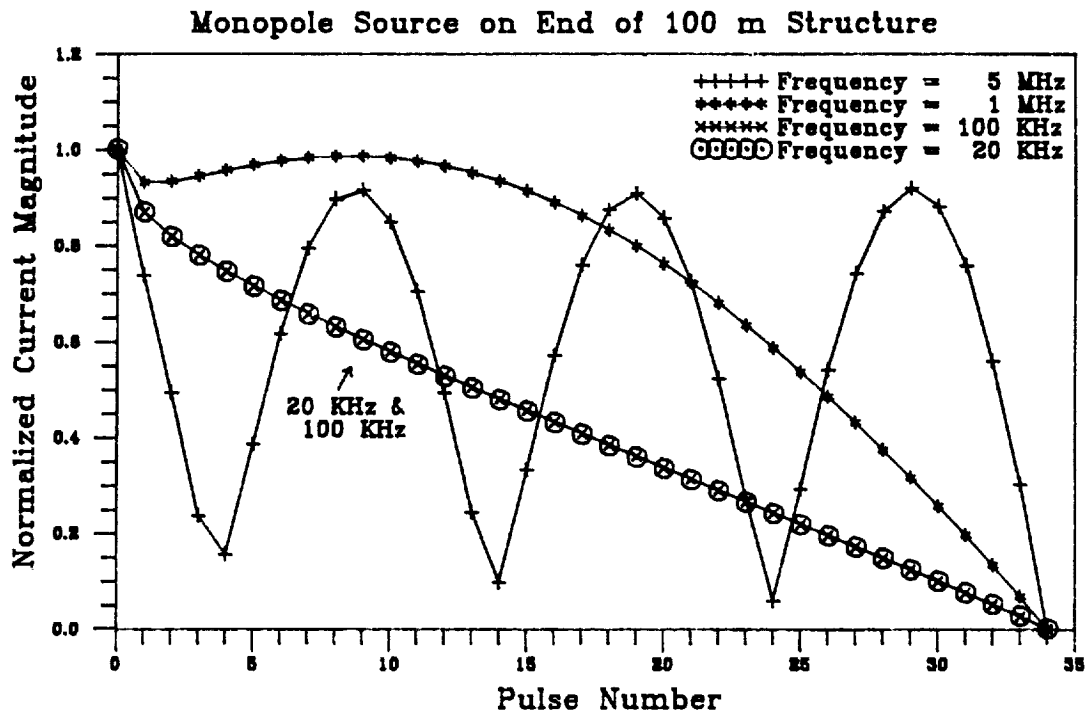


Figure 4.2: Current distribution along a 100 m wire divided into 34 pulse segments with a monopole source on one end at 20 KHz, 100 KHz, 1 MHz, and 5 MHz.

of $5/3$ wavelengths as expected. If the results for 10 MHz were shown, the current waveform would approximate $3\frac{1}{3}$ wavelengths. In the 4 cases shown, the current solutions converge.

4.3 Comparison of Far-Field Results

Although the far-field approximation is not used for the space station configuration, it is the next logical step in validating MININEC3 and further increases confidence in the program. In Figure 4.3, far-field radiation patterns for a $\lambda/2$ dipole antenna with an increasing number of segments calculated with MININEC3

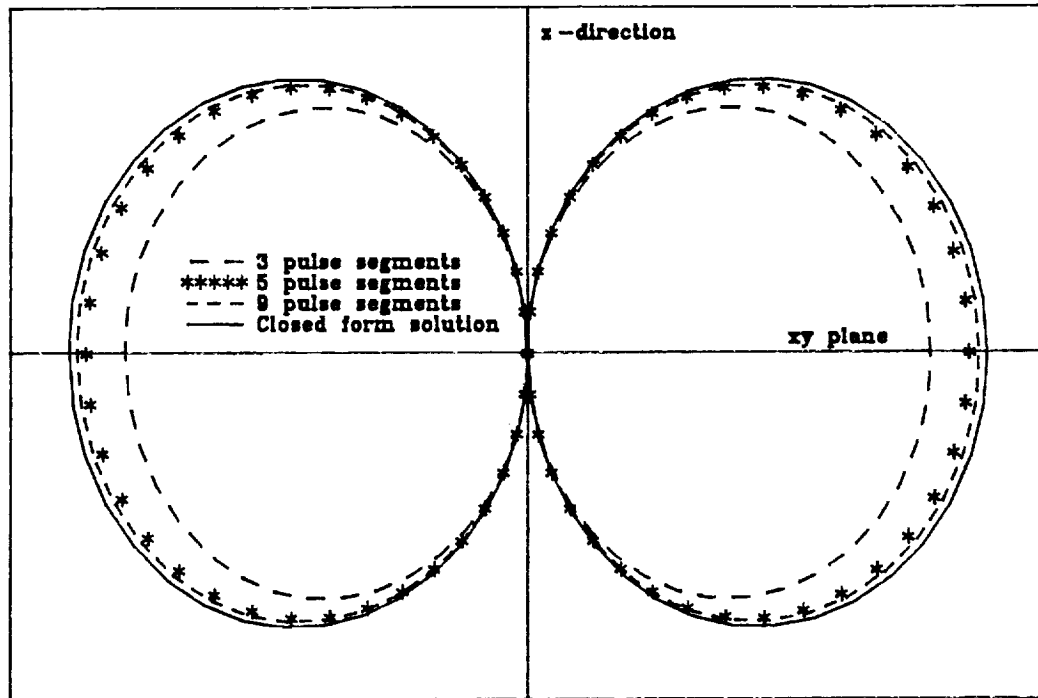


Figure 4.3: Calculated far-field radiation pattern for $\lambda/2$ dipole antenna for an increasing number of segments using MININEC3 and analytical solution.

are compared to the analytical solution. As with the input impedance of the $\lambda/2$ dipole, the results converge to known values for 5 segments. The results for this graph were normalized by dividing through by the source current and length of the dipole.

4.4 Comparison of Near-Field Results

The final step in validating MININEC3 is to compare analytical near field solutions to MININEC3 solutions. This point had been foreseen and was a reason for

developing the dipole simulation. Instead of comparing MININEC3 to analytical solutions for each environment separately, it makes more sense to present them together. In that respect, a detailed description of the dipole and conditions used to determine the electric fields follows.

The dipole used in MININEC3 approximates the elemental dipole used in the analytical solution. The elemental dipole assumes a constant current across its entire length. In the moment method the current was shown to be distributed over several pulse functions. Numerically this has a big advantage because the boundary conditions at the ends of the dipole are satisfied by forcing the currents to be zero. This was shown in Figure 4.2 but not pointed out until now. The elemental dipole on the other hand, had a constant current over its entire length. This difference needs to be corrected for comparison. The dipole used in MININEC3 is divided into 5 pulses with the center being fed by a 1 volt, 100 kHz source. The current distribution on it appears as a step-like triangular function. In a qualitative sense, the analytical current distribution would look like a triangular step distribution if half its length with zero current was added to each end. Therefore, the length used in MININEC3 needs to be twice as long as its equivalent elemental dipole. In both cases, the dipole is centered along the z -axis and the electric fields are calculated along the x and z axis. The x and z components in this configuration then translate to E_r and E_θ as formulated in (2.33) and (2.34).

Figures 4.4 and 4.5 show that MININEC3 results converge very closely to analytical solutions. The wire length and source current determined by MININEC3 (shown on graph) are used as inputs for the analytical solutions. This was done to obtain the actual electric field intensities in $dB\mu V/m$ instead of normalizing the data to the source parameters. As discussed in Chapter 2, the zero-order plasma fields are calculated by multiplying the contribution from each pulse segment by the

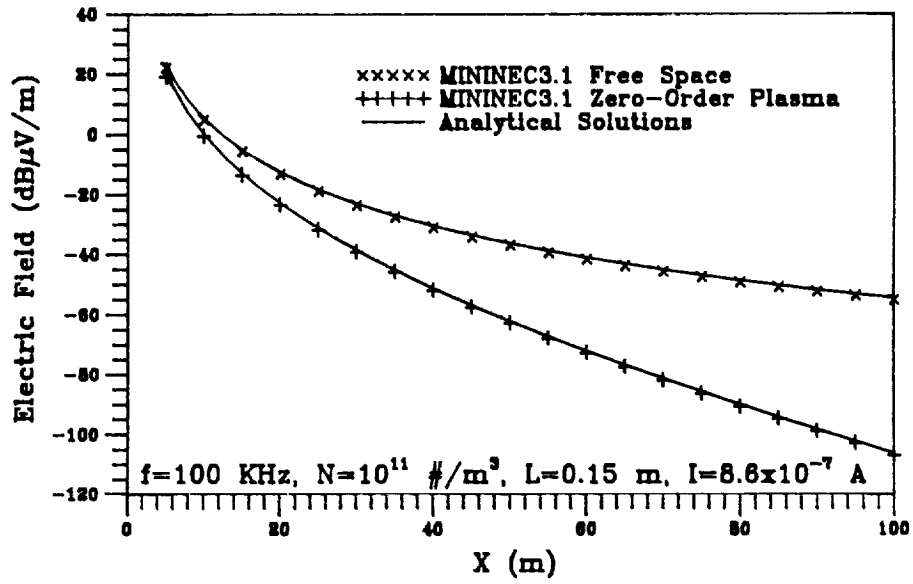


Figure 4.4: x -component of electric field calculated analytically and numerically for unbounded free space and zero-order plasma.

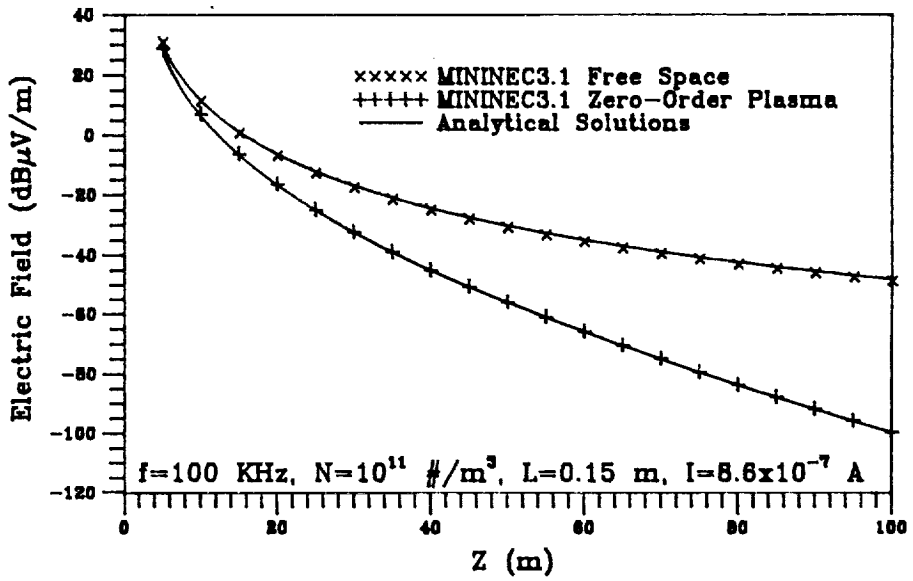


Figure 4.5: z -component of electric field calculated analytically and numerically for unbounded free space and zero-order plasma.

attenuation term, calculated from frequency, electron density, and distance between source and observation point. The same electron density used previously is used here, $N = 10^{11} \text{ \#/m}^3$.

4.5 Electric Field Contour Plots for Space Station Structure

A simple wire model of Space Station Freedom is shown in Figure 4.6. The 100 m

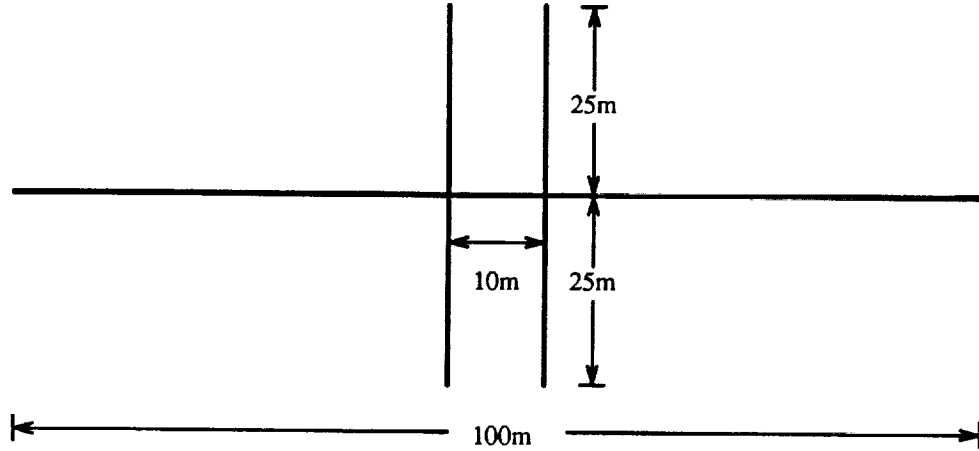


Figure 4.6: Wire model of NASA Space Station Freedom.

longitudinal wire consists of 20 segments, with a one-volt source on the left-most segment. The source location was selected to simulate the switching associated with the photovoltaic solar panels. The two vertical wires, representing habitation and laboratory modules, are 50 m long and spaced 5 m either side from the center of the 100 m wire. Each 50 m wire is divided into 10 segments. Using the rule of thumb, 10 segments per wavelength, the shortest λ for the 5 m wire segments would be 50 m, or $f \leq 6 \text{ MHz}$.

A contour plot of the electric field intensity for unbounded free space is shown in Figure 4.7. To form this, the following parameters were used in MININEC3. The above mentioned space station model was entered in the x-y plane with the source on the 100 m boom at the origin and extending out into the positive x-axis. The free space environment was selected. A source with a frequency of 1 MHz was set, because it offers the worst case for attenuation when the zero-order plasma model is used. Starting at $x = -10$ m and $y = -35$ m, near electric fields were calculated in 2 m increments till $x = 110$ m and $y = 35$ m. There is then a near-field moment-method approximation since multiple field points exist along a single source point. The contour lines are specified in 5 $dB\mu V/m$ increments.

The results show the field strength to be relatively strong around the source as expected. The strong fields at the far end of the structure indicates that conducted EMI (currents induced on the structure) should be a major concern to the space station designer. Especially if the attenuation over distance is a main strategy employed to alleviate EMI. The field then decreases as the distance from the structure increases to a value of about 50 $dB\mu V/m$ at the outer boundary of the grid. For the zero-order plasma the attenuation at the boundary is expected to be much greater.

The same conditions used in the previous free-space contour plot were used to determine the fields in the zero-order plasma model. The only difference being the zero-order plasma environment was selected with an electron density of $N = 10^{11}$ $\#/m^3$. A contour plot of these fields is shown in Figure 4.8.

Immediately, the increase in the number of contour lines shows the electric field to be much more attenuated. The yellow lines starting at 45 $dB\mu V/m$ and below, were not on the free space contour plot. This is the principal benefit of the zero-order plasma, i.e., moving a platform a relatively small distance from the

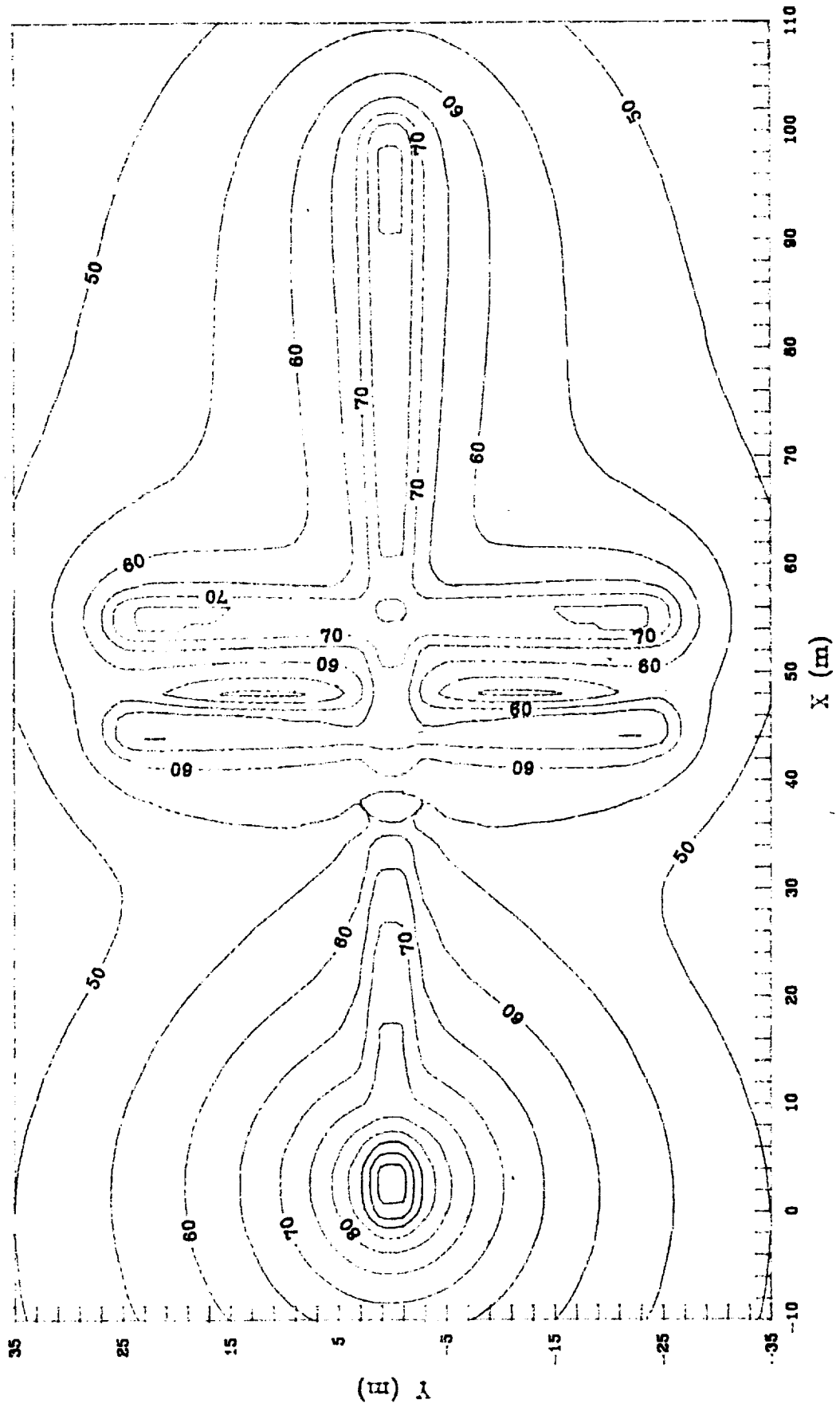


Figure 4.7: Electric field intensity in $\text{dB}\mu\text{V}/\text{m}$ from radiating source on space station model in a free space environment.

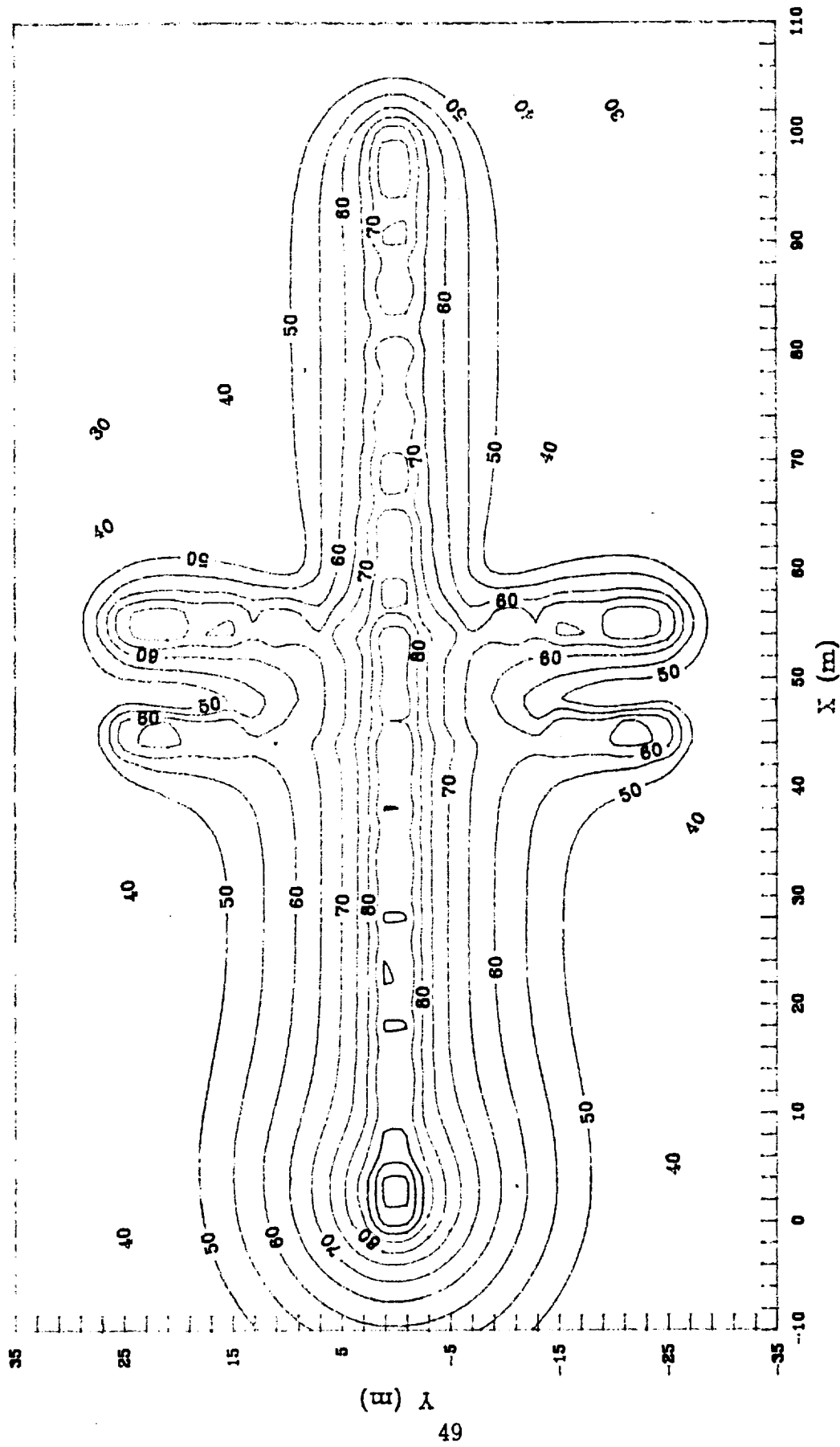


Figure 4.8: Electric field intensity in $dB\mu V/m$ from radiating source on space station model in a zero-order plasma environment.

space station provides a cleaner electromagnetic environment with the plasma than free space would. The fields close to the source, less than 10 m , are only slightly attenuated as the theory would have suggested. But some of other positions near the structure provide some interesting results that were not expected.

The plasma appears to limit the conducted EMI problem, but in doing so the fields near the center of the structure are increased. In some areas (around $x=40\ m$ and $y=0\ m$) the field increases by around $30\ dB\mu V/m$. At first an error was suspected in the data entry because stronger fields in the middle of the structure would be caused by higher currents in the structure. The current data did not support this conjecture because the current in each pulse segment was identical in both mediums, as expected. So how could the sum of the electric fields from each pulse increase in the zero-order plasma? Looking back at the formulations and the difference in the two media indicates a possible explanation. In the zero-order plasma, the fields are evanescent and have no phase term. This makes the individual fields from each pulse segment add as scalar quantities. In the free space case, the fields have phase terms associated with them so they add as vectors. Therefore, at certain locations the field strength in the zero-order plasma could be higher because of field components out of phase negating each other in free space. This effect was not anticipated because the modeling of the plasma by attenuation has only been applied to the far field in the past.

4.6 Summary

MININEC3 has been shown to produce correct results in free space and the zero-order plasma by comparing solutions for input impedance, current distribution on a

wire structure, far-field patterns, and near-field patterns to solutions obtained from analytical results or more advanced moment-method codes. Results are presented in the form of contour plots for electric fields from a simple space station structure, showing the attenuation from the zero-order plasma compared to free space.

Chapter 5

Conclusions and Further Research

The contributions of this research work fall into two general categories. The first is in modeling of the ionosphere and developing a working model for electromagnetic wave propagation. The two interests that distinguish this area from others is the indepth analysis of frequencies below the plasma frequency and the interest in the near-field components. The second contribution centers around incorporating the zero-order plasma into the moment-method and ultimately generating field plots for a simple space structure.

A large portion of this research work, as with any research work, involved collecting data, formulations, and theories on electromagnetic wave propagation in the ionosphere. At the altitude of the space station, the ionosphere was approximated as a zero-order plasma, i.e., the earth's magnetic field was neglected. The characteristic properties are principally determined by the electron density which is mainly

a function of altitude, time of day, and solar activity. From the electron density the plasma frequency was determined. For radiation above the plasma frequency, the waves propagate. For radiation below the plasma frequency, the waves decay exponentially, i.e., they are evanescent. This behavior is similar to electromagnetic wave propagation in a waveguide. It was also shown that up to about half the plasma frequency, the attenuation from the plasma is fairly constant. For the space station, half the minimum plasma frequency is about 1 *MHz*. Since the power system components and their harmonics are usually well under 1 *MHz*, it was set as the upper limit of frequencies to be considered in this analysis.

The moment method was then formulated as an analysis tool for performing calculations. To do this, analytical solutions for the elemental dipole were developed for both media. The solution for the fields radiated by an elemental dipole provided the basis for an explanation of near and far fields. This raised two important conclusions for the research. The first was that the far-field approximation could not be used for the space station versus the more complicated near-field solution because of the low frequency of radiation being analyzed. The second was that the plasma models that have been developed have only been applied to the far field, since the near field was never an issue before. The analytical solutions were then used to test the modified version of MININEC3. This computer program, chosen mostly for its simplicity in implementing the moment method, was shown to be a good program to do test-case calculations. The dipole results showed that the attenuation in a plasma medium was as expected and it provided accurate results for both free space and the zero-order plasma.

Wire models were then formed for the space station. The main reason such a simplistic program could handle something as large as the space station is the low frequency consideration. In order for the moment method solutions to converge,

pulse segments on the structure should be less than 1/10 of a wavelength. The space station longest part is the main boom at about 100 *m*. At the maximum frequency of 1 *MHz* (wavelength=300 *m*), the structure could be modeled with under 4 segments. But because of resolution for determining grid plots, a smaller segment length of 5 *m* was used in the structure. This was determined to be adequate for the resolution in the contour plots and also near the maximum size of a problem MININEC3 is designed for. Although a larger problems could be done, the time to calculate field patterns starts to become an issue. The first test was to calculate the current on a 100 *m* wire for several different frequencies.

A more complicated model of the space station was then developed for calculating field patterns. The electric field contour plots from the wire model for the two media raised several interesting points. The first was the relatively high fields at the opposite end of the structure resulting from the conducted EMI or currents induced in the structure. Also, from the zero-order plasma contour plot, fields were shown to be strongly attenuated for only a short distance from the structure compared to the free space case. A not-so-obvious advantage of this is that EMI from the space station will be reduced for structures that may be near the station, i.e., satellites and the space shuttle.

The zero-order plasma plot also showed some increases in field intensities near the center of the structure. One conclusion was that this effect could be attributed to the lack of a phase term in the waveguide model. But in interpreting these results, they can only be as good as the model. Since this model is only proven in far field cases, where phase would not have a large effect on the field intensities for free space calculations, the waveguide model in the near field needs more work. It is thought that since the currents were the same on the structure in the two media, the fields are not expected to increase in a plasma. But the arguments seem to be

all qualitative in this area.

Indications are that the moment method, MININEC3 in this case, properly models the space station with thin wires and predicts the correct field results in both environments.

5.1 Future Work

There are many areas of work that need further research. The main focus should be around developing better models for near-field electromagnetic wave propagation in the plasma surrounding the space station structure. In particular, adding the contributions for the electric fields from each pulse segment as scalar quantities should be addressed. More testing and development on structures with MININEC3 needs to be completed to determine the effect of plasmas. The major problem of work in this area will continue to be in developing models for near-field electromagnetic radiation and analytical solutions for testing purposes.

Bibliography

- [1] M.A. Kettani and M.F. Hoyaux, *Plasma Engineering*, Halsted Press, New York, 1973.
- [2] R.E. Collin, *Antennas and Radiowave Propagation*, McGraw-Hill, New York, 1985.
- [3] J.M. Goodman and J. Aarons, "Ionospheric Effects on Modern Electronic Systems," *Proceedings of the IEEE*, **78**, pp. 512-528, 1990.
- [4] S.V. Marshall and G.G. Skitek, *Electromagnetic Concepts & Applications*, 2nd Ed., Prentice Hall, Englewood Cliffs, 1987.
- [5] D.B. Snyder, "Environmental Interactions in Low Earth Orbit with Large, High Power, Systems," *Power Technology Division*, NASA Lewis Research Center, Cleveland, Ohio, 1990.
- [6] *Natural Space Environments and Environmental Interactions for Space Station and Earth Observing System*, NASA JPL, Vol. 1, Undated Draft Copy.
- [7] B. Keiser, *Principles of Electromagnetic Compatibility*, 3rd Ed., Artech House, Norwood, 1987.

- [8] R.F. Harrington, *Field Computation by Moment Methods*, Macmillan Company, New York, 1968.
- [9] Science & Engineering Associates, Inc., *Space Station Freedom Electromagnetic Compatibility (EMC)*, Model Development Meeting Minutes, Marshall Space Station Center, January 29-30, 1990.
- [10] P.W.Barber, N.A.O. Demerdash, R. Wang, B. Hurysz, and Z. Luo, "Analysis of Electromagnetic Interference From Power System Processing and Transmission Components for Space Station Freedom," *First Interim Progress Report for the Period January 1 - June 30, 1990*, Grant No. NAG3-1126, submitted to NASA Lewis Research Center, July 1990.
- [11] P.W.Barber, N.A.O. Demerdash, R. Wang, B. Hurysz, and Z. Luo, "Analysis of Electromagnetic Interference From Power System Processing and Transmission Components for Space Station Freedom," *Interim Progress Report for the Period July 1 - December 31, 1990*, Grant No. NAG3-1126, submitted to NASA Lewis Research Center, January 1991.
- [12] J.C. Logan and J.W. Rockway, *The New MININEC (Version 3): A Mini-Numerical Electromagnetic Code*, NOSC TD 938, September 1986.
- [13] G.J. Burke and A.J. Poggio, *Numerical Electromagnetics Code (NEC) - Method of Moments*, NOSC TD 116, January 1981.
- [14] J.D. Kraus, *Antennas*, 2nd Ed., McGraw-Hill, New York, 1988.
- [15] R.F. Harrington, *Time Harmonic Electromagnetic Fields*, McGraw-Hill, New York, 1961.
- [16] *Definition and System of Units, Electromagnetic Interference and Electromagnetic Compatibility Technology*, MIL-STD-463A, September 19, 1988.

Appendix A

Evaluating Partial Derivatives and Simplifying

The applied electric field at location z in terms of a current source at z' was given in (2.43) as

$$-E_{app}(z) = \frac{1}{4\pi j\omega\epsilon} \int_l \left(\frac{\partial^2}{\partial z^2} G_{zz'} + k^2 G_{zz'} \right) I(z') dz', \quad (\text{A.1})$$

where

$$G_{zz'} = \frac{e^{-jkr}}{r}$$

and

$$r = [(z - z')^2 + a^2]^{1/2}.$$

Evaluating in terms of r

$$\frac{\partial^2}{\partial z^2} G_{zz'} = \frac{\partial^2}{\partial z^2} \frac{e^{-jkr}}{r}.$$

Taking one partial

$$\frac{\partial}{\partial z} \frac{e^{-jkr}}{r} = \frac{-jkr e^{-jkr} \left(\frac{\partial r}{\partial z}\right) - e^{-jkr} \left(\frac{\partial r}{\partial z}\right)}{r^2}$$

$$\frac{\partial}{\partial z} \frac{e^{-jkr}}{r} = \frac{-e^{-jkr}}{r^2} \left(\frac{\partial r}{\partial z}\right) (jkr + 1).$$

Then taking the second

$$\begin{aligned} \frac{\partial^2}{\partial z^2} G_{zz'} = \frac{1}{r^4} r^2 \left[jk e^{-jkr} \left(\frac{\partial r}{\partial z}\right)^2 (jkr + 1) - e^{-jkr} \left(\frac{\partial^2 r}{\partial z^2}\right) (jkr + 1) - \right. \\ \left. e^{-jkr} \left(\frac{\partial r}{\partial z}\right)^2 jk \right] + e^{-jkr} \left(\frac{\partial r}{\partial z}\right)^2 (jkr + 1) 2r. \end{aligned}$$

$$\begin{aligned} \frac{\partial^2}{\partial z^2} G_{zz'} = \frac{e^{-jkr}}{r^4} \left[jkr^2 (jkr + 1) \left(\frac{\partial r}{\partial z}\right)^2 - r^2 (jkr + 1) \frac{\partial^2 r}{\partial z^2} - \right. \\ \left. jkr^2 \left(\frac{\partial r}{\partial z}\right)^2 + 2r (jkr + 1) \left(\frac{\partial r}{\partial z}\right)^2 \right]. \end{aligned}$$

$$\begin{aligned} \frac{\partial^2}{\partial z^2} G_{zz'} = \frac{e^{-jkr}}{r^4} \left[-k^2 r^3 \left(\frac{\partial r}{\partial z}\right)^2 - jkr^3 \frac{\partial^2 r}{\partial z^2} - r^2 \frac{\partial^2 r}{\partial z^2} + \right. \\ \left. 2jkr^2 \left(\frac{\partial r}{\partial z}\right)^2 + 2r \left(\frac{\partial r}{\partial z}\right)^2 \right]. \end{aligned}$$

$$\frac{\partial^2}{\partial z^2} G_{zz'} = \frac{e^{-jkr}}{r^4} \left[\left(\frac{\partial r}{\partial z}\right)^2 (-k^2 r^3 + 2jkr^2 + 2r) - \frac{\partial^2 r}{\partial z^2} (jkr^3 + r^2) \right].$$

$$\frac{\partial^2}{\partial z^2} G_{zz'} = \frac{e^{-jkr}}{r^3} \left[\left(\frac{\partial r}{\partial z}\right)^2 (-k^2 r^2 + 2jkr + 2) - \frac{\partial^2 r}{\partial z^2} (jkr^2 + r) \right]. \quad (\text{A.2})$$

Evaluating the partial of r ,

$$r = \sqrt{(z - z')^2 + a^2},$$

yields

$$\frac{\partial r}{\partial z} = (z - z') \sqrt{(z - z')^2 + a^2},$$

$$\left(\frac{\partial r}{\partial z}\right)^2 = \frac{(z - z')^2}{(z - z')^2 + a^2}.$$

But since $(z - z')^2 = r^2 - a^2$,

$$\left(\frac{\partial r}{\partial z}\right)^2 = \frac{r^2 - a^2}{r^2}. \quad (\text{A.3})$$

The second partial of r is

$$\frac{\partial^2 r}{\partial z^2} = -\left((z - z')^2 + a^2\right)^{-\frac{3}{2}} + \left((z - z')^2 + a^2\right)^{-\frac{1}{2}}.$$

$$\frac{\partial^2 r}{\partial z^2} = -r^{-3}(r^2 - a^2) + r^{-1}.$$

$$\frac{\partial^2 r}{\partial z^2} = \frac{a^2 - r^2}{r^3} + \frac{1}{r} = \frac{a^2}{r^3}.$$

$$\frac{\partial^2 r}{\partial z^2} = \frac{1}{r^2} \left(\frac{a^2}{r}\right). \quad (\text{A.4})$$

Substituting (A.3) and (A.4) into (A.2) results in

$$\frac{\partial^2}{\partial z^2} G_{zz'} = \frac{e^{-jkr}}{r^5} \left[(r^2 - a^2) (-k^2 r^2 + 2jkr + 2) - a^2 (jkr + 1) \right].$$

$$\frac{\partial^2}{\partial z^2} G_{zz'} = \frac{e^{-jkr}}{r^5} \left[a^2 - jkra^2 - k^2 r^4 + 2jkr^3 + 2r^2 + a^2 k^2 r^2 - 2jkra^2 - 2a^2 \right].$$

$$\frac{\partial^2}{\partial z^2} G_{zz'} = \frac{e^{-jkr}}{r^5} \left[-k^2 r^4 + 2jkr^3 + 2r^2 + a^2 k^2 r^2 - 3jkra^2 - 3a^2 \right]. \quad (\text{A.5})$$

The final substitution is (A.5) into (A.1).

$$-E_{app}(z) = \frac{1}{4\pi j\omega\epsilon} \int_I \frac{e^{-jkr}}{r^5} (-k^2 r^4 + 2jkr^3 + 2r^2 + a^2 k^2 r^2 - 3jkra^2 - 3a^2 + k^2 r^4) I(z') dz'.$$

$$-E_{app}(z) = \frac{1}{4\pi j\omega\epsilon} \int_I \frac{e^{-jkr}}{r^5} (+2jkr^3 + 2r^2 + a^2 k^2 r^2 - 3jkra^2 - 3a^2) I(z') dz'.$$

$$-E_{app}(z) = \frac{1}{4\pi j\omega\epsilon} \int_I \frac{e^{-jkr}}{r^3} \left((1 + jkr) \left(2 - 3 \left(\frac{a}{r}\right)^2 \right) + k^2 a^2 \right) I(z') dz'. \quad (\text{A.6})$$

(A.6) is the simplified form referred to in the text.